Periodic and locally resonant waveguides for vibration control in an industrial context

Jules Plisson

▶ To cite this version:

Jules Plisson. Periodic and locally resonant waveguides for vibration control in an industrial context. Acoustics [physics.class-ph]. Le Mans Université, 2021. English. NNT : 2021LEMA1043 . tel-03524415

HAL Id: tel-03524415
https://theses.hal.science/tel-03524415v1

Submitted on 13 Jan 2022

DOCTORAT BRETAGNE LOIRE SCIENCES POUR L'INGENIEUR

Le Mans Université

THÈSE DE DOCTORAT DE

LE MANS UNIVERSITÉ

ÉCOLE DOCTORALE N° 602
Sciences pour l'Ingénieur
Spécialité : « *Acoustique*»

Par
Jules PLISSON

Periodic and locally resonant waveguides for vibration control in an industrial context

Thèse présentée et soutenue à Le Mans, le 17 décembre 2021
Unité de recherche : Laboratoire d'Acoustique de l'Université du Mans, UMR CNRS 6613, Avenue Olivier Messiaen, 72085, Le Mans, France
Thèse N° : 2021LEMA1043

Rapporteurs avant soutenance :

Nicolas DAUCHEZ	Professeur, UTC Université de Technologie de Compiègne
Rubén PICÓ	Professeur, Universitat Politècnica de València

Composition du Jury :

Président :	Nicolas DAUCHEZ	Professeur, UTC Université de Technologie de Compiègne
Examinateurs :	Emeline SADOULET-REBOUL	Maître de conférences HDR, Université de Franche Comté
	Rubén PICÓ	Professeur, Universitat Politècnica de València
Dir. de thèse :	François GAUTIER	Professeur, Le Mans Université
Co-dir. de thèse :	Adrien PELAT	Maître de conférences HDR, Le Mans Université
	Vicent ROMERO-GARCIA	Chargé de recherche CNRS, Le Mans Université

Invité :

Thierry BOURDON	Senior Expert NVH simulation, Vitesco Technologies France SAS

Le Mans Université, France
Ecole doctorale Sciences Pour l'Ingénieur
Doctoral Thesis

Conduits périodiques et localement résonants pour le contrôle des ondes vibratoires en contexte industriel

---

by:
Jules PLISSON

Laboratoire d'Acoustique de l'Université du Mans, UMR CNRS 6613
Avenue Olivier Messiaen, 72085 Le Mans cedex 9, France

Vitesco Technologies France SAS
44 Avenue du Général de Croutte 31000 Toulouse, France

Reviewers :	Nicolas DAUCHEZ	Professor, UTC Université de Technologie de Compiègne
	Rubén PICÓ	Professor, Universitat Politècnica de València
Examiners :	Emeline SADOULET-REBOUL	Assistant professor, Université de Franche Comté
Supervisor :	François GAUTIER	Professor, Le Mans Université
Co-supervisors :	Adrien PELAT	Assistant professor, Le Mans Université
	Vicent ROMERO-GARCIA	CNRS Researcher, Le Mans Université
Industrial supervisor :	Thierry BOURDON	Senior Expert NVH simulation, Vitesco Technologies France SAS

Résumé

Le contrôle des vibrations des structures et de leur rayonnement acoustique sont des problématiques importantes dans de nombreux contextes industriels, en particulier liés au transport automobile. Dans un véhicule, l'excitation solidienne générée par une source (le moteur ou un équipement interne tel qu'une pompe) donne lieu à des phénomènes de propagation et de transmission vers des organes qualifiés de récepteurs, susceptibles d'induire un rayonnement acoustique gênant. Les performances acoustiques globales sont alors directement liées à sa capacité à réduire la transmission des vibrations. Dans le but de réduire les nuisances acoustiques induites par des pompes automobiles, nous nous intéressons à une configuration générique où le milieu de propagation est un guide d'ondes élastiques (conduite de carburant) et l'organe récepteur une plaque (représentative d'une cloison pare feu par exemple). Le travail de thèse porte spécifiquement sur la conception de deux architectures du guide d'ondes permettant de contrôler la transmission et l'atténuation simultanément pour les trois types d'ondes vibratoires présentes dans le guide d'ondes (ondes longitudinales, de flexion, de torsion).

La première architecture consiste en une organisation périodique de la structure du guide d'ondes élastiques : un tube de diamètre intérieur constant, présentant des variations de diamètre extérieur et de caractéristiques matériau est un cristal phononique, possédant des bandes d'arrêt pour les ondes longitudinales, de flexion et de torsion. L'optimisation de la géométrie de la cellule unitaire permet de positionner les bandes d'arrêt de façon à ce qu'elles se recouvrent en fréquence. La bande de fréquences d'arrêt, commune aux trois ondes est appelée bande absolue et caractérise un filtre multi-ondes, paramétrable. Les caractéristiques du filtre (diagramme de dispersion du guide d'ondes périodique) sont modélisées par un modèle semi-analytique basé sur le théorème de Floquet-Bloch, validé dans le cas conservatif par des simulations numériques (méthode des éléments finis) et par un démonstrateur expérimental. Le modèle semi-analytique, peu couteux en temps de calcul permet la prise en compte des mécanismes dissipatifs et des explorations paramétriques à des fins d'optimisation. Une réalisation expérimentale démontre la faisabilité pratique d'un filtre multi-ondes à bande absolue.

La deuxième architecture consiste en l'utilisation de résonateurs locaux réalisés au moyen de courtes bagues massiques enfilées sur le guide d'onde et couplées via une couche annulaire élastique. Les modes de corps rigide de ces bagues mettent en jeu des mouvements à dominante longitudinale, de flexion ou de torsion (ce dernier étant non exploitée dans la suite). On distingue deux classes de problèmes : le problème en transmission, conduisant à la conception d'un filtre fixant la transmission des ondes entre deux régions du guide d'onde et le problème en absorption, conduisant à la conception d'une terminaison permettant d'absorber les ondes incidentes sur cette terminaison. Ces types de résonateurs peuvent être accordés en fréquences de façon à contrôler simultanément les ondes longitudinales et de flexion, constituant ainsi des filtres multi ondes. Des groupes de résonateurs, à caractéristiques variables permettent par ailleurs de créer des filtres multi-fréquences. Les performances de ces stratégies sont explorées de façon semi-analytiques et numériques. Une validation expérimentale est fournie dans le cas d'un filtre multi-fréquences, pour le problème de flexion en absorption.

L'intégration d'un filtre vibratoire obtenu au moyen des architectures périodiques est testée dans trois environnements de complexité croissante : 1/ si un tube guide d'onde rectiligne donne lieu à un découplage entre ondes longitudinales et de flexion, l'effet d'une courbure du milieu, inévitable en pratique induit un couplage entre ces deux ondes. L'intérêt pratique d'un filtre multi-ondes à bande absolue apparait alors car il permet de réaliser une absence de transmission entre source et récepteur, même en présence de courbure du milieu. 2/ Le rayonnement acoustique d'une plaque réceptrice est significativement réduit lorsqu'un guide d'onde architecturé est utilisé, 3/ la présence d'un couplage vibroacoustique via un fluide lourd emplissant un conduit architecturé complexifie les courbes de dispersion. On montre que certaines géométries présentent néanmoins des bandes absolues pour les ondes élastiques et vibroacoustiques, ce qui permet un découplage remarquable entre source et organe récepteur, ce qui constitue la configuration recherchée par l'ingénieur.

Abstract

The control of structural vibrations and their acoustic radiation are important issues in many industrial contexts, particularly related to automotive transportation. In a vehicle, the structure-born excitation generated by a source (the engine or an internal equipment such as a pump) gives rise to propagating and transmission phenomena towards the systems qualified as receivers, which are likely to induce a disturbing acoustic radiation. The overall acoustic performance is therefore directly linked to its ability to reduce the transmission of vibrations. In order to reduce the acoustic nuisance induced by automotive pumps, we are interested in a generic configuration where the host medium is an elastic waveguide (fuel line for example) and the receiving system is a plate (representative of a wall of a car for example). The PhD thesis focuses specifically on the design of two waveguide architectures allowing to control the transmission and the attenuation simultaneously for the 3 types of vibratory waves present in the waveguide (longitudinal, bending and torsion waves).

The first architecture consists of a periodic organization of the elastic waveguide: a tube of constant inner diameter, with periodic variations in outer diameter and material characteristics is known as a phononic crystal, with band gaps for longitudinal, bending and torsional waves. By optimizing the geometry of the unit cell, the band gaps can be positioned so that they overlap in the same frequency range. The frequency band, common to all three waves, is called absolute band and characterizes a multi-wave filter, which can be parameterized. The characteristics of the filter (dispersion diagram of the periodic waveguide) are modeled by a semi-analytical approach based on the Floquet-Bloch theorem, validated in the conservative case by numerical simulations (finite element method) and by an experimental demonstrator. The semi-analytical model, inexpensive in computational time, allows the consideration of dissipative mechanisms and parametric explorations for optimization purposes. An experimental realization shows the practical feasibility of a multi-wave absolute band filter.

The second architecture consists in the use of local resonators realized by means of short mass rings threaded on the waveguide and coupled via an elastic ring layer. The rigid body modes of these rings involve predominantly longitudinal, bending or torsional motions (the latter not being considered in the following). We distinguish two types of problems: the transmission problem, leading to the design of a filter fixing the transmission of waves between two regions of the waveguide and the absorption problem, leading to the design of a termination allowing to absorb the waves incident on this termination. These types of resonators can be tuned in frequency so as to simultaneously control longitudinal and bending waves, thus constituting multi-wave filters. Groups of resonators with varying characteristics can also be used to create multi-frequency filters. The performances of these strategies are explored in a semi-analytical and numerical way. An experimental validation is provided in the case of a multi-frequency filter, for the absorption bending problem.

The integration of a vibratory filter obtained by means of periodic architectures is tested in three environments of increasing complexity: 1/ if a straight waveguide pipe gives rise to a decoupling between longitudinal and bending waves, the effect of a curvature of the medium, unavoidable in practice, induces a coupling between these two waves. The practical interest of a multi-wave filter with absolute band gaps appears then because it makes possible to carry out an absence of transmission between source and receiver, even in presence of curvature of the medium. 2/ The acoustic radiation of a receiver plate is significantly reduced when an architecturally designed waveguide is used, 3/ The presence of a vibroacoustic coupling via a heavy fluid filling an architectured waveguide makes the dispersion curves more complex. It is shown that some geometries nevertheless present absolute bands for elastic and vibroacoustic waves, which allows a remarkable decoupling between source and receiver, which is the configuration sought by the engineer.

Key-words: Phononic crystal, Waveguide, Vibration filter, Vibration absorber, Locally resonant structure, Multi-wave vibration control

Remerciements :

Tout d'abord je souhaite remercier les membres du jury, pour avoir accepté d'examiner et de commenter mes travaux de thèse: Nicolas Dauchez et Rubén Picó pour avoir accepté d'être le rôle de rapporteur, Emeline Sadoulet-Reboul pour avoir accepté d'examiner mes travaux lors de la soutenance.

Sans eux rien de tout cela n'aurait été possible, je tiens à remercier la direction de ma thèse: François Gautier, Adrien Pelat et Vicent Romero-garcia qui m'ont accompagné tout le long du chemin, ainsi que Thierry Bourdon pour sa bienveillance et pour m'avoir ouvert les portes de Continental puis Vitesco.

Je tiens également à remercier Simon Felix et Thomas Gallot pour avoir accepté de suivre cette thèse régulièrement au sein de mon comité de suivi.

Merci à mes relecteurs pour avoir subi ma prose laborieuse Fiona, Vincent, Julien, Thibault.
J'ai eu la chance de profiter du dispositif de financement CIFRE, avec le partenariat de Vitesco Technologies (ex-CPT ex-Continental Automotive). Sans ces financements je n'aurais pas pu arriver jusque-là. Merci également à Le Mans Université d'avoir assuré les derniers mois jusqu'à la soutenance.

Je remercie également le LAUM et son directeur Pierrick Lotton de m'avoir accueilli dans le laboratoire, ainsi que Jean-François Tassin pour m'avoir accueilli a l'ENSIM. Bien entendu je tiens également à remercier les nombreuses personnes qui ont rendu tout cela possible : Paola Bertelli, Safia Vierra, Stéphanie Touchard, Christelle Pavard, Sandrine Chassagne et bien d'autres.

Sans eux aucun démonstrateur et aucun résultat expérimental n'auraient pu exister. Merci à Julien Nicolas et Stanislas Renard d'avoir usiné les démonstrateurs et Mathieu Secail-Geraud et Félix Foucart de m'avoir accompagné dans la prise en main du matériel expérimental.

Mes remerciements vont aussi à mes collègues de mes nombreux bureaux. Justine, Julien et Torea pour avoir accueilli le nouveau doctorant dans la joie et la bonne humeur, j'ai énormément appris à votre contact, le bureau en face de la Kfet restera un bon souvenir grâce à vous. Alina, Léo, merci de m'avoir accompagné au fil des bâtiments à Continental puis Vitesco. Erwan, Erwan, Alex, Guillaume, Audrey, Saoucène, Jean-Baptiste, Meryem, Natacha, merci de m'avoir fait une place dans le "bureau des doctorants" lors de mon retour au Mans. Merci aussi aux docteurs ou doctorants avec qui j'ai eu l'occasion d'échanger : Omar, Antoine, Paul, Charlie, Gautier, Samuel, Massimo et Théo.

Sans amis ces dernières années auraient été bien difficiles. Je tiens donc à remercier les tourangeaux, les bons copains et la ligue (et ses nombreux docteurs) pour les moments de partage houblonnés et le soutien inconditionnel. Une ligne spécialement pour toi Thibault qui rentre dans beaucoup trop de catégories, collègue, amis et collocataire merci d'avoir vécu ce doctorat avec moi.

Pour conclure ces remerciements, je tiens à citer ma famille qui m'a toujours soutenu dans mes choix, et tout spécialement Fiona qui partage ma vie et m'a supporté tout au long de ce voyage.

Contents

1 Introduction **1**

1.1 Context and motivation . . . 2

1.1.1 Vitesco Technologies France . . . 2

1.1.2 Challenges of vibration control for light structures . . . 3

1.2 Research ojectives . . . 3

1.3 State of the art . . . 4

1.3.1 Common methods for vibration control . . . 4

1.3.2 Resonant structures . . . 6

1.3.3 Phononic crystals . . . 9

1.4 Outline of the thesis . . . 21

2 Design of multi-wave vibration filter based on Phononic Crystal pipes with absolute bandgap **22**

2.1 Introduction . . . 23

2.2 1D models of periodic structural waveguides using the Floquet method . . . 23

2.2.1 Definition of the waveguide . . . 24

2.2.2 Floquet-Bloch model of the longitudinal and torsional waves dispersion . . . 25

2.2.3 Floquet-Boch model for flexural wave dispersion following Timoshenko theory 26

2.3 Validation of the 1D models . . . 27

2.3.1 Uniform waveguides . . . 28

2.3.2 Periodic waveguides . . . 28

2.4 Evolution on the absolute bandgap based on parametric variations . . . 30

2.4.1 Monomaterial waveguides . . . 30

2.4.2 Bimaterial waveguides . . . 31

2.5 Numerical optimization of the absolute band gap based on Nelder-Mead algorithm . 32

2.5.1 Nelder-mead algorithm . . . 32

2.5.2 Analysis of performance optimisation for various weightings of $\mathcal{F}$ . . . 33

2.6 Study of an experimental demonstrator . . . 35

2.6.1 Design of the experimental demonstrator . . . 35

2.6.2 Experimental set-up . . . 36

2.6.3 Results . . . 37

2.7 Conclusions . . . 38

3 Design of 1D multi-wave vibration filters and absorbers based on local resonators inserted in waveguides **39**

3.1 Introduction . . . 40

3.2 Dynamic behaviour of locally resonant structures . . . 40

3.2.1 Design of a local resonator on a beam . . . 40

3.2.2 Analytical model of the resonant frequency . . . 42

3.2.3 Numerical parametric variation of ring resonators and associated resonance frequencies . . . 42

3.3 Reflection and transmission coefficients of locally resonant structures . . . 43

3.3.1 Study of the variation of the parameters of a local resonator 45
3.4 Examples of vibration filter configurations 48
3.4.1 Parameters of ring resonators 48
3.4.2 Design of a graded flexural filter 49
3.4.3 Design of a graded multi-wave filter 51
3.5 Examples of vibration absorber configuration 53
3.5.1 Design of a graded flexural absorber 54
3.5.2 Design of a tuned vibration absolute absorber 55
3.6 Experimental evidence of peak absorbance 56
3.6.1 Experimental set-up 56
3.6.2 Measurement of the reflection coefficient of the host material 58
3.6.3 Measurement of the frequency of a local resonator 58
3.6.4 Parametric variation of Numerical design of resonators 60
3.6.5 Evidence of the absorption peak 61
3.7 Conclusions 64

4 Implementation of a 1D multi-wave vibration filter in industry-inspired examples 65
4.1 Introduction 66
4.2 Effect of the curvature of the waveguide on the transmission of vibratory waves . . . 66
4.2.1 1D phononic crystal curved waveguides 67
4.2.2 1D phononic crystal waveguide with a bent segment 69
4.2.3 1D phononic crystal waveguide with several bent segments 71
4.3 Acoustic radiation from a plate coupled to a vibrational filter made of a 1D phononic crystal waveguide 74
4.3.1 Set-up of a 1D phononic crystal waveguide coupled to a radiating plate . . . 74
4.3.2 Radiated acoustic power of a 1D phononic crystal waveguide coupled to a radiating plate 76
4.4 Influence of a heavy fluid on the vibration filtering properties of a 1D phononic crystal pipe 79
4.5 Conclusion 83

5 Conclusions and perspectives 84
5.1 Conclusions 84
5.2 Perspectives 86

List of figures 95

List of tables 97

Bibliography 99

A Appendix : Published Article 113

B 1D Model of periodic waveguide with locally resonant structures 119
B.1 Floquet Bloch model for longitudinal and torsional waves dispersion 119
B.2 Floquet Bloch model for flexural wave dispersion 120
B.3 Reflection and transmission coefficients of locally resonant structures 121

Chap. 1

Introduction

Contents

1.1 Context and motivation . . . 2
  1.1.1 Vitesco Technologies France . . . 2
  1.1.2 Challenges of vibration control for light structures . . . 3
1.2 Research ojectives . . . 3
1.3 State of the art . . . 4
  1.3.1 Common methods for vibration control . . . 4
  1.3.2 Resonant structures . . . 6
  1.3.3 Phononic crystals . . . 9
1.4 Outline of the thesis . . . 21

1.1 Context and motivation

1.1.1 Vitesco Technologies France

Vitesco Technologies France SAS, formerly Continental Automotive SAS, designs and produces automotive engine components such as fuel pumps, fuel injection rails and electric motors. One of the recurring needs expressed in this industrial context is the reduction of noise pollution inside and outside the vehicule. Depending on the use of the vehicle, the origin of the noise is different: engine noise at low speed, road noise at medium speed and aerodynamic noise at high speed.

The Noise Vibration Harshness (NVH) division of CPT France, in which this thesis work is positioned, deals specifically with problems related to engine noise. In particular, the objective of this work is to develop techniques to reduce the vibrations emitted by an engine component to the rest of the engine block. Figure 1.1 illustrates a general example of this problem on which the work presented in this document is based on.

In this type of automotive vibro-acoustics problem, the technical complexity elements to be addressed are the following:

- the complex movements of the component playing the role of source cause the generation of various types of waves (flexion, longitudinal, torsion),
- the bent geometry of the transmission path induces couplings between the different types of emitted waves,
- the frequency ranges of interest can be quite wide band (several kHz wide),
- the treatment aimed at limiting the vibratory transmission must not induce a significant addition of mass.

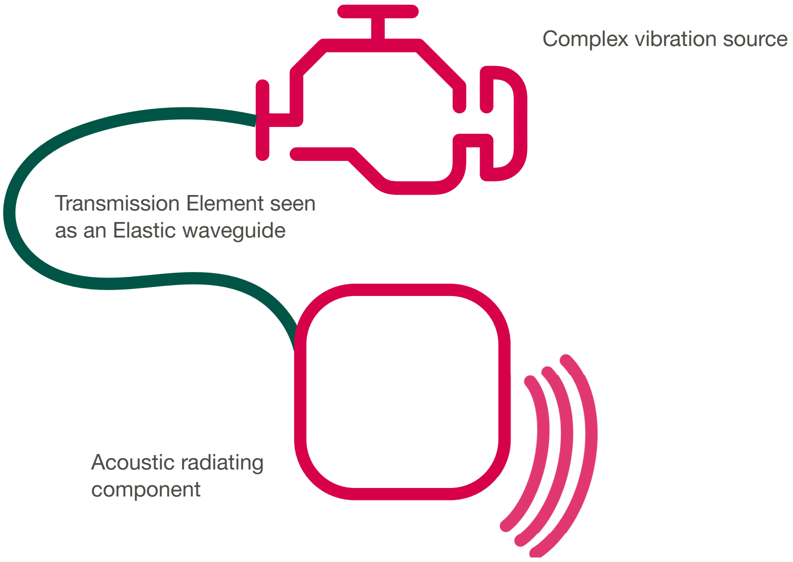

Figure 1.1 – Diagram of a generic industrial system as treated in this thesis. An element is considered as a vibratory source, here schematized as a motor. A transmission elements seen as an elastic waveguide conducts the vibrations produced by the source to a acoustic radiating component, which propagates the vibrations emitted by the source.

As in many other examples of this nature, the design of the vibrating source element is heavily constrained by technology, so that it cannot be modified to reduce structural vibration emission. The same is true for the receiver. However, it is still possible to optimize the transmission element to introduce an additional vibration filtering function into the overall system.

This PhD developed in a collaborative framework between the Acoustics Laboratory of Le Mans University (LAUM) and Vitesco Technologies France SAS, is the result of an end-of-study project between the Ecole Nationale Supérieure d'Ingénieurs du Mans (ENSIM) and Continental Automotive SAS. The objective of this project is to demonstrate the effectiveness of periodic waveguides as vibration filters for flexural waves.

1.1.2 Challenges of vibration control for light structures

The global objective of reducing the energy consumption of vehicles is leading to a trend towards lighter structures. This reduction in consumption is a result of the increasing impact of air pollution on our society. To counteract this impact, increasingly restrictive legislation is pushing manufacturers to improve the efficiency of their propulsion systems. In addition to the use of electric or hybrid motors, this has resulted in a strong trend towards the design of lightweight vehicles that require less energy to move.

To enhance structural integrity, reliability, drivability and passenger safety, lightweight structures are typically also designed for higher strength and stiffness. However, the reduction in mass to stiffness ratio due to this lightweight design results in a lower comfort performance in terms of noise and vibration. Unfortunately, noise is the second most important environmental threat in Europe, just after air pollution [1, 2]. The reduction in sound comfort due to lightweight structures is in contradiction with the demand of the users and also with the legislation on noise exposure, 74 dB(A) for a private car [3].

The traditional method of increasing sound and vibration damping is through the use of passive treatments [4–7]. These rely on adding mass to increase sound absorption, which is incompatible with the concept of lightweighting structures. These classic treatments are therefore no longer used in the modern transport industry [8]. In addition, technological developments are leading to the emergence of new noise sources [9]. The solutions usually used in an internal combustion engine are not going to be relevant in an electric motor. To deal with the inadequacy of traditional noise control solutions, new solutions are being investigated. They must be efficient but also meet the criteria of modern vehicles, i.e. have low mass, low volume, low cost and be adapted to the low frequency range.

1.2 Research ojectives

In the initial framework, the system on which the thesis work is to be applied consists in a fuel pressurisation pump emitting vibrations that are transmitted to a fuel rail through the metal pipe as described in the Chap. 4. When Continental Automotive France became Vitesco technologies France SAS, in 2019, the development of technologies related to thermal engines was abandoned, including the system mentioned earlier, in favor of electric technologies.

The objective of this thesis is to optimize a pipe, in order to create a vibration filter integrated in an industrial part without altering its primary function. The geometry of the pipe, considered as a waveguide for vibration is adapted to be integrated in a complete industrial system, which implies a coupling phenomenon between the different types of waves. For the solution proposed in the thesis to be relevant in an industrial standpoint, the geometry of the waveguide must be constructed in such a way that an effective vibratory solution in the same frequency band for different types of waves (longitudinal, torsional and flexural) is obtained.

There are several works which provide interesting directions to build this solution. Periodic structures have the effect of creating frequency bands in which the propagation of a wave is strongly attenuated. These frequency bands are commonly called band gaps in the case of infinite periodic structures. They are present for different types of elastic waves, longitudinal, torsional and flexural. The band gaps associated with each type of wave are not necessarily in the same frequency range. Locally resonant material does provide possibilities to absorb waves by means of the resonances opening the well-known stop bands. The problem proposed in this thesis is the following: The realisation of a multi-wave vibration filter, or absorber, targeted for a given frequency range, by optimising a periodic waveguide geometry so that it can be integrated into an industrial system.

1.3 State of the art

Before presenting the work done in this PhD, this section gives an overview of the state of art in the field of vibro-acoustics. As this discipline encompasses many different applications and techniques, we will focus on the vibration control in the transport industry, locally resonant structures and periodic structures, as they are used and developed.

1.3.1 Common methods for vibration control

As we have seen, the control of noise and vibration in the transport industry, automotive, aviation and railways, is an important issue. There are many methods to obtain an attenuation of noise and vibration, some of which are based on active and semi-active technologies, others are passive.

Active and semi-active technologies are based on the addition of electrical components that act on the sound signal to be masked or on the noise source to be attenuated. In acoustics, speakers are used to obtain a sound masking effect such as those popularised by active noise suppression headphones [10], which are based on the diffusion of a sound signal in phase inversion with respect to the noise to be suppressed [11]. In the case of an application on vibratory sources, piezoelectric transducers [12] are used. The method is said to be active when a current is applied to the patches [13] and semi-active when it is coupled to an electrical circuit [14] which will dissipate the electrical voltage produced by the deformation of the piezoelectric patch.

For airborne noise control passive methods are based on the use of silencers, absorbers, barriers, mufflers [15]. For reducing structural vibration the solutions are varied. A first method consists in modifying the receiving system by adding stiffness or mass, so that its eigenmodes are no longer excited by the frequency band of the excitation source [16, 17]. However in most cases, the vibrations need to be isolated or dissipated by using isolator or damping materials. Other methods are widely discussed in the literature. There are many books and articles to refer to [4–7, 18–21]. The classic vibro-acoustic treatment is the addition of a viscoelastic layer to increase the damping effects of the structure. This addition of a viscoelastic layer is done in different ways, free-layer damping, see Fig. 1.2(a), constrained-layer (Fig. 1.2(b)), or sandwich-layer (Fig. 1.2(c)).

The free layer damping, Fig. 1.2(a), consists of a layer of viscoelastic added to the structure to be treated. When the host structure undergoes flexural deformation, the viscoelastic deforms mainly in traction and compression in planes parallel to the host structure. The hysteresis loop of cyclic stress and strain dissipates energy. The added damping depends on the amount and properties of the added viscoelastic material. Often, in industrial systems, the degree of damping is limited by thickness and weight restrictions. This technology is used, for example, for automotive floor panels.

The constrained layer damping, Fig. 1.2(b), involves adding a elastic surface layer to the viscoelastic material. This upper stiff layer forces shear deformation of the viscoelastic material when the host structure undergoes flexural vibration. In this way more energy is dissipated into heat by the viscoelastic material. This technology is used for example in aircraft fuselage.

The multilayered viscoelastic beams, Fig. 1.2(c), consist in layering constrained layer treatments. A large number of works have been produced in recent years [22–26] to predict the behaviour of multilayered structures and how they can attenuate vibrations. This technology makes it possible, for example, to anticipate temperature changes of the viscoelastic in a brake pad, or to obtain wider frequency effects.

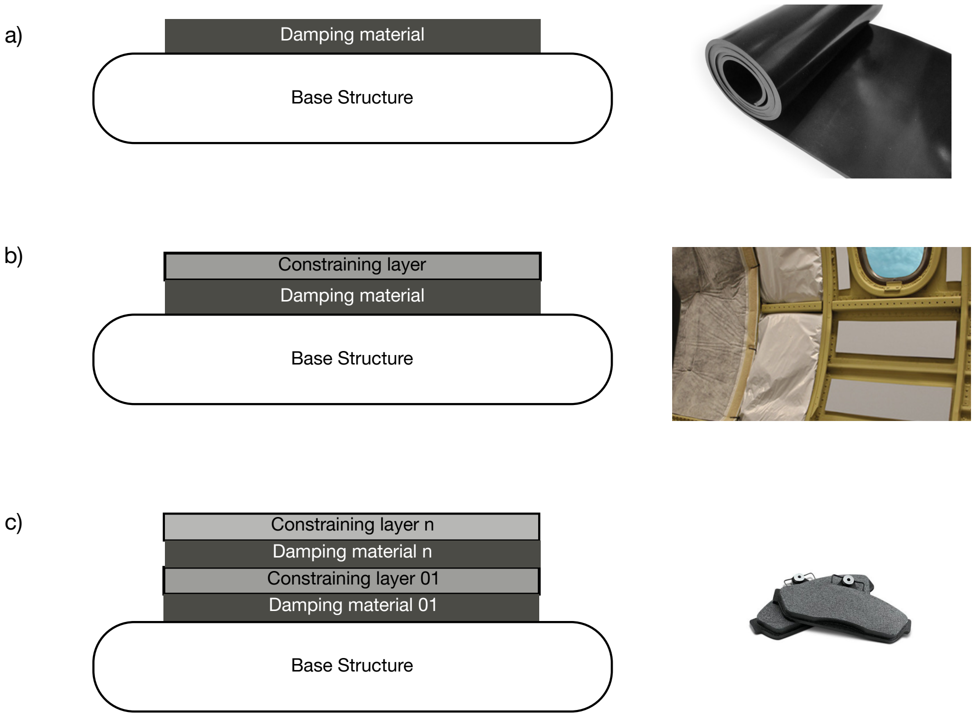

Figure 1.2 – Free layer damping, viscoelastic sheet (a). Constrained layer damping, aircraft fuselage (b). Multi-layered or sandwich damping, brake pad (c). (Figure inspired from Ref. [8])

Although these methods have been used for a long time [27], they are still relevant today thanks to the evolution of knowledge and technologies, allowing us us to obtain better performing viscoelastic materials [28].

In the following sections, we will focus on the advantages brought by the use of resonant structures and the use of phononic crystal to the field of vibration control. In particular, these structures bring possibilities to tune the working frequency range. However, there are many other innovative vibro-acoustic treatments, such as the development of acoustic black holes where an incident wave trapped by a property gradient is dissipated by the addition of a viscoelastic layer [29–36], or the use of granular materials where the interactions between grains lead to an absorption phenomenon [37].

1.3.2 Resonant structures

This section discusses the use of resonators in vibro-acoustic treatments. A resonator consists of three elements:

- a mass M,
- a stiffness k,
- a damping C.

The resonant frequency, ω_0, of the conservative resonator is calculated:

$$\omega_0 = \sqrt{\frac{k}{m}}. \tag{1.1}$$

The use of a resonator tuned to a specific frequency makes it possible to obtain a vibration-absorbing effect [4–7]. This principle is the one of the dynamic absorber and is widely used in industry to dampen the vibrations of rotating machines, we discuss the main features as follows.

In this type of systems the absorbing frequency occurs at the resonant frequency, Eq. 1.1. The objective here is to tune the resonators to the generator frequency. Figure 1.3(a) shows the schematic of a dynamic absorber as commonly described. The effect of an undamped dynamic absorber is to eliminate the vibration for the frequency of interest but also to introduce two resonant frequencies of the system Ω_1 and Ω_2, see Fig. 1.3(b). The addition of damping in the rubber helps to smooth the curve.

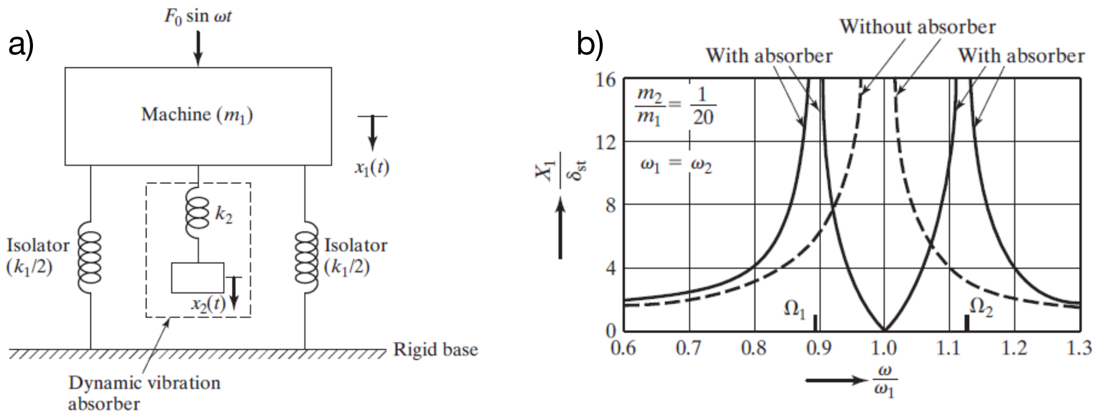

Figure 1.3 – Drawing of an undamped dynamic vibration absorber (a). Effect of undamped vibration absorber on the response of the machine (b). (Figure from Ref. [7])

The disadvantage of this type of system is that it requires a high mass to be effective at low frequencies. It is well suited to the treatment of machines where mass is not an issue in conventional use. In audible acoustics, the use of acoustic resonators to attenuate noise is widely discussed in the literature [38–43], and even already used in architecture [44], but also in the context of automotive [45] or aeronautic [46].

The addition of a mass element is not compatible with the current ligthweigth philosophy of the transport industry. However, it is still possible to use these structures to control the transmission of waves through the waveguides connecting the vibration source to the other elements. There are a number of references in the literature where the control of wave propagation using a local resonator is discussed [40, 45, 47–51].

The addition of a tuned vibration absorber on a beam [47–49] allows us to control the propagation of flexural waves in this beam [50], see Fig. 1.4. This control is evidenced by the reflection and transmission coefficients [52, 53] showing that at the resonance frequency there is not propagation of waves through the waveguide.

The influence of the tuned vibration absorber will depend on many parameters: its resonant frequency, its mass, the damping of the resonator and its distance from the vibration source. If the tuned vibration absorber can be considered in the far field, the distance to the source can be ignored. The far-field condition is considered when the source-resonator distance is large compared to the wavelength of interest. The optimisation of a tuned vibration absorber consists in finding the combination of parameters allowing a minimum of power transmitted or a maximum of power absorbed by the resonator [50].

Figure 1.4 shows the effect of a local resonant vibration absorber. The measurement is performed using two pairs of accelerometers: A_1 and A_2 are the locations of the accelerometers used to estimate the upstream propagating flexural waves. A_3 and A_4 are the same for the downstream propagation waves. The ends of the beam were embedded in sand boxes to reduce waves reflection. The incident wave a^+ experiences a drop in transmission and reflection at the analytically predicted frequency. In this configuration, in transmission, and with a single tuned vibration absorber, a maximum absorption of $\alpha = 0.5$ can be obtained [54]. The flexural wave is partially filtered and absorbed around a frequency corresponding to the resonance frequency of the resonator.

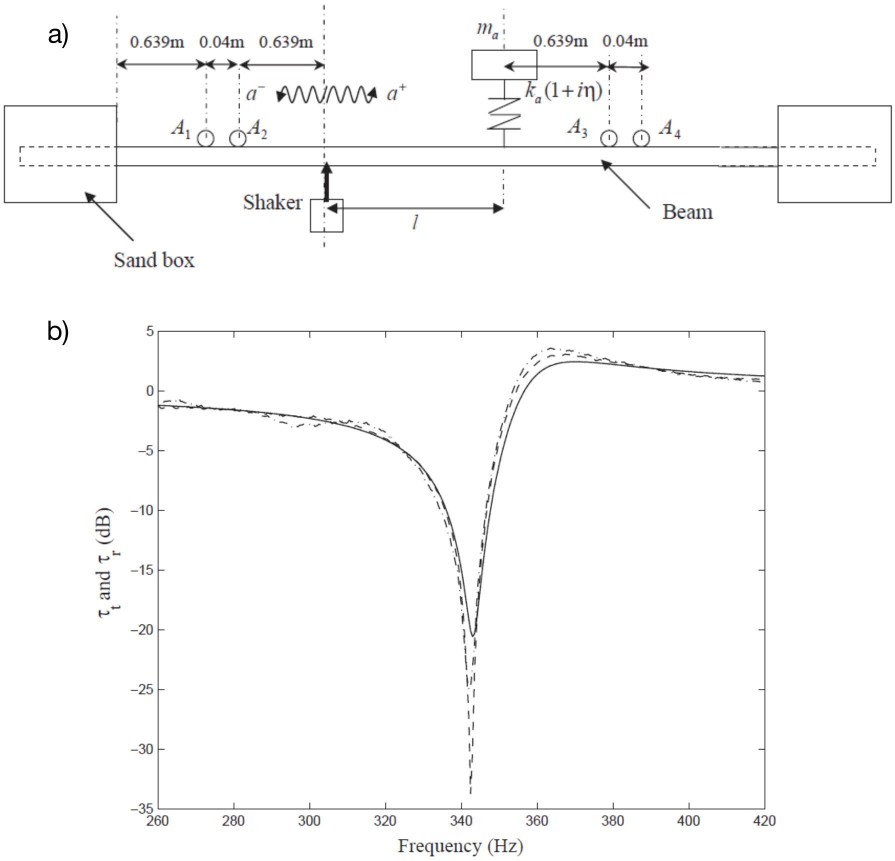

Figure 1.4 – Experimental set-up (a) and reflection and transmission ratio (b), (—) for the analytical method and (- · · ·) for the experimental reflection, and (- - -) fot the experimental transmission, (Figure from Ref. [50])

Vibration absorption phenomena using a local resonator are also used on more atypical structures. Figure 1.5 shows an example of flexural wave control by designing part of the beam as a resonator [54]. Here the beam section that has an absorbing effect can be considered as a resonator placed at the end of the beam (a). In this configuration only the reflection coefficient is playing role. By analyzing the complex frequency plane of the reflection coefficient, perfect absorption is achieved when the zero of $|R|$ is placed in the real frequency axis. This is known as the critical coupling condition and represents the impedance matching of the system (b). With a single tuned vibration absorber and taking into account the losses, a perfect absorption, $\alpha = 1$, can be obtained at the resonance frequency (c). This phenomenon is the interpretation of the acoustic Black Hole effect [29].

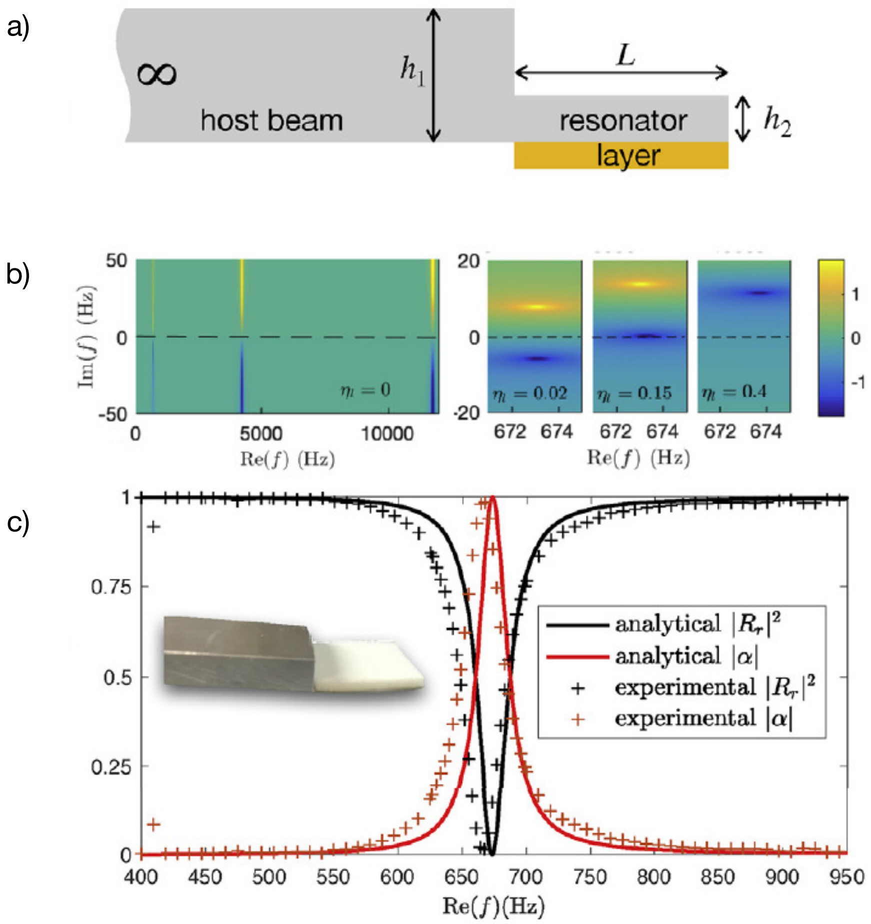

Figure 1.5 – Analysis of the open resonators in reflection configuration. Diagrams of the beam terminaison (a). Representation of $log_{10}(|R_r|)$ in the complex frequency plane for the lossless and lossy configurations respectively (b). Analytical and experimental measurement of the reflection $|R_r|^2$ and absorption α (c). (Figure from Ref. [54])

Many papers discuss the use of a resonator inside the waveguide [55–57], which is of interest for load bearing structures such as automotive substructures. The shape and use of the resonators can be various [58–63].

1.3.3 Phononic crystals

Generalities

The control of elastic waves by periodic structures have been considerably developed during the last decades by using phononic crystals [64] as analogously done for light waves by Photonic crystals [65]. These systems, made of either periodic distributions of scatterers embedded in a physically dissimilar host material [66] (Fig. 1.6(a)), or simply periodic geometries [67–69], are driven by a particular dispersion relation showing band gaps [70, 71], ranges of frequencies produced by the Bragg interferences in which the propagation of waves is forbidden [72–76]. In Fig. 1.6(b) the first band gap occurs at 1670 Hz, identified by the arrows [100].

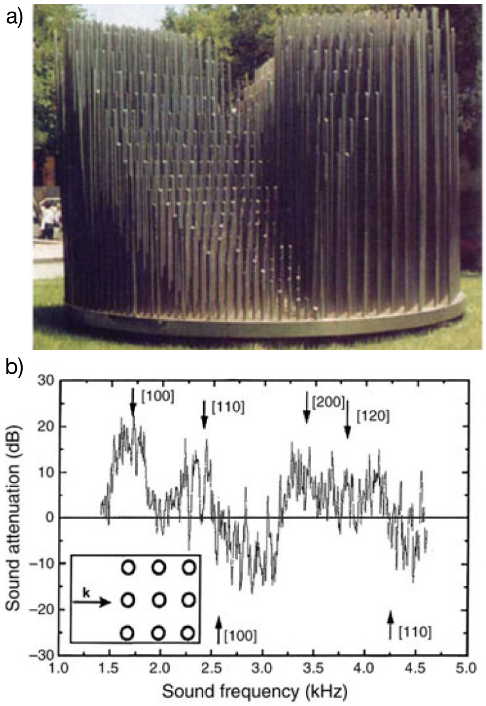

Figure 1.6 – Eusebio Sempere's sculpture in Madrid, Spain, (a). Measured sound attenuation as a function of frequency. The inset illustrates the direction of propagation of sound waves. Arrows indicate the calculated maxima and minima due to interference from the different crystal planes of the sculpture, (b). (Figures from Ref [66])

Dispersion relation of phononic crystals

The dispersion relation of phononic crystals can be obtained by using the Transfer Matrix Method [77–82], Plane Wave Expansion Method [83, 84], Waveguide Finite Element method [85, 86] or varying amplitudes method [87] among others. Significant progress has been made on the control of flexural or longitudinal waves by phononic crystals showing different applications including filtering [88], wave trapping [89, 90], wave-guiding [91], focusing by refracting [92, 93] or scattering waves [94] as well as self-collimation [95, 96], among others [97, 98]. Figure 1.7 show the dispersion diagrams of the acoustic and elastic periodic structures. Evidence of band structure in acoustic wave propagation in a system made up of several dangling side branches periodically grafted at each of the equidistant sites on a slender tube. We can see the relationship between the dispersion relation (right) and the actual transmission (left) in a finite system. A drop in transmission appears around band gap frequencies [99] (Fig. 1.7(a)). Pass and stop bands were found in 1D layered composites, mokume-gane, consisting of steel and copper foils [100] (Fig. 1.7(b)).

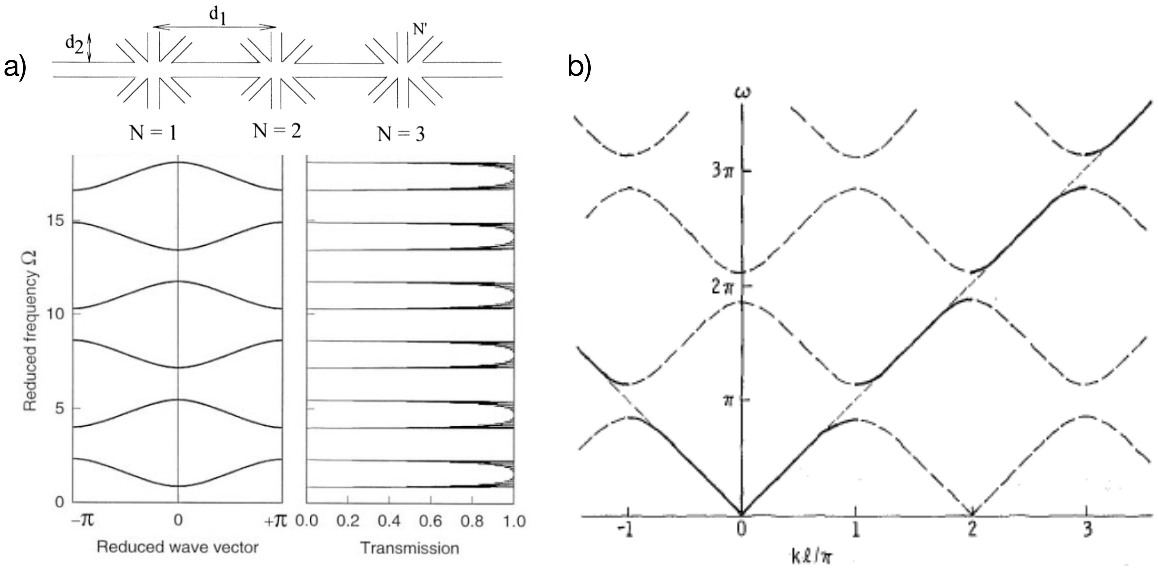

Figure 1.7 – Band structure and transmission spectrum for a system of open tubes. N' is the number of dangling side branches(of length d_2 and cross-section a_2) grafted on N equidistant sites (with period d_1) ofa slender tube. Reduced wave-vector refers to the dimensionless Bloch vector $k_b l_{tot}$ and the reduced frequency is defined by $\Omega = \omega(l_{tot}/c_1)$, ($c_1$ is the speed of sound in the segment 1). We consider identical fluid both inside the dangling side branches and inside slender tube (a). Theorical dispersion of waves propagating normal to the layering in 1D layered composites(b) (Figures from Refs. [99, 100])

Figure 1.8 shows a classic example of a periodic structure from the work of Hvatov and Sorokin [79]. The segments of the periodic cell are defined by their respective lengths l_1 and l_2, with $l_{tot} = l_1 + l_2$, h_1, h_2 the segment width, E, ρ, ν respectively Young's modulus, density and Poisson's ratio. The calculation of the frequency bands is done by writing the continuity equations, at the ends of each segment of the cell, for continuity of displacement v_i, slope Ψ_i, flexural moment M_i and shear force Q_i:

$$\begin{array}{rcl} v_1(l_1) & = & v_2(l_1) \quad , \quad v_2(l_{tot}) = v_3(l_{tot}), \\ \Psi_1(l_1) & = & \Psi_2(l_1) \quad , \quad \Psi_2(l_{tot}) = \Psi_3(l_{tot}), \\ M_1(l_1) & = & M_2(l_1) \quad , \quad M_2(l_{tot}) = M_3(l_{tot}), \\ Q_1(l_1) & = & Q_2(l_1) \quad , \quad Q_2(l_{tot}) = Q_3(l_{tot}). \end{array} \tag{1.2}$$

The periodicity is described by the Floquet conditions

$$\begin{array}{c} v_1(0)=\Lambda v_3(l_{tot}), \\ \Psi_1(0)=\Lambda \Psi_3(l_{tot}), \\ M_1(0)=\Lambda M_3(l_{tot}), \\ Q_1(0)=\Lambda Q_3(l_{tot}), \end{array} \tag{1.3}$$

where $\Lambda = e^{ik_b}$ and k_b is the unknown Bloch wavenumber.

A periodic unit cell can be constructed with segments of different geometry and materials as illustrated in Fig. 1.8(a) and (b). It is the periodicity phenomenon described by Eq. 1.3 that allows the band gap to open. In Fig. 1.8(c), the band gaps are identified when $|\Lambda| \neq 1$, these band gaps are controlled by the parameters of the periodic cell.

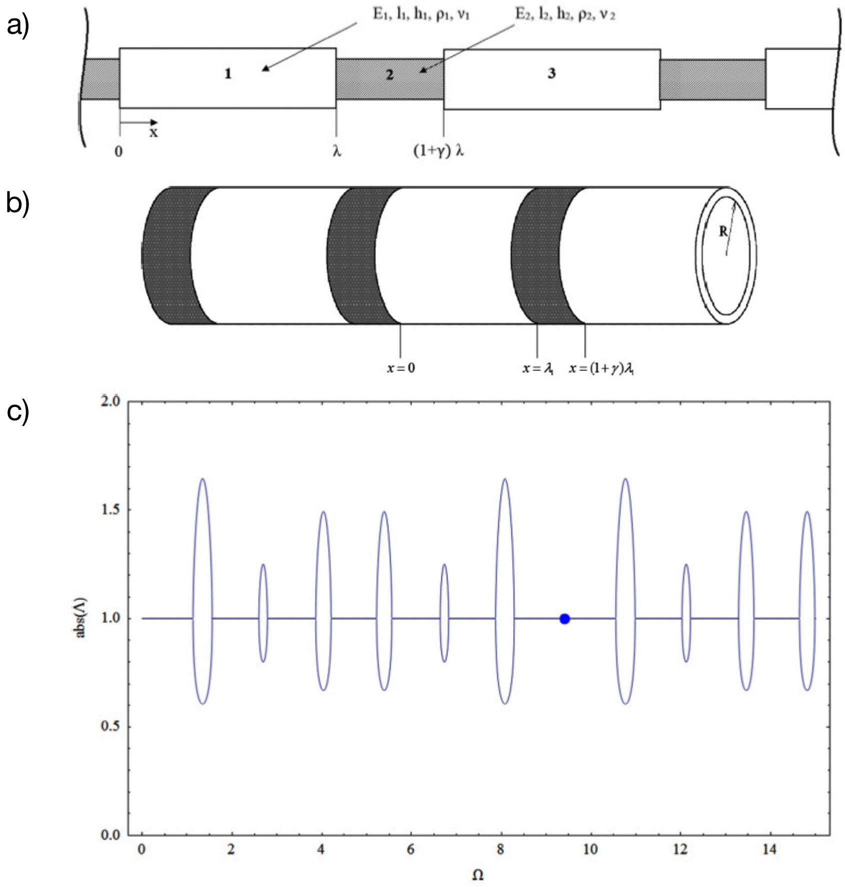

Figure 1.8 – Example of infinite periodic waveguide with two component (a). Periodic cylindrical shell (b). Dependant of $\Lambda = e^{ik_b}$ upon $\Omega = \frac{\omega h_1}{c_1}$, $|\Lambda| \neq 1$: stop-band, $|\Lambda| = 1$: pass-band (c). (Figure from Ref. [79]).

1D phononic crystal

Periodic structures allow to obtain particularly interesting bandgap effects. This periodicity can be obtained by many means, the repetition of segments [79, 101–104], 1D phononic crystals with alternating materials in the radial and axial directions [105]. It is also possible to obtain a band gap with kirigami inspired structure [106, 107] (Fig. 1.9). It is a hexagonal shape that is widely used in bio-inspired honeycomb structures. This shape is used for its mechanical strength properties compatible with the philosophy of lightweight structures [108]. This honeycomb structure allows for multiple band gaps that can be modified by adjusting the parameters of the structure.

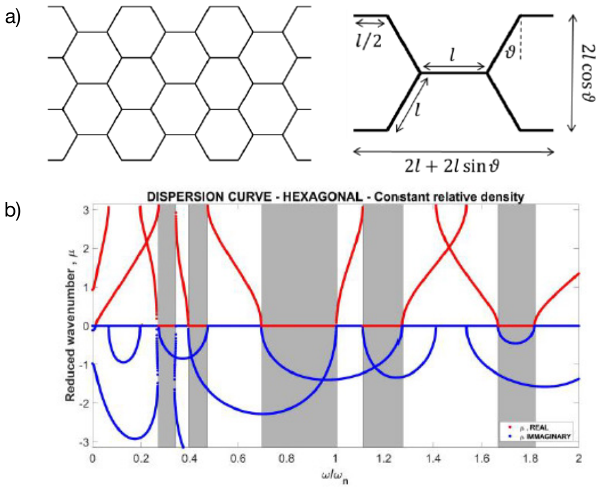

Figure 1.9 – Example of a kirigami phononic crystal with a hexagonal unit cell, (a), this type of cell leads to the following dispersion diagram, real part at the top and imaginary part at the bottom, (b). (Figure from Ref. [106])

Bent or curved structure can also be used to generate periodicity band gaps [109–111]. In this case the curvature taken by the guide is used to design a phononic crystal waveguide, with the presence of a band gap. Figure 1.10 shows an example of the results that can be obtained. Alternating straight and curved waveguides, in a periodic cell (a), allows interesting loss effects to be obtained depending on the number of cells used (b). This logic of using the curvature of the guides to obtain a vibration filter effect can be applied to such common shapes as springs [111]. It is as compact as the conventional design, but provides the stopband effect in virtually significant frequency ranges.

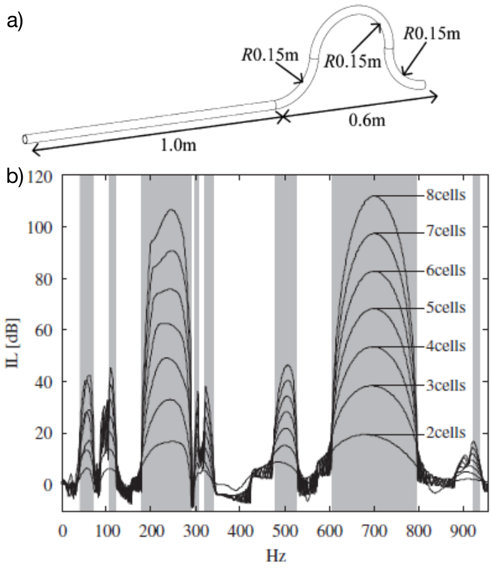

Figure 1.10 – Pipe segments used as a periodique repeated substructure (a). Insertion losses (IL) in a pipe with variable number of inserted periodicity cells. The grey strips indicate Floquet-predicted stop bands, (b). (Figure from Ref. [109])

Absolute band gap

One of the main challenges of phononic crystals has been the design of absolute band gaps over which the propagation of all elastic waves is forbidden, whatever their polarisation and wave vector. Phononic crystals with a fluid-type host medium, known as sonic crystals [66], have theoretically and experimentally reported absolute band gaps in broad ranges of frequencies [88, 112–114]. These systems represent the most simple phononic crystal as only longitudinal waves are propagating in the medium. Perhaps the most known application of sonic crystals is the design of tunable sound screens [41, 115, 116] and are interesting to concept acoustics filter for audible sound [99], seismic protection [117], or ultrasonics filter [118–120]. However, once the host medium is a solid, the problem becomes more complex as different polarisations can be excited in the system. In this case, theoretical evidences of absolute band gaps are also widely reported in the literature. 1D phononic crystals exhibiting absolute band gaps have been analysed by the transfer matrix method [78] and recently, 1D phononic crystals with alternating materials in the radial and axial directions have been used to show absolute band gaps [105], see Fig. 1.11. 2D phononic crystal slabs consisting of either solid [121] or piezoelectric [122] inclusions placed periodically in an isotropic host material have been theoretically analysed, showing absolute band gaps with a variable bandwidth for elastic waves of any polarisation and incidence. Bulk 2D phononic crystals have been also proposed for bulk wave attenuation with solid [123] or magnetostrictive [124] inclusions. Using specialised genetic algorithms, 2D phononic crystal formed from silicon and solid voids have been optimized to obtain unit cell designs exhibiting absolute band gaps for both in- and out-of-plane motions [125].

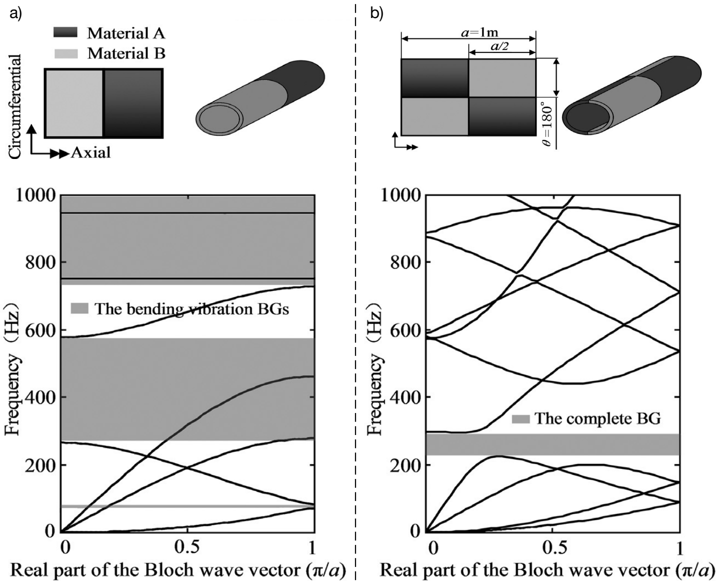

Figure 1.11 – Band structures of the phononic crystal pipes composed of steel and epoxy for a classical Bragg-type cell (a) and for a two parts 180° along circumferential direction cell (b) (Figures from Ref. [105]).

Absolute band gaps are also used in the case of curved waveguides. The dispersion diagrams in Fig.1.12 are obtained by transfer matrix method on curved beam. It is observed that when the band gap concerns both flexural and longitudinal waves, it is preserved in the curved guide. This property is important and will be used in the following. When the bands gap concern longitudinal or flexural waves, they do not appear in the curved waveguide. In order to preserve the filter effects of a phononic crystal, the band gaps must be superposed.

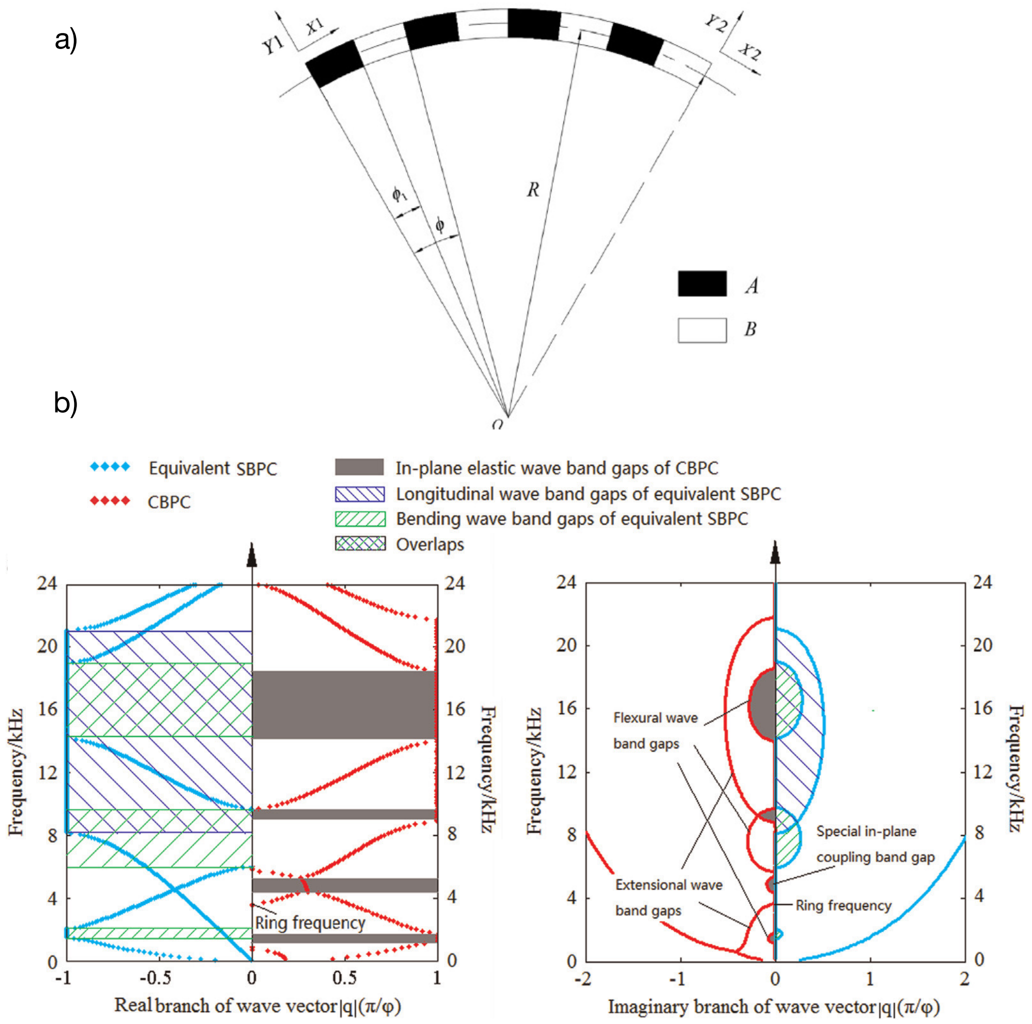

Figure 1.12 – Example of curved beam of phononic crystals (a). (CBPC) Band structures of in-plane elastic wave of curved beam of phononic crystals (CBPC) and equivalent straigth beam of phononic crysals (SBPC). The red lines represent the absolute value of the real and imaginary parts of the in-plane energy band structure of CBPC and the light blue ones represent those of equivalent SBPC. The grey regions are the band gaps of CBPC, The regions with slash are longitudinal and bending wave band gaps of equivalent SBPC. (b) (Figures from Ref. [126])

From the experimental point of view, absolute band gaps have been also reported in the literature. 2D binary solid/solid composite media with cylindrical inclusions embedded in an epoxy resin matrix showed dips of transmission evidencing the presence of absolute band gaps [127]. More recently, the presence of absolute band gaps in pillared phononic crystal slabs have been shown by double-vibrator three-components [128] and temperature-driven adaptive systems [129]. 3D phononic crystals made of face centered cubic unit cells composed of a single material have been used to experimentally show ultra-wide absolute band gaps [130, 131]. Recently, 3D load-bearing architected lattice Fig. 1.13, composed of a single material, have been designed for presenting broadband frequency band gaps for all directions and polarizations for airborne sound and elastic vibrations simultaneously [132]. However, although 2D and 3D phononic crystals have been widely validated experimentally, less attention has been paid to the experimental analysis of 1D case acting simultaneously on longitudinal, flexural and torsional waves. The control of vibrations in such a 1D phononic crystals systems can impact the design of piping systems which can be exploited in areas such as the automotive industry, heat exchanger tubes in chemical plants, oil pipelines, marine risers, pump discharge lines, among others [133].

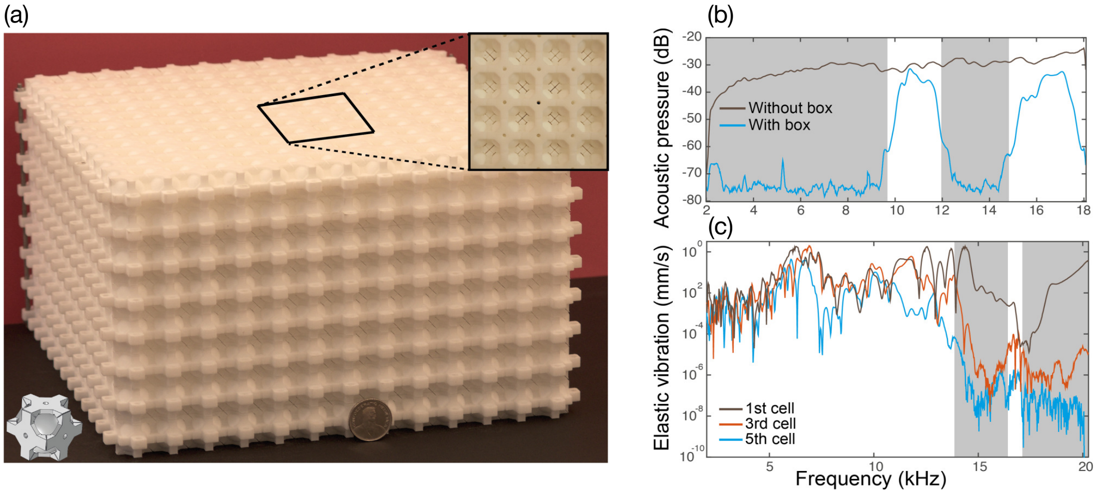

Figure 1.13 – A three-dimensional realization of the metamaterial. The material box encloses a piezoelectric transducer for generating mechanical vibrations and a loudspeaker for airborne sound. (b) The acoustic frequency response of the metamaterial compared with and without metamaterial box. (c) The elastic frequency response of the metamaterial (Figures from Ref. [132]).

Tunability and optimization

In an industrial context it is important to be able to target the frequency ranges to be treated. The tunability and optimization of the band structure has been studied, with for example the study of glass plate structure in water consisting of two subsets with different periods [134] depending on the arrangement, either a narrow or a wide bandwidth can be achieved. To reach the frequency ranges of interest, it is possible to use optimization algorithms to obtain a periodic structure to achieve the desired objectives.

Using specialised genetic algorithms, focusing on one-dimensional layered phononic crystal and longitudinal wave propagation [135], it is possible to obtain an optimised structure (Fig. 1.14). 2D phononic crystal formed from silicon and voids have been optimized to obtain unit cell designs exhibiting absolute band gaps for both in- and out-of-plane motions [125] (Fig. 1.15). Genetic algorithms is an nature-based optimization. It typically starts with a set of candidate according to some cost function, then applies a group of parameter variations, and then a selection in order to tend to the objective. Genetic algorithms are coded according to a binary function, for each parameter 2 solutions are possible (0 or 1). Compared to gradient-based methods, genetic algorithms are less likely to get trapped in local minima, especially for problems with large search spaces and a large number of variables [136].

There are different optimisation methods, all of which try to obtain from a set of parameters a cost function to be minimised. The choice of the optimisation method depends on the input parameters, the design of the component, and the amount of computing time we wish to allocate to it. The algorithm used in Fig. 1.15 is a genetic algorithm, and its cost function is formulated in terms of the size of a particular band-gap width normalized with respect to its midpoint frequency. The results presented are the different configurations obtained according to the optimization parameters: 1st band gap (a), 2nd band gap (b) for an out-of-plane wave. For in-plane waves (c), the second band gap is optimized. In Fig. 1.15(d) and (e), the first bandgap is optimized for combined out-of-plane and in-plane waves, the result of (e) being obtained with the smoothing of sharp edges.

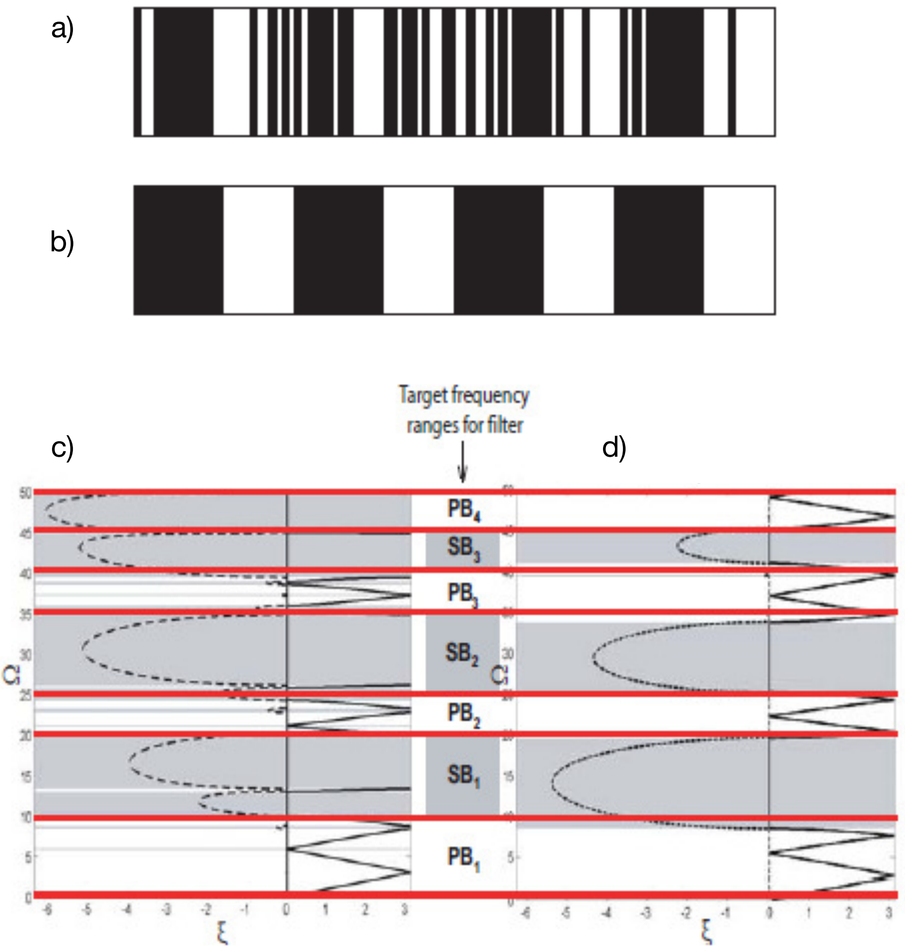

Figure 1.14 – Unit configuration for non-optimised filter design (a), and configuration for optimised filter design (b). The black color denotes material phase with high stifness and density; the white color denotes material phase with low stifness and density. Frequency band diagram for non-optimised filter design (c). Frequency band diagram for optimised filter design (d). Target frequency ranges for phononic filter with pass band (PB) and stop band (SB) shaded in grey. (Figure from Ref. [135])

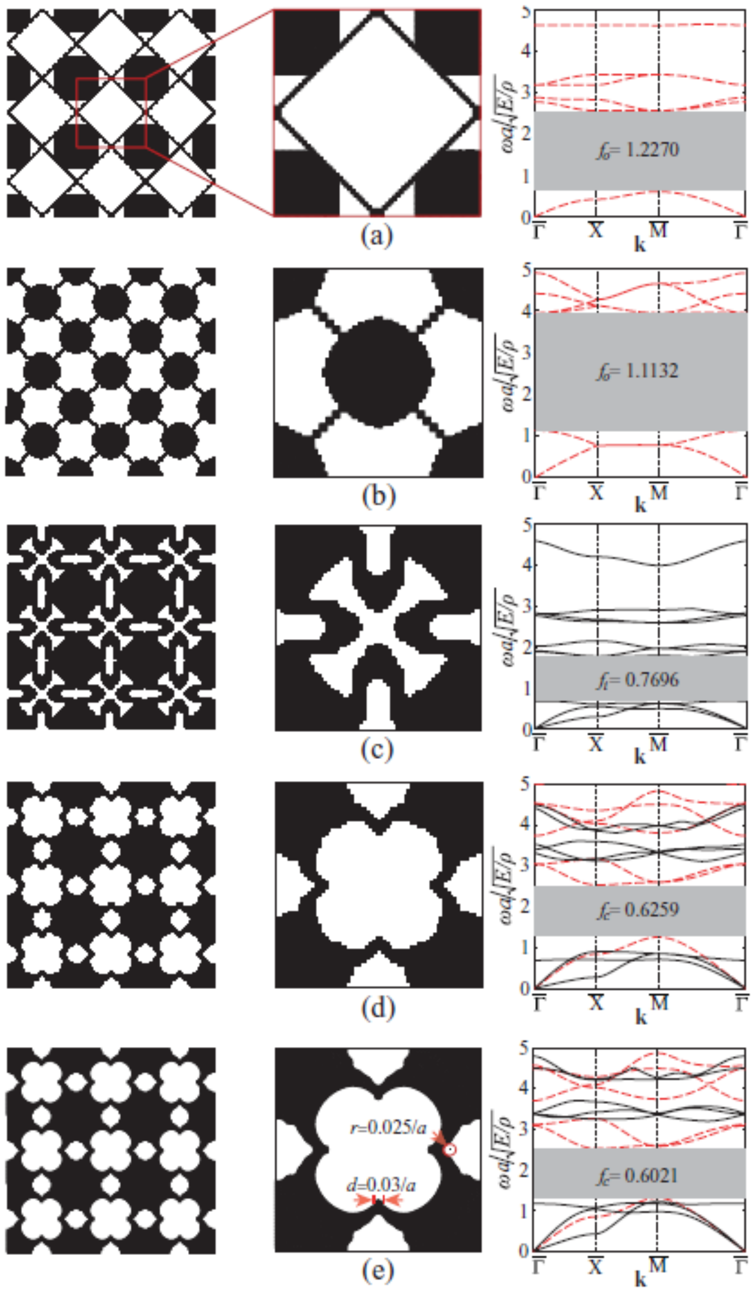

Figure 1.15 – Optimized unit-cell design and band structure for out-of-plane waves: First band gap (a), second band gap (b). Optimized for in-plane waves: second band gap (c). Optimized for combined out-of-plane and in-plane waves, lowest band gap: pixels (d) and splines (e). (Figure from Ref. [125])

Resonant phononic crystals

It is possible to produce phononic crystals by assembling cells consisting of an elastic support with a resonant element [49, 137, 138]. Work has been conducted on 1D phononic crystals [56, 139–149] and 2D [137, 150, 151]. These works include the use of binary materials with the inclusion material being very flexible [58, 59], hollow cylinders or spheres [60], split rings [61], beams or plates with suspended masses, plates or surfaces with pillars [51, 62, 63]. Effects of band gaps coupled to resonance bands [152] and their application for guiding the propagation of a wave [153] in a 2D medium emerged.

Figure 1.16 shows different models of resonators designed to be used fixed to a plate, (a) and (b), or a cylinder, (c) and (d). The resonance frequencies of the resonators and their effects on the structure are calculated numerically. These resonators can be multiplied [154] or periodised [155]. Each resonator is fixed on a unitary support cell, see (a). This coupling allows to take advantage of a periodicity effect in order to exploit the resonant effect in the framework of a phononic crystal, see (e). The use of resonators allows the opening of a resonance band and to obtain a damping effect at lower frequencies than those obtained with a simple phononic crystal for equivalent dimensions.

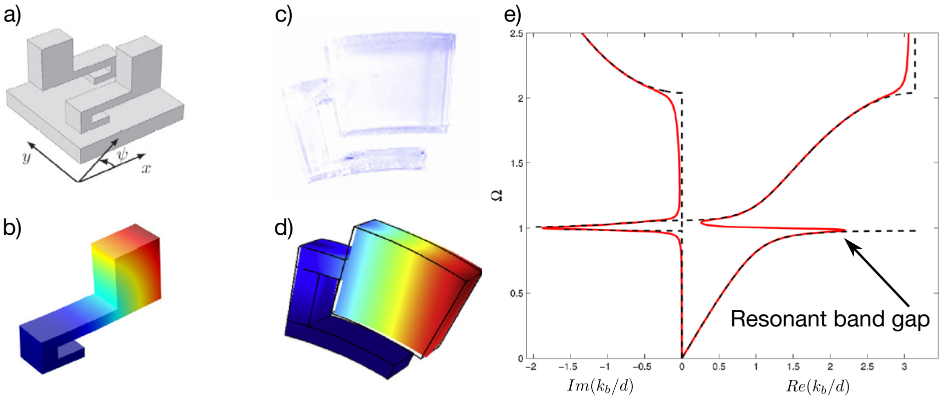

Figure 1.16 – Unite cell of a locally resonant metamaterial plate (a). Flexural mode for a fixed resonator base (b). Picture of a PMMA resonators produced to a vibroacoustic pipe used (c). Finite elements modeling mode shape of the first and second eigenfrequencies of the resonant structure (d). Dispersion curves for a infinite periodic structure with resonators, Compararison between undamped (black dash line), and damped (red solid line) curve (e). (Figures from Refs. [51, 68, 156–158])

A medium consisting of periodically arranged resonators has a resonant band gap at a wavelength much bigger than that corresponding to the band gap based on the spatial periodicity which leads to "Bragg dispersion" [159–162] if the resonance is tuned at very low frequencies. Figure 1.17 shows the results obtained for a geometry that seems close to the one intended in this thesis. The results presented concern only the flexural waves, the longitudinal and torsional waves are not discussed. However, the addition of resonators as complements to a periodic structure allows to obtain a frequency band where the propagation of flexural waves is attenuated due to the increasing of the imaginary part of (k).

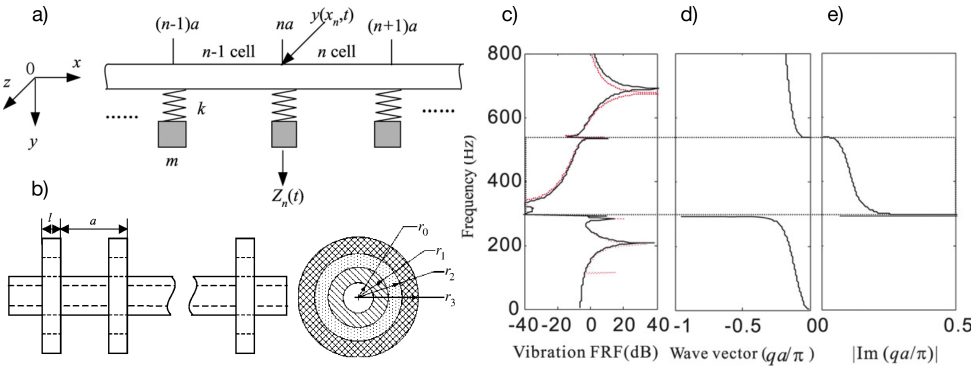

Figure 1.17 – Simple model of a locally resonant beam (a). Sketch of a locally resonant beam with finite local resonators (b).Complex flexural band structure of the locally resonant beam and the displacement FRF of its finite sample (c). Real (d) and imaginary (e) part of the dispersion diagram. (Figures from Ref. [159])

Many other configurations of periodic materials with local resonance have been proposed. These include the use of binary materials with the inclusion material being very flexible [58, 59], hollow cylinders or spheres [60], split rings [61], beams or plates with suspended masses, plates or surfaces with pillars [51, 62, 63]. These exemples use periodic resonators to obtain partial or complete band gap.

In audible acoustics, the use of acoustic resonators to attenuate noise is widely discussed in the literature [38–41], and even already used in architecture [44], but also in the context of automotive [45]. These acoustic systems can also be used with frequency shifting to produce graded materials or rainbow trapping, i.e. the gradual reduction of propagation velocity which leads to energy trapping in graded structures, [42, 43]. Figure 1.18 shows an acoustic rainbow trapping system design to absorb acoustic waves. Resonant frequencies are targeted from 300 Hz to 1000 Hz with sufficient frequency step to be partially coupled. The result is a frequency band producing quasi-perfect sound absorption of the incident wave.

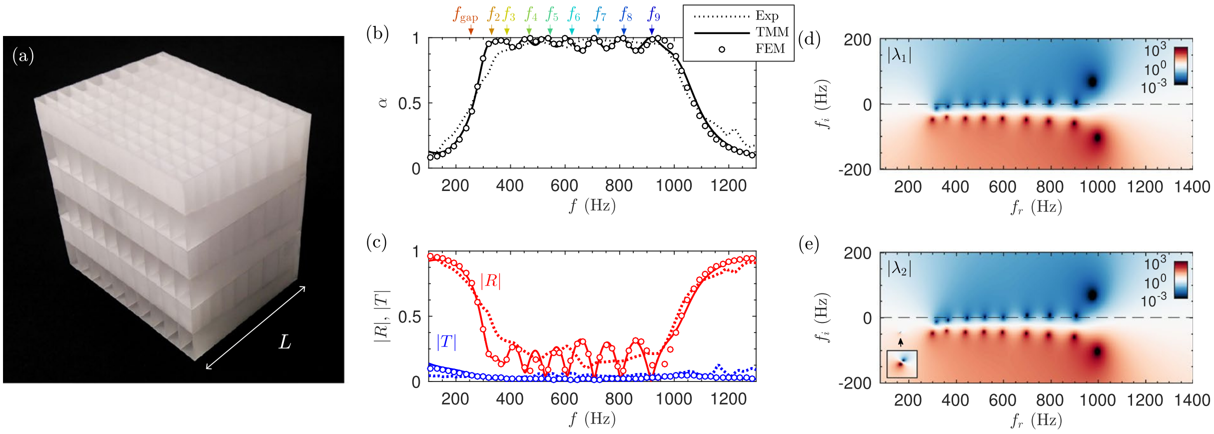

Figure 1.18 – (a) Photograph of an acoustic rainbow-trapping manufactured sample. (b) Absorption obtained by using the TMM (continuous line), FEM simulations (circles) and measured experimentally (dotted line). (c) Corresponding reflection (red curves) and transmission (blue curves) coefficients in amplitude. (d,e) Complex frequency representation of the eigenvalues of the scattering matrix. (Figures from Ref. [42])

In the acoustic medium, the losses are well known and the incident wave is regularly considered to be plane. However the problems become more complex when the host medium is solid. The losses are not well defined as in acoustic [27, 147, 163]. The losses can be related to the materials characteristics, to the interactions between the different parts of the system but also to the viscothermal exchanges between the system and its environment. In a solid medium we consider the propagation of several waves which are polarised according to their direction of propagation. In this work, they are named longitudinal wave for the wave propagating in the same direction as the axis of the waveguide and resulting in a traction-compression motion, flexural wave for the wave resulting in a bending motion and torsional wave for the wave resulting in a torsional deformation of the guide. A solution is usually designed to control only one type of motion.

There are a number of references in the literature where the control of vibration wave propagation using a local resonator is discussed. In the case of flexural waves, the periodic addition of a mass-spring assembly has been discussed in 1D [56, 139–146] and 2D [150] with many variations on the geometries of the supports and resonators. From this work, the effects of band gaps coupled to resonance bands [152] and their application for guiding the propagation of a wave [153] in a 2D medium emerged. Another approach consists in using a reduced number of resonators as vibration absorbers, [50, 54]. These vibration absorbers can be multiplied [154] or periodised [155]. For the case of longitudinal and torsional waves, the influence of the periodic inclusion of mass-spring systems in 1D [148, 149] and 2D [137, 151] media is explored. The influence of torsional vibrations on the propagation of bending waves is also considered [164]. While the damping of flexural [159], longitudinal [148] and torsional [48] waves has been studied and experimentally validated in many configurations [57, 165], there is no ready-to-use solution for 1D waveguides with industrial constraints.

Work has been done to obtain a multi-wave resonator that allows, when a resonant cell is periodized, to obtain an absolute band gap [57]. Figure 1.19 shows a vibration filter obtained with a waveguide made of resonant periodic cells. These periodic cells are composed of acrylic cylinders where a mass is suspended with three types of spring, see Fig. 1.19(a-i). The resonant cylinders are designed so that the resonant frequency of the cylinder is close for the three types of waves. This allows to obtain resonance band gaps in the same frequency range for each type of wave. This absolute band gap is then translated into a damping effect when the waveguide is composed of 10 periodic cells, see Fig. 1.19(j-l). The methodology is similar to the one used in Chap. 2.

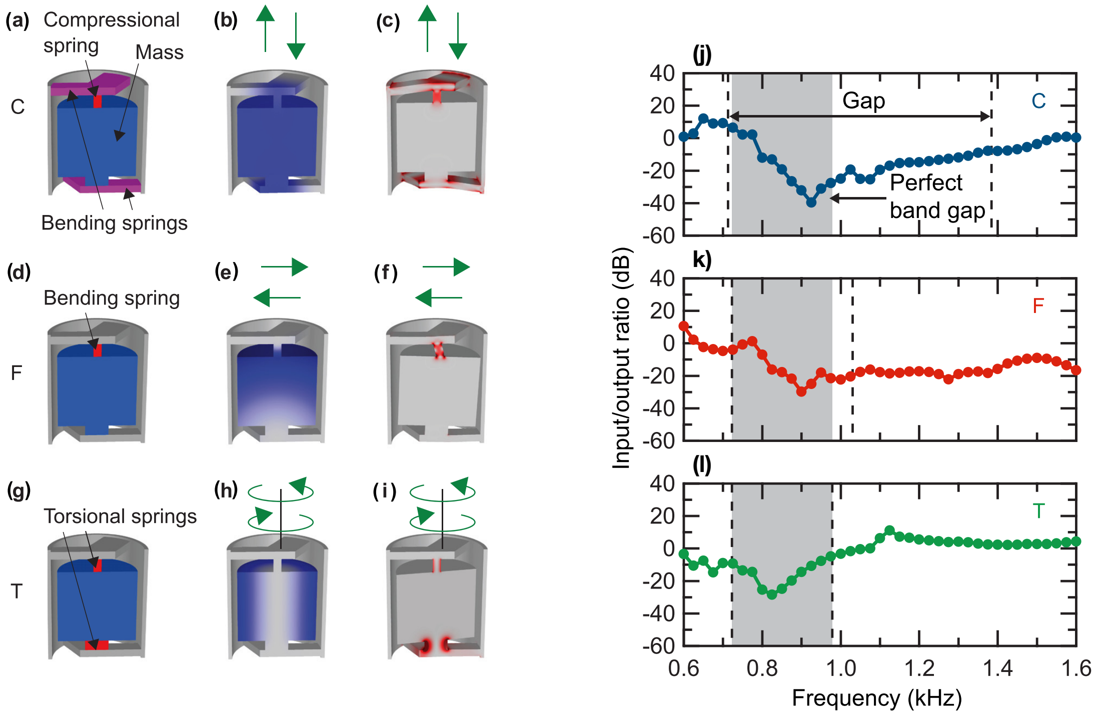

Figure 1.19 – (a-i) Structure of the cell, with resonant mass, periodised. The spring components are identified for each movement as well as the displacement of the mass and the strains on the springs. (j -l) Experimentally observed Input/output ratio for each acoustic eigenmode for a finite metarod, with (j) for longitudinal eigenmode, (k) for flexural, and (l) for torsional. (Figure from Ref. [57])

Many solutions propose the use of a resonator inside the waveguide [55–57]. Ogasawara's work, Fig. 1.19, is close to what we are trying to achieve. However, the materials and dimensions described are not compatible with our industrial context. In the case of piping systems that can be operated in areas such as the automotive industry, heat exchanger tube in chemical plants, oil pipelines, marine risers, pump discharge line, vibration treatments must be applied outside the waveguide. This thesis focuses on solutions to control wave propagation in a targeted frequency range with minimal space requirements.

1.4 Outline of the thesis

The PhD is concerned by the control of vibratory waves in a tube by the use of vibratory filters or absorbers. After presenting the context, the research objectives and a quick overview of the state of the art, we introduce how to obtain a band gap by designing of a vibratory filter composed of a periodically structured tube. Then, the use of local resonances allows to design filter or vibration absorber effects without impacting the geometry and materials of the host waveguide. Finally, the application of the proposed solutions in an industrial setting will be discussed.

This document is structured in 5 chapters:

- Chapter 1: Introduction.

  This chapter provides an introduction to the context. It is rooted in the transportation industry. The problematic of the thesis is to obtain a vibration filter, which can be integrated in a set of industrial elements without altering their primary functions. A state of the art of common solutions for vibration damping, vibration absorbers, and phononic crystals, gives an overview of the work discussed in this thesis.

- Chapter 2: Design of multi-wave vibration filter based on Phononic Crystal pipes with absolute bandgap.

  In this chapter a design of a vibration filter based on phononic crystals is developed. The analytical method for calculating the dispersion diagram of an infinite periodic waveguide is developed. The results are correlated with a numerical model. A parametric optimisation is performed in order to obtain a multi-wave vibratory filter centred on a selected frequency band. The theoretical results are experimentally validated.

- Chapter 3: Design of 1D multi-wave vibration filters and absorbers based on tunable local resonators embedded in pipes.

  In this chapter several designs of vibration filter and vibration absorber are developed. This work uses local resonators to propose a design independent of any industrial context. A set of designs are proposed and an experimental validation is provided.

- Chapter 4: Cases study inspired by industrial situations. Use of multi-wave vibration filter pipes.

  In this chapter previously developed designs are numerically confronted with situations common in the industrial context. Waveguides are bent and the effects of the bends are studied. The waveguides are coupled to radiating elements and the acoustic propagation is observed. Finally the influence of the addition of a heavy fluid in a periodic pipe is investigated.

- Chapter 5: Conclusions.

  In this chapter the work and results of this thesis are summarised, followed by some perspectives for future works.

Chap. 2

Design of multi-wave vibration filter based on Phononic Crystal pipes with absolute bandgap

Contents

2.1 Introduction 23
2.2 1D models of periodic structural waveguides using the Floquet method . 23
  2.2.1 Definition of the waveguide 24
  2.2.2 Floquet-Bloch model of the longitudinal and torsional waves dispersion 25
  2.2.3 Floquet-Boch model for flexural wave dispersion following Timoshenko theory 26
2.3 Validation of the 1D models 27
  2.3.1 Uniform waveguides 28
  2.3.2 Periodic waveguides 28
2.4 Evolution on the absolute bandgap based on parametric variations 30
  2.4.1 Monomaterial waveguides 30
  2.4.2 Bimaterial waveguides 31
2.5 Numerical optimization of the absolute band gap based on Nelder-Mead algorithm 32
  2.5.1 Nelder-mead algorithm 32
  2.5.2 Analysis of performance optimisation for various weightings of $\mathcal{F}$. 33
2.6 Study of an experimental demonstrator 35
  2.6.1 Design of the experimental demonstrator 35
  2.6.2 Experimental set-up 36
  2.6.3 Results 37
2.7 Conclusions 38

2.1 Introduction

This chapter is dealing with the design of architectured waveguide to control vibrations in the framework of this thesis. It is based on the previously published article [166] (Appendix A) which is further developed and detailed here. The developped system is a waveguide periodically structured in order to obtain a vibration filtering effect over a given bandwidth for all types of waves propagating on it. As the waveguide is subjected to complex excitation we apply the concept of absolute band gap in order to design and experimentally validate 1D phononic crystals pipes able to mitigate longitudinal, flexural and torsional waves in a same target frequency band.

The mitigation of noise pollution is a major societal challenge for which extensive research has been conducted [19]. Noise, Vibration and Harshness (NVH) departments have been widely integrated notably in transportation industry. Structure borne sound results from both the flexural vibrations and their couplings with other types of waves, produced by the complex geometries classically encountered in industrial systems [4]. An effective reduction of the radiated sound levels then requires to mitigate all types of waves. To reach such "absolute filter" features, the design strategy is based on the concept of absolute band gap.

The chapter is organised as follows. The study presents first the theoretical model used to analyse the 1D models for the wave propagation in periodic structural waveguides in section. 2.2. The model are validated in Section 2.3. Section 2.4 shows the 1D model used to explore the variability of band gap as a function of various structural parameters. A numerical optimisation of a periodic structure is proposed in Section 2.5. This optimisation is based on the simplex method algorithm.The experimental set-up used to validate the model for the reflection problem is then presented in Section 2.6 as well as the experimental methodology and results.

2.2 1D models of periodic structural waveguides using the Floquet method

A 1D phononic crystal waveguide made of a periodic distribution of a unit cell consisting of two different hollow cylinders made of aluminium and nylon (see Fig. 2.1) is optimised. Considering lossy constitutive materials, the eigenvalue problems of the three types of waves are analytically solved by imposing continuity conditions between the different parts of the unit cell and Floquet-Bloch periodic conditions at its extremities. The three problems are combined via a minimizing algorithm in order to reach the geometry of the 1D phononic crystal pipe that exhibits an absolute band gap of target center frequency and target bandwidth. Full wave 3D finite element simulations and experimental caracterization of a demonstrator of finite size are in good agreement with the analytical results. The results show dips in the transfer functions associated with the predicted absolute band gap.

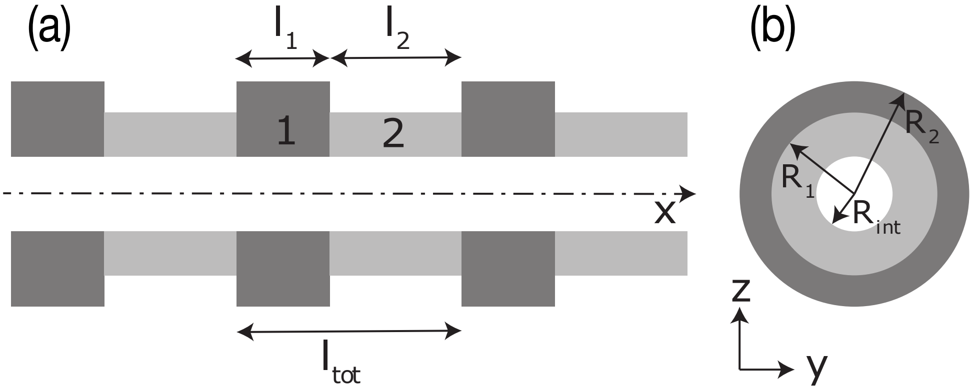

Figure 2.1 – Scheme of the modeled phononic crystal pipe. (a) and (b) show lateral and cross sectional schematic representation of the modeled phononic crystal pipe, respectively.The delimited region of length l_{tot} represents the unit cell

2.2.1 Definition of the waveguide

A detailed scheme with the geometrical parameters of the system is shown in Fig. 2.1(a-b). Each segment of the unit cell is assumed to be a thin-walled pipe of annular cross-section. We define $\gamma = l_2/l_{tot}$ as the length ratio and $\beta = R_2/R_1$ as the outer radius ratio. The inner radius R_{int} is constant for the two segments of the unit cell. These two geometrical parameters will be used to describe the geometry in the optimisation procedure. The 1D phononic crystal pipe is made of aluminium and nylon, considered as linear and isotropic elastic materials. The nylon is characterized by its Young modulus $E_N = 2.3$ GPa, its density $\rho_N = 1240$ kg/m^3 and its Poisson ratio $\nu_N = 0.3$. The aluminium characteristics are $E_A = 71$ GPa, $\rho_A = 2170$ kg/m^3 and $\nu_A = 0.3$.

All the parameters defining this periodic guide are listed in the table 2.1. The ratios of length γ and outside radius β between segments 1 and 2 allow to control the contrasts of geometry of the unit cell. For all the cases presented in this document, the internal radius R_1 will always be kept constant between sections 1 and 2 in order to represent a tube geometry where only the external radius is structured.

parameters	**definition**
l_{tot}	total length of the unit cell [m]
$l_1 = (1-\gamma) \times l_{tot}$	length of the first segment [m]
$l_2 = \gamma \times l_{tot}$	length of the second segment [m]
γ	length ratio
R_1	external radius of the first segment [m]
$R_2 = \beta \times R_1$	radius of the second section of the unit cell [m]
β	outer radius ratio
R_{int}	internal radius [m]
E	Young modulus [Pa]
ρ	density [kg/m^3]
ν	Poisson's ratio

Table 2.1 – Topological and material parameters from which the unit cell of the Fig. 2.1 is defined.

2.2.2 Floquet-Bloch model of the longitudinal and torsional waves dispersion

Motion equation

Here we consider harmonic wave motion with the time convention $e^{\imath\omega t}$. In what follows the subindex $i = N, A$ refers to each section of the unit cell (Nylon and Aluminum, respectively) and the superindex $w = l, t$ represents the wave type (longitudinal and torsional, respectively). On the one hand, the propagation of longitudinal and torsional waves in the i-th part of the unit cell is modeled by a 1D Helmholtz equation [18]

$$\frac{\partial^2 u_i^w}{\partial x^2} + (k_i^w)^2 u_i^w = 0, \tag{2.1}$$

where u_i^w is the displacement of the wave w of the i-th segment of the unit cell. $k_i^w = \frac{\omega}{c_i^w}$ is the wave number with $c_i^w = \sqrt{E_i^w/\rho_i}$ the speed of the wave and $E_i^l = E_i$ is the Young modulus and $E_i^t \equiv G_i = E_i/2(1+\nu_i)$ is the shear modulus and ν_i the Poisson ratio.

General solution

Wave solutions of Eq. 2.1 write

$$u_i^w(x) = A_{i1} e^{ik_i^w x} + A_{i2} e^{-ik_i^w x}, \tag{2.2}$$

where A_{ij} are unknown amplitudesrepresent the left,rigth going waves respectively, $j = 1, 2$.

Condition of continuity

At the interfaces between Nylon and Aluminum waveguide sections Fig 2.1(a), the displacement continuity and equilibrium equations write

$$\begin{aligned} u_1^w(l_1) &= u_2^w(l_1), \\ u_2^w(l_{tot}) &= u_3^w(l_{tot}), \end{aligned} \tag{2.3}$$

and

$$\begin{aligned} E_1 S_1 \frac{\partial u_1^w(l_1)}{\partial x} &= E_2 S_2 \frac{\partial u_2^w(l_1)}{\partial x}, \\ E_2 S_2 \frac{\partial u_2^w(l_{tot})}{\partial x} &= E_3 S_3 \frac{\partial u_3^w(l_{tot})}{\partial x}, \end{aligned} \tag{2.4}$$

respectively, where S_i is the cross section area.

Condition of periodicity

The periodicity is described by the Floquet conditions

$$\begin{aligned} u_1^w(0) &= e^{ik_b} u_3^w(l_{tot}), \\ \frac{\partial u_1^w(0)}{\partial x} &= e^{ik_b} \frac{\partial u_3^w(l_{tot})}{\partial x}, \end{aligned} \tag{2.5}$$

where k_b is the unknown Bloch wavenumber.

Linear system

Applying conditions (2.3-2.5) to solution (2.2) leads to a linear system $M(\omega, k_b) \cdot A = \mathbf{0}$ such as:

$$\begin{bmatrix} e^{ik_1^w l_1} & e^{-ik_1^w l_1} & e^{ik_2^w l_1} & e^{ik_2^w l_1} & 0 & 0 \\ E_1S_1ik_1^w e^{ik_1^w l_1} & -E_1S_1ik_1^w e^{ik_1^w l_1} & E_2S_2ik_2^w e^{ik_2^w l_1} & -E_2S_2ik_2^w e^{ik_2^w l_1} & 0 & 0 \\ 0 & 0 & e^{ik_2^w l_{tot}} & e^{-ik_2^w l_{tot}} & e^{ik_3^w l_{tot}} & e^{ik_3^w l_{tot}} \\ 0 & 0 & E_2S_2ik_2^w e^{ik_2^w l_{tot}} & -E_2S_2ik_2^w e^{ik_2^w l_{tot}} & E_3S_3ik_3^w e^{ik_3^w l_{tot}} & -E_3S_3ik_3^w e^{ik_3^w l_{tot}} \\ 1 & 1 & 0 & 0 & e^{(ik_b^w)}e^{ik_3^w l_{tot}} & e^{(ik_b^w)}e^{ik_3^w l_{tot}} \\ ik_1^w & -ik_1^w & 0 & 0 & e^{(ik_b^w)}ik_1^w e^{ik_3^w l_{tot}} & -ik_1^w e^{(ik_b^w)}e^{ik_3^w l_{tot}} \end{bmatrix} \cdot \begin{bmatrix} A11 \\ A12 \\ A21 \\ A22 \\ A31 \\ A32 \end{bmatrix} = 0. \tag{2.6}$$

For each given ω of a frequency range of interest, the values of k_b (complex) that satisfies $\det(M) = 0$ are found numerically using the Muller method [167].

2.2.3 Floquet-Boch model for flexural wave dispersion following Timoshenko theory

On the other hand, flexural waves are described using the Timoshenko's beam theory [79, 138, 168–170] that takes into account shear deformation and rotational inertia effects. Although this framework is based on low frequency assumptions, it makes possible to analyse the propagation at higher frequencies or for thicker beams than the Euler-Bernoulli's theory.

Equation of motion

Following Timoshenko assumptions from which shear deformation and rotational inertia effects are considered, the flexural displacement v_i satisfies

$$\frac{E_i}{\rho_i}\frac{\partial^4 v_i}{\partial x^4} + \omega^2\left(1 + \frac{E_i}{\kappa_i G_i}\right)\frac{\partial^2 v_i}{\partial x^2} + \left(\frac{S_i\omega^2}{I_i} - \frac{\rho_i I_i \omega^4}{\kappa_i G_i}\right) v_i = 0, \tag{2.7}$$

where κ_i, S_i, and I_i are respectively the shear coefficient, the cross-section area and quadratic moment. In order to obtain the eigenvalue problem whose solutions give the complex dispersion relation, $k_b = k(\omega)l_{tot}/\pi$, we apply the continuity boundary conditions at the interfaces between each segment of the unit cell as well as the Floquet-Bloch periodic conditions at its extremities

General solution

The solution of Eq.(2.7) writes as a combination of 4 waves

$$v_i(x) = B_{i1}e^{ik_{i1}x} + B_{i2}e^{-k_{i2}x} + B_{i3}e^{-ik_{i3}x} + B_{i4}e^{k_{i4}x}, \tag{2.8}$$

where k_i is the flexural wavenumber and B_{i1} to B_{i4} unknown amplitudes.

Condition of continuity

At the interfaces between Nylon and Aluminum pipe sections (see Fig. 2.1(a)), the continuity and equilibrium equations write

$$\begin{array}{rclcrcl} v_1(l_1) & = & v_2(l_1) & , & v_2(l_{tot}) & = & v_3(l_{tot}), \\ \Psi_1(l_1) & = & \Psi_2(l_1) & , & \Psi_2(l_{tot}) & = & \Psi_3(l_{tot}), \\ M_1(l_1) & = & M_2(l_1) & , & M_2(l_{tot}) & = & M_3(l_{tot}), \\ Q_1(l_1) & = & Q_2(l_1) & , & Q_2(l_{tot}) & = & Q_3(l_{tot}), \end{array} \tag{2.9}$$

where Ψ_i is the slope, M_i the bending moment and Q_i the shear force.

Condition of periodicity

The periodicity is described by the Floquet conditions

$$\begin{aligned} v_1(0)&=e^{ik_b}v_3(l_{tot}),\\ \Psi_1(0)&=e^{ik_b}\Psi_3(l_{tot}),\\ M_1(0)&=e^{ik_b}M_3(l_{tot}),\\ Q_1(0)&=e^{ik_b}Q_3(l_{tot}), \end{aligned} \tag{2.10}$$

where k_b is the unknown Bloch wavenumber.

Linear system

The equations (2.8-2.10) lead to a linear system such as $M(\omega, k_b)\cdot\mathbf{B}=0$ with M a [12x12] matrix. For each given ω of a frequency range of interest, the values of k_b (complex) that satisfies $\det(M)=0$ are found numerically to provide the dispersion relation using the Muller method [167].

By solving each 1D model this way we obtain the dispersion relations for all types of waves in the phononic crystal pipe. Solutions obtained by the previous semi-analytical methodology are compared to reference solutions provided by 3D elasticity finite element simulations (solid mechanics COMSOL package [84]).

2.3 Validation of the 1D models

This section presents a set of comparative results obtained by the Floquet model and by reference models in three cases of varying complexity. The objective is to evaluate the accuracy of the 1D approximation of the wave models used in the typical configurations of the studied guides. For each case presented in Fig. 2.2, the topology of the unit cell is given at the top and the dispersion diagrams are presented below.

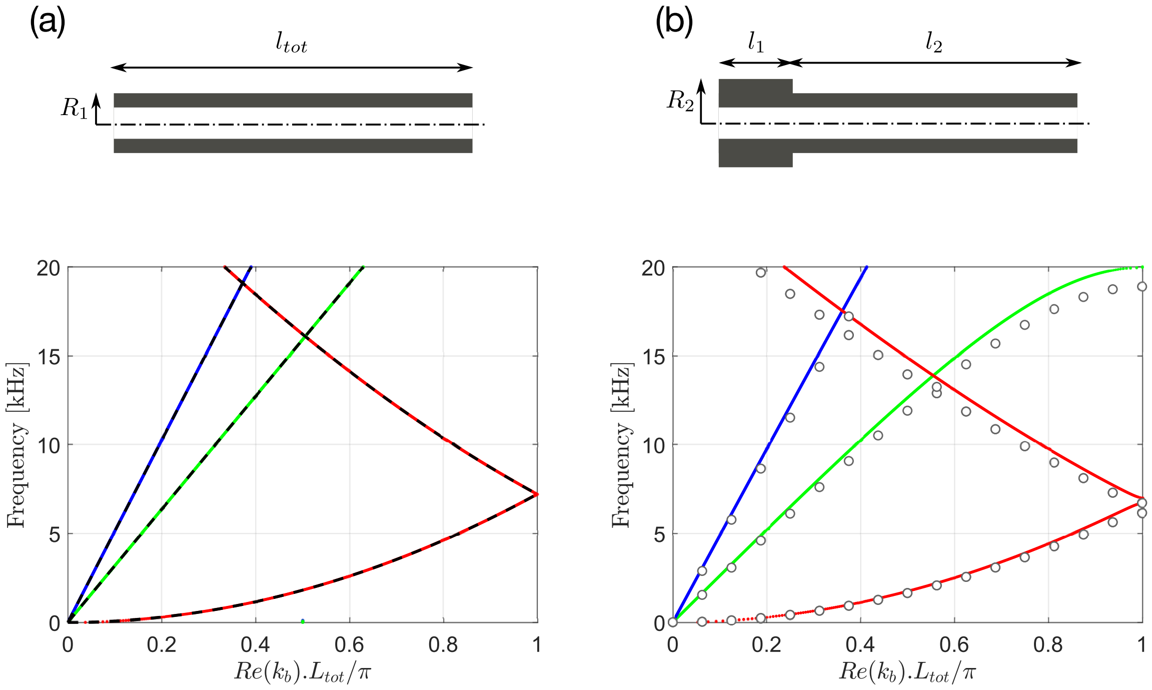

Figure 2.2 – Validation of the Floquet method by comparison with reference results in the cases of uniform structural guide (a), single-material phononic crystal guide (b).

The basic case of the uniform guide with no discontinuities in cross-section and material is first considered in Fig. 2.2(a). For the second configuration, Fig. 2.2(b), the waveguide has a variation of its cross-section for a specified length l_1, this change of cross-section is repeated periodically in order to obtain a single-material phononic crystal. The dual-material configuration, Fig. 2.3, is obtained by modifying both the cross-section of the guide and the material of which it is composed, which has the effect of impacting more directly on the propagation of longitudinal and torsional waves.

2.3.1 Uniform waveguides

For the Floquet model, the geometry of the uniform unit cell is defined as the series connection of two identical aluminium sections. In this basic configuration, the dispersion relationships for each type of wave are analytically computed by the following expressions:

$$\begin{aligned}
k_f &= \pm\left(\frac{-((-D\rho S-\kappa SG\rho I)\omega^2)\pm\sqrt{(-D\rho S-\kappa SG\rho I)\omega^2)^2-4D\kappa SG(-\kappa S^2G\rho\omega^2+\rho^2SI\omega^4)}}{2D\kappa SG}\right)^{\frac{1}{2}} \\
&\quad \text{, for flexural, (with } D = EI \text{ the rigidity),} \\
k_c &= \sqrt{\frac{E}{\rho}}\omega\text{, for longitudinal,} \\
k_t &= \sqrt{\frac{E}{\rho}}\omega\text{, for torsional.}
\end{aligned} \tag{2.11}$$

The superposition of the results in Fig. 2.2(a) constitutes a primary validation of the numerical implementation of the Floquet method.

2.3.2 Periodic waveguides

In a second phase, validation is done for two periodic configurations defined in Fig. 2.2(b) and Fig. 2.3. The reference solutions selected for the comparisons are obtained by a 3D elasticity model solved by the finite element method applied to a unit cell whose incoming (at $x = 0$) and outgoing (at $x = l_{tot}$) faces are associated with Floquet conditions translating the Eq. 2.5 and Eq. 2.10. These models are implemented in the COMSOL environment [84].

For the single-material periodic configuration, the results in Fig. 2.2(b), on a periodic aluminium cell, are in good agreement with the reference results, for the longitudinal (blue), torsional (green) and bending (red) wave dispersion obtained by the Timoshenko beam model.There are some differences between the analytical and numerical results that increase with frequency, these differences result from the limitations of the theoretical models used to produce the dispersion diagrams, the assumption used has variations with the finite element models as the frequency rises.

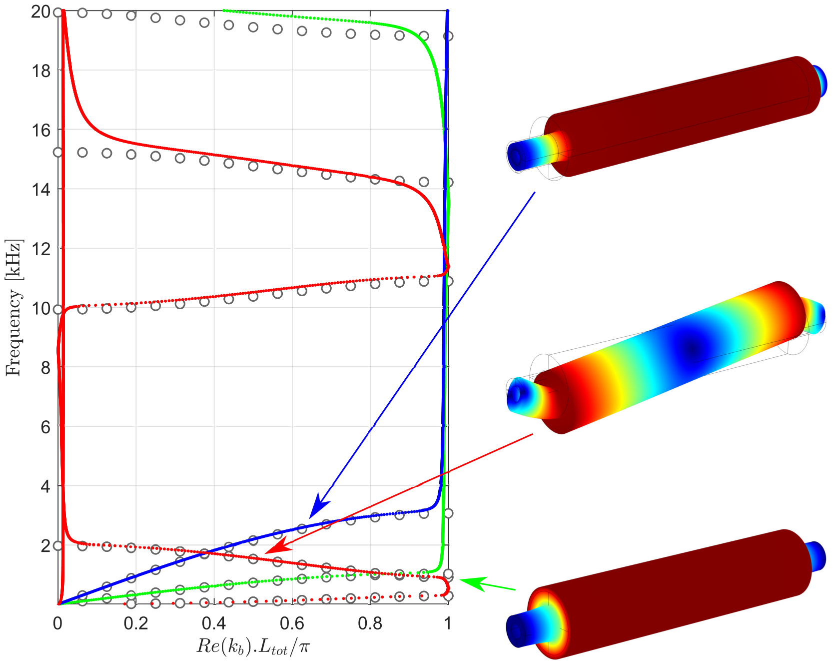

Figure 2.3 – Analysis of the dispersion relation of a periodic two-material cell with $l_{tot} = 0.1$ m; Real part of the dispersion relation with $\gamma = 0.2$, $R_1 = 8$ mm and $\beta = 0.5$ calculated both by the semi-analytical model (coloured points, (●) longidutinal, (●) in flexion and (●) in torsion) and by the full 3D FEM simulation (open circles ○). The colour scale of the deformation fields is chosen arbitrarily in order to clarify the meaning, with red areas corresponding to maximum deformation and blue areas to minimum deformation.

Figure. 2.3 shows the real part of the dispersion relation for a phononic crystal pipe with the following geometry: $l_{tot} = 0.1$ m, $\gamma = 0.2$, $R_1 = 8$ mm and $\beta = 0.5$. This specific geometry is an example extract from the later parametric variation, section. 2.4. The dispersion diagram is calculated by considering the viscoelastic losses for aluminium and nylon via the complex Young's modulus $E_i^c = E_i(1 + \imath\eta_i)$ with η_A = 1e-4 and η_N = 4e-2. Coloured dots (each colour a wave type) represent the results obtained from the semi-analytical model while gray circles represent the FEM reference solutions. Results are in very good agreement and so the semi-analytical modeling is well validated. However, some disagreements appear for flexural waves at high frequencies (dispersion branch just under 20 kHz) due to the expected limitations of the Timoshenko's beam model. Anyway, the dispersion relation obtained for this geometrical layout exhibit a wide absolute band gap in the range $[3 - 10]$ kHz.

Moreover, the combined use of these three 1D models is of great interest for the calculation costs. For example, using a desktop computer with an Intel Xeon processor clocked at 3GHz and 16 GB of RAM, the calculation time for a complete dispersion diagram is less than 2min by the Floquet method and around 20 min by the finite element method. These low calculation times make it possible to envisage without prohibitive cost numerous parametric variations as in the Section 2.4 or even numerical optimisations as in the Section 2.5. These semi-analytical 1D models are therefore well suited for pre-dimensioning. The 3D finite element elastic model then allows the final performance frequency template to be corrected and specified on an already optimised case at a low numerical cost.

2.4 Evolution on the absolute bandgap based on parametric variations

The objective of this section is to evaluate the performance of the vibratory filtering characteristics that can be achieved in the case of a very simple unit cell topology involving two uniform sections. In Fig. 2.4 the colored areas represented the range of frequencies limited by the upper and the lower frequency edge of the band gap. Each wave type is represented by its coloured area (flexural in red, longitudinal in blue, torsional in green) with the center frequency represented by a continuous red line. The evolution of these band gaps are studied as a function of the variations in the total length of the cell l_{tot} (Fig. 2.4(1)), the length ratio γ (Fig. 2.4(2)) and the outside diameter contrast β (Fig. 2.4(3)). In this section, the parameters vary independently of each other.

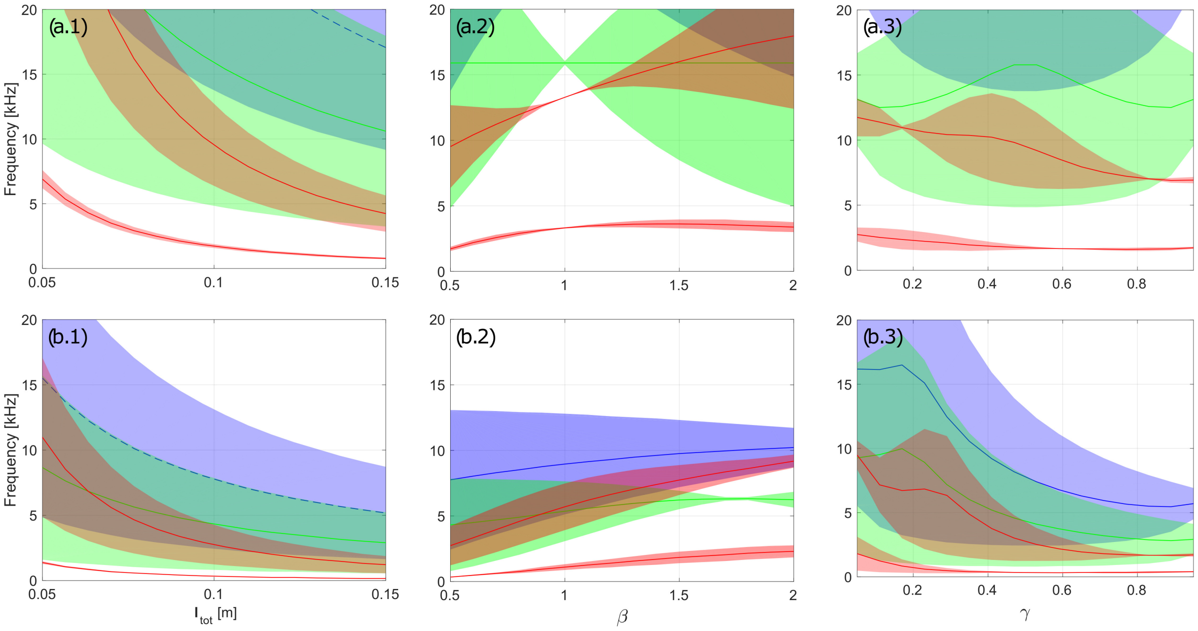

Figure 2.4 – Evolution of the band gap of the bending (red), longitudinal (blue) and torsional (green) waves in the cases of a single-material aluminium cell (a) and of a two-material aluminium/nylon cell (b), as a function of the variations of the total length of the cell l_{tot} for $\gamma = 0.5$ and $\beta = 0.5$ (1); the outer radius contrast β for $\gamma = 0.5$ and $l_{tot} = 0.1$m (2); the length ratio γ for $\beta = 0.5$ and $l_{tot} = 0.1$m (3). All simulations are performed for $R_1 = 8$mm.

2.4.1 Monomaterial waveguides

The first parametric variation (Fig. 2.4(a)) concerns the case of an aluminium single-material cell for which $E = 71$ GPa, $\rho = 2170$ kg/m^3 and $\nu = 0.3$. The basic topology around which the variations are made is such that $l_{tot} = 0.1$ m, $\gamma = 0.5$, $R_1 = 8$ mm and $\beta = 0.5$. Regardless of the type of wave considered, band gaps of attractive frequency width and frequency position exploitable for the application context appear.

The following trends emerge from the results and illustrate the sensitivity of the band gaps to the geometry of the system:

- The total length of the l_{tot} cell controls the frequency position of the band gaps (Fig. 2.4(a.1)): f_c decreases when l_{tot} increases. This result is expected and already observed in many contexts of use of periodic media. Furthermore, the relative width of the band gaps in relation to the center frequency changes modestly with l_{tot}.

- The β contrast (Fig. 2.4(a.2)) controls the frequency width of the band gaps. Results indicate that β essentially controls band gaps bandwidth and has a relatively weaker effect on their central frequencies. Such tendency has already been observed in the case of monolitic corrugated beams [84]. Also note that in the particular case of the uniform guide ($\beta = 1$), the closure of the band gaps is well found.

- The length ratio γ (Fig. 2.4(a.3)) acts in a more complex way on the characteristics of the features of the band gaps: variations of the same order of magnitude appear for both center frequency and bandwidth.

Independently of these trends it is difficult to obtain a configuration where the band gaps of each type of wave are combined in order to obtain an "absolute band gap". Only extreme topologies that are inapplicable in practice can lead to total bandgaps in very high frequencies (Fig. 2.4(a.1) for $l_{tot} < 0.07$ and Fig. 2.4(a.2) for $\beta < 1.6$). The frequency differences between the bands can be interpreted by the differences in the order of magnitude of the velocities of the 3 types of waves in such a single-material guide.

2.4.2 Bimaterial waveguides

A two-material aluminium/nylon cell with the same geometry as in the single-material case is now considered (Fig. 2.4(b)). The introduction of Nylon is intended to reduce the equivalent celerity of compressional and torsional waves, thereby lowering their typical Bragg band frequencies to the same range as for bending waves. The nylon characteristics used are $E = 4$ GPa, $\rho = 1240$ kg/m^3 and $\nu = 0.3$.

The results of Fig. 2.4(b) show that the introduction of nylon makes it possible to obtain absolute band gaps for topologies that are acceptable in practice. This triple vibratory filtering effect is obtained in the range $[3.8 - 8]$ kHz for $l_{tot} = 0.075$ m in Fig. 2.4(b.1) or $[4 - 11]$ kHz for $\gamma = 0.2$ in Fig. 2.4(b.3), for example. In this case the second flexural band gap and the first longitudinal and torsional band gaps are involved. These full filtering effects involve the second band, the first being positioned too low in frequency. Subsequently, the aim will be to optimise the alignment of this second band with the first compression and torsion bands.

The parametric variations shown in Fig. 2.4(b.2) reveal several interesting results. First, there are band gap closings, as for torsional waves for $\beta = 1.75$, for example. This closing effect is recently used as the initial point of the topological edge states [171].

The previous variations show that the evolution of the band gaps does not follow simple rules from which the dimensioning of a filter is possible in order to reach a targeted filtering template. On the contrary, it appears that the topological parameters control the characteristics of the total bandgap in a combined way.

Analogously, Fig. 2.4(b.3) shows the evolution of the band gaps as γ changes. Both the center frequency and width display non monotonous variations of the same range. In particular, some optimal band widths appear around $\gamma = 0.2$. Finally γ has a more complex effect on the band gap features that do not follow any clearly identifiable law.

However, Fig. 2.6 shows that it is difficult to tune by hand the absolute band gap to a target band. In order to achieve this goal, a numerical optimization procedure is proposed below.

2.5 Numerical optimization of the absolute band gap based on Nelder-Mead algorithm

2.5.1 Nelder-mead algorithm

A Nelder-Mead local minimisation algorithm [172] is used in this work to provide the geometrical parameters of a phononic crystal pipe with an absolute band gap defined from both a target center frequency f_0 and a target band width Δf_0. The set of parameters subject to the optimisation is defined as $X = [l_{tot}, \gamma, R_1, \beta]$. The cost function $\mathcal{F}$ is defined as a weighted sum of two convergence indicators and reads

$$\mathcal{F} = \alpha_{f_c} I_{fc} + \alpha_{\Delta f} I_{\Delta f}. \tag{2.12}$$

The weighting coefficients α_{f_c} and $\alpha_{\Delta f}$ are adjustable such that $\alpha_{f_c} + \alpha_{\Delta f} = 1$ and the convergence indicators are defined by

$$I_{\Delta f} = \left| 1 - \frac{\Delta f - \Delta f_0}{\Delta f + \Delta f_0} \right|, \tag{2.13}$$

$$I_{fc} = \left| 1 - \frac{f_c - f_0}{f_c + f_0} \right|, \tag{2.14}$$

with Δf=min$\left(f_{max}^{(i)}\right)$-max$\left(f_{min}^{(i)}\right)$ the absolute band width and $f_c = \frac{1}{2}\left[\max\left(f_{min}^{(i)}\right) + \min\left(f_{max}^{(i)}\right)\right]$ the center frequency. $f_{max,min}^{(i)}$ represents the upper (index max) and lower (index min) edges of the band gap for the i-th wave where the subindex i represents each type of wave type $i = F, L, T$ for flexural, longitudinal and torsional waves respectively. I_{f_c} and $I_{\Delta f}$ evaluate the deviation between the band gap features f_c and Δf and the target features f_0 and Δf_0, respectively. These definitions are chosen so that the cost function is unitary $(0 < \mathcal{F} < 1)$.

Numerical simulations, the results of which are shown in Fig. 2.4, based on the wave models described Section 2.2 show that it is possible to obtain an absolute band gap, a frequency band where any type of wave is damped. However, it is hard to control the band gap features (bandwidth and center frequency) only from manual variations of the unit cell parameters. Hence, the three wave models are combined in an optimization procedure in order to find the set of geometrical parameters that lead to an absolute band whose features reach target bandwidth Δf_0 and a center frequency f_0.

To do that, we use the Nelder-Mead local minimization algorithm [172] as available in the MatLab function *fminsearch.m* and whose iterative process is represented in Fig. 2.5. Following the initialization step, for each iteration n, up to 5 methods are successively applied to find a new set of parameters $\mathbf{X_{n+1}}$ that leads to optimize a cost function $\mathcal{F}$. Note that $0 < \mathcal{F} < 1$ and that the optimization aims to reach $\mathcal{F} = 1$.

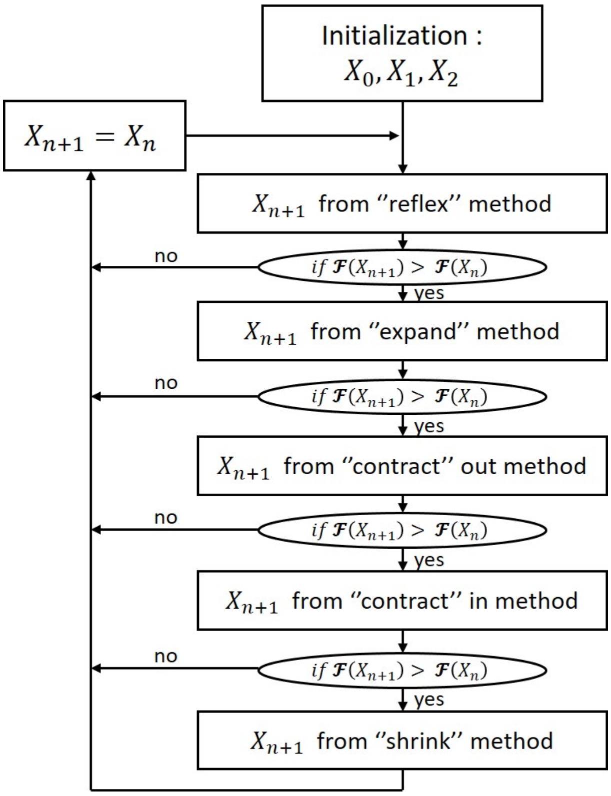

Figure 2.5 – Schematic representation of the Nelder-Mead algorithm [172].

Moreover, to ensure convergence towards slender pipe-like, non-aberrant and manufacturable geometries, the values of the geometrical parameters are restricted to the following ranges:

- $l_1 > 3R_1$ and $l_2 > 3R_2$ to ensure a slender pipe geometry,
- $0 < \gamma < 1$ to obtain a non-aberrant geometry,
- $R_{int} = 2$ mm is imposed for all simulations,
- $4\text{mm} < R_1 < \lambda_{alu}/12$ (with λ_{alu} the flexural wavelength in the aluminium for $f = 2$ kHz), which corresponds to sufficiently thick pipe walls to be manufacturable, but sufficiently small cross-section so that Timoshenko assumptions remain valid (an error of 5% at 2kHz with FEM results as reference is for example tolerated),
- $4\text{mm} < R_2 < \lambda_{nyl}/12$ (with λ_{nyl} the bending wavelength in nylon for $f = 2$ kHz), for the same reasons as R_1,
- $\beta < 0.8$ and $\beta > 1.2$ to ensure a minimum diameter contrast which facilitates the assembly of the pipe sections.

For all following cases, the set of parameters is initialized with $[l_{tot}, \gamma, R_1, \beta] = [60\text{ mm}, 0.5, 8\text{ mm}, 0.5]$, in agreement with results obtained in Fig. 2.6 where non optimized absolute band gap is obtained. The optimized geometry is assumed to be converged when when both $(\mathcal{F}_{n-1} - \mathcal{F}_n)/\mathcal{F}_n < 1\%$ and $(X_{n-1} - X_n)/X_n < 1\%$ stop conditions are simultaneously reached.

2.5.2 Analysis of performance optimisation for various weightings of $\mathcal{F}$

Figure 2.6 reports some typical results we obtained when studying the impact of the weighting coefficients α_{f_c} and $\alpha_{\Delta f}$ on the convergence of $\mathcal{F}$. In Fig. 2.6 the absolute target band is arbitrary chosen according to the results obtained in Fig. 2.4, the frequency band $[3 - 7]$ kHz is selected to be close to the configurations used for the parametric variation . The results in Fig. 2.6 show that convergence is easily ensured and several cell geometrical settings can be found for a same target band, depending on the weights coefficients. Given the restrictions to the set of parameter $\mathbf{X}$, these geometries remain relatively similar and so the variation of the parameters is about 10% around their average value in the 3 reported cases.

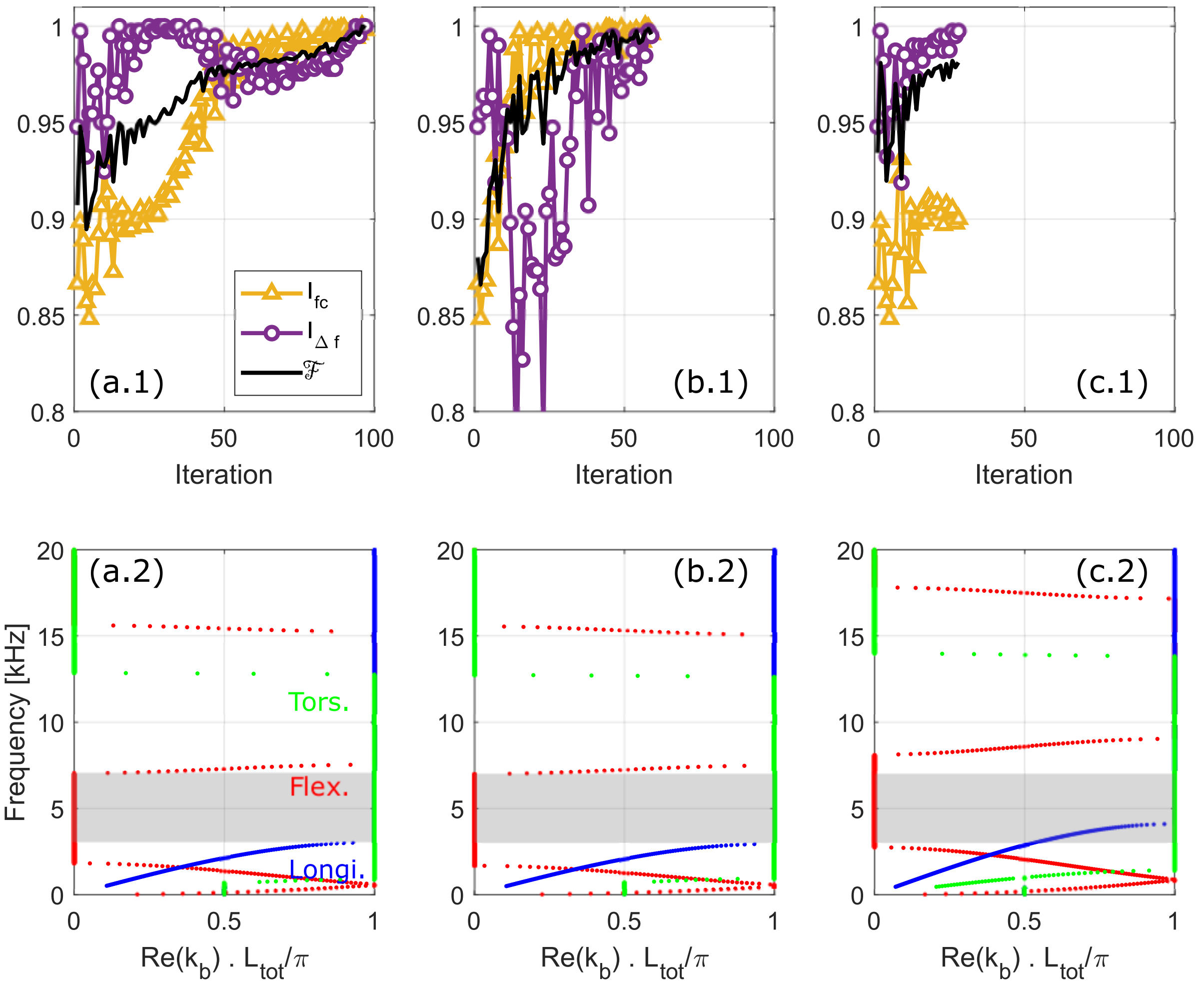

Figure 2.6 – Convergence of $\mathcal{F}$, I_{fc} and $I_{\Delta f}$ with the number of iterations (upper part), and associated optimized dispersion diagrams (lower part) when considering 3 couples of weighting coefficients: (a) $[\alpha_{f_c}, \alpha_{\Delta f}]$=[1/2, 1/2], leading to $\mathbf{X}$=[97.1 mm, 0.42, 7.9 mm, 0.58]; (b) $[\alpha_{f_c}, \alpha_{\Delta f}]$=[5/6, 1/6], leading to $\mathbf{X}$=[79.9 mm, 0.5, 8.7 mm, 0.48]; (c) $[\alpha_{f_c}, \alpha_{\Delta f}]$=[1/6, 5/6], leading to $\mathbf{X}$=[81.4 mm, 0.47, 7.2 mm, 0.58]. The target absolute band gap is [3; 7] kHz, that is $f_0 = 5$ kHz and $\Delta f_0 = 4$ kHz. See Tab. 2.2 for detailed results.

A more detailed analysis of the results in Fig. 2.6 leads to the following interpretations:

- When the weighting is the same for $I_{\Delta f}$ and I_{f_c} (Fig. 2.6(a)), the fastest feature to converge is the band width. The center frequency appears to converge more slowly. Many other optimizations not presented here confirm this general trend.

- When I_{f_c} is over-weighted (α_{f_c}=5α_{Δ_f}, Fig. 2.6(b)) in order to compensate for the slower convergence of the center frequency, the overall convergence is significantly accelerated: about 40% fewer iterations are required to reach the target without degrading $I_{\Delta f}$ (see detailed values in Tab. 2.2). This confirms the ease of obtaining the desired band width without error.

- When $I_{\Delta f}$ is over-weighted (α_{Δ_f}=$5\alpha_{\alpha_{f_c}}$, Fig. 2.6(c), the convergence is greatly accelerated (70% less iterations) due to the already fast convergence of $I_{\Delta f}$. But by the same, the convergence of I_{f_c} being more slowly and under-weighted, the resulting absolute band gap is a well-dimensioned bandwidth but with an inaccurate center frequency.

In order to extend the analysis, Tab. 2.2 reports the results from a set of optimization cases. Mainly, the high values obtained for I_{f_c} and I_{Δ_f} whatever the target illustrate the ability of the procedure to well find out the design of a phononic crystal pipe with desired filtering template. Generally, the results well confirm the trends figured out in Fig. 2.6 but some results highlight more difficult cases where either the number of iterations required is increased or the accuracy of the optimized performances with respect to the target is reduced. These cases typically correspond to wide band gaps centered at low frequency.

weights		target [kHz]		result [kHz]		convergence			
α_{fc}	$\alpha_{\Delta f}$	f_0	Δf_0	f_c	Δf	Nb it.	$\mathcal{F}$	I_{fc}	$I_{\Delta f}$
1/2	1/2	5	4	5.02	4	97	99.9%	99.8%	100%
		5	2	5	2	80	100%	100%	100%
		3	4	3.84	4	120	93.86%	87.72%	100%
		3	2	3	2	121	100%	100%	100%
5/6	1/6	5	4	4.96	4.04	59	99.58%	99.6%	99.5%
		5	2	4.92	2.08	42	99%	99.19%	98.04%
		3	4	3.02	3.28	110	98.07%	99.67%	90.11%
		3	2	3.01	2.02	77	99.78%	99.83%	99.5%
1/6	5/6	5	4	6.11	3.98	28	98.13%	90.01%	99.75%
		5	2	4.72	1.96	36	98.68%	97.12%	98.99%
		3	4	6.08	4	73	94.35%	66.08%	100%
		3	2	4720	2	79	96.29%	77.72%	100%

Table 2.2 – Detailed values obtained for the converged cost function $\mathcal{F}$ and its deviation indicators I_{Δ_f} and I_{f_c} for a set of optimization cases defined by 4 absolute band targets, each associated with three weighting configurations.

2.6 Study of an experimental demonstrator

The objective of this section is to experimentally verify the absolute filtering effects. This verification is carried out on a straight-line demonstrator of finite length consisting of a periodic bi-material as defined above.

2.6.1 Design of the experimental demonstrator

The optimisation procedure is applied to the solution of the semi-analytical eigenvalue problems described above with a target absolute band gap 3 kHz to 6 kHz, which is a typical range of interest for injection applications in the context of automotive industry [17]. A detailed study of the optimisation is given in section. 2.5, the choice of weighting coefficients which allow to obtain a fast convergence and a precise result of the cost function are $[\alpha_{f_c}, \alpha_{\Delta f}] = [5/6, 1/6]$ see at Fig. 2.6(b), this case leads to a the following topology $[l_{tot}, \gamma, R_1, \beta] = [79.9\text{ mm}, 0.5, 8.7\text{ mm}, 0.48]$.

For reasons of simplicity of fabrication, the radius finally retained are $R_1 = 8$ mm and $R_2 = 4$ mm. Preliminary tests, in order to equalise the first numerical and experimental resonance frequencies, also lead to correcting the values of Young's moduli and loss factors. The values obtained are $E_{alu} = 75$ GPa, $E_{nyl} = 2.6$ GPa and are considered frequency independent later. From these parameters an optimisation procedure is carried out under the same weighting conditions but only on the parameter space $X = [l_{tot}; \gamma]$. The optimal geometry of the 1D phononic crystal pipe obtained under these conditions and without considering material losses is $X = [87\ \text{mm}, 0.44, 7.5\ \text{mm}, 0.5]$.

A sectional view of the designed unit cell is shown in Fig. 2.7(a). The aluminium/nylon sections are assembled by forced interlocking, which avoids the use of glue and therefore minimises the introduction of unwanted losses.

A 6-cell demonstrator is simulated by the finite element method applied to a 3D elasticity model of the structure. The mesh is represented in Fig. 2.7(b). Free/free boundary conditions are applied to all external surfaces. At the lower end, 3 cases of harmonic point loads are studied: loading in flexion ($\mathbf{F_z}$, in red) or in pure compression ($\mathbf{F_x}$, in blue), loading off-center with respect to the axis of revolution ($O\tilde{x}$) and in an oblique direction according to the normal to the cut edge, which allows the excitation of the 3 types of wave of interest ($\mathbf{F_{full}}$, in grey). At the other end of the system, the acceleration response is measured at 2 points symmetrically positioned with respect to the axis of revolution.

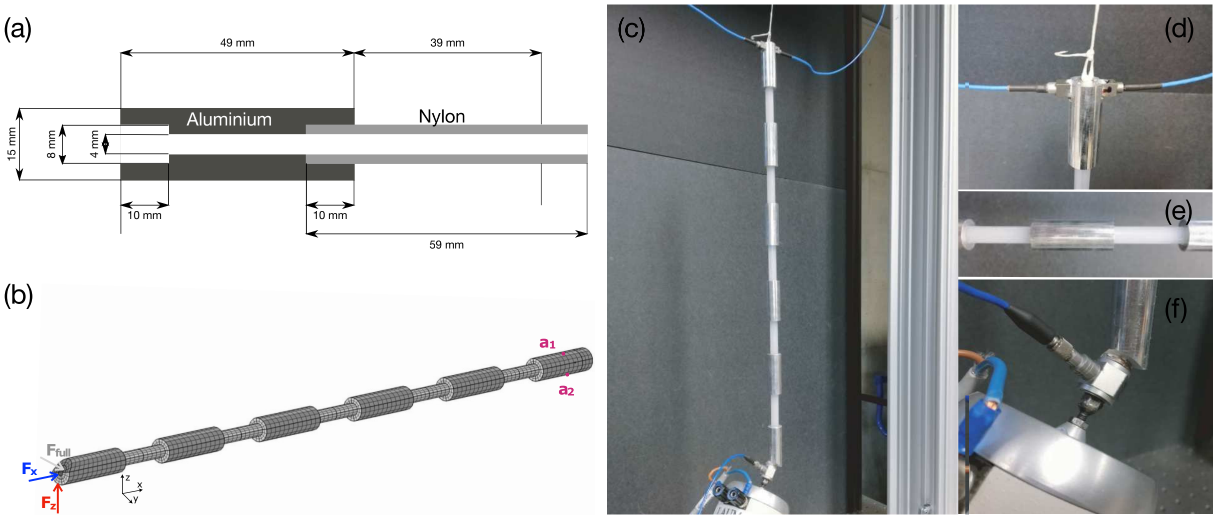

Figure 2.7 – Pictures of the fabricated phononic crystal tube. The nylon and aluminum sections are force-fitted together, holding the assembly together without the use of glue and thus minimizing unwanted losses. Sizing of a total filter demonstrator: (a) view of the view of the longitudinal cross section of the cell showing the interlocking assembly of the sections; (b) 6 cell digital demonstrator FEM mesh with representation of the 3 load cases and measurement points. (c) Experimental setup; (d) Detail of the 2 face-to-face three-axis accelerometers; (e) view of the 2 aluminium/nylon unit cells of the demonstrator; (f) view of the shaker excitation implemented in the oblique position such that all wave types are excited.

2.6.2 Experimental set-up

From the optimised geometry in the conservative case, the dispersion relation of the phononic crystal pipe shown in Fig. 2.8(a) is calculated in the dissipative case, by considering the viscoelastic losses for both aluminium and nylon via the complex Young modulus $E_i^c = E_i(1+\imath\eta_i)$ with $\eta_A = 1\text{e-}4$ and $\eta_N = 4\text{e-}2$. Each wave type displays band gaps where the real part of the wavenumber is low while imaginary part is high (see coloured patches in Fig. 2.8(b)). In the target range of frequencies, band gaps are well overlapping, the obtained absolute band gap is [3.2-5.7] kHz (grey patch in Fig. 2.8(a)), which is slightly narrower than the target, due to the losses.

In the experimental set-up the demonstrator is suspended vertically from a rigid gallows mounted on an optical breadboard. A shaker (LDS V201) excites the demonstrator at its bottom end with a harmonic point force $F = F_x.x + F_y.y + F_z.z$ (see axis definition in Fig. 2.1(a-b)) with a step-by-step sine in the range [0-10] kHz with a frequency step of 5 Hz.

The acceleration response $a = a_x.x + a_y.y + a_z.z$ is measured at the upper end by 2 three-axial accelerometers (PCB 356A01) that face each other (Fig. 2.7(d)). This experimental situation is also numerically simulated from a full wave 3D FEM model in order to compare transfer functions. Only the oblique case is pictured on the enlarged view of the figure Fig. 2.7(f). The unit is controlled by an LMS by Siemens SCADAS Mobile SPM 50 acquisition system. Each measurement is averaged over 3 acquisitions.

2.6.3 Results

The numerical and experimental results obtained on the demonstrator are gathered in Fig. 2.8. The dispersion diagrams (Fig. 2.8(a, b)) obtained with the Floquet-Bloch Models (colour points) and finite element (grey circles) methods are compared with the transfer functions simulated and measured on the demonstrator (Fig. 2.8(c, d, e)). The analysis is based on 3 types of transfer functions: $\|\mathbf{a}/\mathbf{F_{full}}\|$ in the case of the oblique excitation of the 3 movements (Fig. 2.8(e)), $\|\mathbf{a_z}/\mathbf{F_z}\|$ in the case of pure bending excitation (Fig. 2.8(c)), $\|\mathbf{a_x}/\mathbf{F_x}\|$ in the case of pure compression excitation (Fig. 2.8(d)). The accelerations $\mathbf{a}$, $\mathbf{a_z}$ and $\mathbf{a_x}$ are obtained by averaging the signals $\mathbf{a_1}$ and $\mathbf{a_2}$ from the 2 accelerometers.

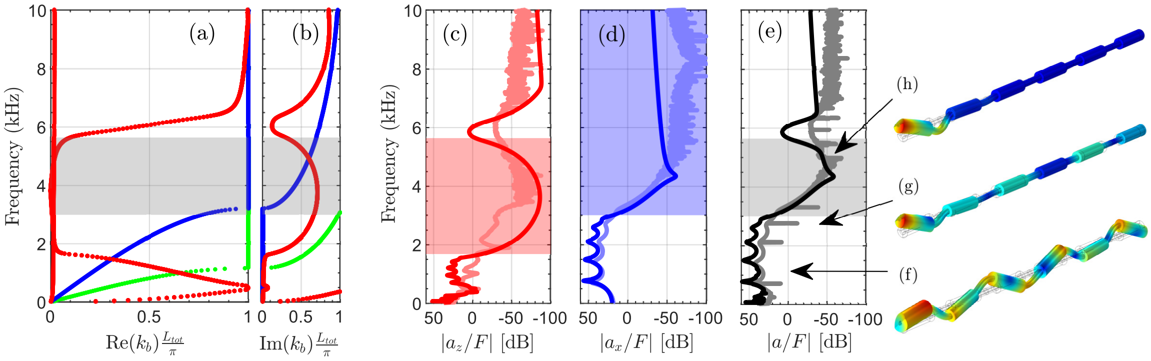

Figure 2.8 – Numerical analysis and experimental characterisation of the optimal phononic crystal pipe: (a) real part and (b) imaginary part of the optimised complex dispersion relation obtained by the Floquet-Bloch method and considering the viscoelastic losses (see main text). (●) longidutinal, (●) flexural and (●) torsional; measured (light line) and simulated (dark line) acceleration transfer functions in the (c) flexural, (d) longitudinal, (e) full loading cases; 3D views of the simulated total displacement in the full loading case at (f) 900 Hz where all wave types propagate, (g) 2500 Hz where only flexural band gap is opened and (h) 4500 Hz whithin the absolute band gap.

Figure 2.8(c) represents both numerical and experimental transfer functions $|a_z/F|$ in the flexural loading case. The measurements corroborate very well with the simulations especially in the low frequency passband and at the lower frequencies of the band gaps symbolised by coloured areas. Note that in this case of pure flexural loading. Unwanted bend/longitudinal couplings in the experimental set-up disturb the numerically predicted abrupt attenuation at the opening of the band gap at 2 kHz. It should also be noted that a filtering effect due to the first Bragg bandgap in the range $[0.45 - 0.6]$ kHz is identifiable both numerically and experimentally. The transfer functions show an attenuation of about 70 dB in the frequency range corresponding to the predicted flexural band gap.

The same trend is exhibited in Fig. 2.8(d) which plots the transfer functions $|a_x/F|$ in the longitudinal loading case. The full loading case is shown in Fig. 2.8(e) with the highlight of a strong attenuation in the transfer function $|a/F|$ in the range corresponding to the predicted absolute band gap. It is also interesting to note that finite size effects can be seen at low frequencies with peaks of the transfer function corresponding to the Fabry-Pérot resonances of the system.

Because of the frequency dependence of the Young's moduli and of the loss factors (which are assumed here to be constant). Some deviation in frequency and amplitude may occur at higher frequencies. The typical values of these deviations vary with movement, indicating a possible anisotropy of the material properties.

To complete the analysis, 3D views of the simulated total displacement field (operational deflection shapes) are shown in Fig. 2.8(f-h). At 900 Hz where all wave types propagate (Fig. 2.8(f)), the superposition of all motions results in a complex total displacement field. At 2.5 kHz (Fig. 2.8(g)) the field mainly exhibits the longitudinal component, the flexural component being strongly attenuated due to band gap effect. At 4.5 kHz (Fig. 2.8(h)) the total field vanishes close to the excitation due to the total filtering effect associated to the absolute band gap.

2.7 Conclusions

We have applied the concept of absolute band gap to a two-material phononic crystal pipe. Three 1D analytical Floquet-Bloch models giving the dispersion of both longitudinal, flexural and torsional waves considering losses have been combined in an optimisation procedure to reach a unit cell design that exhibit absolute band gaps with target features. The hand-ability and reliability of such design methodology has been shown through a set of cases. On the top of that, the study of a 6-cells demonstrator have shown both numerically and experimentally some dips of the transfer functions corresponding to the absolute band gap analytically predicted, bringing a second main insight. These results have shown how absolute band gaps in the high frequency domain can be applied to mitigate vibrations that may result in structure borne sound in some industrial systems. The design and optimisation of such phononic crystal pipes could be extended considering for example an enclosed pressurized liquid, hence considering couplings between acoustic and elastic waves.

Chap. 3

Design of 1D multi-wave vibration filters and absorbers based on local resonators inserted in waveguides

Contents

3.1 Introduction . . . 40
3.2 Dynamic behaviour of locally resonant structures . . . 40
  3.2.1 Design of a local resonator on a beam . . . 40
  3.2.2 Analytical model of the resonant frequency . . . 42
  3.2.3 Numerical parametric variation of ring resonators and associated resonance frequencies . . . 42
3.3 Reflection and transmission coefficients of locally resonant structures . . . 43
  3.3.1 Study of the variation of the parameters of a local resonator . . . 45
3.4 Examples of vibration filter configurations . . . 48
  3.4.1 Parameters of ring resonators . . . 48
  3.4.2 Design of a graded flexural filter . . . 49
  3.4.3 Design of a graded multi-wave filter . . . 51
3.5 Examples of vibration absorber configuration . . . 53
  3.5.1 Design of a graded flexural absorber . . . 54
  3.5.2 Design of a tuned vibration absolute absorber . . . 55
3.6 Experimental evidence of peak absorbance . . . 56
  3.6.1 Experimental set-up . . . 56
  3.6.2 Measurement of the reflection coefficient of the host material . . . 58
  3.6.3 Measurement of the frequency of a local resonator . . . 58
  3.6.4 Parametric variation of Numerical design of resonators . . . 60
  3.6.5 Evidence of the absorption peak . . . 61
3.7 Conclusions . . . 64

3.1 Introduction

In the previous chapter, the concept of absolute band gap was explored by considering Bragg diffraction in pipes with periodic material and geometrical properties. The results showed attractive performances for the design of multi-wave filters. However, modifying the pipe properties as it was done can be inappropriate in many application falling within the industrial context of the thesis for other engineering considerations as thermal or chemical behavior, mechanical strength, long-term aging, manufacturing process, ...

The aim of the chapter is to evaluate how multi-wave filtering but also absorbing features can be obtained by adopting an "additive" strategy that consists of inserting resonators on a host homogeneous elastic waveguide without changing its material and geometrical properties. In practice, the host waveguide under study in this chapter is a cylindrical pipe made in steel on which a set of annular resonators are mounted. The key point is to correctly tune the resonators to selected frequencies and according to the different wave types of interest. We focus on a frequency band around 1kHz, inspired by industrial issues.

This chapter is organised as follows. First, the dynamic behavior of a resonator is presented in section 3.2. In section 3.3 the reflection and transmission coefficients are calculated. Then several waveguide configurations are studied. In a first step as a vibration filter with two gradually tuned resonator configurations in section 3.4, in a second step as a vibration absorber with a gradually tuned flexural absorber and an absolute absorber configuration in section 3.5. The experimental set-up used to validate the model for the reflection problem is then presented in section 3.6 as well as the experimental methodology and results.

3.2 Dynamic behaviour of locally resonant structures

The geometry adopted in this chapter is based on the same application context as before, i.e. a hollow cylindrical pipe. The local resonator chosen is a steel annular ring mounted on a rubber ring. The objective of this section is to define the parameters associated with the resonators, their resonance frequencies as well as the movements that can be associated with them.

3.2.1 Design of a local resonator on a beam

Figure 3.1 shows an example of a ring resonator, (a), and its associated parameters, as well as the different motions of the mass-spring system, (b.1) to (b.4). In Fig. 3.1(a) the annular mass-spring system is characterized by the following parameters: a section of a steel pipe of mass M_s, length $l_s = 0.02\ m$, and thickness $r_{ext} - r_{int} = 1$ mm; a rubber ring of length, l, and thickness, $r_k - r_{ext}$. A steel ring of mass, M, and thickness $r_m - r_k$ completes the local resonator.

Figures 3.1(b) shows the different motions associated with the resonator modes. The mode shown in Fig. 3.1(b.1) shows a translational motion of the mass along the y direction (y-translation). In the case of a symmetric cylindrical structure, this motion also exists in z-translation. The mode shown in Fig. 3.1(b.2) shows x-translation motion of the mass. The mode shown in Fig. 3.1(b.3) shows a rotational motion of the mass around the z-axis (z-rotation). In the case of a symmetric cylindrical structure, this motion also exists in y-rotation. The mode shown in Fig. 3.1(b.4) shows a motion of the mass in x-rotation.

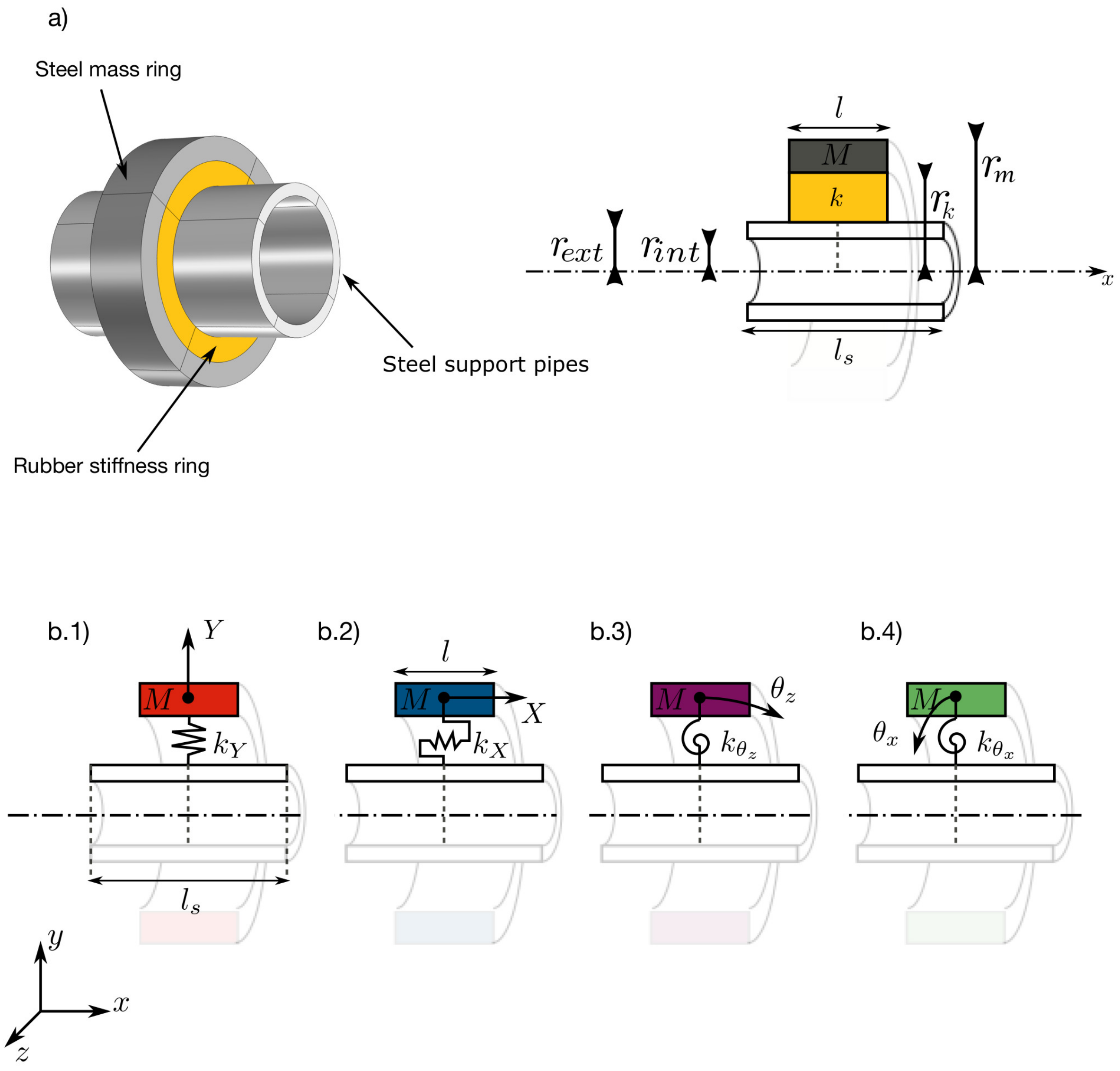

Figure 3.1 – 3D view of the considered annular resonators mounted on a host pipe (a) ; schematic representation of the motion associated to the 4 resonances admitted by such resonator (b): *y*-translation (b.1), *x*-translation (b.2), *z*-rotation (rotation around z) (b.3), *x*-rotation (b.4)

These movements can be coupled with the waves propagating in the guide: *y*-translation and *z*-rotation with flexural waves, *x*-translation with longitudinal waves and *x*-rotation with torsional waves. At the resonance frequencies of these resonators, it is possible to obtain filtering or absorbing effects.

3.2.2 Analytical model of the resonant frequency

The resonance frequencies are determined by $\omega_r = \sqrt{\frac{k_{(Y,X)}}{M}}$ for translational motion and by $\omega_r = \sqrt{\frac{k_{(\theta_x,\theta_z)}}{J}}$ for rotational motion, with J the rotational inertia. The mass of the ring, M, can be easily estimated or measured. The stiffness, k, can be estimated with Eqs. 3.1, from the literature [145, 173]:

$$\begin{aligned} k_{(Y)} &= \frac{\pi(5+3.29H^2)Gl}{log_e(r_k/r_{ext})}, \\ k_{(X)} &= \frac{2\pi Gl}{log_e(r_k/r_{ext})}, \\ k_{(\theta_x)} &= \frac{4\pi Gl r_{ext}^2 r_k^2}{r_k^2 - r_{ext}^2}, \end{aligned} \tag{3.1}$$

with $H = \frac{l}{(r_{ext}+r_k)log_e(r_{ext}/r_k)}$.

The geometry of the resonators can be adapted to choose the target resonance frequency. The mass of the resonator is chosen according to its length to obtain a frequency of 1 kHz, $M(\omega_r, l) = \rho_m\pi(r_m^2 - r_k^2)l = k_{X,Y}(l)/\omega_r^2$. The configurations are shown in Fig. 3.2 according to the targeted eigenmode: red (a) for y-translation, blue (b) for x-translation and green (d) for x-rotation. The low computational cost of analytical methods allows the implementation of early design tools. A large number of configurations can be rapidly tested to carry out an optimization process.

3.2.3 Numerical parametric variation of ring resonators and associated resonance frequencies

To check if the geometries identified analytically with Eqs. 3.1 are correct, a numerical simulation is set up. Its considers a steel ring of variable mass M and a rubber ring of variable lenght l. The inner boundary of the rubber ring is clamped. In Fig. 3.2, sets of geometries are explored by varying the ratios, M/M_s and l/l_s. Mass M varies from $0.05 \times M_s$ to $2 \times M_s$. Lenght l varies from $0.05 \times l_s$ to $0.5 \times l_s$. Two types of rubber are explored, a 2 mm thick rubber with Young's modulus $0.77E6$ Pa from the literature [145] (Fig. 3.2(a)), and a 1 mm thick rubber ring with Young's modulus $2.866E6$ Pa from Continental Automotive datasheets (Fig. 3.2(b, c, d)). The colormap is between 500 Hz and 1 kHz.

Figure 3.2(a) shows the evolution of the eigen freqency of the y-translation mode whose motion is illustrated by the 3D view. Geometrical configurations leading to an eigen frequency of 1 kHz are depicted by a red square while the red line goes for the results obtained by the analytical model. By the same, Fig. 3.2(b),(c) and (d) correspond to x-translation, z-rotation and x-rotation resonances, respectively. Note that no analytical model is presented for z-rotation motion. The results show that the analytical estimation of eigen frequencies is only suitable for x-translation and x-rotation modes. In the following, only numerical modeling is considered to ensure accurate predictions.

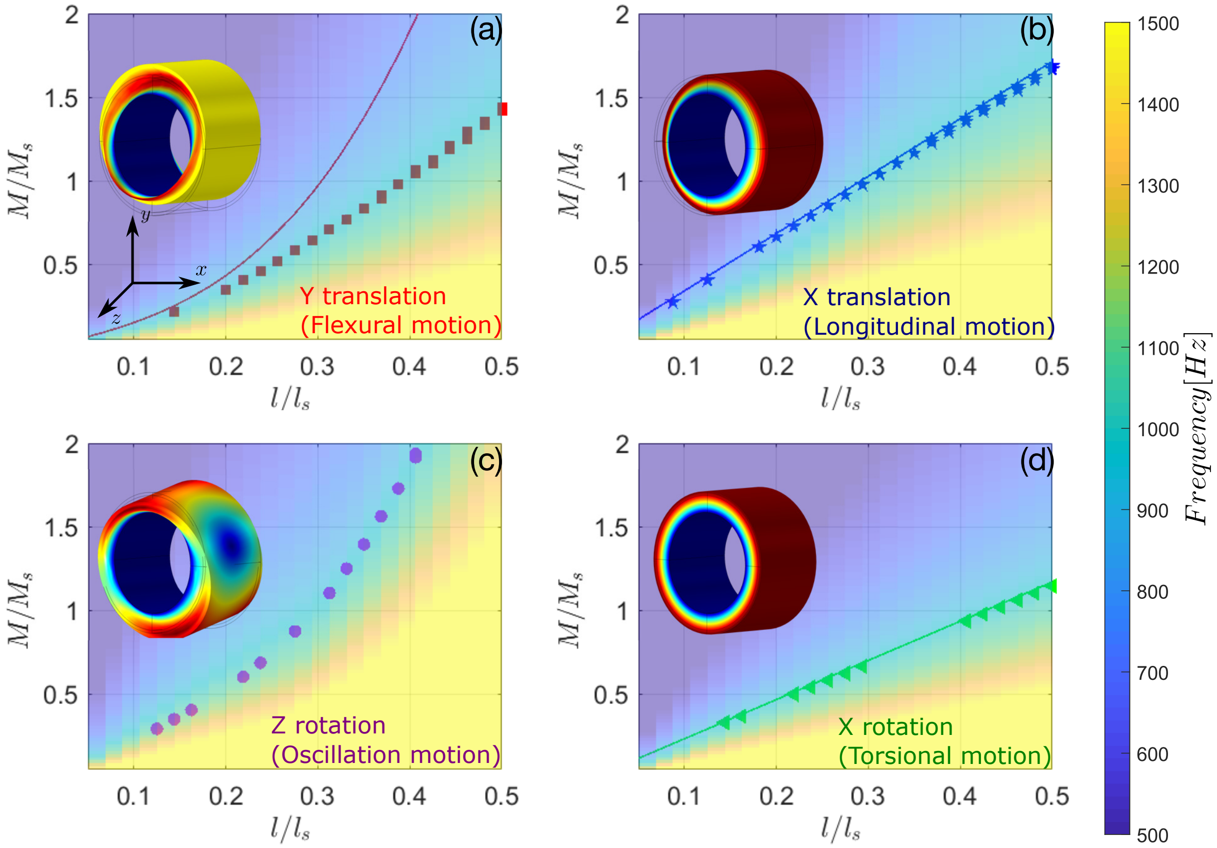

Figure 3.2 – Map representation of the evolution of the eigen frequencies of the ring resonator for varying ring length l and mass M. Resonant rings have 4 solid body movements that can be associated to a type of wave. The curves represent the operating points for a resonator tuned to 1 kHz, respectively □ for *y*-translation or *z*-translation, ⋆ for *x*-translation, ○ for *z*-rotation or *y*-rotation, and ◁ for *x*-rotation. The straight line are for the analytical calculation.

3.3 Reflection and transmission coefficients of locally resonant structures

The objective of this section is to calculate the reflection and transmission coefficients from simulated vibratory fields. Two resonator configurations are studied. A filter configuration, Fig. 3.3, with a transmission and reflection calculation, and an absorber configuration, Fig. 3.4 with a purely reflection calculation.

Figure 3.3 shows the filter configuration, the objective of the filter is to minimize the vibration transmission. The configuration consists of a steel tube on which is mounted a ring resonator. A force is applied to one end of the waveguide according to the chosen movement, flexural to study the impact of the resonator on the flexural waves, longitudinal to study the impact on the transmission of the longitudinal wave. The displacement field is identified on the upstream (x_1, x_2, x_3, x_4) and downstream (x_5, x_6, x_7, x_8) points. The PMLs at the ends of the guide are used in order to avoid the spureous reflections the end of the waveguide.

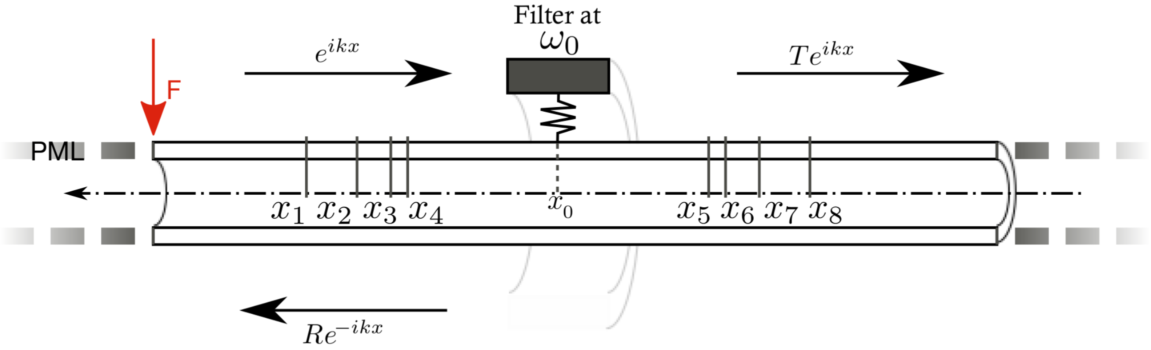

Figure 3.3 – Schematic diagram for the numerical calculation of the R and T coefficients in the case of configuration of the guide as a flexural vibration filter.

Figure 3.4 shows absorption configuration, the objective of a vibration absorber is to maximize the absorption of the reflected wave. The configuration consists of a steel pipe with a ring resonator mounted at its end. A force is applied to one end of the waveguide according to the chosen motion. Flexural to study the impact of the resonator on the flexural waves, longitudinal to study the impact on the transmission of the longitudinal wave. The displacement field is identified on the upstream points (x_1, x_2, x_3, x_4). The end of the waveguide is either clamped (Fig. 3.4(a)) or free (Fig. 3.4(b)). The resonator is placed near the end of the waveguide.

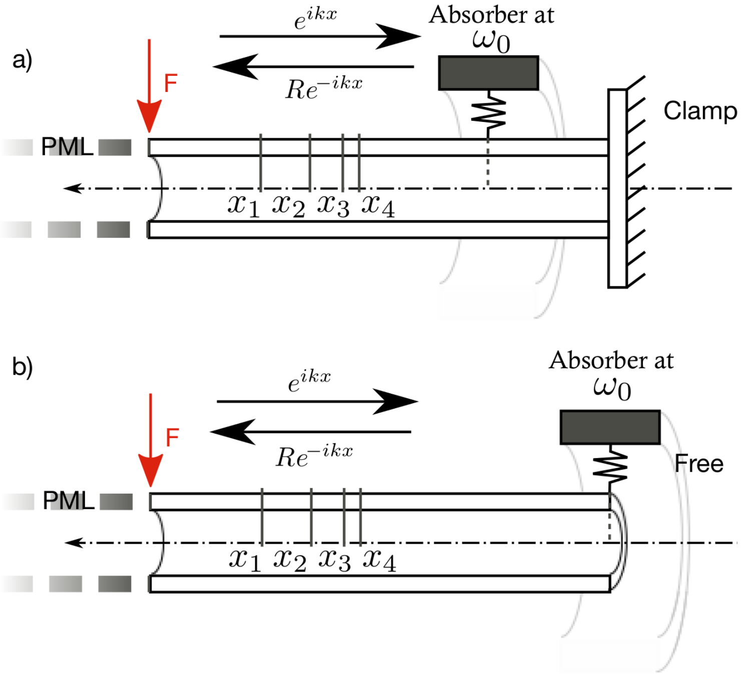

Figure 3.4 – Schematic diagram for the numerical calculation of the R-factor in the case of a configuration of the guide as an absorber with recessed termination (a), with free termination (b).

Considering a host cylinder on which aring resonator is inserted, the flexural displacement field $v_i(x_i, \omega)$ that is simulated can be analysed following a wave base decomposition such as:

$$v_i(x_i, \omega) = B_1^w(\omega)e^{ik_ix_i} + B_2^w(\omega)e^{-k_ix_i} + B_3^w(\omega)e^{-ik_ix_i} + B_4^w(\omega)e^{k_ix_i}, \tag{3.2}$$

with $k_i = (\frac{\rho S}{EI}\omega^2)^{\frac{1}{4}}$ the wavenumber and B_+^w and B_-^w the unknown amplitudes of the waves propagating to $x+$ and $x-$ respectively. The superindex w can be u or d for waves upstream or downstream of the resonator, respectively [31].

Considering 8 point of interest as shown in Fig. 3.3 where the field can be picked up, the set of unknown wave amplitudes satifies the following linear system:

$$\begin{pmatrix} v(x_1,\omega) \\ v(x_2,\omega) \\ \vdots \\ v(x_7,\omega) \\ v(x_8,\omega) \end{pmatrix} = \begin{pmatrix} e^{ik_ix_1} & e^{-k_ix_1} & e^{-ik_ix_1} & e^{k_ix_1} \\ e^{ik_ix_2} & e^{-k_ix_2} & e^{-ik_ix_2} & e^{k_ix_2} \\ \vdots & \vdots & \vdots & \vdots \\ e^{ik_ix_7} & e^{-k_ix_7} & e^{-ik_ix_7} & e^{k_ix_7} \\ e^{ik_ix_8} & e^{-k_ix_8} & e^{-ik_ix_8} & e^{k_ix_8} \end{pmatrix} \begin{pmatrix} B_1^u(\omega) \\ B_2^u(\omega) \\ \vdots \\ B_3^d(\omega) \\ B_4^d(\omega) \end{pmatrix}. \tag{3.3}$$

In the far field, $kx_i >> 1$, the ratio between the incident and reflected wave gives the reflection coefficient R and the ratio between the incident wave upstream and downstream of the resonator gives the transmission coefficient T. After inversion, the reflection and transmission coefficients for an $x+$ incoming propagative wave are respectively:

$$\begin{aligned} R+ &= \frac{B_2^u(\omega)}{B_1^u(\omega)}, \\ T+ &= \frac{B_1^d(\omega)}{B_1^u(\omega)}. \end{aligned} \tag{3.4}$$

These reflection and transmission coefficients depend on the characteristics of the materials used for both the waveguide and the resonators, in particular the complex Young's modulus of the rubber. When we introduce losses with a complex Young's modulus, $E' = E(1+i\eta)$, the incident wave cannot be perfectly reflected anymore, it is partially absorbed by the resonator. This absorption, introduced by the complex Young's modulus, is quantified by an absorption coefficient $\alpha = 1-|R|^2-|T|^2$.

3.3.1 Study of the variation of the parameters of a local resonator

In this section, the resonators are numerically characterized and variations of several parameters are performed to characterize the behaviour of the resonators. A filter configuration (Fig. 3.5) and an absorber configuration (Fig. 3.6) are implemented.

A schematic of the vibrational filter is shown, Fig. 3.5(a), along with the transmission and reflection coefficients for a resonator tuned to 1 kHz (b). A schematic of the vibration absorber is shown, Fig. 3.6(a), as well as the reflection and absorption coefficients for a resonator tuned to 1 kHz (b). The following parametric variations are studied: resonator mass with the resonator geometries identified in section 3.2 (Fig. 3.5(c)), damping introduced by the rubber (Fig. 3.5(d)), and distance of the resonator from the end of the waveguide (Fig. 3.6(c)).

In the configuration of a vibration filter, this absorption will have a negative impact on the filtering effects by influencing the transmission coefficient. But in the case of a vibration absorber, we will try to maximize the absorption because it will allow to obtain a low reflection coefficient, which means that a large part of the incident wave will be absorbed.

Waveguide in filter configuration

In this section, the parametric variations are applied on the resonator which allows to obtain a vibratory filter effect. According to the chosen motion, flexural in red, or longitudinal, in blue, the waveguide is excited with either a flexural or longitudinal force, (see Fig. 3.5(a)).

In Fig. 3.5(b), the red curve is obtained for a resonator tuned at 1kHz for a flexural motion. The blue curve is obtained for a resonator tuned at 1kHz for a longitudinal motion. The reflection and transmission coefficients are calculated according to the method described in section. 3.3. The chosen resonator configuration leads to a quasi-zero transmission, $|T| \to 0$ and a quasi-perfect reflection, $|R| \to 1$. Δf represents the frequency range where the transmission is less than half of its minimum value, and for reflection half of its maximum value.

Figure 3.5(c) shows the evolution of Δf when both the length and mass (external radius) of the ring of the resonator are increased, keeping the resonance at 1 kHz. The complete set of configurations is detailed in Tab. 3.1. We can see that the heavier the resonator, the wider is the transmission drop.

	Resonator n^o	l/l_s	m/m_s		Resonator n^o	l/l_s	m/m_s
Flexural	1	0.14	0.22	Longitudinal	1	0.09	0.35
	2	0.20	0.35		2	0.14	0.58
	3	0.26	0.52		3	0.18	0.75
	4	0.29	0.65		4	0.22	0.92
	5	0.33	0.77		5	0.26	1.06
	6	0.37	0.92		6	0.29	1.23
	7	0.41	1.06		7	0.33	1.38
	8	0.44	1.20		8	0.37	1.54
	9	0.48	1.35		9	0.41	1.69
	10	0.50	1.43		10	0.44	1.86

Table 3.1 – Flexural and longitudinal ring resonators parameters for a $1kHz$ tuning. Each configuration can be link with Fig. 3.2

Figure 3.5(d)shows the influence of adding damping in the system. Damping is introduced as a loss factor η into the Young's modulus of the rubber $E'_{rubber} = E_{rubber}(1 + i\eta)$. The minimum value of the transmission coefficient, maximum of the reflection coefficient and maximum of the absorption coefficient α is plotted for each value of η adopted.

The addition of a damping factor has a direct influence on the transmission and reflection factors. When it increases, the transmission factor goes from zero to close to 1, and from perfect reflection to almost zero. If we consider the absorption coefficient, it evolves differently depending on the type of rubber used. We note that there is a value η for which the absorption α is maximum, $\alpha = 0.5$, which is obtained when the two values $|R|$ and $|T|$ are equal $|R| = |T| = 0.5$ [54].

In the case of a vibration filter, we want to obtain an effect where the transmission of vibration will be zero, i.e. $|T| = 0$. In this case, $\eta_{filter} = 0$ is a solution to obtain a perfect filtering effect. This value is used to design resonant vibration filters. In the case of a vibration absorber, we seek to obtain a waveguide where the absorption will be maximum for the targeted frequency range. In this case, $\eta_{longi} = 2\%$ and $\eta_{flex} = 10\%$ allow to obtain an absorption effect. These values are used to design vibration absorbers.

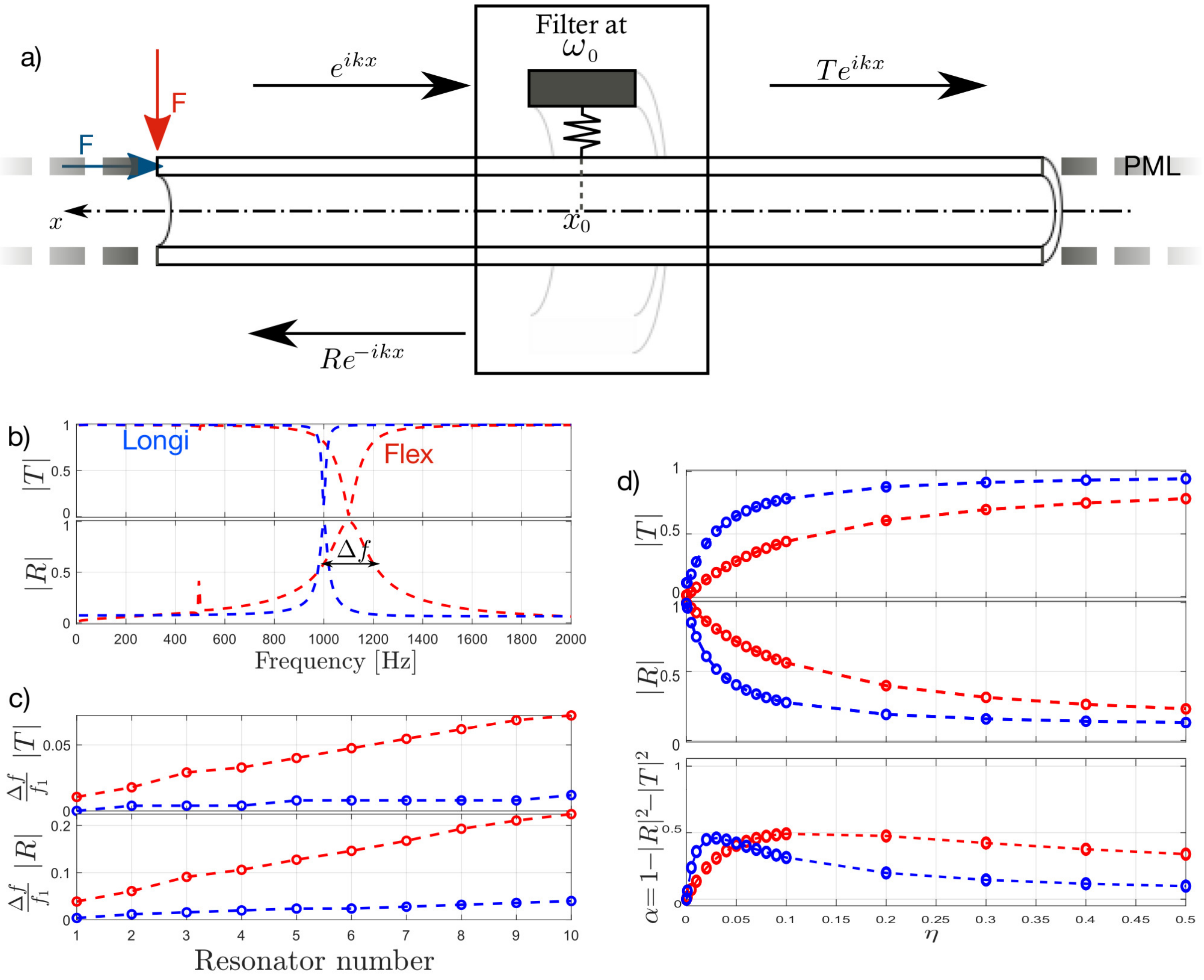

Figure 3.5 – Illustration of the principle of functioning of a vibration filter made of a resonator, (a). Example of a filter effect with any resonator tuned for 1 kHz, with a structural damping value in the rubber $\eta = 0$, (b). Evolution of the flexural (○) and longitudinal (○) values of Δf for the configurations described in Tab. 3.1, (c). Evolution of the limit value of a vibration filter according to the evolution of the structural damping factor η (d).

Waveguide in absorption configuration

As done in previous sections, here parametric variations are applied on the resonator which allows to obtain a vibration absorption effect. Depending on the chosen motion, flexural in red, or longitudinal in blue, the waveguide is excited by a flexural or longitudinal force (see Fig. 3.6(a)).

In Fig. 3.6(b), the curve is obtained for 10th resonator tuned at 1kHz from Tab. 3.1 in flexural motion. The reflection and absorption coefficients are calculated according to the method described in section. 3.3. The chosen resonator configuration allows to obtain a quasi-zero reflection, $|R| \rightarrow 0$ and a quasi-perfect absorption, $|\alpha| \rightarrow 1$. The curves in Fig. 3.6(b) are obtained for a maximum introduced damping of $\eta = 10\%$ for the rubber used for the flexural resonator, which explains why we do not obtain an absorption value, $\alpha = 1$, for longitudinal wave.

In Fig. 3.6(c) the distance l_l between the resonator and the free end of the waveguide is gradually increased. The minimum value of the reflection coefficient and the maximum value of the absorption coefficient are plotted. The distance on the x-axis is expressed as a function of the flexural wavelength for the target value of 1 kHz, $\lambda_{flex}(1\ kHz) = \frac{c_{steel}}{f} = 0.35$ m. The position of the resonator has a strong influence on the maximum absorption allowed by the absorber. When the resonator is located on a node of the deformation field, it interacts weakly with the host structure.

This results in a lower absorption. When it is located on an anti-node, it interacts more with the host structure, resulting in near perfect absorption. We note that the absorption of longitudinal modes is not affected by the range of values taken by I_l.

This influence of the spacing between the resonator and the waveguide termination deserves to be further developed through numerical and analytical models. In our case we will just consider carefully the position that each resonator will take, see Fig. 3.6(c).

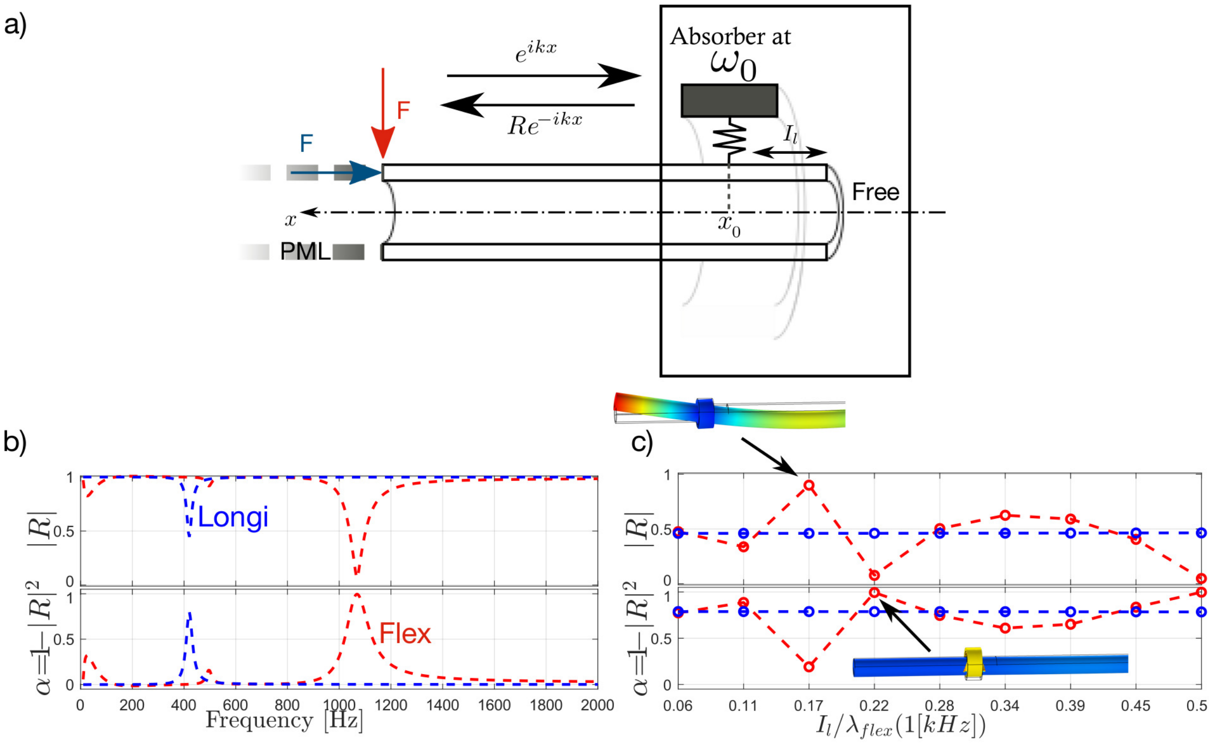

Figure 3.6 – Example of absorption effect with a resonator tuned for 1 kHz in flexural, with a structural damping value in the rubber $\eta = 10\%$, (b). Evolution of the threshold value of a vibration absorber as a function of the distance I_l between the resonator and the free end of the waveguide. (c).

3.4 Examples of vibration filter configurations

In this section, examples of resonators in the vibration filter configuration are studied. The objective is to achieve a stop band for one or more types of waves. The objective is to minimize the vibration transmission to obtain a filter effect, for flexural waves in a first step, and for flexural waves and longitudinal waves simultaneously in the same range of frequencies in a second step. The filters are designed to have a broadband frequency effect. The use of a series of resonators with close resonance frequencies allows to enlarge the stop band [42].

3.4.1 Parameters of ring resonators

The resonators are chosen from the numerical calculation, and are gathered in Tab. 3.2. They are selected close in frequency so that the attenuation peaks overlap over part of the chosen frequency range. Ideally, an optimization process can be used to obtain a perfect filter for a wide frequency range using a coupled resonator configuration. However, the cost of numerical calculation does not allow us to consider it. In our case, we rely on the previous curves and estimate that a 50 Hz gap between the resonance frequencies of the flexural resonators (25Hz for the longitudinal ones) allows us to obtain an overlap of the resonancesand to approach a wide frequency band filter configuration.

Flexural resonator	Frequency [Hz]	l/l_s	m/m_s
ω_4	850	0.5	2
ω_3	900	0.5	1.7917
ω_2	950	0.5	1.6042
ω_1	1000	0.5	1.4375

Longitudinal resonator	Frequency [Hz]	l/l_s	m/m_s
ω_4	875	0.44375	1.9583
ω_3	900	0.48125	2
ω_2	925	0.5	1.9792
ω_1	950	0.5	1.4375

Table 3.2 – Flexural and longitudinal resonator parameters for graded vibration filters

3.4.2 Design of a graded flexural filter

A first set of resonators tuned for flexural is assembled on a waveguide, with the objective of calculating the reflection and transmission coefficients of the set of resonators.

In Fig. 3.7(a) the waveguide is excited in flexural at one end. The far field scattering matrix $S = \begin{pmatrix} T & R^+ \\ R^- & T \end{pmatrix}$ is obtained from two numerical simulations and allows to evaluate the transmission coefficient $|T|$ (in −−), the reflection coefficients of the forward $|R^+|$ (in −−) and backward $|R^-|$ (in ...) waves. The resonators in the order $[\omega_1, \omega_2, \omega_3, \omega_4]$ show the reflection coefficient $|R^+|$. The resonators in the order $[\omega_4, \omega_3, \omega_2, \omega_1]$ give the reflection coefficient $|R^-|$. Notice that in the farfield the problem corresponds to a 1D reciprocal and non-symmetric scattering problem.

Despite the non-optimized coupling between the resonators, the addition of resonators in series provides a broadband filtering effect around a target frequency (Fig. 3.7(b)). While a frequency band ranging from 850 Hz to 1000 Hz is expected, the observed filtered frequency band ranges from 850 Hz to 1200 Hz. The interaction between the host structure and the resonators, but also between the resonators themselves, has the effect of shifting the resonance frequency of the resonators. This coupling between the components of the vibratory filter leads to a wide frequency band where a vibratory filter effect is observed. The numerical results presented in this figure are obtained for resonators without structural damping $\eta = 0$, which allows to maximize the effects of the filter. In this case, we notice that $|R^+| = |R^-|$.

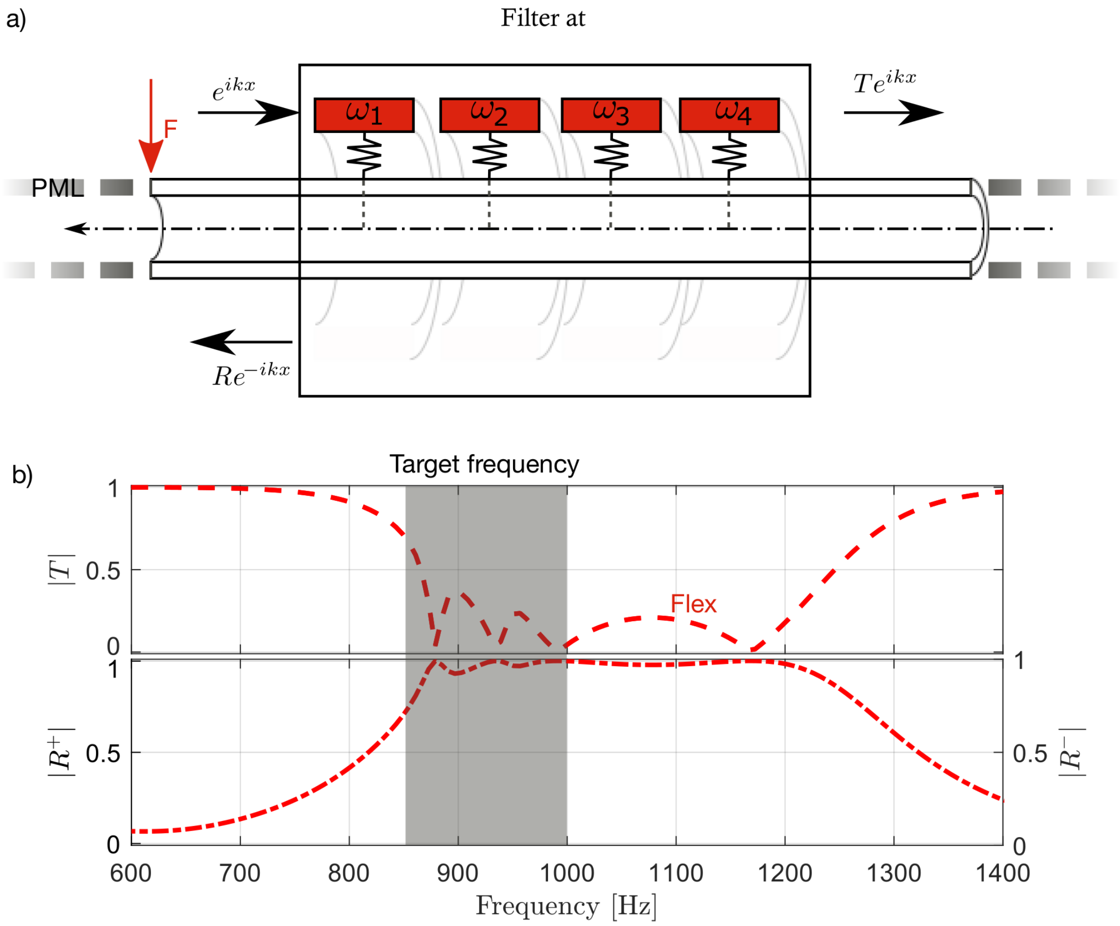

Figure 3.7 – Coefficient of reflection $(|R^+|, |R^-|)$ and transmission $([T|)$ of a graded filter without structural damping $\eta = 0$. The geometry of the resonators is available Tab. 3.2. The reflection coefficients obtained for the forward ($|R^+|$ in −−) and return ($|R^-|$ in . . .) waves are superposed.

With a series of resonators it is possible to obtain a broadband filter. However, it is expected that the rubber ring will introduce some damping. In the following section we study the influence of the addition of a damping η on the transmission and reflection coefficients of the graded vibratory filter.

In Fig. 3.8 the Young's modulus of the rubber introduces a damping $\eta = 10\%$. Coefficients $|\alpha^+|$ and $|\alpha^-|$ identify the proportion of the wave that is absorbed by the resonator array. The peaks of transmission decrease are no longer marked and the behavior of the resonators appears more coupled (a). The behavior of the reflection ($|R^+|$, $|R^-|$) and absorption ($|\alpha^+|$, $|\alpha^-|$) coefficients is more affected by the introduced damping (b)(c). In the frequency band from 850 Hz to 1000 Hz, the forward waves are absorbed by the resonators. We note that the absorption coefficients are higher than $|\alpha| = 0.5$ which shows an interaction of the resonators between them. A part of the waves reflected by the downstream resonators interacts again with the upstream resonators which leads to an absorption comparable with that obtained for the vibration absorbers.

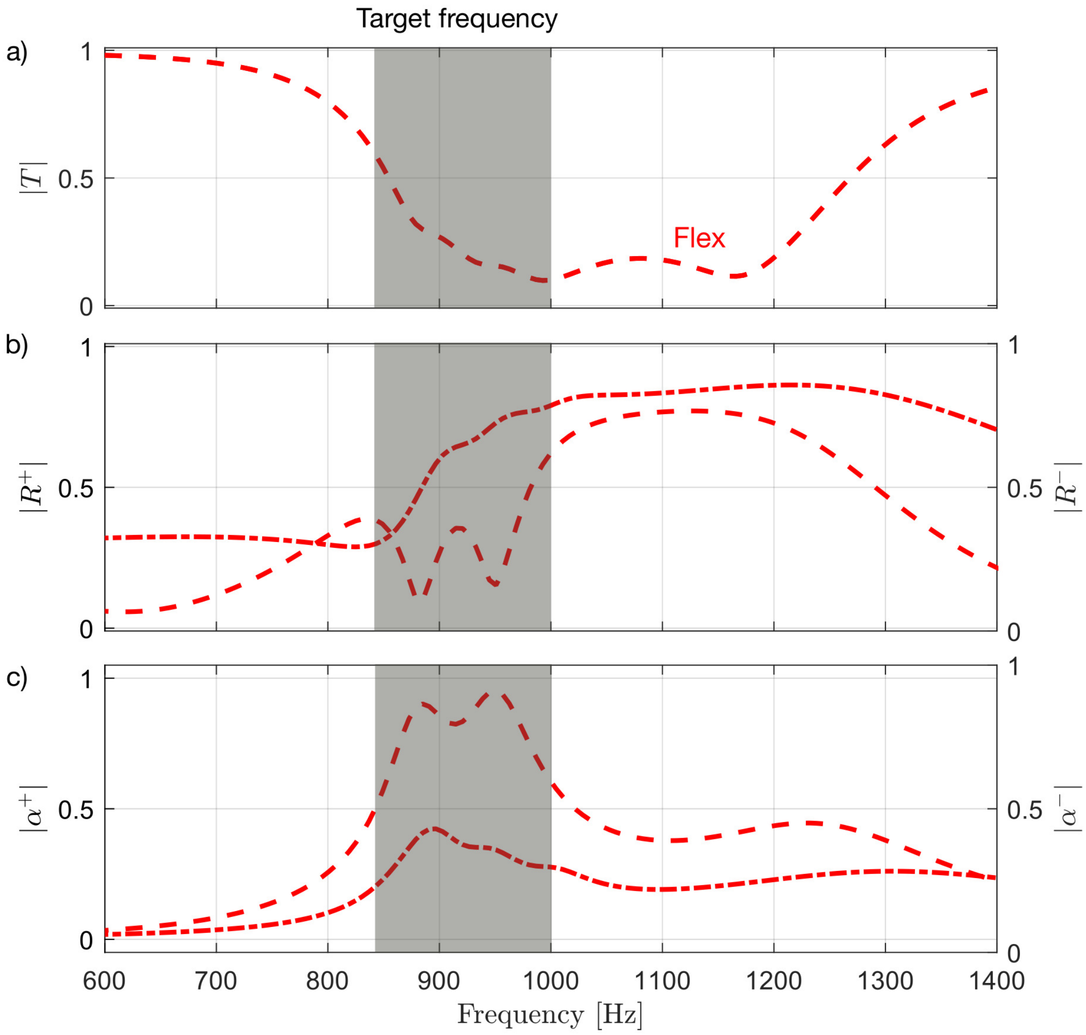

Figure 3.8 – Coefficient of reflection, transmission and absorption of a graded vibration filter with structural damping $\eta = 10\%$. The geometry of the resonators is available Tab. 3.2. The reflection coefficients is obtain for the forward ($|R^+|$ in $--$) and return ($|R^-|$ in $\ldots$) waves. Due to the presence of damping, $\eta \neq 0$, we see an absorption effect, $\alpha \neq 0$.

3.4.3 Design of a graded multi-wave filter

After obtaining a vibration filter for the flexural waves, tuned resonators for the longitudinal waves are added to the waveguide. The objective is to minimize the transmission of the longitudinal wave to obtain a filter for several types of waves in a common frequency band.

In Fig. 3.9(a), the vibration filter consists of the resonators from the Tab. 3.2, tuned for flexural and longitudinal waves. To obtain the flexural transmission and reflection coefficients, a force F is applied in the y direction perpendicular to the end of the guide. To obtain the longitudinal transmission and reflection coefficients a force F is applied in the x direction parallel to the end of the guide. As illustrated by the red and blue arrows respectively. At first we consider a structural damping $\eta = 0$.

In Fig. 3.9(b) the transmission coefficient $|T|$ of the longitudinal waves does not allow to observe a frequency band with a filter effect, the lack of coupling between the resonators leads to the presence of several peaks of transmission decrease which are not coupled between them. A flexural filtering effect is observed for a frequency range from 850 Hz to 1100 Hz. We note a peak at 1150 Hz due to the flexural movement of one of the longitudinal resonators, as illustrated by the operational deflection shape.

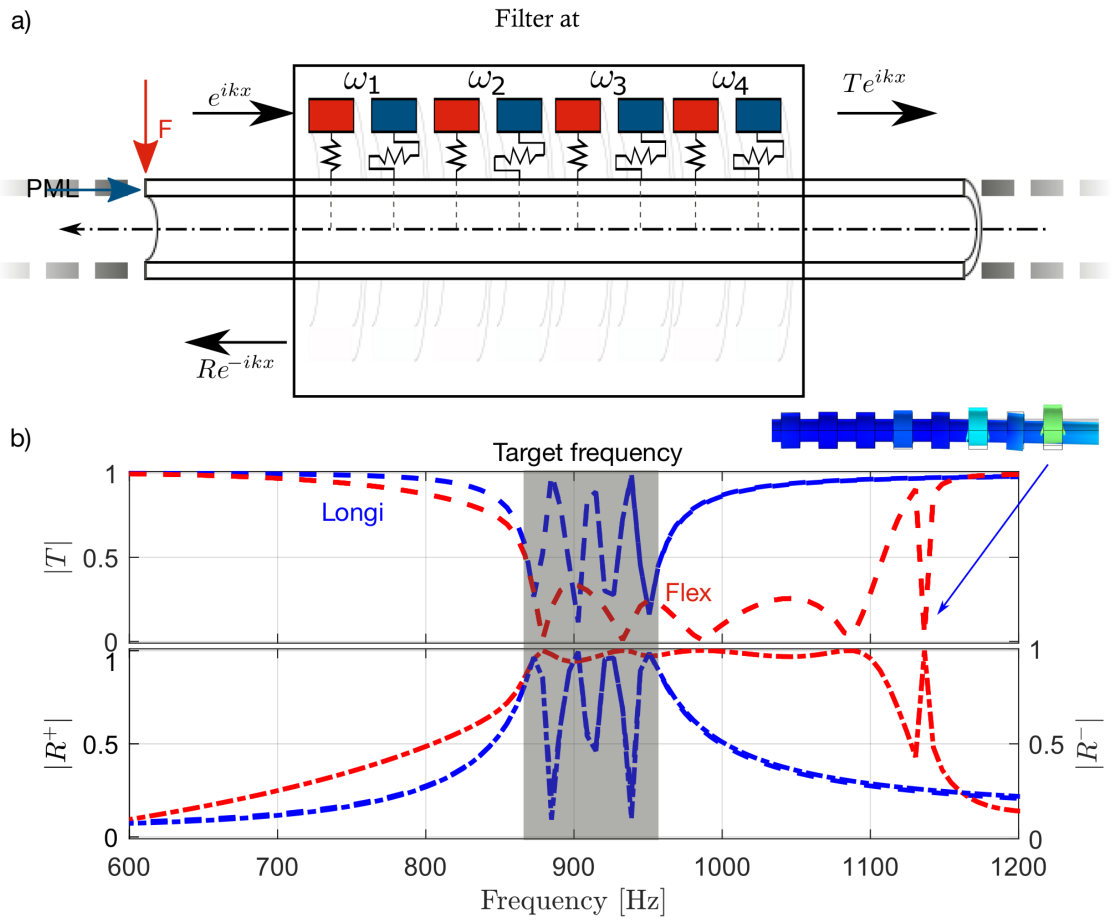

Figure 3.9 – Coefficient of reflection and transmission of a graded filter type vibration filter without structural damping $\eta = 0$. The geometry of the resonators is available Tab. 3.2. The reflection coefficients is obtain for the forward ($|R^+|$ in – –) and return ($|R^-|$ in ...) waves.

The lack of structural damping does not allow a wide frequency band to be filtered out for longitudinal and flexural waves. However, as discussed earlier, adding η damping to the Young's modulus of the rubber changes the shape of the transmission and reflection coefficients. In the following, $\eta_{flex} = 10\%$ damping is added for the flexural resonators and $\eta_{longi} = 2\%$ damping is added to the longitudinal resonators (see section 3.3.1).

Figure 3.10 studies the influence of the addition of damping on the vibration filter. For flexural waves the influence of damping is similar to that observed previously in section 3.4.2. The resonators provide a high absorption between 850 Hz and 1000 Hz. For longitudinal waves, the peaks of the transmission coefficients $|T|$ are more coupled together but only allow to reach a coefficient $|T| = 0.5$ (a). The reflection coefficient ($|R^+|$, $|R^-|$) and the absorption coefficient ($|\alpha^+|$, $|\alpha^-|$) are slightly different depending on the direction of propagation of the wave. As with the flexural resonators in the direction of travel we obtain an absorption higher than $|\alpha| = 0.5$ which implies a cumulative absorption effect between the different resonators (b), (c).

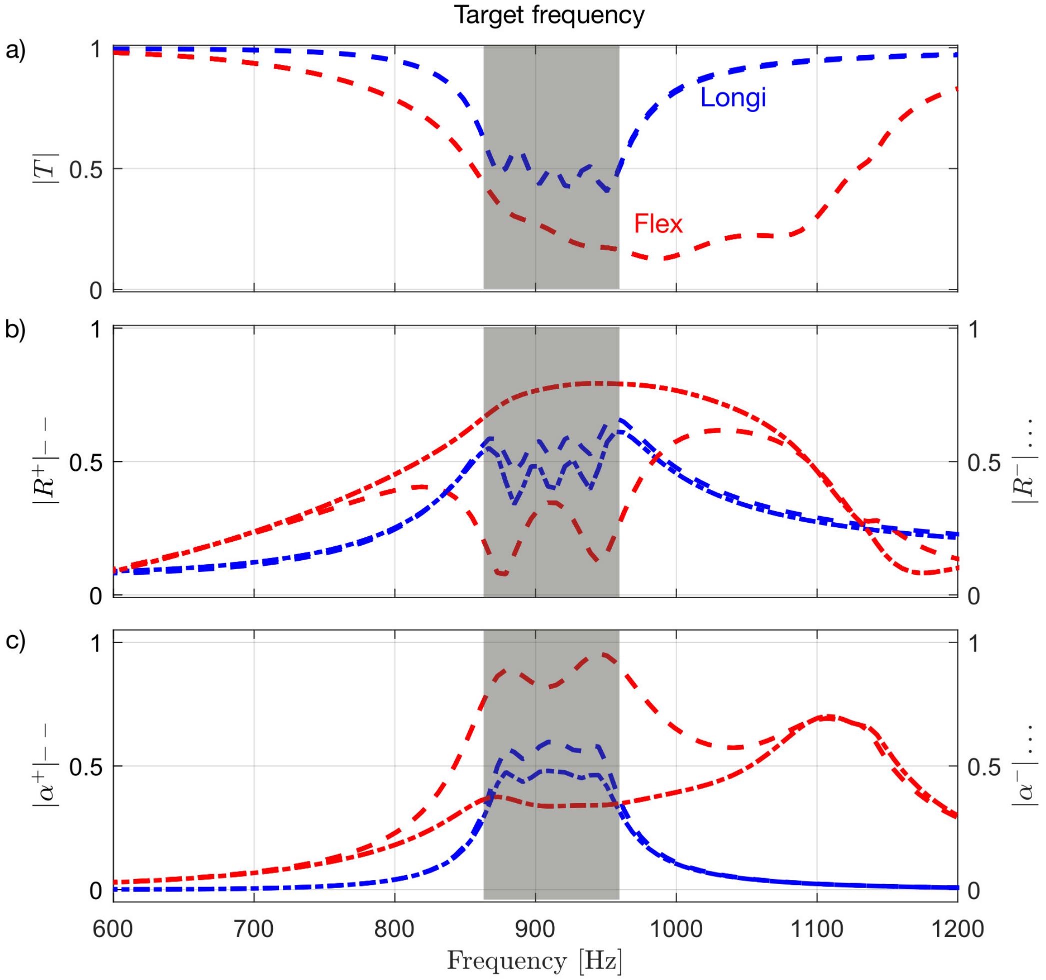

Figure 3.10 – Coefficient of reflection, transmission and absorption of a graded filter type vibration filter with structural damping $\eta_{flex} = 10\%$ and $\eta_{longi} = 2\%$. The geometry of the resonators is available Tab. 3.2. The reflection coefficients is obtain for the forward ($|R^+|$ in $--$) and return ($|R^-|$ in $\ldots$) waves.

The use of several resonators tuned for both flexural and longitudinal waves allows us to obtain a vibratory filter effect from 850 Hz to 950 Hz for several types of waves. However, the transmission drop allowed by the filter is unequal depending on the wave type. The chosen resonator geometry is more efficient for flexural waves. We also note that these configurations with several resonators allow to obtain similar effects to the vibratory absorbers when we introduce damping.

3.5 Examples of vibration absorber configuration

In this section, we look for application cases of the local resonators previously characterized but for the absorbing configuration. The objective is to obtain response configurations to industrial problems by using absorption. In the two cases presented in vibration absorber configuration, the objective is to obtain a maximum vibration absorption effect. The first configuration uses tuned resonators for flexural waves. The second configuration uses a resonator tuned for flexural waves, a resonator tuned for longitudinal waves and a resonator tuned for torsional waves. The objective is to obtain a maximum asorption at a given frequency for the three types of waves.

3.5.1 Design of a graded flexural absorber

In this configuration a vibration absorber is made of the same resonator assembly as in the section 3.4.2, see Tab. 3.2.

In Fig. 3.11(a), the waveguide is excited in flexural at one end, a series of 4 resonators is attached to the clamped end of a waveguide. The far field scattering matrix $S = \begin{pmatrix} T & R^{+} \\ R^{-} & T \end{pmatrix}$ is obtained from a numerical simulations. For the vibration absorber configuration, the structural loss factor η is chosen according to section 3.3.1, i.e. $\eta = 10\%$ for the flexural resonators.

Despite the non-optimized coupling between the resonators, the addition of resonators in series provides a broadband absorbing effect around a target frequency (Fig. 3.11(b)). While a frequency band ranging from 850 Hz to 1000 Hz is expected, the observed filtered frequency band ranges from 750 Hz to 1200 Hz. The frequency shift is not the same as that observed in the case of a vibratory filter. The position on the waveguide influences the coupling between the resonators and the host structure. In this case, an optimization would allow to adjust the coupling between the waves in order to obtain a perfect absorption effect $|\alpha| = 1$. In the absence of analytical results correlated to numerical calculation methods, the calculation cost of an optimization is too high.

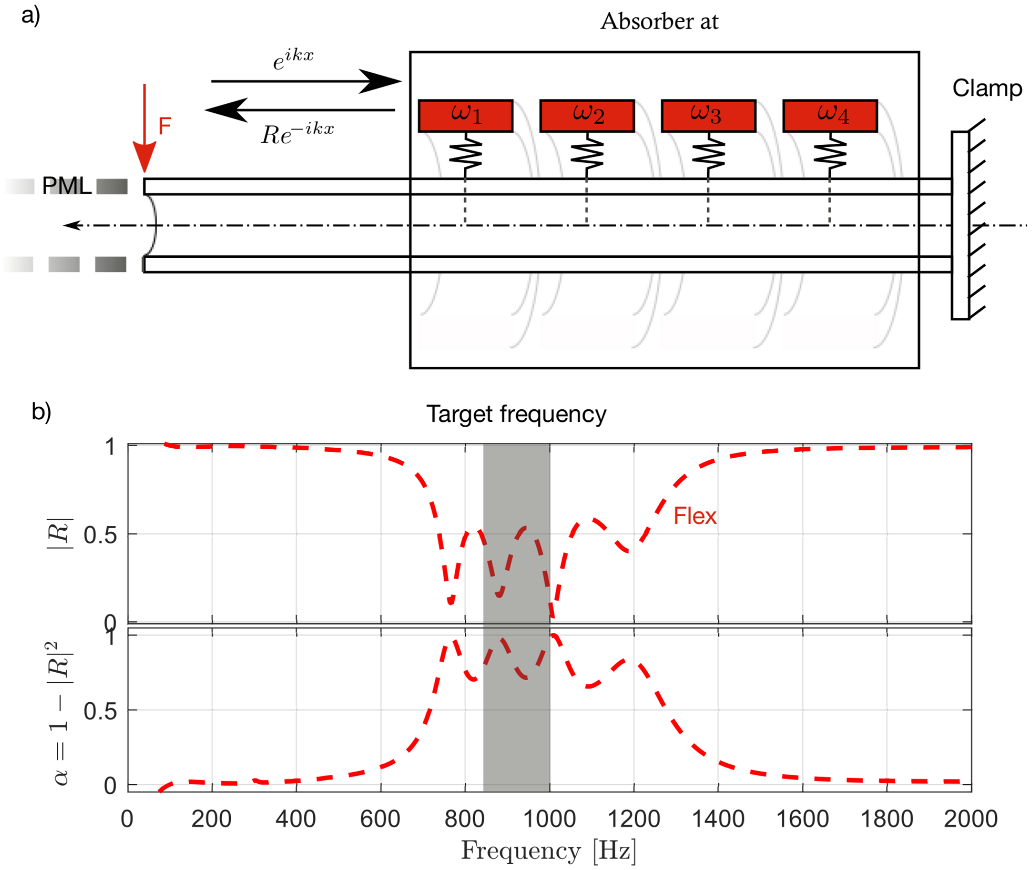

Figure 3.11 – Vibration absorber configuration with 4 resonators attached to the clamped end of the waveguide (a). Reflection and absorption coefficient of a graded trapping type vibration absorber with structural damping in rubber $\eta = 10\%$. The geometry of the resonators is available Tab. 3.2 (b).

3.5.2 Design of a tuned vibration absolute absorber

After having obtained a vibration absorber for the flexural waves, the objective is to obtain a frequency where the absorption is maximum for the three types of wave treated, i.e. flexural, longitudinal and torsional waves. To obtain this vibration absorber, longitudinal, flexural and torsional resonators are placed on the free end of the waveguide. The position of the resonators is established according to section 3.3.1.

Table. 3.3 gives the parameters used to configure the resonators to create a waveguide that will act as a vibration absorber for longitudinal, flexural and torsional waves. As we have seen in the previous figures, the interaction between the resonators and the host waveguide leads to a shift in the frequency where a filter or absorption effect is obtained. This shift is particularly marked for flexural resonators. In order to obtain a maximum of absorption for the three types of waves at the same frequency, we choose to tune the flexural resonator differently from the longitudinal and torsional resonators. The structural damping of the rubber η is chosen according to section 3.3.1, i.e. $\eta = 10\%$ for the rubber of the flexural resonator and $\eta = 2\%$ for the rubber of the longitudinal and torsional resonators.

Resonator	l **[mm]**	$\mathrm{r_k}$ **[mm]**	$\mathrm{r_M}$**[mm]**	**Frequency [Hz]**
Flexural	10	8	10.4	850
Longitudinal	8	7	9.5	950
Torsional	10	7	8.75	950

Table 3.3 – Parameters of the resonators for the absolute type vibration absorber.

Figure 3.12(a) shows the configuration with three resonators positioned at the free end of the waveguide. A flexural force applied to the other end of the waveguide. The reflection coefficient and the absorption coefficient for the flexural waves are shown in red. Similarly, a longitudinal force, in blue, and a torsional moment, in green, give the associated reflection and absorption coefficients for the corresponding polarizations.

The reflection and absorption coefficients show an effect centered around 950 Hz for flexural, longitudinal and torsional waves. The effect of the flexural resonator allows us to obtain an absorption for a wide frequency band. The peaks obtained for the longitudinal and torsion waves are narrower. The absorption allows to obtain a non-negligible reflection coefficient, $|R| > 0.5$ for three types of waves centered on the same frequency.

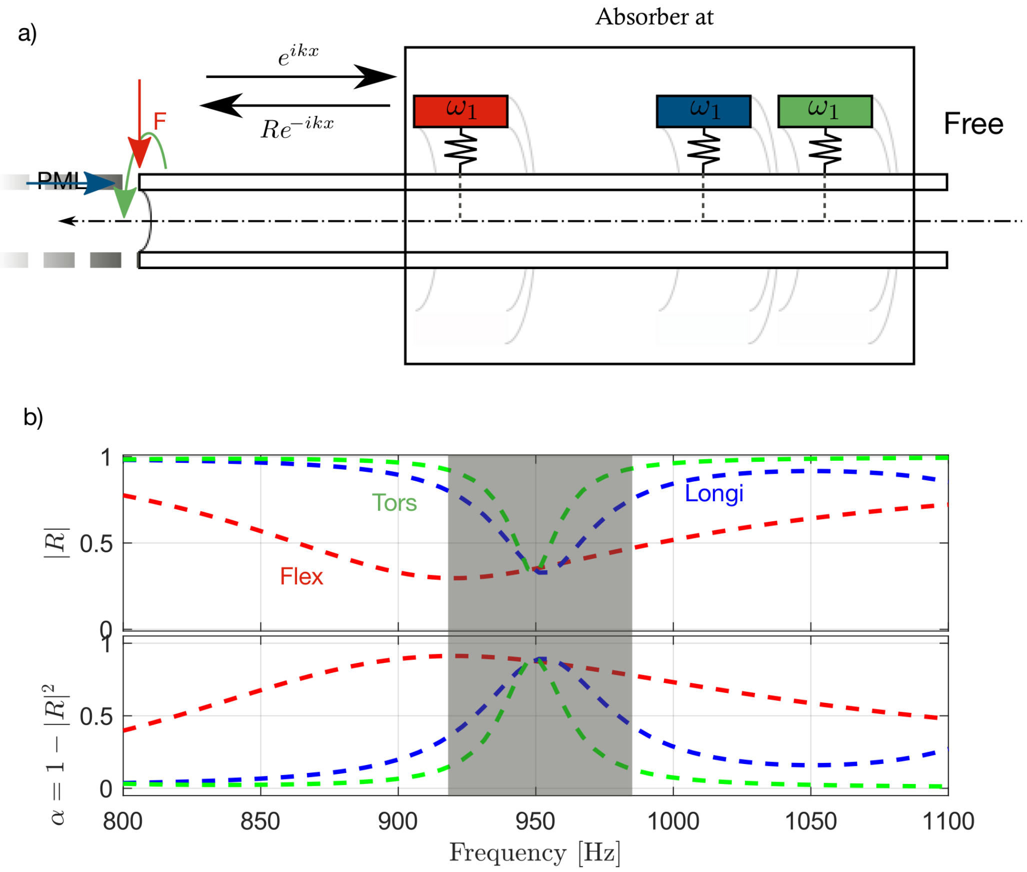

Figure 3.12 – Reflection and absorption coefficient of an absolute vibration absorber with optimized structural damping according to Fig. 3.5. The absorber consists of three resonators: one tuned for flexural waves (–), one for longitudinal waves (–), and the third for torsional waves (–).

The proposed configurations make it possible to obtain a vibratory filter effect for a frequency band slightly larger than that expected. A vibration absorption effect is obtained for three types of waves at a given frequency.

3.6 Experimental evidence of peak absorbance

A series of experimental demonstrators is set up to confirm the presence of an absorption effect when one or more resonators are attached to a host waveguide. The objective is to obtain a measurable vibration absorption effect correlated to a numerical estimate. In this experimental demonstration, the difficulties encountered to measure the reflection coefficients on the pipe described in section 3.6.2, and the manufacturing delays of the cylindrical resonators led us to adopt a waveguide of rectangular section.

3.6.1 Experimental set-up

Figure 3.13 shows the configuration for the waveguide suspended in parallel to the ground. Measurements are made along the waveguide at 21 points equidistant by 1 cm and located on the neutral axis to avoid torsional components (a). An impact hammer (b) excites the structure with flexural motion. The displacement field is obtained with a single axis accelerometer (c). The resonator is placed at a distance dr from the end of the waveguide (d).

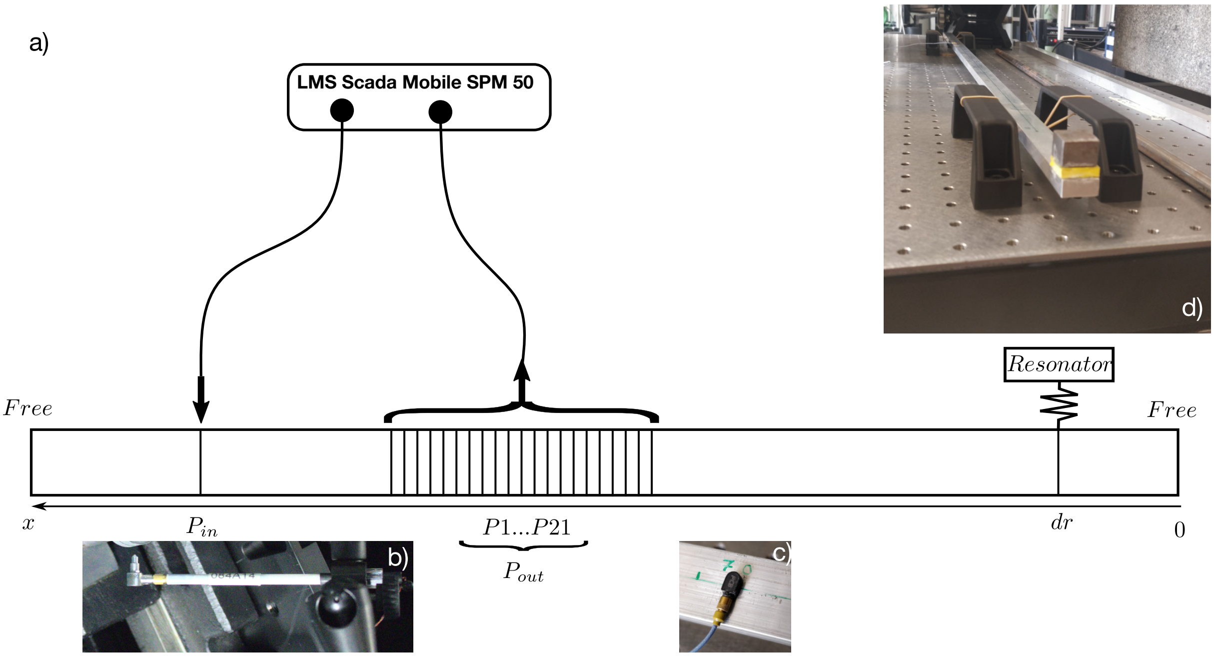

Figure 3.13 – Diagram of the measurement performed to obtain the reflection coefficient of a structure composed of a host element and one or more resonant elements (a). Picture of the impact hammer (b) used to excite the structure, the single-axis accelerometer (c) and the experimental setup with a resonator on a host waveguide (d)

The reflection coefficient is measured experimentally from the frequency response measurements performed on the 21 measurement points. The flexural displacement $W(x_i, \omega)$ measured at point x_i for a given angular frequency ω is considered to be equal to:

$$W(x_i, \omega) = A(\omega)e^{ikx_i} + B(\omega)e^{-ikx_i} + C(\omega)e^{kx_i} + D(\omega)e^{-kx_i}. \tag{3.5}$$

The set of $W(x_i, \omega)$ for each measurement point can be written in a matrix format [54] such as

$$\begin{pmatrix} W(x_1,\omega) \\ W(x_2,\omega) \\ \vdots \\ W(x_{21},\omega) \end{pmatrix} = \begin{pmatrix} e^{ikx_1} & e^{-ikx_1} & e^{kx_1} & e^{-kx_1} \\ e^{ikx_2} & e^{-ikx_2} & e^{kx_2} & e^{-kx_2} \\ \vdots & \vdots & \vdots & \vdots \\ e^{ikx_{21}} & e^{-ikx_{21}} & e^{kx_{21}} & e^{-kx_{21}} \end{pmatrix} \begin{pmatrix} A(\omega) \\ B(\omega) \\ C(\omega) \\ D(\omega) \end{pmatrix}. \tag{3.6}$$

The amplitudes $A(\omega)$ and $B(\omega)$ can be derived from Eq. 3.6 which form an overdetermined system. From these amplitudes, the reflection coefficient of the propagating and evanescent waves can be deduced for any ω as:

$$R_{exp}(\omega) = \frac{A(\omega)}{B(\omega)}. \tag{3.7}$$

This method of calculating the reflection coefficient is first applied to the host waveguide, without resonator, which should theoretically have a perfect reflection coefficient $|R_{exp}(\omega)|^2 = 1$ and a zero absorption coefficient $\alpha = 1 - |R|^2 = 0$. In a second step, once a satisfactory result is obtained, a measurement will be performed with a resonator of a given frequency, then a series of resonators.

3.6.2 Measurement of the reflection coefficient of the host material

Two types of waveguides are compared, as shown in Fig. 3.14: a steel cylinder of diameter 12 mm and thickness 1 mm (a); and a beam of rectangular cross section 20 × 10 mm (b). Each guide is one meter long.

Figure 3.14(a) shows the reflection coefficient and associated phase of a steel pipe. The structure is excited in flexural by an impact hammer, represented by a black arrow. The measurement shows an incident around 1500 Hz. This incident is unexpected, in the case of a waveguide without treatment we expect a reflection coefficient close to $|R|^2 = 1$. The cylindrical geometry makes the measurements delicate. Indeed, the impact hammer slides easily on the surface of the cylinder and the alignment of the accelerometer and the impact point on the neutral axis is difficult to achieve.

Figure. 3.14(b) shows a coefficient $|R^2| > 1$ on the first frequencies. From 700 Hz the reflection coefficient is close to $|R^2| = 1$. The low frequency peaks can be explained by measurement errors with the impact hammer, insufficient resolution of the measurement points or an imperfect surface condition, evanescent waves also have an effect.

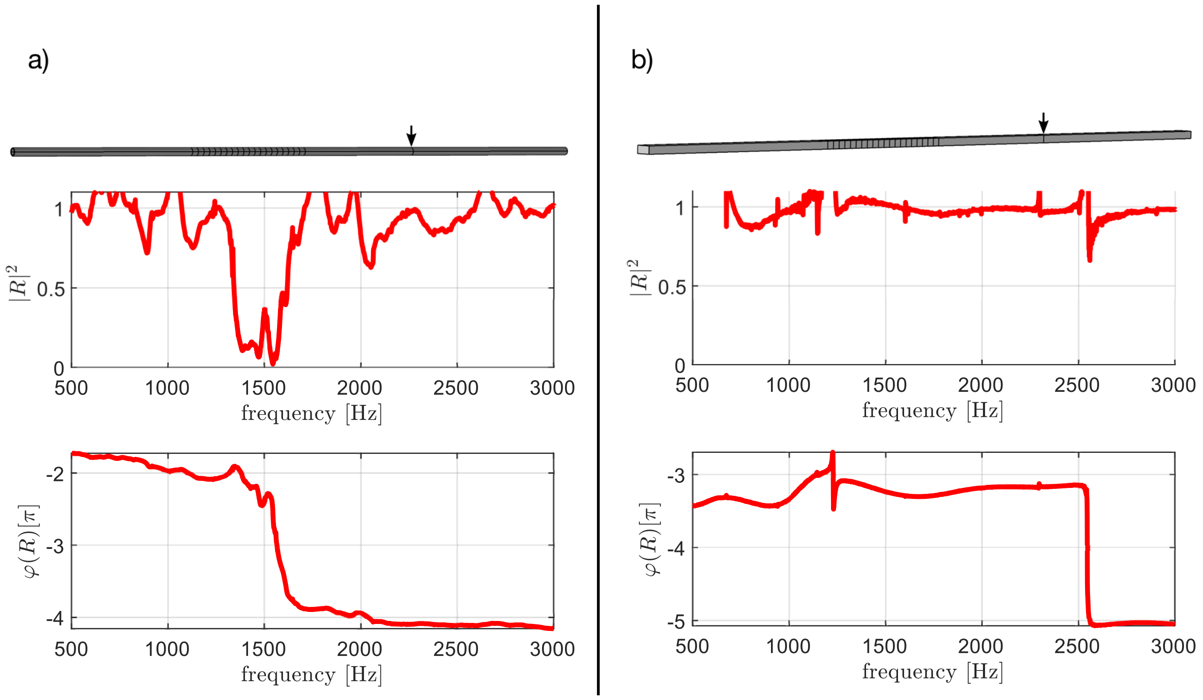

Figure 3.14 – Reflection coefficient of an incident flexural wave on a hollow cylindrical steel structure, 12 mm external diameter, 1 mm thick (a). Reflection coefficient of an incident flexural wave on a rectangular aluminium structure, 20 × 10 mm (b).

The rectangular waveguide section gives more satisfactory results than the cylindrical waveguide. The peaks due to the experimental measurement are not localized in the frequency band of interest, around 1 kHz. The rectangular section also allows to decouple the two flexural waves. The resonators are sized to interact with one of the two polarizations of the flexural wave on a rectangular aluminum waveguide.

3.6.3 Measurement of the frequency of a local resonator

The properties of elastic materials are not well documented by the manufacturers. Previous numerical work has been based on information from the literature [145, 173]. A measurement of the resonance frequencies of the resonators is performed (Fig. 3.15) by experimentally identifying the modes obtained for a given resonator configuration. The objective is to experimentally obtain the pumping mode of the resonator to extract the Young's modulus and the damping coefficients η of the rubber.

A numerical simulation, in black dotted lines, is superposed on the measured curves, to check if the measured Young's modulus is correct (Fig. 3.15(a)). The colors of the curves correspond to the measurement points identified on the photograph. A resonator is assembled with a rubber pad $20 \times 20 \times 5$ mm and a steel mass of 40 g is fixed on the rubber pad. In order to determine experimentally its resonances, the beam is embedded as close as possible to the resonator (b). Measurements are made with a differential fiber optic vibrometer on a series of points. A series of impacts is made by the hammer to excite the pumping mode of the resonator. The different points of measurement allow to measure the different modes of the structure. The measured frequency response allows to isolate the different modes. The vibrometer being a single point, the direction of acquisition is the same as the laser. In our case it corresponds to the flexural of the host beam and the compression of the rubber pad by the steel mass.

The performed excitation helps the acquisition of the pumping mode of the resonator, in y-translation, it is this mode that we seek to identify. Figure. 3.15(c) to (f) show the calculation of eigenvalues from the numerical model allowing us to identify the eigenmodes of the system. These modes are partially visible on the experimental frequency responses. We identify the oscillation mode around the beam at 200 Hz (c), the mass rotation mode, x-rotation and z-rotation at 590 Hz (d), and the pumping mode, y-translation at 720 Hz (e). Numerically, the rotation of the mass, y-rotation at 230 Hz (f), is identified but the experimental setup does not allow it to be excited.

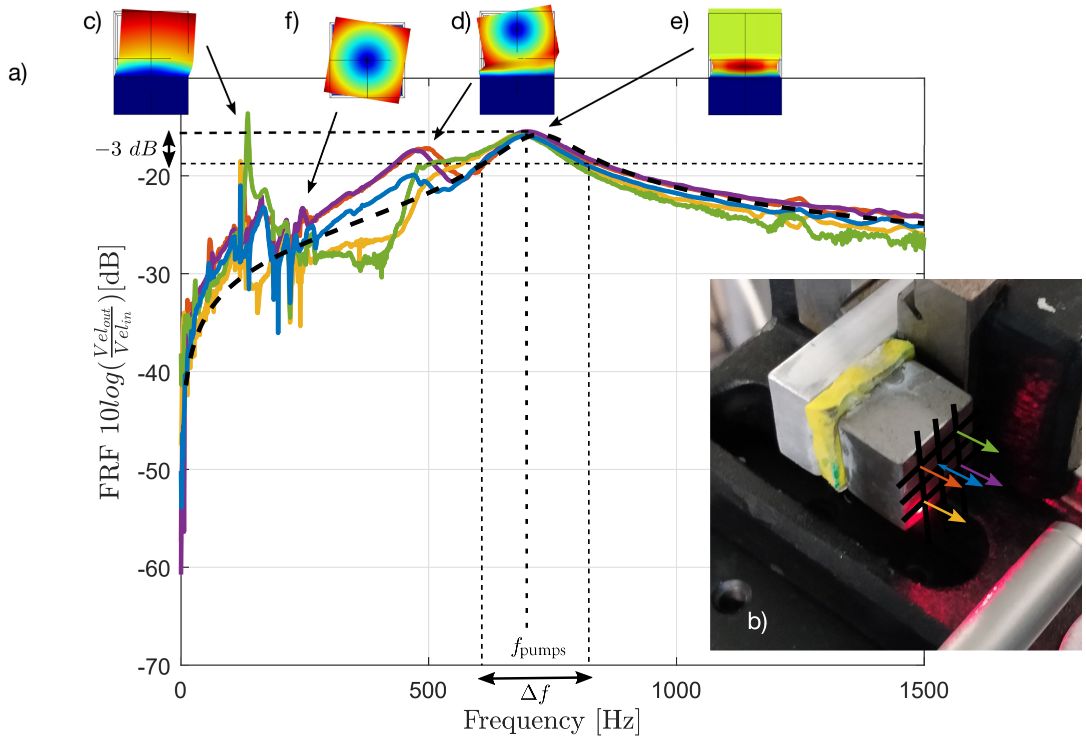

Figure 3.15 – Frequency response of the different measurement points on the structure. In black dots the frequency response calculated by a finite element model (a). Picture of the experimental setup with the identified measurement points (b). 3D views of the simulated displacement fields for the eigenmode at 190 Hz (c), 590 Hz (d), 720 Hz (e), 230 Hz (f).

Measurements with a mass of 40 g allow us to experimentally identify the frequencies of the pumping mode and to deduce the characteristics of the rubber: Young's modulus $E = 3.3E6$ Pa and $\eta = \frac{\Delta f_{-3db}}{f_{pumps}} = 0.2$ [7]. Once the rubber parameters are known, it is possible to numerically predict the performance of a vibration absorber before implementing it. The resonance frequency of the resonator is determined by the properties of the rubber and the added mass. Adding a 40 g mass gives a resonant frequency of 720 Hz. A mass of 60 g gives a resonant frequency of 600 Hz, and a mass of 90 g a resonant frequency of 490 Hz.

3.6.4 Parametric variation of Numerical design of resonators

As previously seen in section 3.3.1, the position of the resonator on the waveguide will influence these absorption performances. In this section, we numerically vary the position of the resonators on the waveguide. The objective is to obtain the distances dr for which the resonator allows to obtain a maximum absorption.

Figure 3.16 shows the influence of the resonator position, dr (see Fig. 3.13), on the reflection coefficient of the structure. When the resonator is close to the end of the structure, $dr < 0.05$ m, the effect of the resonator is shifted with respect to the resonant frequency of the resonator. This frequency results from a coupling between the resonator and the host structure. For each resonator, a position is identified by a red cross. These positions are chosen to obtain a broadband effect by superimposing the frequency bands where the reflection coefficient drops. The 40 g resonator, Fig. 3.16(a), is placed at $dr = 0$. The 60 g resonator, Fig. 3.16(b), is placed at $dr = 0.15$ m. The 90 g resonator, Fig. 3.16(c), is placed at $dr = 0.08$ m

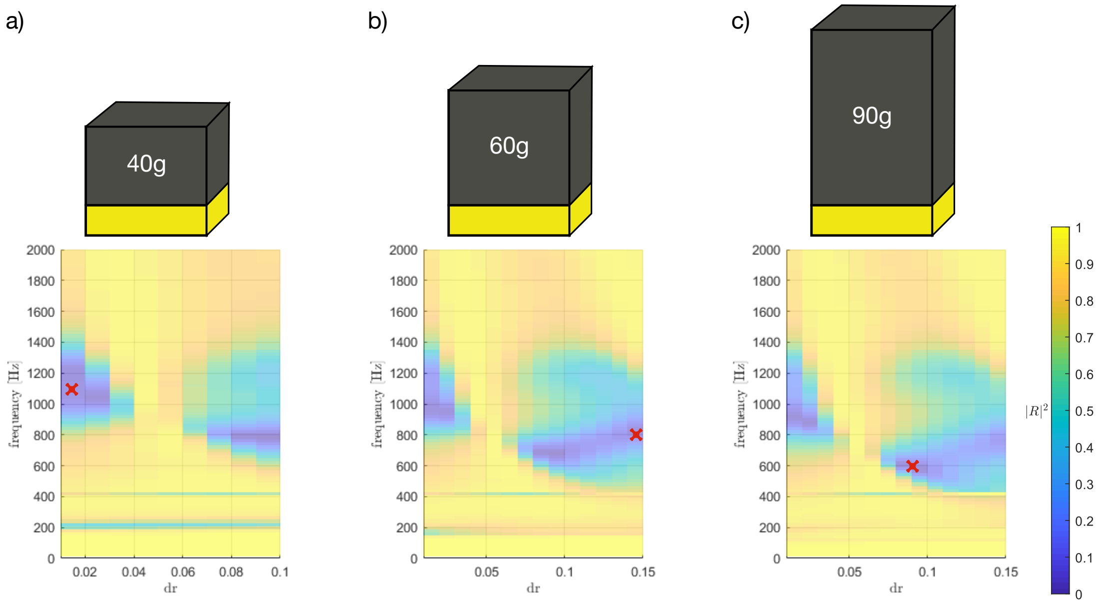

Figure 3.16 – Mapping of the reflection coefficient as a function of resonator position tuned to 720 Hz (a), 600 Hz (b) and 490 Hz (c). The red cross indicates the selected resonator positions.

The maps presented are from experimental simulations: before integrating a set of three resonators on the waveguide it is necessary to experimentally validate the case of a single resonator on the host structure.

3.6.5 Evidence of the absorption peak

This section compares experimental and numerical results for vibration absorbers. A first demonstrator with one resonator is implemented to validate the numerical predictions. A second demonstrator is then implemented with three resonators to observe a broadband effect.

Host structure with a single resonator

Figure 3.17 shows the reflection coefficient and the associated phase of a 40 g resonator placed at the end of a host beam. The experimental results, in red, are compared to the numerical simulations, in black. The structure is excited in flexural by an impact hammer. The reflection coefficient shows an absorption effect from 900 Hz to 1200 Hz. The incident that appears around 1200 Hz is the torsion mode of the rectangular waveguide. The impact of the hammer is probably not perfectly on the neutral axis on the beam which has the effect of exciting the torsion mode. Due to the coupling effect identified earlier, between the resonator and the host waveguide, the resonant frequency of the isolated resonator (720 Hz) is not visible.

The numerical and experimental data follow the same trend. A poor approximation of the rubber parameters or a lack of knowledge of the properties of the host structure, may explain the frequency shift between the two data sets.

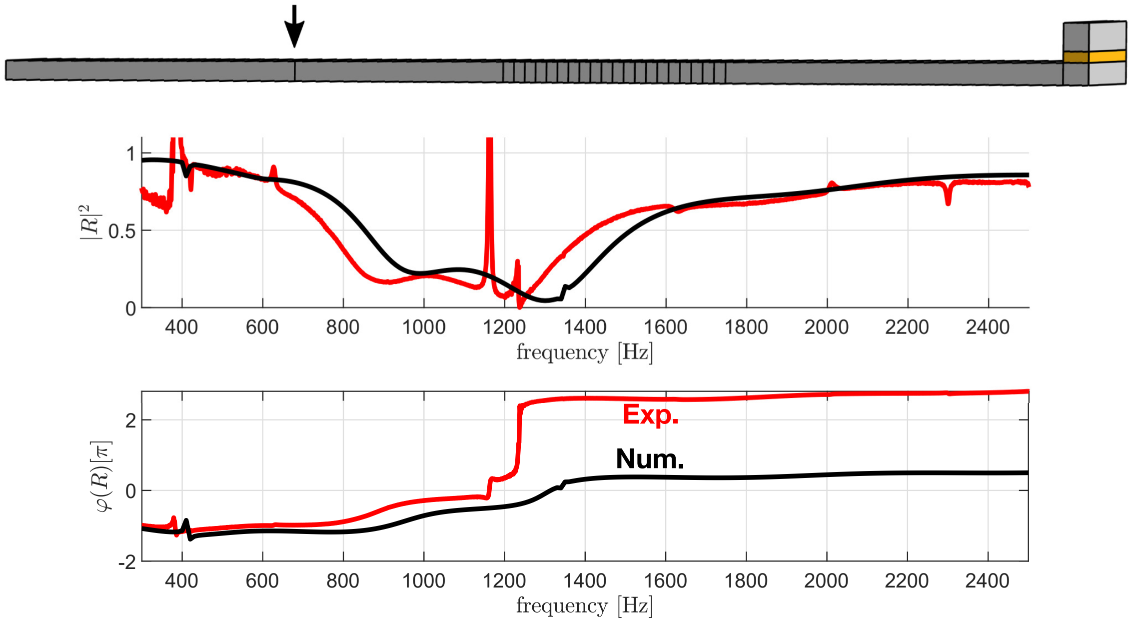

Figure 3.17 – Reflection coefficient and associated phase, experimental in red— and numerical in black —, of a rectangular aluminium waveguide with a resonator of mass 40 g. The excitation point of the structure is shown with an arrow on the 3D model.

By adding a resonator to the waveguide, vibration absorption, $|\alpha| = 1 - |R|^2$, is achieved for flexural waves. By using a series of resonators tuned to a slightly different frequency than the first resonator, we seek to achieve a broadband effect.

Host structure with an array of resonators

As highlighted in section 3.5.1, the expected effect of adding multiple resonators to a host structure is a coupling between absorption peaks to achieve a broadband effect. Figures 3.18 and 3.19 show the experimental and numerical reflection coefficients obtained for a waveguide with three resonators arranged at its end. Two configurations are represented: the first one with the resonators placed on the host structure according to the configurations that are highlighted in Fig. 3.16 and the second with a new parametric variation to optimize the coupling between the resonators.

Figure 3.18 shows the reflection coefficient and associated phase of a rectangular aluminum waveguide with three resonators. One of mass 40 g placed at the end of the waveguide, one of mass 60 g placed at a distance $dr = 150$ mm, and one of mass 90 g placed at a distance $dr = 80$ mm. The reflection coefficient shows a drop from 450 Hz to 1500 Hz due to the resonators tuned from 490 Hz to 720 Hz implying an increase of absorption. The numerical and experimental curves are well correlated with each other. Nevertheless, the absorption peaks could be more coupled to each other.

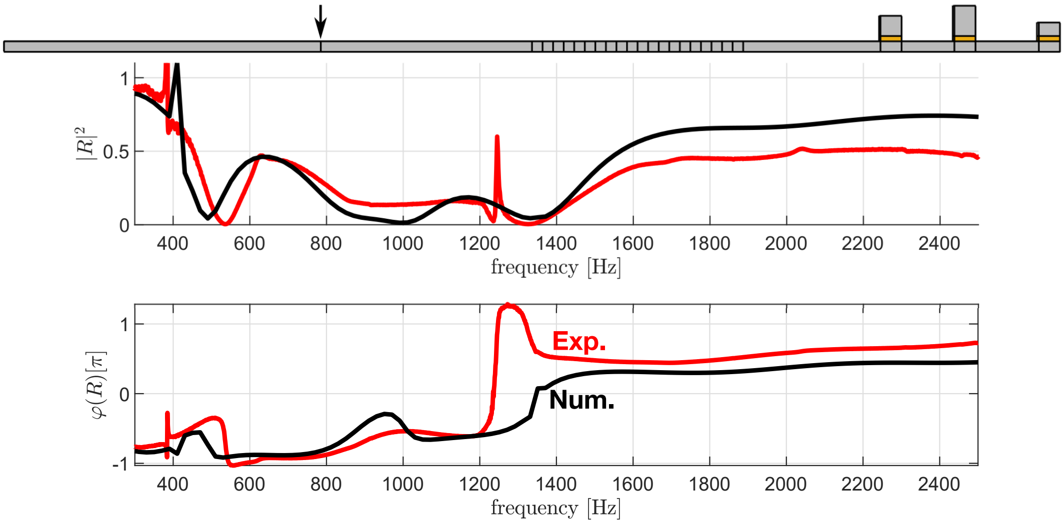

Figure 3.18 – Reflection coefficient and associated phase, experimentally in red— and numerically in black—, of a rectangular aluminium waveguide with 3 resonators of a mass of 40 g placed at a distance $dr = 0$ mm from the end of the waveguide, a mass of 60 g placed at a distance of $dr = 150$ mm, and a mass of 90 g placed at a distance $dr = 80$ mm.

In order to obtain an absorption frequency range where the absorption peaks induced by each resonator are more tightly coupled to each other, it is interesting to consider the influence that each resonator will have on the others when choosing its position on the host structure. The mapping (Fig. 3.19(a)) is obtained by varying the dr position of a resonator from 30 mm to 120 mm surrounded by a resonator at one end $dr = 0$ mm and another at $dr = 150$ mm. A configuration $dr = 60$ mm, where the resonators are coupled, is identified by a red cross.

Figure 3.19(b) shows the reflection coefficient and associated phase of a rectangular aluminum waveguide with three resonators. One of mass 40 g placed at the end of the waveguide, one of mass 60 g placed at a distance $dr = 60$ mm, and one of mass 90 g placed at a distance $dr = 150$ mm. The reflection coefficient shows an absorption from 500 Hz to 1500 Hz. This absorption band is more homogeneous than the one obtained by the configuration presented in Fig. 3.18.

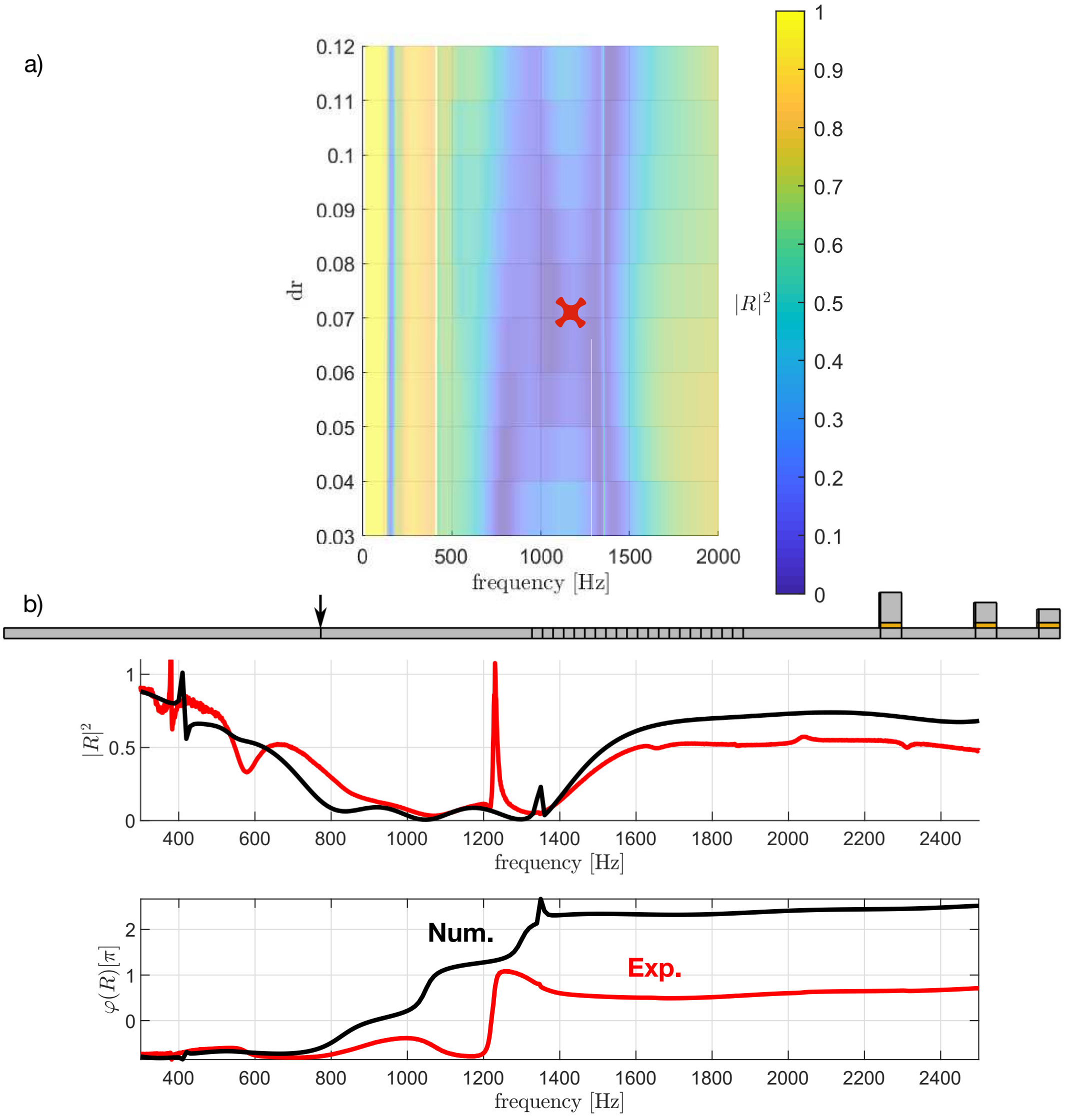

Figure 3.19 – Mapping of the reflection coefficients as a function of the position of the resonator of a mass of 60 g, the resonator of 40 g being placed at the end of the guide and the resonator of 90 g being fixed at 150 mm, (a). Reflection coefficient and associated phase, experimental in red— and numerical in black—, of a rectangular aluminium waveguide with 3 resonators of a 40 g mass placed at a distance $dr = 0$ mm from the end, a 60 g mass placed at a distance $dr = 60$ mm, and a 90 g mass placed at a distance $dr = 150$ mm, (b).

This result shows that it is possible to obtain a broadband absorption effect with a set of resonators. The position and the choice of the resonators are determining a relevant absorption effect.

3.7 Conclusions

This chapter has shown the possibility of obtaining a filter or an absorber, for a given frequency band for several types of waves, by using local resonators. The waveguide chosen for the study comes from the industrial context of the thesis and has a cylindrical geometry. This geometry is not very suitable for experimental manipulation and is simplified hereafter to facilitate the experimental demonstration. The implementation of resonators on the waveguide allows us to transform this guide into a vibration filter. The effect of vibratory absorption is obtained when the losses induced by the damping of the material constituting the resonator are sufficiently high.

The first models made of a set of resonators on a host structure are interested in vibratory filters. The results obtained show a decrease in the transmission of the incident flexural wave for a frequency range from 900 Hz to 1200 Hz. In the case of vibratory absorbers, the modeling of a set of resonators allows to obtain an absorption effect of the flexural wave for a frequency range of 800 Hz to 1200 Hz. The case of a vibratory absorber for flexural waves being the simplest to realize, it is on this configuration that an experimental demonstrator has been realized. An assembly of three resonators thus makes it possible to obtain an absorption effect of the flexural waves for a range of frequency from 800 Hz to 1400 Hz.

The work carried out shows that the use of local resonators allows to obtain filter and vibratory absorption effects. Depending on the parameters of the different resonators, it is possible to obtain broadband effects for different types of waves. The advantage of locally resonante structures is that they allow to keep the structural integrity of the structure to be treated, which makes them fast and inexpensive solutions for various geometries.

Chap. 4

Implementation of a 1D multi-wave vibration filter in industry-inspired examples

Contents

4.1 Introduction 66
4.2 Effect of the curvature of the waveguide on the transmission of vibratory waves 66
  4.2.1 1D phononic crystal curved waveguides 67
  4.2.2 1D phononic crystal waveguide with a bent segment 69
  4.2.3 1D phononic crystal waveguide with several bent segments 71
4.3 Acoustic radiation from a plate coupled to a vibrational filter made of a 1D phononic crystal waveguide 74
  4.3.1 Set-up of a 1D phononic crystal waveguide coupled to a radiating plate 74
  4.3.2 Radiated acoustic power of a 1D phononic crystal waveguide coupled to a radiating plate 76
4.4 Influence of a heavy fluid on the vibration filtering properties of a 1D phononic crystal pipe 79
4.5 Conclusion 83

4.1 Introduction

The work developed in the two previous chapters focuses specifically on the design of two architectures of vibro-acoustic waveguides, able to control either the transmission (design of filters) or the absorption (design of absorbers). Material and geometrical parameters are set in order to open so called absolute band gap in which band gaps are obtained for all wave types in the same frequency range. In this chapter, we propose to illustrate the interest of this type of filters by presenting three case studies with the idea of examining the relevance of an integration in an application or industrial context.

The three proposed case studies use variants of the phononic crystal constructed in Chap. 2. In section 4.2, the effect of a curvature introduced on the waveguide is examined. In section 4.3, the interest of the absolute filter effect is highlighted by coupling the waveguide to a radiating plane panel (vibroacoustic coupling in light fluid). Section 4.4 concerns a waveguide filled with water (vibroacoustic coupling in heavy fluid).

4.2 Effect of the curvature of the waveguide on the transmission of vibratory waves

The axis of the waveguide studied in Chap. 2 is straight. When the section of the waveguide is symmetrical with respect to its main symmetry axis, the flexural and longitudinal movements are decoupled. It is with this assumption that the model of Chap. 2 has been developed.

In many practical applications, for reasons of space, straight waveguides are often have long bends or curved segments. In Fig. 4.1, the waveguide between points A and B is excited by a source (pump located upstream) and coupled to a receiving member (injection rail located downstream). The AB tube is clearly not rectilinear. This situation is easily encountered in practice.

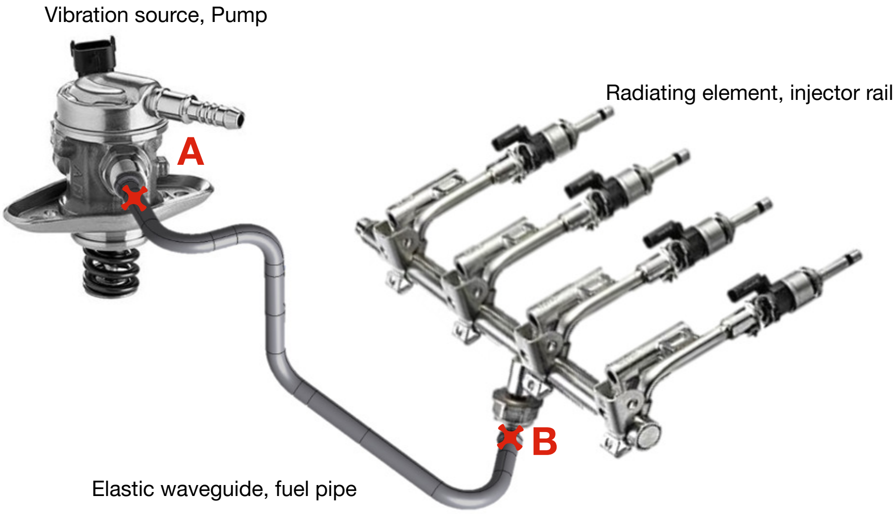

Figure 4.1 – Overview of an internal combustion engine injection system in which the fuel pressure pump (right) acts as a vibration source, the pipe as a structural waveguide transmitting the vibrations and the injection rail as a receiver from which the vibrations propagate to the entire engine block and result in the radiation of noise by surface elements (e.g. firewall, not shown here).

4.2.1 1D phononic crystal curved waveguides

The introduction of a curvature in the medium, localized in a bend, or distributed on a consequent portion of the duct has for main effect to couple the vibratory movements of flexural and longitudinal. We propose to examine the effect of this coupling on the vibratory transmission of the phononic crystal.

Figure 4.2 shows the straight and curved waveguide geometries. The curved waveguides studied consist of n cells, organized along a circular arc. Each arc has a radius $r = (l_{tot}n - l_2)/(\theta\pi/180)$, where l_2 is the length of the nylon segment of the cell, l_{tot} is the total length of the cell and the parameter θ gives the orientation of the last cell. Several orientations are compared, a straight waveguide with $\theta = 0°$ and 3 curved waveguides with $\theta = 15°$, $30°$ and $160°$. These three examples of curvatures are chosen to observe the impact of a more and more pronounced curve. The waveguides are excited by a longitudinal force on the section of the first cell, the acceleration a_y is measured, perpendicular to the waveguide axis at its end.

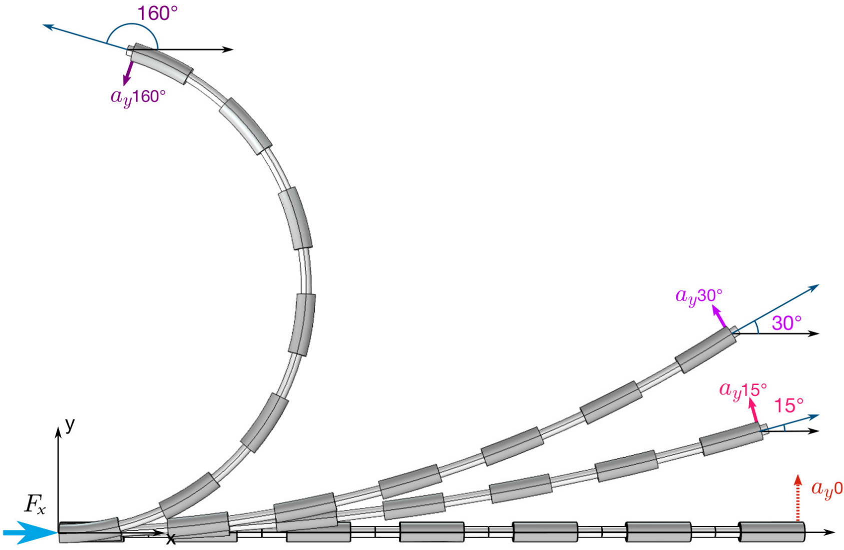

Figure 4.2 – Diagram of the waveguides, with the applied force and measured acceleration identified, (a).

Figure 4.3(a) shows the accelerance transfer function a_y/F_x, where a_y correspond to the flexural motion and F_x denotes the applied force in tne x direction. The phononic crystal provides band gaps for the flexural waves, represented by the red area between 1.8 kHz to 5.5 kHz, and for the longitudinal waves between 3 kHz to 7 kHz, represented by the blue area, the absolute band gap of the straight waveguide is from 3 kHz to 5.5 kHz where the two areas overlap.

For $\theta = 0°$ the flexural and longitudinal movements are decoupled in the case of the straight waveguide. The longitudinal excitation imposed on the waveguide does not allow to observe any flexural movements. The red dotted curve shown in Fig. 4.3(a) corresponds to the numerical noise at a level much lower, of the order of 100 dB, than that obtained for curved guides even in the absolute band gap.

When the waveguide is bent, the movements are no longer decoupled and the longitudinal excitation generates a flexural movement in the waveguide. This coupling effect is clearly seen in the frequency responses at 15°, 30° and 160° for the curved waveguides: the amplitudes of the frequency responses (a_y/F_x) of the curved waveguides are much higher than that of the straight waveguide. The frequency responses associated with the weakly curved waveguides (15° and 30°) have identical structures but show an amplitude shift of about 10dB, which is almost independent of frequency. For the strongly curved waveguide (160°), the frequency response is qualitatively similar to those calculated for the weak curvatures (15° and 30°). However, the differences between this highly curved waveguide and the low curvature waveguides are significant above 6 kHz (i.e., beyond the absolute band gap).

The behavior of the system can be analyzed by means of the operational deflection shapes of the curved waveguide at particular frequencies (see Fig. 4.3):

- For an excitation at 1.5 kHz (Fig. 4.3(b)), which is below the flexural wave band gap, [1.8-5 kHz], longitudinal excitation generates large flexural displacements due to curvature-related coupling. These displacements are even more important as the curvature is important.
- For an excitation at 2.5 kHz, (see Fig. 4.3(c)), located in the band gap of the flexural waves, these flexural movements exist. This would not be the case if the guide were straight. Therefore, it is the coupling induced by the curvature that generates the existence of these flexural movements.
- For an excitation at 4kHz (see Fig. 4.3(d)), located in the absolute bandgap, the displacements are concentrated in the first cells of the waveguide, which is characteristic of a lack of propagation. The absolute filter then plays its role.

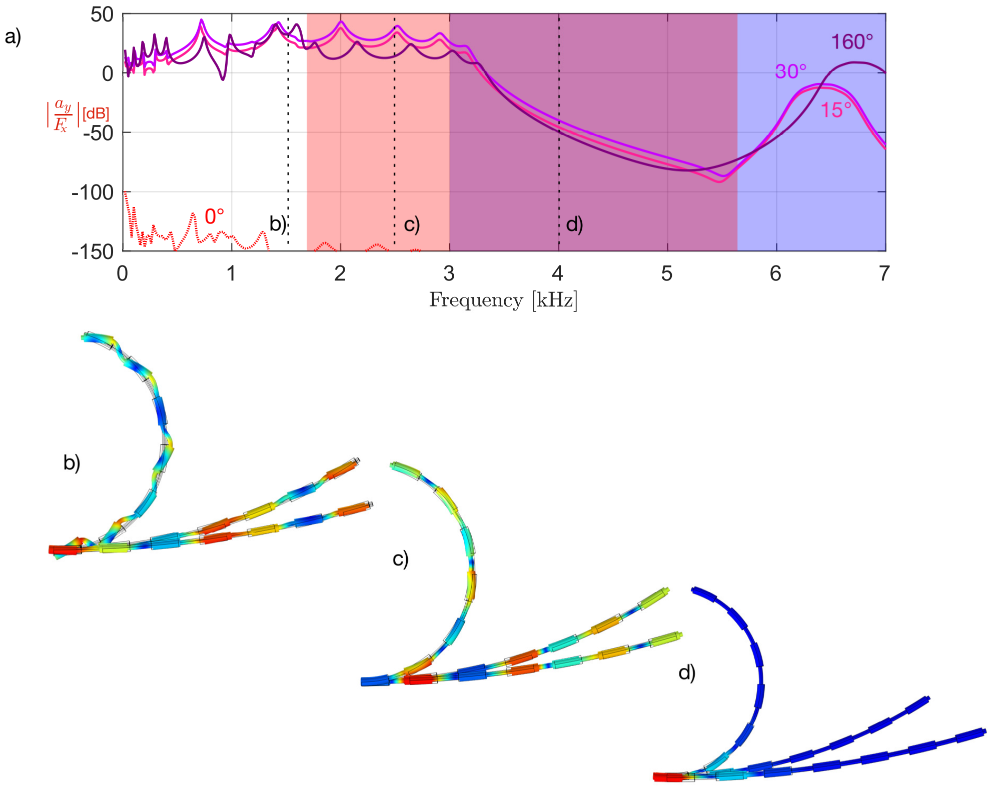

Figure 4.3 – Frequency response of straight and curved waveguides, (a). The coloured areas show the gap bands, predicted in Chap. 2, flexural, in *red*, and longitudinale, in *blue*, the absolute gap band is located at the intersection of these two. The operational deflection shapes, representing the displacement of the waveguides at different frequencies of interest are shown. At 1.5 kHz outside any band gap the presence of a curve leads to the generation of flexural waves, (b). At 2.5 kHz in the band gap for flexural waves the operational deflection shapes are dominated by longitudinal motions, (c). At 4 kHz within the absolute band gap where displacement field is rapidly damped (d).

The simulations presented in this section show that the absolute (i.e., longitudinal and flexural) and partial (flexural only) band gaps calculated for a straight waveguide can be used to analyze the characteristics of a curved waveguide. It is shown that in the absolute band gap, the operational deformations of the curved waveguide remain confined near the excitation, which is a signature of low vibrational transmission. In the partial band gap (of the straight waveguide), this is not the case because the curvature effect induces a coupling between longitudinal and flexural motions, which finally allows the transmission of flexural waves. The existence of an absolute band gap guarantees a low transmission, even in the presence of curvature.

4.2.2 1D phononic crystal waveguide with a bent segment

Curved segments used in pipes can have a localized character, as suggested in Fig. 1.1 and not only distributed as studied in section 4.2.1. We propose the study of localized bends, starting with a single bent segment configuration.

Figure 4.4 shows the geometries of the straight waveguide (a) and two straigth waveguide separated with a bent segment (b). The guides with a bent segment are built with a center cell introducing a curvature at the angle θ. This central cell is made with a circular arc of radius $r = (l_{tot}/2)/(tan(\theta\pi/360))$, where the parameter θ gives the orientation of the last cell.

Several orientations are compared: a straight waveguide with $\theta = 0°$, and three guides with a bent segment with $\theta = 5°$, $15°$ and $45°$. These four examples are chosen to observe the impact of an increasing angle of curvature. All waveguides are excited by a unitary longitudinal force on the input section of the first cell. The acceleration a_y is measured perpendicular to the waveguide axis, at its end, in order to highlight the flexural motions.

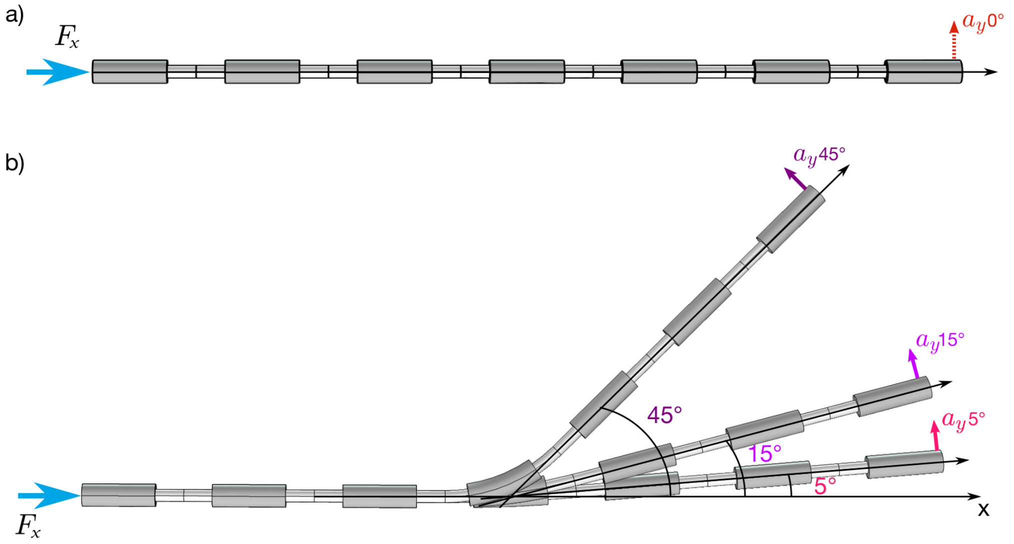

Figure 4.4 – Reference straight waveguide, with the applied force and measured acceleration identified, (a). Bent waveguide, with the applied force and measured acceleration identified, (b).

Figure 4.5(a) shows the acceleration a_y for the four chosen orientations. As mentioned previously, the flexural band gap is shown in red and the longitudinal band gap in blue. The flexural and longitudinal movements are decoupled in the case of the straight waveguide, $\theta = 0$. The longitudinal excitation imposed on the waveguide does not allow the observation of flexural motions. When the central cell is curved the motions are no longer decoupled, the longitudinal excitation then generates a flexural motion in the waveguide. This coupling effect appears distinctly with frequency responses of 5°,15°, and 45° bent waveguides. Increasing the cell curvature angle increases the coupling between longitudinal and flexural wave propagation. The frequency responses follow the same trend and show an amplitude shift of about 10 dB increasing with the curvature angle.

The operational deformations at particular frequencies show (see Fig. 4.5):

- For an excitation at 1.5 kHz (Fig. 4.5(b)), which is below the flexural wave band gap, as before the longitudinal excitation generates flexural displacements due to the coupling related to the bent segment.
- For an excitation at 2.5 kHz, (see Fig. 4.5(c)), located in the band gap of the flexural waves, a flexural motion exists at the bent segment. This bend causes the coupling between longitudinal excitation and flexural movements of the guide.
- For an excitation at 4kHz (see Fig. 4.5(d)), located in the absolute bandgap, the displacements are confined near the excitation. As in the case of the uniformly curved waveguide, this is characteristic of a lack of propagation.

As in the previous section, the presented simulations show that the absolute (i.e., longitudinal and flexural) and partial (flexural only) bandgaps calculated for a straight waveguide can be used to analyze the characteristics of a waveguide with a bent segment. The coupling between longitudinal and flexural motions does not result in low vibration transmission in the partial band gap (of a straight waveguide). However, the existence of an absolute band gap ensures low transmission, even in the presence of a bent segment.

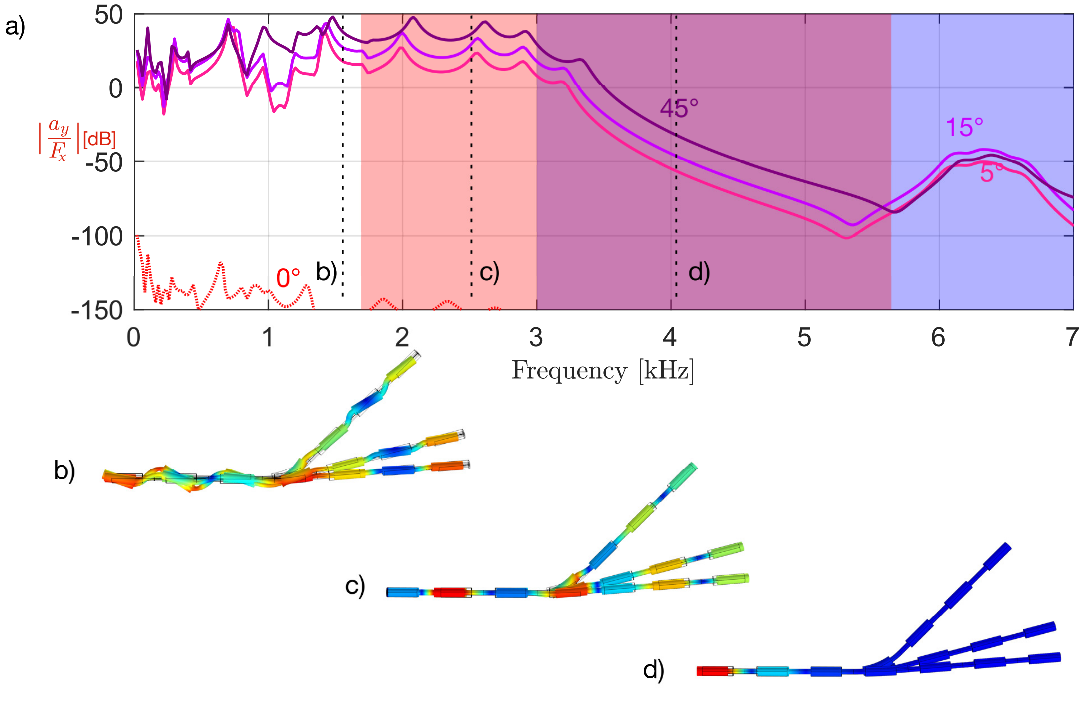

Figure 4.5 – Frequency response of straight and bent waveguides, (a). The operational deflection shapes represent the displacement of the waveguides at different frequencies of interest. The first at 1.5 kHz, outside any band gap (b). The second at 2.5 kHz belinging to the band gap for flexural waves (c). The third at 4 kHz within the absolute band gap (d).

4.2.3 1D phononic crystal waveguide with several bent segments

As suggested in Fig. 4.1, curved segments can be multiple in a tube. Section 4.2.2, proposes waveguides with one curved segment. This section proposes to study the configuration of two successive bent segments.

Figure 4.6 compares a waveguide with one bent segment at 45°, (a) with a waveguide with two bent segments, one at 15° and the other at 30°, (b). This example focuses on the influence on wave propagation in the waveguide of a two bent segments structure versus a one bent segment structure. As before, we look at the flexural acceleration induced by longitudinal excitation.

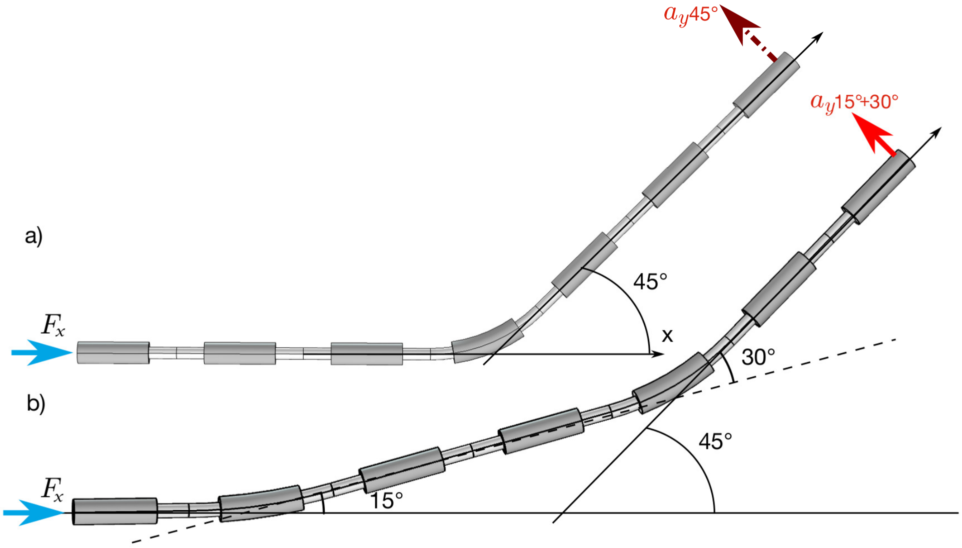

Figure 4.6 – Schematic of the reference waveguide, with the applied force and measured acceleration identified, (a). Schematic of the waveguide with two bent cells, with the applied force and measured acceleration identified, (b).

Figure 4.7(a) shows the accelerance (a_y/F_x), wich are characterize the coupling between longitudinal and flexural motions. in the flexural wave direction. The curve obtained for the waveguide with one bent section at 45° is shown in dotted line. The curve obtained for the waveguide with two bent sections is shown as a solid line. In both configurations, we observe a coupling of the longitudinal waves with the flexural waves. As before, we observe an attenuation in the frequency band associated with the absolute band gap. Both curves follow the same trend, with the frequency response of the two bent segments waveguide slightly lower by about 10 dB than the one bent segment waveguide. At 6 kHz, the trend reverses with the response of the two bent section waveguide being higher than 30 dB.

The operational deformations at particular frequencies show (see Fig. 4.7):

- For an excitation at 1.5 kHz (Fig. 4.7(b)), which is below the flexural wave band gap, as before the longitudinal excitation generates flexural displacements due to the coupling related to the bent segments. Note that the displacement is less important near the excitation for the guide with two bent segments.
- For an excitation at 2.5 kHz, (see Fig. 4.7(c)), located in the band gap of the flexural waves, a flexural motion exists at the bent segments. In the case of the waveguide with two bent segments the coupling is visible at each bend.
- For an excitation at 4kHz (see Fig. 4.7(d)), located in the absolute bandgap, the displacements are confined near the excitation. The lack of wave propagation prevents the curved segments from playing a role.

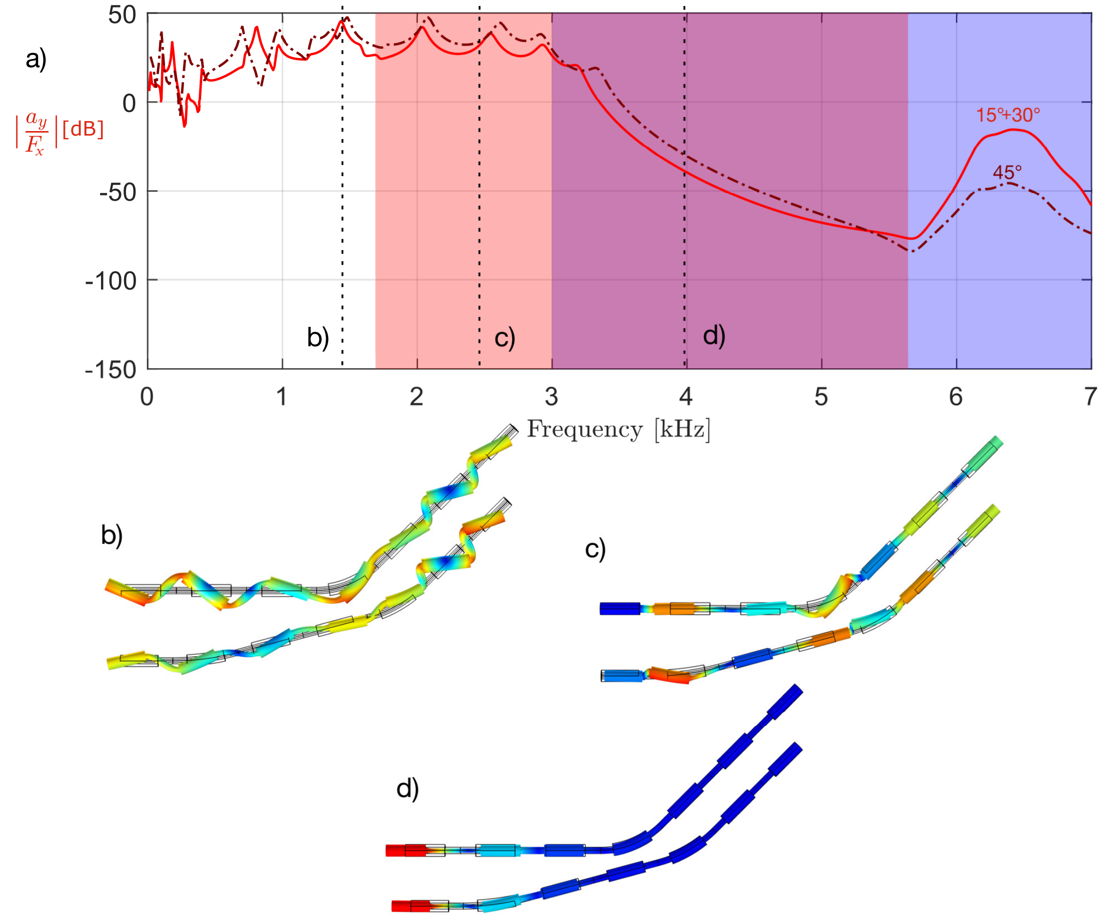

Figure 4.7 – Frequency response of the one segment bent waveguide and the two segments bent waveguide (a). The coloured areas show the flexural, *red*, and longitudinal, *blue*, band gaps, with the absolute band gap located at the junction of the two. The 3D fields, representing the displacement of the waveguides at different frequencies of interest. The first at 1.5 kHz, outside any band gap(b). The second at 2.5 kHz, belonging to the band gap for flexural waves (c). The third at 4 kHz within the absolute band gap (d).

The frequency responses of both configurations follow the same trend. We observe a slight shift, probably due to the modification of the geometry of the bent cells. We observe that the transfer function $|a_y/F_x|$ has a globally lower modulus in the case of the waveguide with two bent segments. The coupling between longitudinal and deflection movements is therefore globally weaker when the pipe has two bent segments.

Figure 4.8 is a second example of a waveguide with several curved cells. A straight waveguide (a) is compared to an example of a waveguide where the two bent segments lead to a zero angle, (b). A first section is curved at 15° and a second section is curved at -15°.

The flexural and longitudinal movements are decoupled in the case of the straight waveguide. The longitudinal excitation imposed on the straight waveguide does not allow the observation of flexural movements. In Fig. 4.9(a) the frequency response of the straight waveguide, red dashed curve, is at a level much lower than that observed with a waveguide with two bent segments, solid curve.

The frequency response $|a_y/F_x|$ has a significant module in a configuration with two curved cells. The low level of $|a_y/F_x|$ shows the existence of a flexural band gap above 1.8 kHz. As shown in the previous sections the operational deformations (Fig. 4.9(b) to (c)) show the coupling between longitudinal excitation and flexural displacements at the bent segments ((b) and (c)) and the propagation of flexural and longitudinal displacements stopped by the absolute band gap.(d).

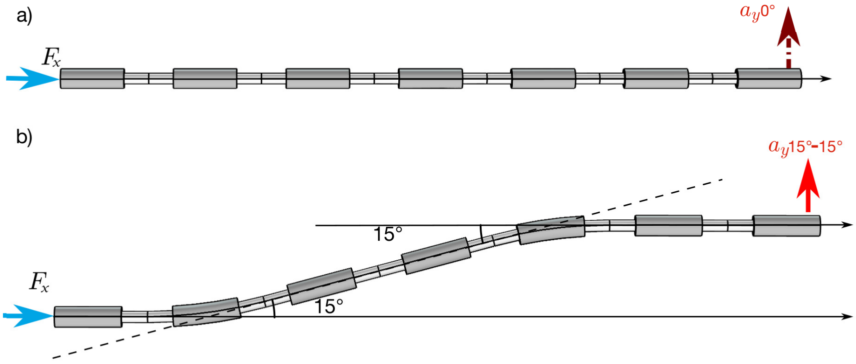

Figure 4.8 – Schematic of the reference waveguide, with the applied force and measured acceleration identified, (a). Schematic of the waveguide with two bent cells, with the applied force and measured acceleration identified, (b).

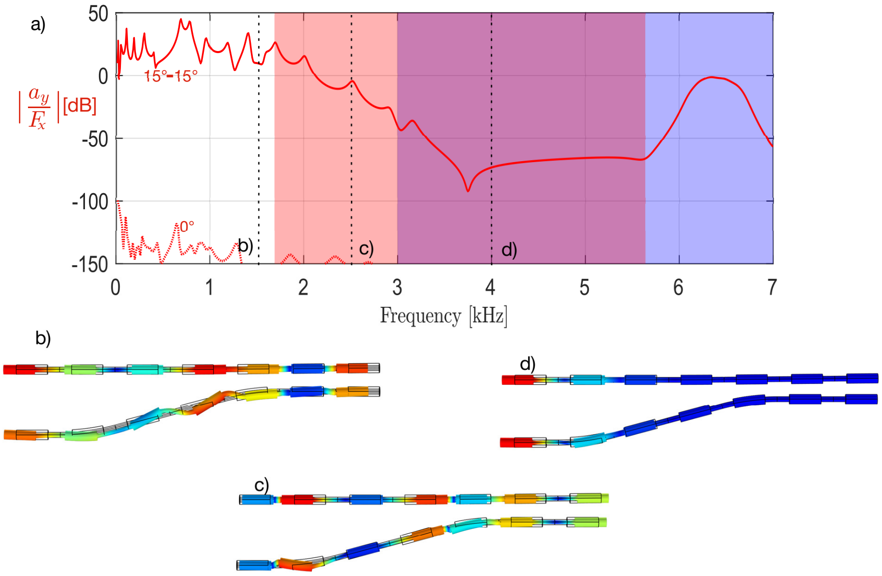

Figure 4.9 – Frequency response of straight, dot line, and two-cell, straigth line, bent waveguides, (b). The coloured areas show the flexural, *red*, and longitudinal, *blue*, band gaps, with the absolute band gap located at the junction of the two. The operational deflection shapes, represent the displacement of the waveguides at different frequencies of interest. The first at 1.5 kHz outside any band gap (c). The second at 2.5 kHz belonging to band gap for flexural waves (d). The third at 4 kHz within the absolute band gap(e).

To conclude, the three configurations studied above are demonstrating that wave conversion phenomenon is induced when curvature is present in the waveguide. It occurs both for local bends and for for curved segments. If the waveguide is designed as in Chap. 2 that is in order to have an absolute band gap, it ensures that this wave conversion phenomenon will not induce unwanted wave transmission. This shows the advantage brought by the absolute band gap.

4.3 Acoustic radiation from a plate coupled to a vibrational filter made of a 1D phononic crystal waveguide

Up to now, we have analyzed the vibrational properties of a 1D phononic crystal waveguide analyzing different effects due to the possibly curvature of it. Now, we increase the complexity of the system by coupling the 1D phononic waveguide to a plate that can radiate acoustic waves. The goal is to show how the absolute band gap of the phononic crystal waveguide can be used to reduce the vibrations transmited to the plate in this frequency range and as a consequence reduce the acoustic radiation produced by the plate. The interest of this system is directly related to the industrial problem analyzed in this work, in which a source is connected to the structured waveguide, which itself transmits the vibrations to an organ that can produce acoustic radiation (plate). It is the acoustic radiation of this plate that is the subject of the section.

4.3.1 Set-up of a 1D phononic crystal waveguide coupled to a radiating plate

The set-up is shown in Fig. 4.10(a). The 1D phononic crystal waveguide is excited by a longitudinal force as indicated by the blue arrow. The 1D phononic crystal waveguide is the one optimized in the Chap. 2 to obtain an absolute band gap in the frequency range from 3 kHz to 5.5 kHz. This 1D phononic crystal waveguide presents two unit cells introducing two angles of curvature. In this case we have chosen 15° as an example. The periodic waveguide is coupled to a circular steel plate of radius 0.15 m and thickness 1 mm. This plate is considered clamped along its perimeter. The plate is connected to a fluid domain from the radiation side, as shown in Fig. 4.10(b), a spherical half-space, of radius 0.2 m,. The fluid domain is air. For the numerical simulations we consider a perfectly matched layer domain, of thickness 0.05 m, around the fluid one in order to avoid the spureous reflections and to simulate the Sommerfeld conditions of radiation.

This system is numerically analyzed by using COMSOL Multiphysics. In particular for the vibroacoustic coupling, we have used the already existing acoustic-structure interaction modul. The continuity condition between solid and fluid is introduced in the boundaries separating the plate domain and the fluid one. It allows to compute the acoustic pressure in the fluid domain produced by the flexural motion of the plate.

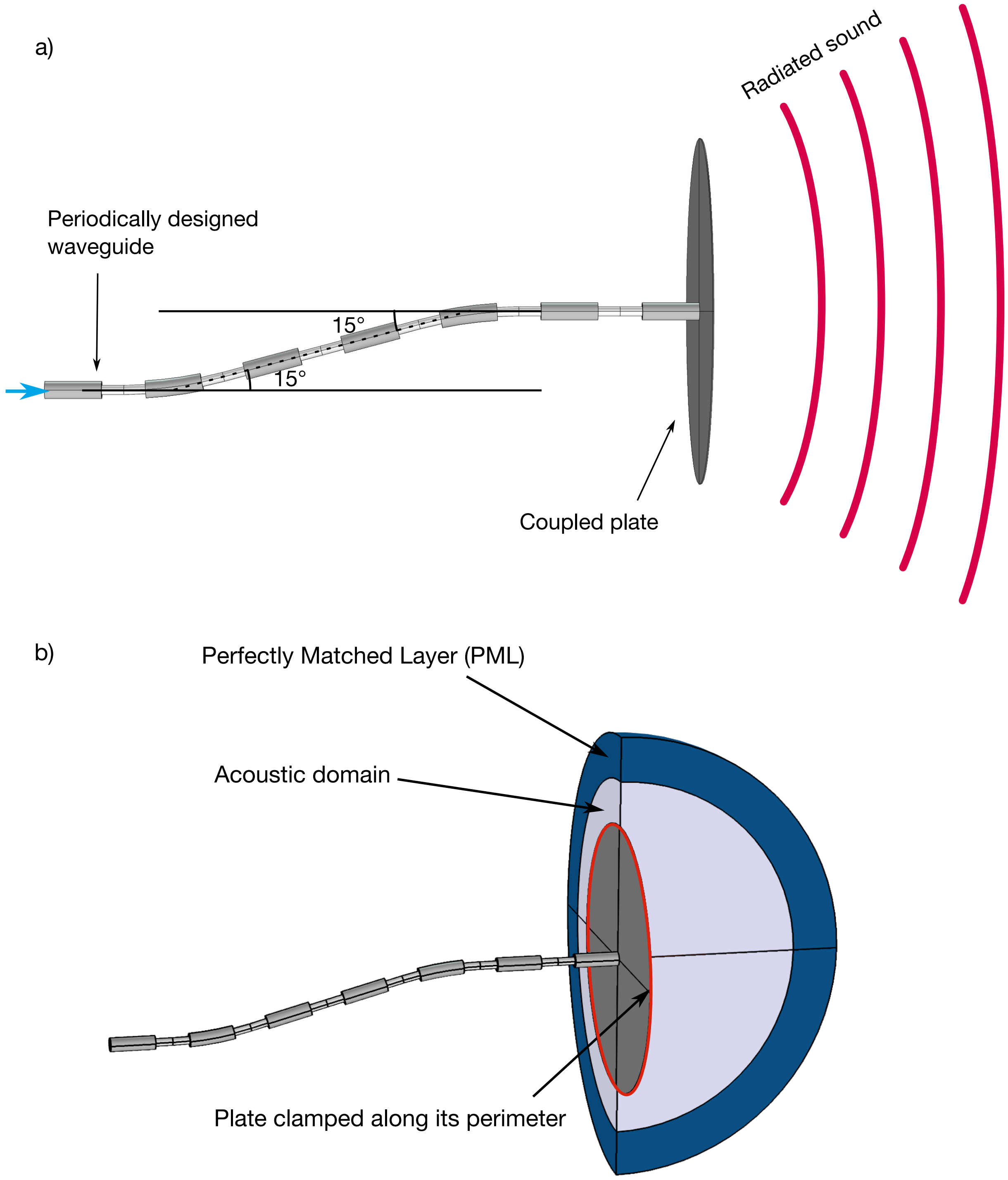

Figure 4.10 – Diagram of the coupling of a phononic crystal vibration filter with a resonant plate. The waveguide is curved by 15° on two cells and excited longitudinally. The plate is coupled to the waveguide by its center and will act as a "speaker" by diffusing the vibrations transmitted through the guide, (a). Numerical model of a bent phononic crystal coupled to a clamped circular steel plate. The plate is coupled to an infinite spherical half-space, with perfectly matched layer (b)

4.3.2 Radiated acoustic power of a 1D phononic crystal waveguide coupled to a radiating plate

The sound power, P_{ray}, radiated by the plate surface, S_{plate}, is a global indicator characterizing the acoustic radiation of the plate. It is given by:

$$P_{ray} = \frac{1}{2} Re \left(\int_{S_{plate}} |p \; v^{\star}| \, \partial S \right) . \tag{4.1}$$

where p and v are the pressure and velocity on the plate surface.

Figure. 4.11 shows several simulated configurations for which different types of waveguides are connected to the same radiating plate. The selected configuration is placed above the curve giving the radiated acoustic power. A snapshot shows the operational displacement of the waveguide and the acoustic field: at 4 kHz, this frequency belongs to the absolute band gap of the phononic crystal. The color scale is identical for all representations of Fig. 4.11. The one of the right tube is used as a reference to fix this scale. The acoustical levels obtained for the different representation can thus be compared.

In the reference case, Fig. 4.11(a), the waveguide is a straight aluminum tube of 8 mm diameter and 2 mm thickness. Its longitudinal motion is directly coupled to the flexural motion of the plate, producing effective radiation in the acoustic domain, as seen in the numerically calculated domain.

In Fig. 4.11(b), the waveguide is a 8 mm diameter and 2 mm thick aluminum tube with two bent segments at 15° and $-15°$. The longitudinal movement is coupled at the bent segments of the waveguide with a flexural movement. The plate is not only excited by the longitudinal movement of the beam but also by the flexural moment generated at its end, which produces acoustic radiation by the plate. At 4 kHz, the 3D view shows an operational deflection shape with a huge amplitude due to the presence of bent segments in the waveguide. These both longitudinal and flexural displacements in the waveguide also result in strong acoustic radiation.

In Fig. 4.11(c), the waveguide is a single-material periodic tube that takes the dimensions of the phononic crystal from Chap. 2, an 8 mm diameter, 38 mm long aluminum section and a 16 mm diameter, 47 mm long aluminum section, periodized throughout the guide. The periodic waveguide also has two bent segments at 15° and $-15°$. The periodic waveguide structure has a flexural band gap from 2 kHz to 3 kHz but no absolute band gap. At 4 kHz no mode is particularly excited which explains a less visible radiation for this frequency range.

In Fig. 4.11(d), the waveguide is the bi-material phononic crystal, a 16 mm diameter aluminum section of length 47 mm and a 8 mm diameter nylon section of length 38 mm, periodized over the entire guide. The waveguide has two bent segments at 15° and $-15°$. For this phononic crystal the bandwidth is between 3 kHz and 5.5 kHz. The radiated acoustic energy is in accordance with what one would expect with a strong decrease in the frequency band where the absolute band gap is located. However, it can be noted that upstream of this frequency band, the radiated power seems slightly higher than that observed in the other guides. The 3D view shows that the waveguide displacement is concentrated in the first cells near the longitudinal excitation and is not transmitted to the plate, which does not radiate.

In Fig. 4.11, the radiated powers of the straight (a), curved (b) and periodic (c) waveguides vary with frequency but are of the same order of magnitude. Over the entire frequency range [0-7kHz], the average power is of the order of 10^{-5} W for the unit excitation applied to the waveguide input.

For the architecturally designed waveguide (bi-material with phononic crystal (d)) the radiated power is between 10^{-16} and 10^{-13} W in the range [3-6 kHz]. This level is more than 8 decades lower than the average radiated power in the untreated configurations (a,b,c). The interest of the architectural waveguide is demonstrated here in that it considerably reduces the acosutic radiation in the absolute band gap.

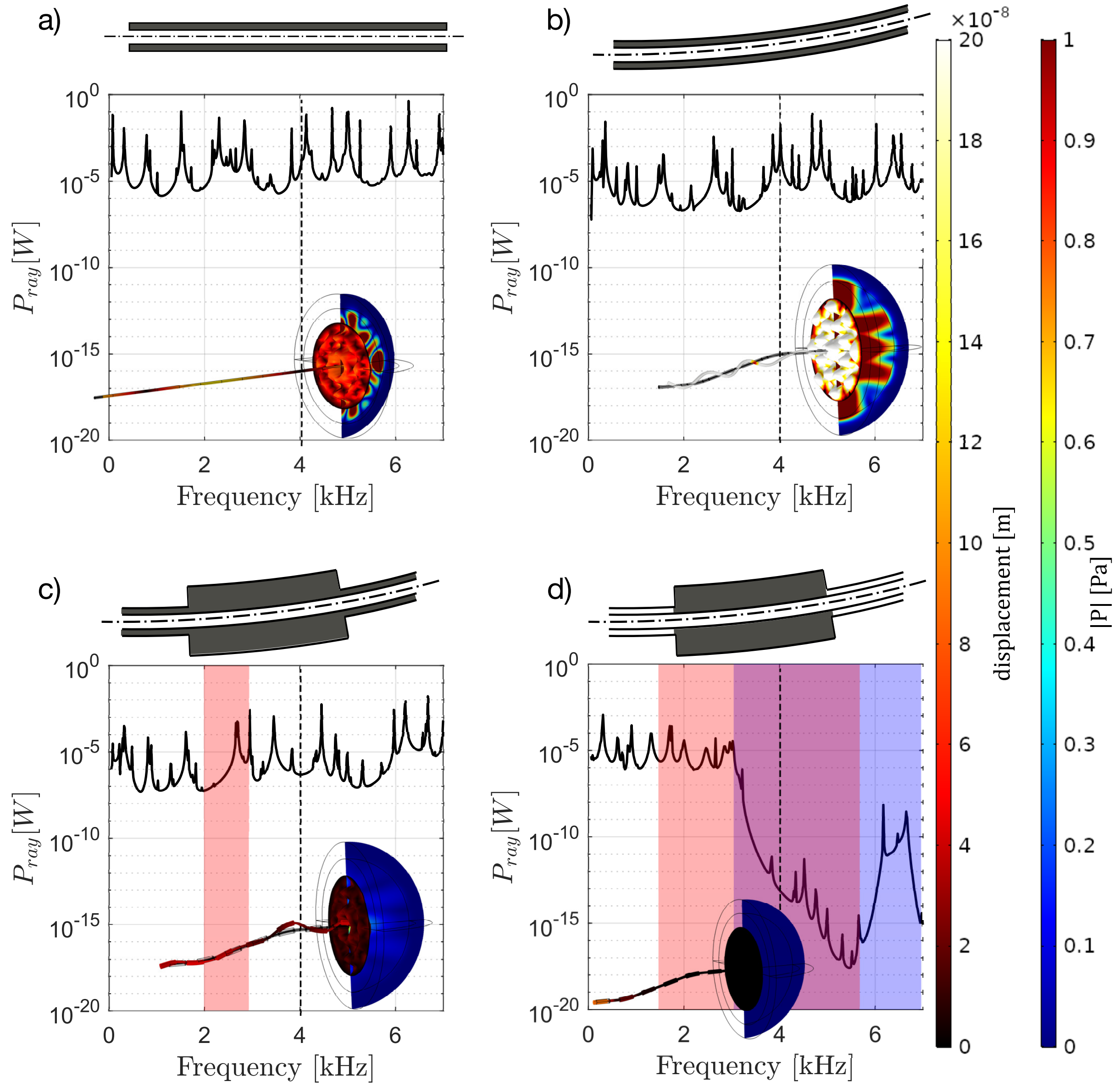

Figure 4.11 – Schematic, radiated power and 3D views, at 4 kHz, of the displacement and sound pressure fields for 4 configurations. Straight aluminum pipe coupled to a steel plate, (a). Bent aluminum pipe coupled to a steel plate, (b). Bent aluminum phononic crystal pipe coupled to a steel plate, (c). Bent phononic crystal pipe in bi-material, aluminum and nylon, coupled to a steel plate, (d).

In order to observe the improvement brought by the PC waveguide, we define an indicator, IL, based on the comparison of the radiated sound power, P_{ref}, by a plate connected to an aluminum pipe (without periodicity) with two curved segments versus the radiated power, P_{PC}, by a plate connected to a bi-material PC waveguide with the same two curved segments as follows :

$$IL = 10log_{10}(P_{ref}/P_{PC}). \tag{4.2}$$

In Fig. 4.12(a) on the graph the red area delineates the flexural band gap, the blue area delineates the longitudinal band gap, the absolute band gap is from 3 kHz to 5.5 kHz where the two areas overlap. The graph highlights the previously observed results. Replacing the aluminum waveguide by a dual material phononic crystal slightly increases the radiated noise level, up to 3 kHz. In the absolute band gap, from 3 kHz to 5.5 kHz, the radiated noise level is strongly attenuated before rising again once out of the absolute band gap.

The operational deflection shape, at 2.6 kHz (Fig. 4.12(b)) illustrates the displacement of the longitudinally excited phononic crystal waveguide and the acoustic pressure field radiated by the coupled plate, out of the absolute band gap. The longitudinal displacement is coupled to flexural displacements at the bent sections leading to a strong radiation from the plate. In Fig. 4.12(a), on the graph the red area delineates the flexural band gap, the blue area delineates the longitudinal band gap, the absolute band gap is from 3 kHz to 5.5 kHz where the two areas overlap. The insertion loss indicator, highlights the previously observed results. Replacing the aluminum waveguide with a dual material phononic crystal slightly increases the radiated noise level, up to 3 kHz. In the absolute band gap, from 3 kHz to 5.5 kHz, the radiated noise level is strongly attenuated before rising again once out of the absolute band gap.

Figure 4.12(c) shows two snapshots taken at 3.2 kHz. On the left, the displacement of the aluminum waveguide excites the plate, resulting in strong acoustic radiation. On the right, the wave propagation in the bi-material phononic crystal is attenuated, resulting in weak acoustic radiation.

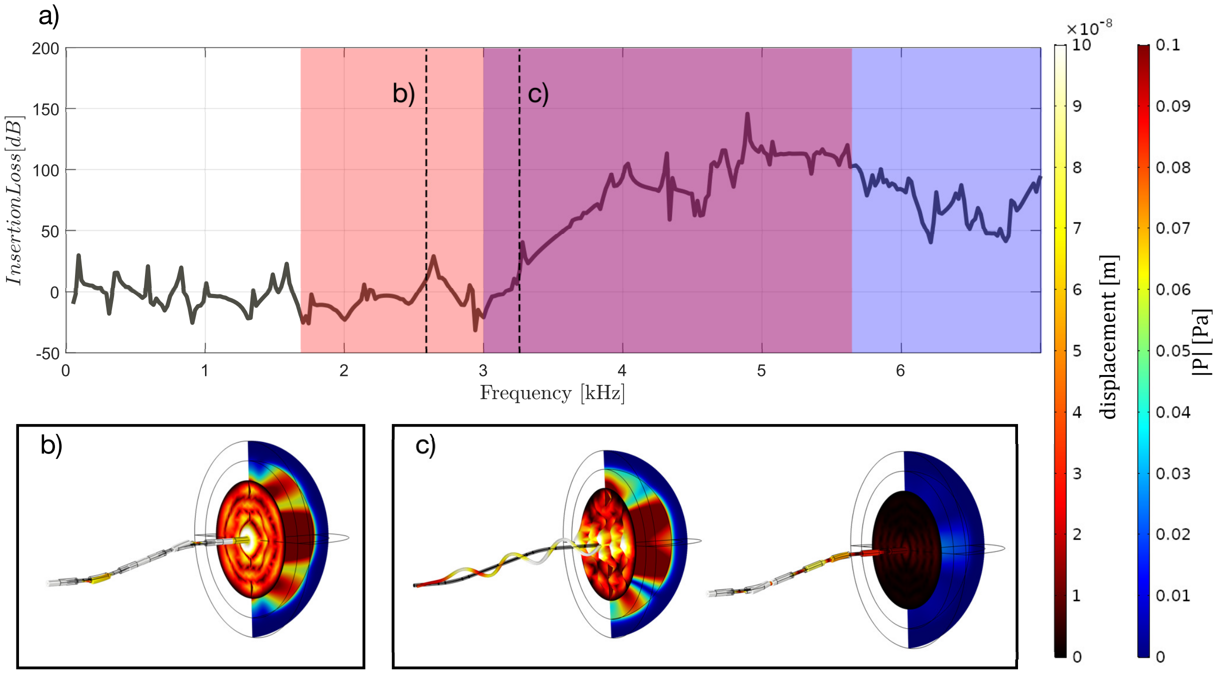

Figure 4.12 – Attenuation of the field radiated by a plate coupled to a bi-material phononic crystal compared to the same plate coupled to an untreated pipe, (a). The 3D views illustrate the solid displacement field in the pipe and the plate and illustrate the acoustic pressure field in the spherical half-space coupled to the plate. The frequency of interest is outside the absolute band gap, at 2.6 kHz, for the bi-material phononic crystal (b), and inside the absolute band gap, at 3.2 kHz, for a thin aluminum waveguide, (left) compared to the bi-material phononic crystal (right) (c).

The vibratory filter obtained with the phononic crystal developed in Chap. 2 keeps its properties in the targeted frequency band. The presence of an absolute band gap allows to limit the acoustic propagation of a plate coupled to the waveguide.

4.4 Influence of a heavy fluid on the vibration filtering properties of a 1D phononic crystal pipe

The presence of a fluid can influence the wave propagation in the waveguide and must be taken into account when designing the periodic filter. In the initial context (Fig. 4.1) the pump pressurizes the fuel which is conveyed through the tube to the injection rail. The content of the waveguide is then fuel under pressure. To simplify the calculations, we choose here to consider the fluid as water at atmospheric pressure. A mass effect is expected to be added to the waveguide to disrupt the wave propagation compared to the empty waveguide considered so far. Figure. 4.13 shows the dispersion diagram of a periodic cell loaded or unloaded with a heavy fluid, here water.

The dispersion diagram (Fig. 4.13(a)) shows the analytical color curves and numerical simulations for an empty infinite periodic waveguide (o), and compares them to the numerical simulations of an infinite periodic waveguide loaded with water (•). The operational deflection shapes illustrate three cases of eigenforms that can be related to the propagation of a wave type in the loaded waveguide. Fig. 4.13(b), shows the flexural displacement of the solid part of the waveguide. Fig. 4.13(c), shows the propagation of an acoustic wave in the fluid part of the guide. Figure 4.13(d) shows the propagation of a longitudinal wave in the solid part of the guide.

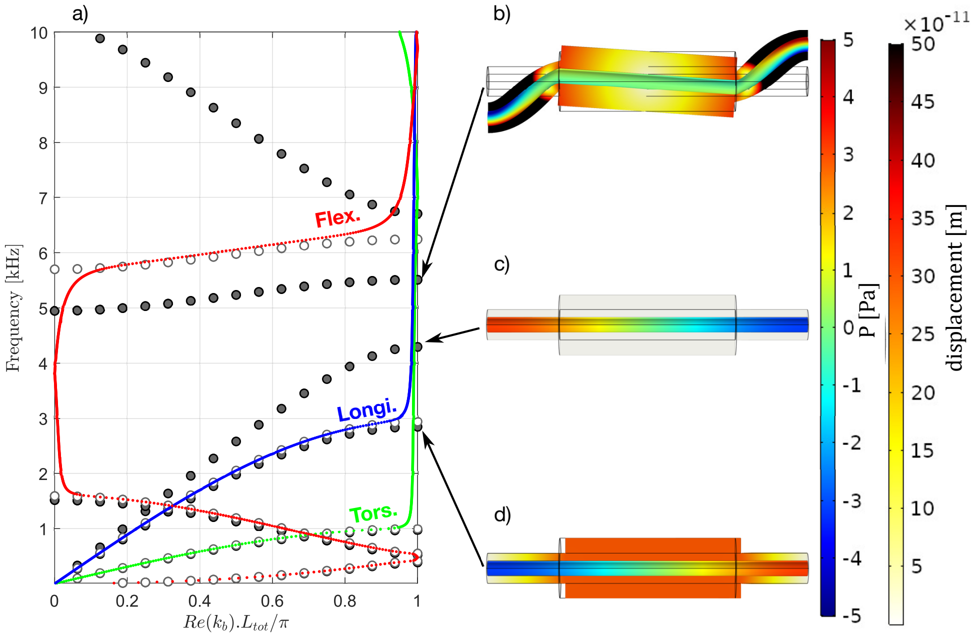

Figure 4.13 – Real part of the dispersion relation of a bi-material phononic crystal pipe obtained from 3D finite element numerical simulations without (o) or with (•) a heavy fluid (water) enclosed in the pipe. As comparison, the results obtained from the analytical models without added fluid are also reported (flexural (•), longitudinal (•) and (•) torsional waves), (a). 3D views of the eigen shapes at selected frequencies for $k_b Ltot/\pi = 1$ show the coupled motions between the solid displacement of the pipe and the acoustic pressure in the water column enclosed in the pipe, 5.5 kHz (b), 4.2 kHz (c) and 3 kHz (d)

Figure 4.14 presents the 3D view already observed in Fig. 4.13(c), the scales, of colors and deformation, have been adjusted in order to observe the coupling between the waves moving in the acoustic domain and in the elastic domain. We observe in the nylon cylinders a deformation of the structure according to the pressure differential in the fluid.

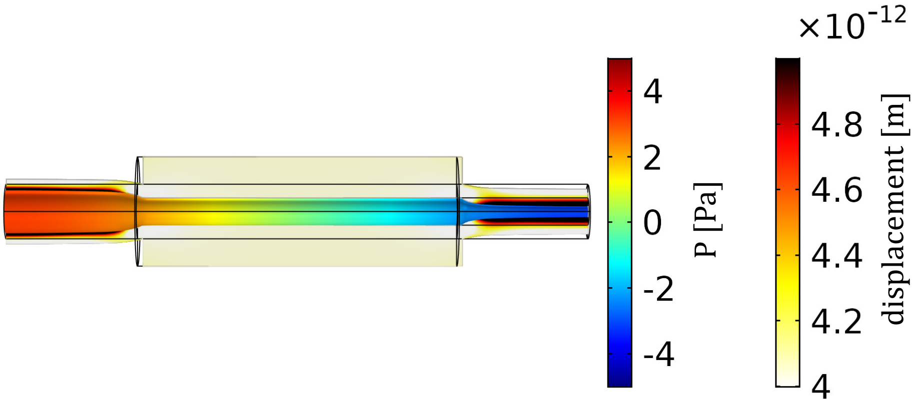

Figure 4.14 – 3D views of the eigen shapes at 4.2 Hz for $k_b Ltot/\pi = 1$ show the coupled motions between the solid displacement of the pipe and the acoustic pressure in the water column enclosed in the pipe (Zoom of Fig. 4.13(c)).

The differences between with and without fluid loading are due to the coupling between the different waves excited in the system, in particular between the pressure wave in the water and the elastic wave in the pipe. The propagation of the flexural wave is impacted around 5 kHz, due to the additional mass of the water. We observe the emergence on the dispersion diagram of a curve associated with the propagation of an acoustic wave in the fluid. The presence of an acoustic band gap is due to the coupling between the elastic structure and the fluid, it is a phenomenon similar to that used to obtain band gaps in pipes with periodically arranged resonators [157]. This interesting result shows that a complete band gap for both sound and elastic waves is possible.

A finite structure, composed of 7 periodic cells, is numerically simulated (Fig. 4.15). The water column is excited at the input with a unitary plane incident wave. The COMSOL Plane wave radiation module provides an anechoic termination at the end. The ratio between the incoming P_{in} and outgoing P_{out} pressure is displayed, in gray. The ratio between the incoming a_{in} and outgoing a_{out} elastic wave in displayed, in blue for the longitudinal wave and in red for the flexural. The acoustic band gap observed in Fig. 4.13 and indicated by the gray area, allows to obtain an attenuating effect on the propagation of a plane wave.

The propagation of a plane wave in the fluid leads to a displacement of the waveguide (see Fig. 4.15(a)). This interaction is made possible by the bi-material structure of the waveguide resulting in a periodic change of the boundaries of the fluid column. In the frequency range of the acoustic band gap, the propagation is rapidly attenuated in both the elastic and acoustic propagation (see Fig. 4.15(b)). The propagation of flexural waves is impacted by the pass band from 5 kHz to 5.5 kHz. Outside the acoustic band gap (Fig. 4.15(c)) the plane wave propagation is no longer attenuated, unlike the elastic wave propagation which is damped. It can be seen on the 3D view that the nylon sections are deformed by the propagation of the acoustic wave in the fluid column, but there is no propagation of an elastic wave, the aluminum sections remaining slightly impacted.

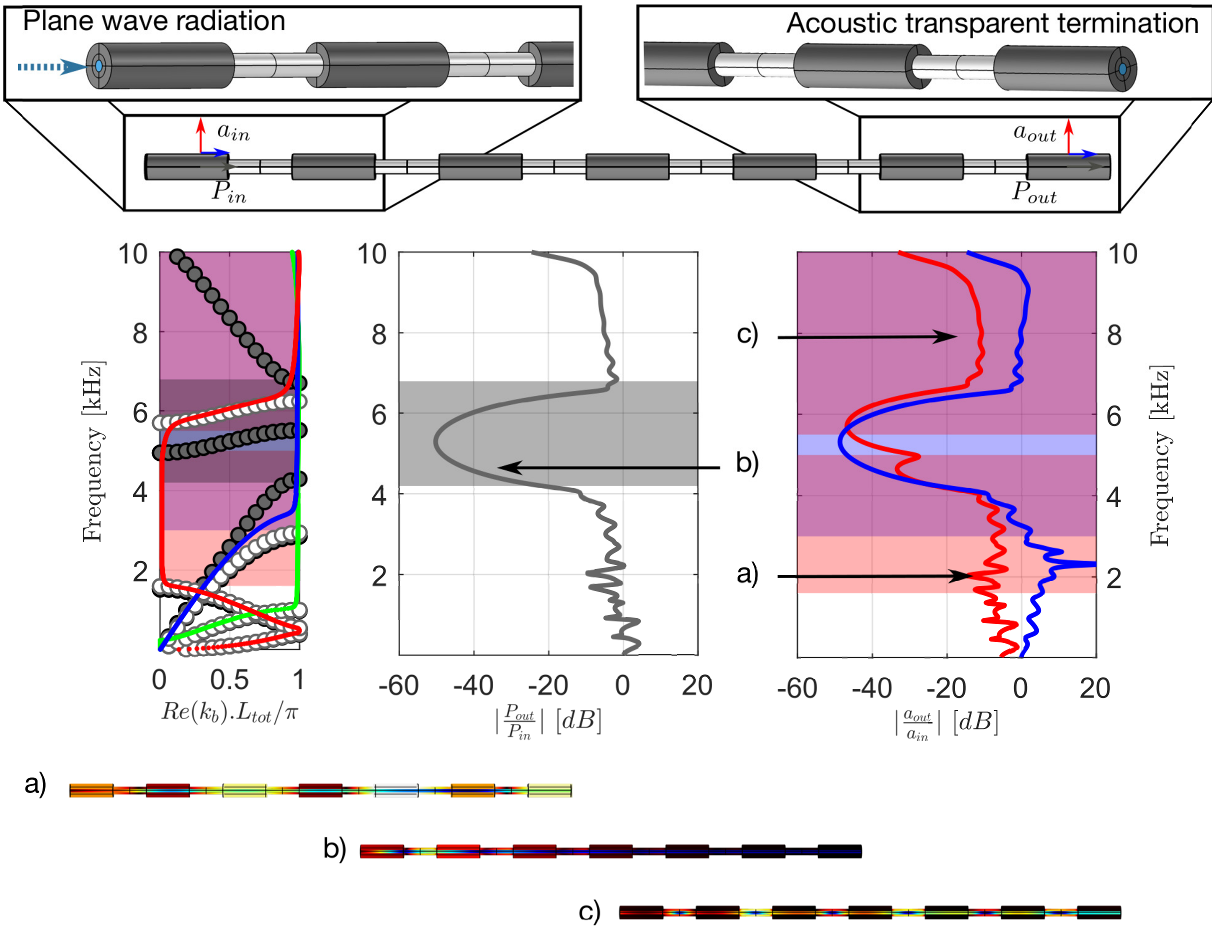

Figure 4.15 – Real part of the dispersion relation of a bi-material phononic crystal pipe obtained from 3D finite element numerical simulation, frequency response of a finite structure composed of 7 cells. The fluid inside the waveguide is excited with a piston generating a plane wave at $x = 0$ (waveguide input). 3D views of the deformation at 2 kHz (a), 5 kHz (b), 8 kHz (c)

A finite structure consisting of 7 periodic cells and an aluminum cap, is numerically simulated. In Fig. 4.16, the structure is excited by an unitary oblique incident force on the cap surface. Longitudinal and flexural elastic waves propagate through the waveguide and an acoustic wave is generated by the displacement of the cap. A anechoic acoustic boundary is placed at the end of the waveguide simulating the continuity of the water column.

Figure 4.16(a), at 4.5 kHz elastic and acoustic band gap lead to a damping. Figure 4.16(b), the band gap for flexural waves from 5 kHz to 5.5 kHz results in a propagation of flexural waves visible on the graph and the 3D view. Outside the acoustic band gap at 8 kHz (see Fig. 4.16(c)), we observe the same results as in Fig. 4.15(c), the acoustic wave propagates in the water column but the elastic waves are rapidly damped.

As in Chap. 2 with the phononic crystal waveguide, the longitudinal waves are impacted at the exit of the absolute band gap by the flexural waves. Nevertheless, the loaded waveguide allows to obtain two absolute band gaps from 4.2 kHz to 5 kHz and from 5.5 kHz to 6.8 kHz.

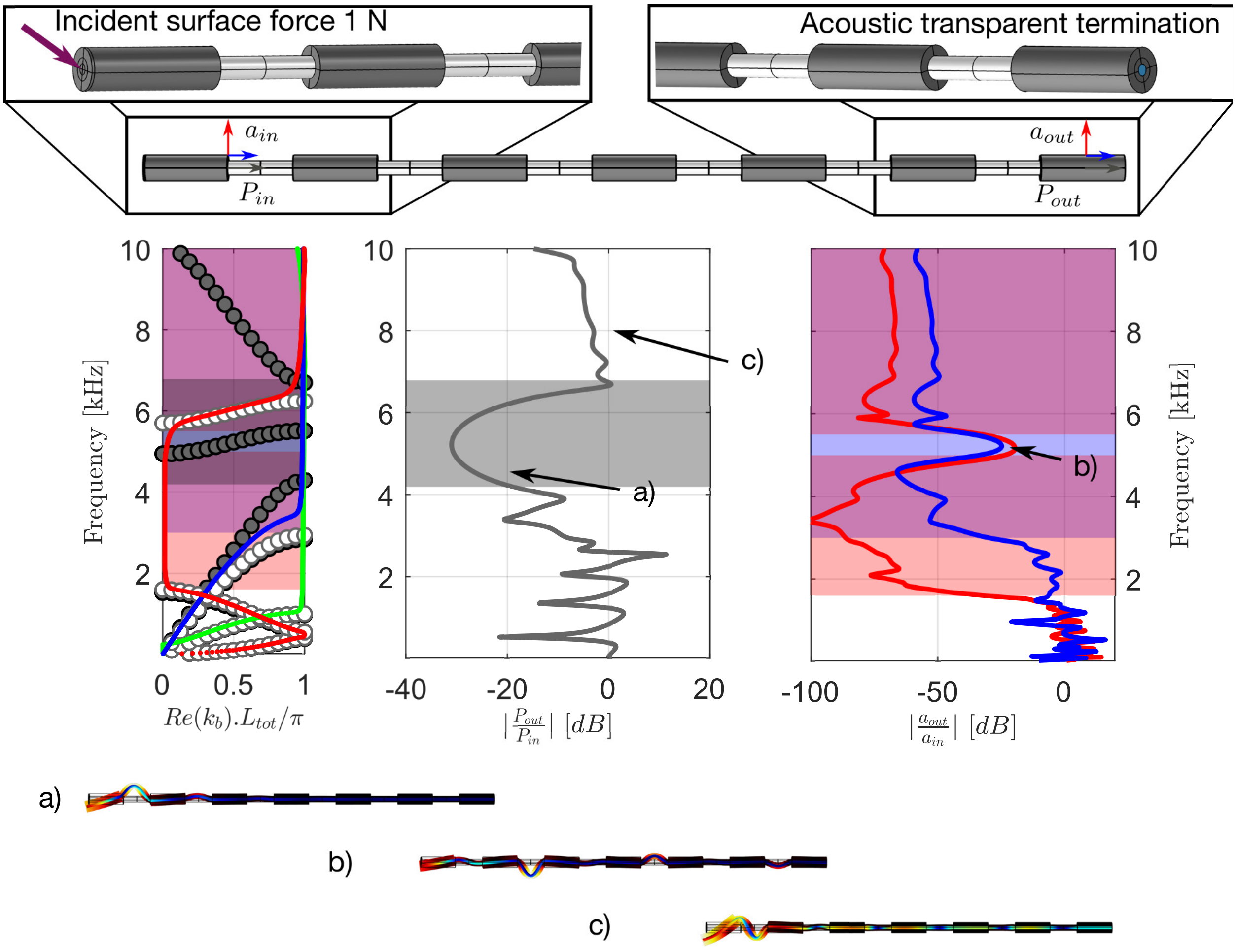

Figure 4.16 – Real part of the dispersion relation of a bi-material phononic crystal pipe obtained from 3D finite element numerical simulation, frequency response of a finite structure composed of 7 cells. The fluid inside the waveguide is excited with a plane wave radiation. 3D views of the dlectionshapes at 4.5 kHz (a). 5.25 kHz (b). 8 kHz (c)

4.5 Conclusion

This chapter presents the study of several applications of a bi-material phononic crystal tube. The objective is to highlight the elements of complexity that appear when the system developed in the laboratory evolves towards an integration in the industrial environment. These elements of complexity are addressed by the curve of the waveguide, the coupling with a radiating plate and the presence of a heavy fluid inside the waveguide. In the design of the bi-material phononic crystal, the obtaining of an absolute band gap is valid for a simple waveguide and this chapter is interested in verifying if these elements of complexity are detrimental to the efficiency of the vibratory filter previously obtained.

The complexity of a waveguide with bent segments until 45° leads to the appearance of wave conversion effects, the longitudinal waves will excite the flexural structure and reciprocally. The results showed that an absolute band gap from 3 kHz to 6 kHz, filtering the flexural, torsional and longitudinal waves, allows to predict these wave conversion effects and to filter their propagation for a targeted frequency band. Thus, in this frequency band the radiating structure coupled to the waveguide is not excited, which limits the acoustic propagation. The two-material phononic crystal is still valid and effective for a curved waveguide coupled to a plate as a vibration filter but also as an acoustic filter.

The loading of a hollow waveguide by a fluid introduces not only vibration but also acoustic wave propagation. When designing the phononic crystal, only the propagation of vibration waves is taken into account. However, the bi-material phononic crystal can also achieve a band gap from 4.2 kHz to 6.8 kHz in the acoustic domain. The superposition of the vibration and acoustic band gaps allows to obtain a vibro-acoustic filter for a targeted frequency band. Because the hollow waveguide optimization process targeted a frequency band for vibrational waves, the acoustic wave bandgap obtained by adding a fluid does not match the vibrational bandgap from 3 kHz to 6 kHz. In future work, the optimization process could consider acoustic waves to achieve the desired vibro-acoustic band gap.

Chap. 5

Conclusions and perspectives

Contents

5.1 Conclusions 84
5.2 Perspectives 86

5.1 Conclusions

The main objective of this thesis was the realisation of a multi-wave vibration filter, or absorber, for a target frequency range. Several approaches have been studied to design a multi-wave filter, or absorber.

Periodic structures have the effect of creating frequency bands in which the propagation of a wave is strongly attenuated. These frequency bands are commonly called band gaps in the case of infinite periodic structures. They are present for different types of elastic waves, longitudinal, torsional and flexural. In general case, the band gaps associated with each type of wave are not necessarily in the same frequency range.

Locally resonant structures have the effect of creating frequency bands in which the transmission of a vibration wave is strongly attenuated due to the resonance of the building blocks. Depending on the configuration of the resonator and its position on the waveguide, it is also possible to obtain an absorption effect if losses are considered. These filtering and absorption effects exist for different types of elastic, longitudinal, torsion and flexural waves. It is possible to obtain a broadband frequency range by combining a series of resonators.

The application of the proposed design to cases of increasing complexity, allows to judge the relevance of the proposed system in the hypothesis of an industrial integration. The influence of the waveguide geometry on its vibration filtering properties has been investigated. The influence of the coupling with a radiating element has been investigated. The influence of the presence of a heavy fluid on a periodic cell has been investigated.

The main contributions presented in this work are summarised below as well as the perspectives of this research.

Design of multi-wave vibration filter based on Phononic Crystal pipes with absolute bandgap.

In Chapter 2 a design of a vibrating filter based on phononic crystals has been developed. Three 1D analytical Floquet-Bloch models giving the dispersion of longitudinal, flexural and torsional waves, taking into account losses, were combined in an optimization procedure to achieve a unit cell design that has absolute band gaps with target frequency characteristics. The applicability and reliability of this design methodology has been demonstrated through a series of cases. In addition, the study of a 6-cells demonstrator showed both numerically and experimentally drops in transfer functions corresponding to the analytically predicted absolute bandgap, providing a second main insight. These results showed how absolute bandgaps in the high frequency domain can be applied to mitigate vibrations that can lead to structure-borne noise in some industrial systems.

Design of 1D multi-wave vibration filters and absorbers based on tunable local resonators loaded in pipes.

In Chapter 3 several designs of vibration filter and vibration absorber are developed. Three resonators tuned for flexural, longitudinal and torsional waves, taking into account losses, are combined to achieve configurations that exhibit absolute attenuation (filter) and absorption (absorber) around the target frequencies for the selected wave type. A series of cases is detailed to show the practical application and results of such a design.

With an analytical code, and an optimization, it is possible to obtain an overlap between the reflection coefficients of the different resonators. As the numerical calculations are relatively expensive, an optimization of the resonator parameters has not been performed. Ideally, each resonator is designed and placed in such a way that to obtain attenuation and absorption over a wide frequency band.

These results illustrate how local resonators can be applied to attenuate and absorb vibrations in a waveguide with little additional mass and space. This type of resonator also has the main advantage of being easy to add to an already existing device, at the end of the design, or adapted to a specific use, electric motor for the automotive industry for example.

Cases study based on industrial situations of multi-wave vibration filter pipes.

In Chapter 4 the previously developed designs are numerically confronted with situations common in the industrial context. The objective is to highlight the elements of complexity that appear when we start to think about the integration of systems developed in the laboratory in an industrial environment. The topics discussed are the curvature of the waveguide, the coupling with a radiating plate and the presence of a heavy fluid inside the waveguide.

An absolute band gap that filters out flexural, torsional, and longitudinal waves has the advantage of avoiding the wave conversion effects that occur in a waveguide with curved sections. The filtered waves will not excite the radiating structure coupled to the waveguide, thus limiting acoustic propagation. However, the presence of fluid inside the waveguide introduces a new type of propagation that was not anticipated when the phononic crystal was designed. The acoustic wave is impacted by the design of the pipe. The bandgap frequencies associated with the acoustic wave are not optimal because they were not controlled during the optimization process.

5.2 Perspectives

The work done in this thesis has led to potential results with possibilities to be applied: A damped frequency range, for longitudinal, flexural and torsional waves, can be obtained with a phononic crystal waveguide. A range of filtered or absorbed frequencies is can also be obtained with a series of resonators added locally on a waveguide.

This work can be completed by the following axes:

In the case of waveguides based on phononic crystals, the design and optimization of crystal phononic waveguide could be extended to consider a liquid inside the waveguide under some pressure. This will allow to take into account the couplings between acoustic and elastic waves. In order to obtain a multi-wave filter anticipating these drawbacks, it is necessary to add the prediction of the acoustic wave band gaps in the design and optimization process of the phononic crystal.

In the case of waveguides with local resonators, it is necessary to develop an analytical model taking into account the couplings between the waveguide and the resonator in order to predict its behavior more accurately. Once this analytical model is reliable, an optimization process can be performed to obtain a damped frequency range around a target frequency. A connection with laboratories specialized in polymers and their characterizations would also be a positive point for the conception and design of custom resonators.

List of Figures

1.1 Diagram of a generic industrial system as treated in this thesis. An element is considered as a vibratory source, here schematized as a motor. A transmission elements seen as an elastic waveguide conducts the vibrations produced by the source to a acoustic radiating component, which propagates the vibrations emitted by the source. 2

1.2 Free layer damping, viscoelastic sheet (a). Constrained layer damping, aircraft fuselage (b). Multi-layered or sandwich damping, brake pad (c). (Figure inspired from Ref. [8]) 5

1.3 Drawing of an undamped dynamic vibration absorber (a). Effect of undamped vibration absorber on the response of the machine (b). (Figure from Ref. [7]) 6

1.4 Experimental set-up (a) and reflection and transmission ratio (b), (—) for the analytical method and (- · - ·) for the experimental reflection, and (- - -) fot the experimental transmission, (Figure from Ref. [50]) 7

1.5 Analysis of the open resonators in reflection configuration. Diagrams of the beam terminaison (a). Representation of $log_{10}(|R_r|)$ in the complex frequency plane for the lossless and lossy configurations respectively (b). Analytical and experimental measurement of the reflection $|R_r|^2$ and absorption α (c). (Figure from Ref. [54]) . . 8

1.6 Eusebio Sempere's sculpture in Madrid, Spain, (a). Measured sound attenuation as a function of frequency. The inset illustrates the direction of propagation of sound waves. Arrows indicate the calculated maxima and minima due to interference from the different crystal planes of the sculpture, (b). (Figures from Ref [66]) 9

1.7 Band structure and transmission spectrum for a system of open tubes. N' is the number of dangling side branches(of length d_2 and cross-section a_2) grafted on N equidistant sites (with period d_1) ofa slender tube. Reduced wave-vector refers to the dimensionless Bloch vector $k_b l_{tot}$ and the reduced frequency is defined by $\Omega = \omega(l_{tot}/c_1)$, ($c_1$ is the speed of sound in the segment 1). We consider identical fluid both inside the dangling side branches and inside slender tube (a). Theorical dispersion of waves propagating normal to the layering in 1D layered composites(b) (Figures from Refs. [99, 100]) 10

1.8 Example of infinite periodic waveguide with two component (a). Periodic cylindrical shell (b). Dependant of $\Lambda = e^{ik_b}$ upon $\Omega = \frac{\omega h_1}{c_1}$, $|\Lambda| \neq 1$: stop-band, $|\Lambda| = 1$: pass-band (c). (Figure from Ref. [79]). 11

1.9 Example of a kirigami phononic crystal with a hexagonal unit cell, (a), this type of cell leads to the following dispersion diagram, real part at the top and imaginary part at the bottom, (b). (Figure from Ref. [106]) 12

1.10 Pipe segments used as a periodique repeated substructure (a). Insertion losses (IL) in a pipe with variable number of inserted periodicity cells. The grey strips indicate Floquet-predicted stop bands, (b). (Figure from Ref. [109]) 12

1.11 Band structures of the phononic crystal pipes composed of steel and epoxy for a classical Bragg-type cell (a) and for a two parts 180° along circumferential direction cell (b) (Figures from Ref. [105]). 13

1.12 Example of curved beam of phononic crystals (a). (CBPC) Band structures of in-plane elastic wave of curved beam of phononic crystals (CBPC) and equivalent straigth beam of phononic crysals (SBPC). The red lines represent the absolute value of the real and imaginary parts of the in-plane energy band structure of CBPC and the light blue ones represent those of equivalent SBPC. The grey regions are the band gaps of CBPC, The regions with slash are longitudinal and bending wave band gaps of equivalent SBPC. (b) (Figures from Ref. [126]) 14

1.13 A three-dimensional realization of the metamaterial. The material box encloses a piezoelectric transducer for generating mechanical vibrations and a loudspeaker for airborne sound. (b) The acoustic frequency response of the metamaterial compared with and without metamaterial box. (c) The elastic frequency response of the metamaterial (Figures from Ref. [132]). 15

1.14 Unit configuration for non-optimised filter design (a), and configuration for optimised filter design (b). The black color denotes material phase with high stifness and density; the white color denotes material phase with low stifness and density. Frequency band diagram for non-optimised filter design (c). Frequency band diagram for optimised filter design (d). Target frequency ranges for phononic filter with pass band (PB) and stop band (SB) shaded in grey. (Figure from Ref. [135]) 16

1.15 Optimized unit-cell design and band structure for out-of-plane waves: First band gap (a), second band gap (b). Optimized for in-plane waves: second band gap (c). Optimized for combined out-of-plane and in-plane waves, lowest band gap: pixels (d) and splines (e). (Figure from Ref. [125]) 17

1.16 Unite cell of a locally resonant metamaterial plate (a). Flexural mode for a fixed resonator base (b). Picture of a PMMA resonators produced to a vibroacoustic pipe used (c). Finite elements modeling mode shape of the first and second eigenfrequencies of the resonant structure (d). Dispersion curves for a infinite periodic structure with resonators, Compararison between undamped (black dash line), and damped (red solid line) curve (e). (Figures from Refs. [51, 68, 156–158]) 18

1.17 Simple model of a locally resonant beam (a). Sketch of a locally resonant beam with finite local resonators (b).Complex flexural band structure of the locally resonant beam and the displacement FRF of its finite sample (c). Real (d) and imaginary (e) part of the dispersion diagram. (Figures from Ref. [159]) 18

1.18 (a) Photograph of an acoustic rainbow-trapping manufactured sample. (b) Absorption obtained by using the TMM (continuous line), FEM simulations (circles) and measured experimentally (dotted line). (c) Corresponding reflection (red curves) and transmission (blue curves) coefficients in amplitude. (d,e) Complex frequency representation of the eigenvalues of the scattering matrix. (Figures from Ref. [42]) . 19

1.19 (a-i) Structure of the cell, with resonant mass, periodised. The spring components are identified for each movement as well as the displacement of the mass and the strains on the springs. (j -l) Experimentally observed Input/output ratio for each acoustic eigenmode for a finite metarod, with (j) for longitudinal eigenmode, (k) for flexural, and (l) for torsional. (Figure from Ref. [57]) 20

2.1 Scheme of the modeled phononic crystal pipe. (a) and (b) show lateral and cross sectional schematic representation of the modeled phononic crystal pipe, respectively.The delimited region of length l_{tot} represents the unit cell 24

2.2 Validation of the Floquet method by comparison with reference results in the cases of uniform structural guide (a), single-material phononic crystal guide (b). 27

2.3 Analysis of the dispersion relation of a periodic two-material cell with $l_{tot} = 0.1$ m; Real part of the dispersion relation with $\gamma = 0.2$, $R_1 = 8$ mm and $\beta = 0.5$ calculated both by the semi-analytical model (coloured points, (●) longidutinal, (●) in flexion and (●) in torsion) and by the full 3D FEM simulation (open circles $\circ$). The colour scale of the deformation fields is chosen arbitrarily in order to clarify the meaning, with red areas corresponding to maximum deformation and blue areas to minimum deformation. 29

2.4 Evolution of the band gap of the bending (red), longitudinal (blue) and torsional (green) waves in the cases of a single-material aluminium cell (a) and of a two-material aluminium/nylon cell (b), as a function of the variations of the total length of the cell l_{tot} for $\gamma = 0.5$ and $\beta = 0.5$ (1); the outer radius contrast β for $\gamma = 0.5$ and $l_{tot} = 0.1$m (2); the length ratio γ for $\beta = 0.5$ and $l_{tot} = 0.1$m (3). All simulations are performed for $R_1 = 8$mm. 30

2.5 Schematic representation of the Nelder-Mead algorithm [172]. 33

2.6 Convergence of $\mathcal{F}$, I_{fc} and $I_{\Delta f}$ with the number of iterations (upper part), and associated optimized dispersion diagrams (lower part) when considering 3 couples of weighting coefficients: (a) $[\alpha_{f_c}, \alpha_{\Delta f}]$=[1/2, 1/2], leading to $\mathbf{X}$=[97.1 mm, 0.42, 7.9 mm, 0.58]; (b) $[\alpha_{f_c}, \alpha_{\Delta f}]$=[5/6, 1/6], leading to $\mathbf{X}$=[79.9 mm, 0.5, 8.7 mm, 0.48]; (c) $[\alpha_{f_c}, \alpha_{\Delta f}]$=[1/6, 5/6], leading to $\mathbf{X}$=[81.4 mm, 0.47, 7.2 mm, 0.58]. The target absolute band gap is [3; 7] kHz, that is $f_0 = 5$ kHz and $\Delta f_0 = 4$ kHz. See Tab. 2.2 for detailed results. 34

2.7 Pictures of the fabricated phononic crystal tube. The nylon and aluminum sections are force-fitted together, holding the assembly together without the use of glue and thus minimizing unwanted losses. Sizing of a total filter demonstrator: (a) view of the view of the longitudinal cross section of the cell showing the interlocking assembly of the sections; (b) 6 cell digital demonstrator FEM mesh with representation of the 3 load cases and measurement points. (c) Experimental setup; (d) Detail of the 2 face-to-face three-axis accelerometers; (e) view of the 2 aluminium/nylon unit cells of the demonstrator; (f) view of the shaker excitation implemented in the oblique position such that all wave types are excited. 36

2.8 Numerical analysis and experimental characterisation of the optimal phononic crystal pipe: (a) real part and (b) imaginary part of the optimised complex dispersion relation obtained by the Floquet-Bloch method and considering the viscoelastic losses (see main text). (●) longidutinal, (●) flexural and (●) torsional; measured (light line) and simulated (dark line) acceleration transfer functions in the (c) flexural, (d) longitudinal, (e) full loading cases; 3D views of the simulated total displacement in the full loading case at (f) 900 Hz where all wave types propagate, (g) 2500 Hz where only flexural band gap is opened and (h) 4500 Hz whithin the absolute band gap. 37

3.1 3D view of the considered annular resonators mounted on a host pipe (a) ; schematic representation of the motion associated to the 4 resonances admitted by such resonator (b): y-translation (b.1), x-translation (b.2), z-rotation (rotation around z) (b.3), x-rotation (b.4) 41

3.2 Map representation of the evolution of the eigen frequencies of the ring resonator for varying ring length l and mass M. Resonant rings have 4 solid body movements that can be associated to a type of wave. The curves represent the operating points for a resonator tuned to 1 kHz, respectively □ for y-translation or z-translation, ⋆ for x-translation, ○ for z-rotation or y-rotation, and ◁ for x-rotation. The straight line are for the analytical calculation. 43

3.3 Schematic diagram for the numerical calculation of the R and T coefficients in the case of configuration of the guide as a flexural vibration filter. 44

3.4 Schematic diagram for the numerical calculation of the R-factor in the case of a configuration of the guide as an absorber with recessed termination (a), with free termination (b). 44

3.5 Illustration of the principle of functioning of a vibration filter made of a resonator, (a). Example of a filter effect with any resonator tuned for 1 kHz, with a structural damping value in the rubber $\eta = 0$, (b). Evolution of the flexural (○) and longitudinal (○) values of Δf for the configurations described in Tab. 3.1, (c). Evolution of the limit value of a vibration filter according to the evolution of the structural damping factor η (d). 47

3.6 Example of absorption effect with a resonator tuned for 1 kHz in flexural, with a structural damping value in the rubber $\eta = 10\%$, (b). Evolution of the threshold value of a vibration absorber as a function of the distance l_l between the resonator and the free end of the waveguide. (c). 48

3.7 Coefficient of reflection ($|R^+|, |R^-|$) and transmission ($[T|$) of a graded filter without structural damping $\eta = 0$. The geometry of the resonators is available Tab. 3.2. The reflection coefficients obtained for the forward ($|R^+|$ in $--$) and return ($|R^-|$ in $\ldots$) waves are superposed. 50

3.8 Coefficient of reflection, transmission and absorption of a graded vibration filter with structural damping $\eta = 10\%$. The geometry of the resonators is available Tab. 3.2. The reflection coefficients is obtain for the forward ($|R^+|$ in $--$) and return ($|R^-|$ in $\ldots$) waves. Due to the presence of damping, $\eta \neq 0$, we see an absorption effect, $\alpha \neq 0$. 51

3.9 Coefficient of reflection and transmission of a graded filter type vibration filter without structural damping $\eta = 0$. The geometry of the resonators is available Tab. 3.2. The reflection coefficients is obtain for the forward ($|R^+|$ in $--$) and return ($|R^-|$ in $\ldots$) waves. 52

3.10 Coefficient of reflection, transmission and absorption of a graded filter type vibration filter with structural damping $\eta_{flex} = 10\%$ and $\eta_{longi} = 2\%$. The geometry of the resonators is available Tab. 3.2. The reflection coefficients is obtain for the forward ($|R^+|$ in $--$) and return ($|R^-|$ in $\ldots$) waves. 53

3.11 Vibration absorber configuration with 4 resonators attached to the clamped end of the waveguide (a). Reflection and absorption coefficient of a graded trapping type vibration absorber with structural damping in rubber $\eta = 10\%$. The geometry of the resonators is available Tab. 3.2 (b). 54

3.12 Reflection and absorption coefficient of an absolute vibration absorber with optimized structural damping according to Fig. 3.5. The absorber consists of three resonators: one tuned for flexural waves (−), one for longitudinal waves (−), and the third for torsional waves (−). 56

3.13 Diagram of the measurement performed to obtain the reflection coefficient of a structure composed of a host element and one or more resonant elements (a). Picture of the impact hammer (b) used to excite the structure, the single-axis accelerometer (c) and the experimental setup with a resonator on a host waveguide (d) 57

3.14 Reflection coefficient of an incident flexural wave on a hollow cylindrical steel structure, 12 mm external diameter, 1 mm thick (a). Reflection coefficient of an incident flexural wave on a rectangular aluminium structure, 20 × 10 mm (b). 58

3.15 Frequency response of the different measurement points on the structure. In black dots the frequency response calculated by a finite element model (a). Picture of the experimental setup with the identified measurement points (b). 3D views of the simulated displacement fields for the eigenmode at 190 Hz (c), 590 Hz (d), 720 Hz (e), 230 Hz (f). 59

3.16 Mapping of the reflection coefficient as a function of resonator position tuned to 720 Hz (a), 600 Hz (b) and 490 Hz (c). The red cross indicates the selected resonator positions. 60
3.17 Reflection coefficient and associated phase, experimental in red— and numerical in black —, of a rectangular aluminium waveguide with a resonator of mass 40 g. The excitation point of the structure is shown with an arrow on the 3D model. 61
3.18 Reflection coefficient and associated phase, experimentally in red— and numerically in black—, of a rectangular aluminium waveguide with 3 resonators of a mass of 40 g placed at a distance $dr = 0$ mm from the end of the waveguide, a mass of 60 g placed at a distance of $dr = 150$ mm, and a mass of 90 g placed at a distance $dr = 80$ mm. 62
3.19 Mapping of the reflection coefficients as a function of the position of the resonator of a mass of 60 g, the resonator of 40 g being placed at the end of the guide and the resonator of 90 g being fixed at 150 mm, (a). Reflection coefficient and associated phase, experimental in red— and numerical in black—, of a rectangular aluminium waveguide with 3 resonators of a 40 g mass placed at a distance $dr = 0$ mm from the end, a 60 g mass placed at a distance $dr = 60$ mm, and a 90 g mass placed at a distance $dr = 150$ mm, (b). 63

4.1 Overview of an internal combustion engine injection system in which the fuel pressure pump (right) acts as a vibration source, the pipe as a structural waveguide transmitting the vibrations and the injection rail as a receiver from which the vibrations propagate to the entire engine block and result in the radiation of noise by surface elements (e.g. firewall, not shown here). 66
4.2 Diagram of the waveguides, with the applied force and measured acceleration identified, (a). 67
4.3 Frequency response of straight and curved waveguides, (a). The coloured areas show the gap bands, predicted in Chap. 2, flexural, in *red*, and longitudinale, in *blue*, the absolute gap band is located at the intersection of these two. The operational deflection shapes, representing the displacement of the waveguides at different frequencies of interest are shown. At 1.5 kHz outside any band gap the presence of a curve leads to the generation of flexural waves, (b). At 2.5 kHz in the band gap for flexural waves the operational deflection shapes are dominated by longitudinal motions, (c). At 4 kHz within the absolute band gap where displacement field is rapidly damped (d). 68
4.4 Reference straight waveguide, with the applied force and measured acceleration identified, (a). Bent waveguide, with the applied force and measured acceleration identified, (b). 69
4.5 Frequency response of straight and bent waveguides, (a). The operational deflection shapes represent the displacement of the waveguides at different frequencies of interest. The first at 1.5 kHz, outside any band gap (b). The second at 2.5 kHz belinging to the band gap for flexural waves (c). The third at 4 kHz within the absolute band gap (d). 70
4.6 Schematic of the reference waveguide, with the applied force and measured acceleration identified, (a). Schematic of the waveguide with two bent cells, with the applied force and measured acceleration identified, (b). 71
4.7 Frequency response of the one segment bent waveguide and the two segments bent waveguide (a). The coloured areas show the flexural, *red*, and longitudinal, *blue*, band gaps, with the absolute band gap located at the junction of the two. The 3D fields, representing the displacement of the waveguides at different frequencies of interest. The first at 1.5 kHz, outside any band gap(b). The second at 2.5 kHz, belonging to the band gap for flexural waves (c). The third at 4 kHz within the absolute band gap (d). 72

4.8 Schematic of the reference waveguide, with the applied force and measured acceleration identified, (a). Schematic of the waveguide with two bent cells, with the applied force and measured acceleration identified, (b). 73
4.9 Frequency response of straight, dot line, and two-cell, straigth line, bent waveguides, (b). The coloured areas show the flexural, *red*, and longitudinal, *blue*, band gaps, with the absolute band gap located at the junction of the two. The operational deflection shapes, represent the displacement of the waveguides at different frequencies of interest. The first at 1.5 kHz outside any band gap (c). The second at 2.5 kHz belonging to band gap for flexural waves (d). The third at 4 kHz within the absolute band gap(e). 73
4.10 Diagram of the coupling of a phononic crystal vibration filter with a resonant plate. The waveguide is curved by 15° on two cells and excited longitudinally. The plate is coupled to the waveguide by its center and will act as a "speaker" by diffusing the vibrations transmitted through the guide, (a). Numerical model of a bent phononic crystal coupled to a clamped circular steel plate. The plate is coupled to an infinite spherical half-space, with perfectly matched layer (b) 75
4.11 Schematic, radiated power and 3D views, at 4 kHz, of the displacement and sound pressure fields for 4 configurations. Straight aluminum pipe coupled to a steel plate, (a). Bent aluminum pipe coupled to a steel plate, (b). Bent aluminum phononic crystal pipe coupled to a steel plate, (c). Bent phononic crystal pipe in bi-material, aluminum and nylon, coupled to a steel plate, (d). 77
4.12 Attenuation of the field radiated by a plate coupled to a bi-material phononic crystal compared to the same plate coupled to an untreated pipe, (a). The 3D views illustrate the solid displacement field in the pipe and the plate and illustrate the acoustic pressure field in the spherical half-space coupled to the plate. The frequency of interest is outside the absolute band gap, at 2.6 kHz, for the bi-material phononic crystal (b), and inside the absolute band gap, at 3.2 kHz, for a thin aluminum waveguide, (left) compared to the bi-material phononic crystal (right) (c). 78
4.13 Real part of the dispersion relation of a bi-material phononic crystal pipe obtained from 3D finite element numerical simulations without (o) or with (•) a heavy fluid (water) enclosed in the pipe. As comparison, the results obtained from the analytical models without added fluid are also reported (flexural (•), longitudinal (•) and (•) torsional waves), (a). 3D views of the eigen shapes at selected frequencies for $k_b Ltot/\pi = 1$ show the coupled motions between the solid displacement of the pipe and the acoustic pressure in the water column enclosed in the pipe, 5.5 kHz (b), 4.2 kHz (c) and 3 kHz (d) 79
4.14 3D views of the eigen shapes at 4.2 Hz for $k_b Ltot/\pi = 1$ show the coupled motions between the solid displacement of the pipe and the acoustic pressure in the water column enclosed in the pipe (Zoom of Fig. 4.13(c)). 80
4.15 Real part of the dispersion relation of a bi-material phononic crystal pipe obtained from 3D finite element numerical simulation, frequency response of a finite structure composed of 7 cells. The fluid inside the waveguide is excited with a piston generating a plane wave at $x = 0$ (waveguide input). 3D views of the deformation at 2 kHz (a), 5 kHz (b), 8 kHz (c) 81
4.16 Real part of the dispersion relation of a bi-material phononic crystal pipe obtained from 3D finite element numerical simulation, frequency response of a finite structure composed of 7 cells. The fluid inside the waveguide is excited with a plane wave radiation. 3D views of the dlectionshapes at 4.5 kHz (a). 5.25 kHz (b). 8 kHz (c) . . 82

B.1 Locally resonant mass spring with longitudinal excitation 121
B.2 Locally resonant mass spring with flexural excitation 123

B.3 Comparison between the numerical, dotted line, and analytical, solid line values of a local resonator. The reflection $|R|$ and transmission $|T|$ values are plotted for each type of movement through the waveguide. Longitudinal waves in blue (●), torsional in green (●), flexural in red (●). 125

List of Tables

2.1 Topological and material parameters from which the unit cell of the Fig. 2.1 is defined. 24
2.2 Detailed values obtained for the converged cost function $\mathcal{F}$ and its deviation indicators I_{Δ_f} and I_{f_c} for a set of optimization cases defined by 4 absolute band targets, each associated with three weighting configurations. 35

3.1 Flexural and longitudinal ring resonators parameters for a $1kHz$ tuning. Each configuration can be link with Fig. 3.2 46
3.2 Flexural and longitudinal resonator parameters for graded vibration filters 49
3.3 Parameters of the resonators for the absolute type vibration absorber. 55

Bibliography

[1] B. Nuria *et al.*, « Noise in Europe 2017: updated assessment », European Topic Centre on Air Pollution and Climate Change Mitigation (ETC/ACM): Bilthoven, The Netherlands 2017.

[2] F. Theakston and Weltgesundheitsorganisation, Eds., *Burden of Disease from Environmental Noise: Quantification of Healthy Life Years Lost in Europe*. Copenhagen: World Health Organization, Regional Office for Europe, 2011, 106 pp.

[3] *Directive 92 97 CEE du Conseil du 10 novembre 1992*.

[4] L. Cremer, M. Heckl, and B. A. T. Petersson, *Structure-Borne Sound: Structural Vibrations and Sound Radiation at Audio Frequencies*, 3rd ed. Berlin ; New York: Springer, 2005, 607 pp.

[5] D. Thorby, *Structural Dynamics and Vibration in Practice [Recurso Electrónico]: An Engineering Handbook*. Paises Bajos; Estados Unidos; Reino Unido: Elsevier/Butterworth-Heinemann, 2008.

[6] M. J. Crocker, Ed., *Handbook of Noise and Vibration Control*. Hoboken, N.J: John Wiley, 2007, 1569 pp.

[7] S. S. Rao, *Mechanical Vibrations*, 5th ed. Upper Saddle River, N.J: Prentice Hall, 2011, 1084 pp.

[8] M. D. Rao, « Recent applications of viscoelastic damping for noise control in automobiles and commercial airplanes », *Journal of Sound and Vibration*, vol. 262, no. 3, pp. 457–474, May 2003.

[9] A. Lysak and T. Bourdon, « Nvh optimization methods applied to e-motors », SAE Technical Paper, Tech. Rep., 2020.

[10] H. F. Olson and E. G. May, « Electronic Sound Absorber », *The Journal of the Acoustical Society of America*, vol. 25, no. 6, pp. 1130–1136, Nov. 1953.

[11] R. Boulandet *et al.*, « Duct modes damping through an adjustable electroacoustic liner under grazing incidence », *Journal of Sound and Vibration*, vol. 426, pp. 19–33, Jul. 2018.

[12] C. Bricault *et al.*, « Multimodal reduction of acoustic radiation of thin plates by using a single piezoelectric patch with a negative capacitance shunt », *Applied Acoustics*, vol. 145, pp. 320–327, Feb. 2019.

[13] M. Berardengo, « Improved resistive shunt by means of negative capacitance: new circuit, performances and multi-mode control », *Smart Mater. Struct.*, p. 24, 2016.

[14] N. Hagood and A. von Flotow, « Damping of structural vibrations with piezoelectric materials and passive electrical networks », *Journal of Sound and Vibration*, vol. 146, no. 2, pp. 243–268, Apr. 1991.

[15] E. Metral, B. Zotter, and B. Salvant, « Resistive-wall impedance of an infinitely long multi-layer cylindrical beam pipe », in *2007 IEEE Particle Accelerator Conference (PAC)*, Albuquerque, NM: IEEE, 2007, pp. 4216–4218.

[16] T. Bourdon and R. Bouete, « Development of Fuel System Components through a Virtual NVH Prototyping - Focus on High Pressure Pumps », presented at the 9th International Styrian Noise, Vibration & Harshness Congress: The European Automotive Noise Conference, Jun. 15, 2016, pp. 2016-01–1763.

[17] T. Bourdon, R. Weber, and J. Massinger, « Virtual NVH Prototyping of Fuel Components Design - Focus on High Pressure Pumps and SCR Injectors », presented at the Noise and Vibration Conference and Exhibition, Jun. 5, 2017, pp. 2017-01–1840.

[18] K. F. Graff, *Wave Motion in Elastic Solids*. Dover Publications, 1975.

[19] M. Crocker, *Handbook of Noise and Vibration Control*, 3rd ed. New Jersey: John Wiley & Sons, New Jersey, 2007.

[20] D. Rao, « Vibration of short sandwich beams », *Journal of Sound and Vibration*, vol. 52, no. 2, pp. 253–263, May 1977.

[21] F. Gautier, « Reflection, Transmission and Coupling of Longitudinal and Flexural Waves at Beam Junctions. Part I: Measurement Methods. », *Acta Acoustica United With Acustica*, vol. 92, p. 16, 2006.

[22] D. L. Knighton and D. I. G. Jones, « Utilization of the RKU equations to design constrained layer damping treatments », *The Journal of the Acoustical Society of America*, vol. 65, no. S1, S110–S110, Jun. 1979.

[23] V. Kahya and M. Turan, « Bending of Laminated Composite Beams by a Multi-Layer Finite Element Based on a Higher-Order Theory », *Acta Physica Polonica A*, vol. 132, no. 3, pp. 473–475, Sep. 2017.

[24] N. Alam and N. Asnani, « Vibration and damping analysis of multilayered rectangular plates with constrained viscoelastic layers », *Journal of Sound and Vibration*, vol. 97, no. 4, pp. 597–614, Dec. 1984.

[25] P. Butaud, « Sandwich structures with tunable damping properties: On the use of Shape Memory Polymer as viscoelastic core », *Composite Structures*, p. 8, 2016.

[26] A. Climente, D. Torrent, and J. Sánchez-Dehesa, « Omnidirectional broadband insulating device for flexural waves in thin plates », *Journal of Applied Physics*, vol. 114, no. 21, p. 214 903, Dec. 7, 2013.

[27] S. Crandall, « The role of damping in vibration theory », *Journal of Sound and Vibration*, vol. 11, no. 1, 3–IN1, 1970.

[28] L. Salari-Sharif, S. M. Ryan, M. Pelacci, J. K. Guest, L. Valdevit, and S. Szyniszewski, « Damping of selectively bonded 3D woven lattice materials », *Scientific Reports*, vol. 8, no. 1, Dec. 2018.

[29] A. Pelat, F. Gautier, S. C. Conlon, and F. Semperlotti, « The acoustic black hole: A review of theory and applications », *Journal of Sound and Vibration*, vol. 476, p. 115 316, Jun. 2020.

[30] V. Denis, « Vibration damping in beams using the acoustic black hole effect », 149 pp.

[31] V. Denis, F. Gautier, A. Pelat, and J. Poittevin, « Measurement and modelling of the reflection coefficient of an Acoustic Black Hole termination », *Journal of Sound and Vibration*, vol. 349, pp. 67–79, Aug. 2015.

[32] V. Denis, A. Pelat, and F. Gautier, « Scattering effects induced by imperfections on an acoustic black hole placed at a structural waveguide termination », *Journal of Sound and Vibration*, vol. 362, pp. 56–71, Feb. 2016.

[33] O. Aklouche, A. Pelat, S. Maugeais, and F. Gautier, « Scattering of flexural waves by a pit of quadratic profile inserted in an infinite thin plate », *Journal of Sound and Vibration*, vol. 375, pp. 38–52, Aug. 2016.

[34] O. Aklouche, « Reduction des niveaux vibratoires d'un panneau au moyen de trous noirs acoustiques structurés en réseau périodique : conception d'une méta-plaque », Université Bretagne Loire, Le MANS Université, 2017, 162 pp.

[35] J. Leng, « Controlling flexural waves using subwavelength perfect absorbers: application to Acoustic Black Holes ».

[36] G. Raybaud, A. Pelat, M. Ouisse, and F. Gautier, « Zero reflections by a 1D Acoustic Black Hole termination using thermally controlled damping », *Journal of Sound and Vibration*, vol. 510, p. 116 282, Oct. 2021.

[37] A. Sternberger, J.-M. Génevaux, and A. Pelat, « Experimental analysis of the vibration dissipation induced by granular materials included into a 1 degree of freedom oscillator », *Granular Matter*, vol. 21, no. 3, p. 57, Aug. 2019.

[38] V. Romero-García *et al.*, « Design of acoustic metamaterials made of Helmholtz resonators for perfect absorption by using the complex frequency plane », p. 38, 2020.

[39] D. Guan, J. H. Wu, L. Jing, N. Gao, and M. Hou, « Application of a Helmholtz structure for low frequency noise reduction », *Noise Control Engineering Journal*, vol. 63, no. 1, pp. 20–35, Jan. 1, 2015.

[40] A. I. Komkin, M. A. Mironov, and A. I. Bykov, « Sound absorption by a Helmholtz resonator », *Acoustical Physics*, vol. 63, no. 4, pp. 385–392, Jul. 2017.

[41] T. Cavalieri, A. Cebrecos, J.-P. Groby, C. Chaufour, and V. Romero-García, « Three-dimensional multiresonant lossy sonic crystal for broadband acoustic attenuation: Application to train noise reduction », *Applied Acoustics*, vol. 146, pp. 1–8, 2019.

[42] N. Jiménez, V. Romero-García, V. Pagneux, and J.-P. Groby, « Rainbow-trapping absorbers: Broadband, perfect and asymmetric sound absorption by subwavelength panels for transmission problems », *Scientific Reports*, vol. 7, no. 1, p. 13 595, Dec. 2017.

[43] J. Zhu *et al.*, « Acoustic rainbow trapping », *Scientific Reports*, vol. 3, no. 1, p. 1728, Dec. 2013.

[44] A. Vachez, *Des Eches ou vases acoustiques dans les théâtres antiques et les églises du Moyen Age*. Delesques, 1886.

[45] T. Yasuda, C. Wu, N. Nakagawa, and K. Nagamura, « Studies on an automobile muffler with the acoustic characteristic of low-pass filter and Helmholtz resonator », *Applied Acoustics*, vol. 74, no. 1, pp. 49–57, Jan. 2013.

[46] T. Abily, V. Zorgnotti, G. Gabard, J. Regnard, and S. Durand, « Non-linear effects of thin structures with slits for low frequency acoustic absorption », 2 pages, 2020.

[47] D. Yu, Y. Liu, G. Wang, H. Zhao, and J. Qiu, « Flexural vibration band gaps in Timoshenko beams with locally resonant structures », *Journal of Applied Physics*, vol. 100, no. 12, p. 124 901, Dec. 15, 2006.

[48] D. Yu, Y. Liu, G. Wang, L. Cai, and J. Qiu, « Low frequency torsional vibration gaps in the shaft with locally resonant structures », *Physics Letters A*, vol. 348, no. 3-6, pp. 410–415, Jan. 2006.

[49] D. Yu, Y. Liu, H. Zhao, G. Wang, and J. Qiu, « Flexural vibration band gaps in Euler-Bernoulli beams with locally resonant structures with two degrees of freedom », *Physical Review B*, vol. 73, no. 6, Feb. 10, 2006.

[50] H. El-Khatib, B. Mace, and M. Brennan, « Suppression of bending waves in a beam using a tuned vibration absorber », *Journal of Sound and Vibration*, vol. 288, no. 4-5, pp. 1157–1175, Dec. 2005.

[51] C. C. Claeys, K. Vergote, P. Sas, and W. Desmet, « On the potential of tuned resonators to obtain low-frequency vibrational stop bands in periodic panels », *Journal of Sound and Vibration*, vol. 332, no. 6, pp. 1418–1436, Mar. 2013.

[52] B. Mace, « Wave reflection and transmission in beams », *Journal of Sound and Vibration*, vol. 97, no. 2, pp. 237–246, Nov. 1984.

[53] S.-K. Lee, B. Mace, and M. Brennan, « Wave propagation, reflection and transmission in non-uniform one-dimensional waveguides », *Journal of Sound and Vibration*, vol. 304, no. 1-2, pp. 31–49, Jul. 2007.

[54] J. Leng, F. Gautier, A. Pelat, R. Picó, J.-P. Groby, and V. Romero-García, « Limits of flexural wave absorption by open lossy resonators: reflection and transmission problems », *New Journal of Physics*, vol. 21, no. 5, p. 053 003, May 7, 2019.

[55] E. Nobrega, F. Gautier, A. Pelat, and J. Dos Santos, « Vibration band gaps for elastic metamaterial rods using wave finite element method », *Mechanical Systems and Signal Processing*, vol. 79, pp. 192–202, Oct. 2016.

[56] B. Sharma and C. Sun, « Local resonance and Bragg bandgaps in sandwich beams containing periodically inserted resonators », *Journal of Sound and Vibration*, vol. 364, pp. 133–146, Mar. 2016.

[57] A. Ogasawara, K. Fujita, M. Tomoda, O. Matsuda, and O. B. Wright, « Wave-canceling acoustic metarod architected with single material building blocks », *Applied Physics Letters*, vol. 116, no. 24, p. 241 904, Jun. 15, 2020.

[58] G. Wang, X. Wen, J. Wen, L. Shao, and Y. Liu, « Two-Dimensional Locally Resonant Phononic Crystals with Binary Structures », *Physical Review Letters*, vol. 93, no. 15, p. 154 302, Oct. 5, 2004.

[59] J.-C. Hsu and T.-T. Wu, « Lamb waves in binary locally resonant phononic plates with two-dimensional lattices », *Applied Physics Letters*, vol. 90, no. 20, p. 201 904, May 14, 2007.

[60] R. Sainidou, B. Djafari-Rouhani, Y. Pennec, and J. O. Vasseur, « Locally resonant phononic crystals made of hollow spheres or cylinders », *Physical Review B*, vol. 73, no. 2, p. 024 302, Jan. 6, 2006.

[61] S. Guenneau, A. Movchan, G. Pétursson, and S. Anantha Ramakrishna, « Acoustic metamaterials for sound focusing and confinement », *New Journal of Physics*, vol. 9, no. 11, pp. 399–399, Nov. 6, 2007.

[62] Y. Pennec, B. Djafari-Rouhani, H. Larabi, J. O. Vasseur, and A. C. Hladky-Hennion, « Low-frequency gaps in a phononic crystal constituted of cylindrical dots deposited on a thin homogeneous plate », *Physical Review B*, vol. 78, no. 10, p. 104 105, Sep. 5, 2008.

[63] T.-T. Wu, Z.-G. Huang, T.-C. Tsai, and T.-C. Wu, « Evidence of complete band gap and resonances in a plate with periodic stubbed surface », *Applied Physics Letters*, vol. 93, no. 11, p. 111 902, Sep. 15, 2008.

[64] P. Deymier, Ed., *Acoustic Metamaterials and Phononic Crystals*. Springer, 2013.

[65] J. D. Joannopoulus, S. G. Johnson, J. N. Winn, and R. D. Meade, *Photonic Crystals. Molding the Flow of Light*. Princeton University press, 2008.

[66] R. Martínez-Sala, J. Sancho, J. V. Sánchez, V. Gómez, J. Llinares, and F. Meseguer, « Sound Attenuation by sculpture », *Nature*, vol. 378, p. 241, 1995.

[67] M. Sigalas, M. S. Kushwaha, E. N. Economou, M. Kafesaki, I. E. Psarobas, and W. Steurer, « Classical vibrational modes in phononic lattices: theory and experiment », p. 45, 2005.

[68] M. I. Hussein, M. J. Leamy, and M. Ruzzene, « Dynamics of Phononic Materials and Structures: Historical Origins, Recent Progress, and Future Outlook », *Applied Mechanics Reviews*, vol. 66, no. 4, p. 040 802, Jul. 1, 2014.

[69] M. S. Kushwaha, « Classical band structure of periodic elastic composites », *International Journal of Modern Physics B*, vol. 10, no. 09, pp. 977–1094, Apr. 20, 1996.

[70] E. N. Economou and M. M. Sigalas, « Classical wave propagation in periodic structures: Cermet versus network topology », *Phys. Rev. B*, vol. 48 (18), p. 13 434, 1993.

[71] M. S. Kushwaha, P. Halevi, L. Dobrzynski, and B. Djafari-Rouhani, « Acoustic Band Structure of Periodic Elastic Composites », *Phys. Rev. Lett.*, vol. 71, no. 13, pp. 2022–2025, 1993.

[72] L. Brillouin and M. Parodi, *Propagation Des Ondes Dans Les Milieux Périodiques*. Masson et Cie, 1956.

[73] D. Mead, « Wave propagation and natural modes in periodic systems: II. Multi-coupled systems, with and without damping », *Journal of Sound and Vibration*, vol. 40, no. 1, pp. 19–39, May 1975.

[74] D. Mead, « Wave propagation and natural modes in periodic systems: I. Mono-coupled systems », *Journal of Sound and Vibration*, vol. 40, no. 1, pp. 1–18, May 1975.

[75] D. Mead, « Wave propagation in continuous periodic structures : research contributions from southampton, 1964-1995 », *Journal of Sound and Vibration*, vol. 190, no. 3, pp. 495–524, Feb. 1996.

[76] G. Sen Gupta, « Natural flexural waves and the normal modes of periodicaly supported beams and plates », *Journal of Sound and Vibration*, vol. 13, pp. 89–101, 1970.

[77] Y. Xu, X. Zhou, W. Wang, L. Wang, F. Peng, and B. Li, « On natural frequencies of non-uniform beams modulated by finite periodic cells », *Physics Letters A*, vol. 380, no. 40, pp. 3278–3283, Sep. 2016.

[78] H. Shen, J. Wen, D. Yu, and X. Wen, « The vibrational properties of a periodic composite pipe in 3D space », *Journal of Sound and Vibration*, vol. 328, no. 1-2, pp. 57–70, Nov. 2009.

[79] A. Hvatov and S. Sorokin, « Free vibrations of finite periodic structures in pass- and stop-bands of the counterpart infinite waveguides », *Journal of Sound and Vibration*, vol. 347, pp. 200–217, Jul. 2015.

[80] J. Plisson, A. Pelat, F. Gautier, V. R. Garcia, and T. Bourdon, « Experimental evidence of absolute bandgaps in phononic crystal pipes », *Applied Physics Letters*, vol. 116, no. 20, p. 201 902, May 18, 2020.

[81] Z.-Q. Ni, Y. Zhang, L.-H. Jiang, and L. Han, « Bending vibration band structure of phononic crystal beam by modified transfer matrix method », *International Journal of Modern Physics B*, vol. 28, no. 15, p. 1 450 093, Jun. 20, 2014.

[82] G. Carta and M. Brun, « Bloch–Floquet waves in flexural systems with continuous and discrete elements », *Mechanics of Materials*, vol. 87, pp. 11–26, Aug. 2015.

[83] J. Wen, G. Wang, D. Yu, H. Zhao, and Y. Liu, « Theoretical and experimental investigation of flexural wave propagation in straight beams with periodic structures: Application to a vibration isolation structure », *Journal of Applied Physics*, vol. 97, no. 11, p. 114 907, Jun. 2005.

[84] A. Pelat, T. Gallot, and F. Gautier, « On the control of the first Bragg band gap in periodic continuously corrugated beam for flexural vibration », *Journal of Sound and Vibration*, vol. 446, pp. 249–262, Apr. 2019.

[85] N. Olhoff, B. Niu, and G. Cheng, « Optimum design of band-gap beam structures », *International Journal of Solids and Structures*, vol. 49, no. 22, pp. 3158–3169, Nov. 2012.

[86] C. W. Zhou, J. P. Lainé, M. N. Ichchou, and A. M. Zine, « Wave Finite Element Method Based on Reduced Model for One-Dimensional Periodic Structures », *International Journal of Applied Mechanics*, vol. 07, no. 02, p. 1 550 018, Apr. 2015.

[87] V. S. Sorokin and J. J. Thomsen, « Eigenfrequencies and eigenmodes of a beam with periodically continuously varying spatial properties », *Journal of Sound and Vibration*, vol. 347, pp. 14–26, Jul. 2015.

[88] J. V. Sánchez-Pérez *et al.*, « Sound Attenuation by a Two-Dimensional Array of Rigid Cylinders », *Phys. Rev. Lett.*, vol. 80, no. 24, pp. 5325–5328, 1998.

[89] M. M. Sigalas and E. N. Economou, « Elastic and acoustic wave band structure », *J. Sound Vib.*, vol. 158, p. 377, 1992.

[90] A. Khelif, A. Choujaa, B. Djafari-Rouhani, M. Wilm, S. Ballandras, and V. Laude, « Trapping and guiding of acoustic waves by defect modes in a full-band-gap ultrasonic crystal », *Phys. Rev. B*, vol. 68, p. 214 301, 2003.

[91] A. Khelif, M. Wilm, V. Laude, S. Ballandras, and B. Djafari-Rouhani, « Guided elastic waves along a rod defect of a two-dimensional phononic crystal », *Phys. Rev. E*, vol. 69, p. 067 601, 2004.

[92] F. Cervera, L. Sanchis, J. V. Sánchez-Pérez, R. Martínez-Sala, C. Rubio, and F. Meseguer, « Refractive Acoustic Devices for Airborne Sound », *Phys. Rev Lett.*, vol. 88, no. 2, pp. 023 902–4, 2002.

[93] S.-C. Lin, T. Huang, J.-H. Sun, and T.-T. Wu, « Gradient-index phononic crystals », *Phys. Rev. B*, vol. 79, no. 094302, 2009.

[94] L. Feng *et al.*, « Negative refraction of acoustic waves in two-dimensional sonic crystals », *Phys. Rev. B*, vol. 72, p. 033 108, 2005.

[95] I. Pérez-Arjona, V. J. Sánchez-Morcillo, J. Redondo, V. Espinosa, and K. Staliunas, « Theoretical prediction of the nondiffractive propagation of sonic waves through periodic acoustic media », *Phys. Rev. B*, vol. 75, no. 014304, p. 014 304, 2007.

[96] A. Cebrecos *et al.*, « Formation of collimated sound beams by three-dimensional sonic crystals », *Journal of Applied Physics*, vol. 111, no. 10, p. 104 910, 2012.

[97] V. Romero-García and A.-C. Hladky-Hennion, Eds., *Fundamentals and Applications of Acoustic Metamaterials: From Seismic to Radio Frequency*. Wiley-ISTE, 2019.

[98] C. Goffaux *et al.*, « Evidence of Fano-Like Interference Phenomena in Locally Resonant Materials », *Physical Review Letters*, vol. 88, no. 22, p. 225 502, May 15, 2002.

[99] M. Kushwaha, A. Akjouj, B. Djafari-Rouhani, L. Dobrzynski, and J. Vasseur, « Acoustic spectral gaps and discrete transmisson in slender tubes », *Solid State Communications*, vol. 106, no. 10, pp. 659–663, Apr. 1998.

[100] C. W. Robinson and G. W. Leppelmeier, « Experimental Verification of Dispersion Relations for Layered Composites », *Journal of Applied Mechanics*, vol. 41, no. 1, pp. 89–91, Mar. 1, 1974.

[101] S. Sorokin and O. Ershova, « Plane wave propagation and frequency band gaps in periodic plates and cylindrical shells with and without heavy fluid loading », *Journal of Sound and Vibration*, vol. 278, no. 3, pp. 501–526, Dec. 2004.

[102] S. V. Sorokin, « On the bi-orthogonality conditions for multi-modal elastic waveguides », *Journal of Sound and Vibration*, vol. 332, no. 21, pp. 5606–5617, Oct. 2013.

[103] S. Sorokin, « On propagation of plane symmetric waves in a periodically corrugated straight elastic layer », *Journal of Sound and Vibration*, vol. 349, pp. 348–360, Aug. 2015.

[104] A. Hvatov and S. Sorokin, « Assessment of reduced-order models in analysis of Floquet modes in an infinite periodic elastic layer », *Journal of Sound and Vibration*, vol. 440, pp. 332–345, Feb. 2019.

[105] Y. Zhang, D. Yu, and J. Wen, « Study on the band gaps of phononic crystal pipes with alternating materials in the radial and axial directions », *Extreme Mechanics Letters*, vol. 12, pp. 2–6, 2017.

[106] S. del Broccolo, M. Ouisse, E. Foltete, and F. Scarpa, « Bandgap capability of hybrid Kirigami inspired cellular structures », *Advances in Aircraft and Spacecraft Science*, vol. 6, no. 6, pp. 481–497, 2019.

[107] S. Broccolo, M. Ouisse, E. Foltete, and F. Scarpa, « Interlocked hybrid-cell Kirigami inspired cellular structures and their vibroacoustic performance », presented at the International Conference on Noise and Vibration Engineering, Leuven, Belgium, Sep. 2018, p. 15.

[108] S. Hou, T. Li, Z. Jia, and L. Wang, « Mechanical properties of sandwich composites with 3d-printed auxetic and non-auxetic lattice cores under low velocity impact », *Materials & Design*, vol. 160, pp. 1305–1321, 2018.

[109] A. Søe-Knudsen and S. Sorokin, « Modelling of linear wave propagation in spatial fluid filled pipe systems consisting of elastic curved and straight elements », *Journal of Sound and Vibration*, vol. 329, no. 24, pp. 5116–5146, Nov. 2010.

[110] A. Søe-Knudsen, « Design of stop-band filter by use of curved pipe segments and shape optimization », *Structural and Multidisciplinary Optimization*, vol. 44, no. 6, pp. 863–874, Dec. 2011.

[111] A. Søe-Knudsen, R. Darula, and S. Sorokin, « Theoretical and experimental analysis of the stop-band behavior of elastic springs with periodically discontinuous of curvature », *The Journal of the Acoustical Society of America*, vol. 132, no. 3, pp. 1378–1383, Sep. 2012.

[112] V. Romero-García, J. V. Sánchez-Pérez, S. Castiñeira-Ibáñez, and L. M. Garcia-Raffi, « Evidences of evanescent Bloch waves in Phononic Crystals », *Appl. Phys. Lett.*, vol. 96, p. 124 102, 2010.

[113] A. Cebrecos, V. Romero-García, and J. P. Groby, « Complex Dispersion Relation Recovery from 2D Periodic Resonant Systems of Finite Size », *Applied Sciences*, vol. 9, no. 3, 2019.

[114] C. Barbarosie and M. Neves, « Periodic structures for frequency filtering: analysis and optimization », *Computers & Structures*, vol. 82, no. 17-19, pp. 1399–1403, Jul. 2004.

[115] J. V. Sánchez-Pérez, C. Rubio, R. Martínez-Sala, R. Sánchez-Grandia, and V. Gómez, « Acoustic barriers based on periodic arrays of scatterers », *Appl. Phys. Lett.*, vol. 81, p. 5240, 2002.

[116] V. Romero-García, J. V. Sánchez-Pérez, and L. M. Garcia-Raffi, « Tunable wideband bandstop acoustic filter based on two-dimensional multiphysical phenomena periodic systems. », *Jour. Appl. Phys.*, p. 149 041, 2011.

[117] A. Colombi, P. Roux, S. Guenneau, P. Gueguen, and R. V. Craster, « Forests as a natural seismic metamaterial: Rayleigh wave bandgaps induced by local resonances », *Scientific Reports*, vol. 6, no. 1, p. 19 238, May 2016.

[118] A. Ahmed, « 3D-Printed Gradient-Index Phononic Crystal Lens for Underwater Acoustic Wave Focusing », p. 7, 2020.

[119] R. James, S. M. Woodley, C. M. Dyer, and V. F. Humphrey, « Sonic bands, bandgaps, and defect states in layered structures—Theory and experiment », *The Journal of the Acoustical Society of America*, vol. 97, no. 4, pp. 2041–2047, Apr. 1995.

[120] J. S. Whittier and J. C. Peck, « Experiments on Dispersive Pulse Propagation in Laminated Composites and Comparison With Theory », *Journal of Applied Mechanics*, vol. 36, no. 3, pp. 485–490, Sep. 1, 1969.

[121] J. O. Vasseur, P. A. Deymier, B. Djafari-Rouhani, Y. Pennec, and A.-C. Hladky-Hennion, « Absolute forbidden bands and waveguiding in two-dimensional phononic crystal plates », *Phys. Rev.B*, vol. 77, p. 085 415, 2008.

[122] A. Khelif, B. Aoubiza, S. Mohammadi, A. Adibi, and V. Laude, « Complete band gaps in two-dimensional phononic crystal slabs », *Phys. Rev. E*, vol. 74, no. 4, p. 046 610, Oct. 2006.

[123] M. S. Kushwaha, P. Halevi, G. Martínez, L. Dobrzynski, and B. Djafari-Rouhani, « Theory of acoustic band structure of periodic elastic composites », *Physical Review B*, vol. 49, no. 4, pp. 2313–2322, Jan. 15, 1994.

[124] J.-F. Robillard *et al.*, « Tunable magnetoelastic phononic crystals », *Applied Physics Letters*, vol. 95, no. 12, p. 124 104, 2009.

[125] O. R. Bilal and M. I. Hussein, « Ultrawide phononic band gap for combined in-plane and out-of-plane waves », *Physical Review E*, vol. 84, no. 6, Dec. 20, 2011.

[126] L. Shaogang *et al.*, « Research on the elastic wave band gaps of curved beam of phononic crystals », *Physica B: Condensed Matter*, vol. 457, pp. 82–91, Jan. 2015.

[127] J. O. Vasseur, P. A. Deymier, G. Frantziskonis, G. Hong, B. Djafari-Rouhani, and L. Dobrzynski, « Experimental evidence for the existence of absolute acoustic band gaps in two-dimensional periodic composite media », *Journal of Physics: Condensed Matter*, vol. 10, no. 27, pp. 6051–6064, Jul. 1998.

[128] H.-J. Zhao, H.-W. Guo, M.-X. Gao, R.-Q. Liu, and Z.-Q. Deng, « Vibration band gaps in double-vibrator pillared phononic crystal plate », *Journal of Applied Physics*, vol. 119, no. 1, p. 014 903, 2016.

[129] K. Billon *et al.*, « Design and experimental validation of a temperature-driven adaptive phononic crystal slab », *Smart Materials and Structures*, vol. 28, no. 3, p. 035 007, Feb. 2019.

[130] T. Delpero, S. Schoenwald, A. Zemp, and A. Bergamini, « Structural engineering of three-dimensional phononic crystals », *Journal of Sound and Vibration*, vol. 363, pp. 156–165, 2016.

[131] L. D'Alessandro, E. Belloni, R. Ardito, A. Corigliano, and F. Braghin, « Modeling and experimental verification of an ultra-wide bandgap in 3D phononic crystal », *Applied Physics Letters*, vol. 109, no. 22, p. 221 907, 2016.

[132] O. R. Bilal, D. Ballagi, and C. Daraio, « Architected Lattices for Simultaneous Broadband Attenuation of Airborne Sound and Mechanical Vibrations in All Directions », *Physical Review Applied*, vol. 10, no. 5, p. 054 060, Nov. 27, 2018.

[133] G. H. Koo and Y. S. Park, « Vibration analysis of a 3-dimensional piping system conveying fluid by wave approach », *International Journal of Pressure Vessels and Piping*, vol. 67, no. 3, pp. 249–256, 1996.

[134] M. Shen and W. Cao, « Acoustic band-gap engineering using finite-size layered structures of multiple periodicity », *Applied Physics Letters*, vol. 75, no. 23, pp. 3713–3715, Dec. 6, 1999.

[135] M. I. Hussein and M. A. El-Beltagy, « Optimization of phononic filters via genetic algorithms », *Journal of Physics: Conference Series*, vol. 92, p. 012 110, Dec. 1, 2007.

[136] D. E. Goldberg and J. H. Holland, « Genetic algorithms and machine learning », 1988.

[137] I.-L. Chang, Z.-X. Liang, H.-W. Kao, S.-H. Chang, and C.-Y. Yang, « The wave attenuation mechanism of the periodic local resonant metamaterial », *Journal of Sound and Vibration*, vol. 412, pp. 349–359, Jan. 2018.

[138] L. Liu and M. I. Hussein, « Wave Motion in Periodic Flexural Beams and Characterization of the Transition Between Bragg Scattering and Local Resonance », *Journal of Applied Mechanics*, vol. 79, no. 1, p. 011 003, 2012.

[139] L. Raghavan and A. S. Phani, « Local resonance bandgaps in periodic media: Theory and experiment », *The Journal of the Acoustical Society of America*, vol. 134, no. 3, pp. 1950–1959, Sep. 2013.

[140] Y. Xiao, B. R. Mace, J. Wen, and X. Wen, « Formation and coupling of band gaps in a locally resonant elastic system comprising a string with attached resonators », *Physics Letters A*, vol. 375, no. 12, pp. 1485–1491, Mar. 2011.

[141] H. Zhang, Y. Xiao, J. Wen, D. Yu, and X. Wen, « Flexural wave band gaps in metamaterial beams with membrane-type resonators: theory and experiment », *Journal of Physics D: Applied Physics*, vol. 48, no. 43, p. 435 305, Nov. 4, 2015.

[142] X. Wang and M. Y. Wang, « An analysis of flexural wave band gaps of locally resonant beams with continuum beam resonators », *Meccanica*, vol. 51, no. 1, pp. 171–178, Jan. 2016.

[143] Y. Xiao, J. Wen, G. Wang, and X. Wen, « Theoretical and Experimental Study of Locally Resonant and Bragg Band Gaps in Flexural Beams Carrying Periodic Arrays of Beam-Like Resonators », *Journal of Vibration and Acoustics*, vol. 135, no. 4, p. 041 006, Jun. 6, 2013.

[144] M. Y. Wang and X. Wang, « Frequency band structure of locally resonant periodic flexural beams suspended with force–moment resonators », *Journal of Physics D: Applied Physics*, vol. 46, no. 25, p. 255 502, Jun. 26, 2013.

[145] Z. Wang, P. Zhang, and Y. Zhang, « Locally Resonant Band Gaps in Flexural Vibrations of a Timoshenko Beam with Periodically Attached Multioscillators », *Mathematical Problems in Engineering*, vol. 2013, pp. 1–10, 2013.

[146] T. Wang, M.-P. Sheng, and Q.-H. Qin, « Multi-flexural band gaps in an Euler–Bernoulli beam with lateral local resonators », *Physics Letters A*, vol. 380, no. 4, pp. 525–529, Feb. 2016.

[147] X. Wang and C. Hopkins, « Bending, longitudinal and torsional wave transmission on Euler-Bernoulli and Timoshenko beams with high propagation losses », *J. Acoust. Soc. Am.*, p. 22, 2016.

[148] Y. Xiao, J. Wen, and X. Wen, « Longitudinal wave band gaps in metamaterial-based elastic rods containing multi-degree-of-freedom resonators », *New Journal of Physics*, vol. 14, no. 3, p. 033 042, Mar. 30, 2012.

[149] K. Wang, J. Zhou, D. Xu, and H. Ouyang, « Tunable low-frequency torsional-wave band gaps in a meta-shaft », *Journal of Physics D: Applied Physics*, vol. 52, no. 5, p. 055 104, Jan. 30, 2019.

[150] Y. Xiao, J. Wen, and X. Wen, « Flexural wave band gaps in locally resonant thin plates with periodically attached spring–mass resonators », *Journal of Physics D: Applied Physics*, vol. 45, no. 19, p. 195 401, May 16, 2012.

[151] J. Jensen, « Phononic band gaps and vibrations in one- and two-dimensional mass–spring structures », *Journal of Sound and Vibration*, vol. 266, no. 5, pp. 1053–1078, Oct. 2003.

[152] A. Khelif, Y. Achaoui, S. Benchabane, V. Laude, and B. Aoubiza, « Locally resonant surface acoustic wave band gaps in a two-dimensional phononic crystal of pillars on a surface », *Physical Review B*, vol. 81, no. 21, p. 214 303, Jun. 10, 2010.

[153] M. Oudich, M. B. Assouar, and Z. Hou, « Propagation of acoustic waves and waveguiding in a two-dimensional locally resonant phononic crystal plate », *Applied Physics Letters*, vol. 97, no. 19, p. 193 503, Nov. 8, 2010.

[154] C. Yang and L. Cheng, « Suppression of bending waves in a beam using resonators with different separation lengths », *The Journal of the Acoustical Society of America*, vol. 139, no. 5, pp. 2361–2371, May 2016.

[155] A. Casalotti, S. El-Borgi, and W. Lacarbonara, « Metamaterial beam with embedded nonlinear vibration absorbers », *International Journal of Non-Linear Mechanics*, vol. 98, pp. 32–42, Jan. 2018.

[156] L. Van Belle, C. Claeys, E. Deckers, and W. Desmet, « The impact of damping on the sound transmission loss of locally resonant metamaterial plates », *Journal of Sound and Vibration*, vol. 461, p. 114 909, Nov. 2019.

[157] A. Nateghi, L. Sangiuliano, C. Claeys, E. Deckers, B. Pluymers, and W. Desmet, « Design and experimental validation of a metamaterial solution for improved noise and vibration behavior of pipes », *Journal of Sound and Vibration*, vol. 455, pp. 96–117, Sep. 2019.

[158] C. Claeys, N. G. Rocha de Melo Filho, L. Van Belle, E. Deckers, and W. Desmet, « Design and validation of metamaterials for multiple structural stop bands in waveguides », *Extreme Mechanics Letters*, vol. 12, pp. 7–22, Apr. 2017.

[159] Y. Liu, D. Yu, L. Li, H. Zhao, J. Wen, and X. Wen, « Design guidelines for flexural wave attenuation of slender beams with local resonators », *Physics Letters A*, vol. 362, no. 5-6, pp. 344–347, Mar. 2007.

[160] Y. Xiao, J. Wen, D. Yu, and X. Wen, « Flexural wave propagation in beams with periodically attached vibration absorbers: Band-gap behavior and band formation mechanisms », *Journal of Sound and Vibration*, vol. 332, no. 4, pp. 867–893, Feb. 2013.

[161] Z. Liu, « Locally Resonant Sonic Materials », *Science*, vol. 289, no. 5485, pp. 1734–1736, Sep. 8, 2000.

[162] Z. Liu, H.-W. Dong, and G.-L. Yu, « Topology optimization of periodic barriers for surface waves », *Structural and Multidisciplinary Optimization*, Aug. 26, 2020.

[163] G. Teyssèdre and C. Lacabanne, « Caractérisation des polymères par analyse thermique », p. 14, 1996.

[164] A. Banerjee, « Influence of the torsional vibration of the periodically attached perpendicular beam resonator on the flexural band of a Euler-Bernoulli beam », *Physics Letters A*, vol. 384, no. 29, p. 126 757, Oct. 2020.

[165] L. Fan, Y. He, X. Chen, and X. Zhao, « Elastic metamaterial shaft with a stack-like resonator for low-frequency vibration isolation », *Journal of Physics D: Applied Physics*, vol. 53, no. 10, p. 105 101, Mar. 6, 2020.

[166] J. Plisson, A. Pelat, F. Gautier, V. Romero-Garcia, and T. Bourdon, « Design of a Multiwaves Vibration Filtering », presented at the 11th International Styrian Noise, Vibration & Harshness Congress: The European Automotive Noise Conference, Sep. 30, 2020, pp. 2020-01–1560.

[167] D. E. Muller, « A Method for Solving Algebraic Equations Using an Automatic Computer », *Mathematics of Computation*, vol. 10, pp. 208–215, 1956.

[168] S. P. Timoshenko, « On the transverse vibrations of bars of uniform cross-section », *Philos. Mag.*, vol. 43, pp. 125–131, 1922.

[169] J. R. Hutchinson, « Shear Coefficients for Timoshenko Beam Theory », *Journal of Applied Mechanics*, vol. 68, no. 1, p. 87, 2001.

[170] S. P. Timoshenko, « On the Correction for Shear of the Differential Equation for Transverse Vibrations of Bars of Prismatic Bars, » *Philos. Mag*, vol. 41, pp. 744–746. 1921.

[171] M. Xiao, G. Ma, Z. Yang, P. Sheng, Z. Q. Zhang, and C. T. Chan, « Geometric phase and band inversion in periodic acoustic systems », *Nature Physics*, vol. 11, no. 3, pp. 240–244, Mar. 2015.

[172] J. C. Lagarias, J. A. Reeds, M. H. Wright, and P. E. Wright, « Convergence Properties of the Nelder–Mead Simplex Method in Low Dimensions », *SIAM Journal on Optimization*, vol. 9, no. 1, pp. 112–147, Jan. 1998.

[173] M.-J. Garcia, « Engineering rubber bushing stiffness formulas including dynamic amplitude dependence », p. 33,

Chap. A

Appendix : Published Article

Applied Physics Letters ARTICLE scitation.org/journal/apl

Experimental evidence of absolute bandgaps in phononic crystal pipes

Cite as: Appl. Phys. Lett. **116**, 201902 (2020); doi: 10.1063/5.0007532
Submitted: 13 March 2020 · Accepted: 11 May 2020 ·
Published Online: 19 May 2020

Jules Plisson,[1,a)] Adrien Pelat,[1] François Gautier,[1] Vicente Romero Garcia,[1] and Thierry Bourdon[2]

AFFILIATIONS

[1]Laboratoire d'Acoustique de l'Université du Mans, CNRS, Av. O. Messaien, 72085 Le Mans, France
[2]Vitesco Technologies France SAS, 44 Av. du General de Croutte, 31036 Toulouse, France

[a)]**Present address:** Vitesco Technologies France SAS. **Author to whom correspondence should be addressed:** jules.plisson.etu@univ-lemans.fr

ABSTRACT

The vibration filtering properties of a phononic crystal pipe whose unit cell consists of two segments of different materials and cross sections are studied numerically and experimentally. Such an architected bi-material pipe leads to the alignment of the dispersion branches in the same frequency ranges for all types of waves (flexural, longitudinal, and torsional), leading to an absolute bandgap. Each motion is studied by a 1D model in which the propagation of Floquet–Bloch waves in lossy media is considered. Numerical optimization is based on the simplex algorithm and aims to control both the central frequency and the bandwidth of the absolute bandgap on a selected target. Experimental characterization of a demonstrator confirms the filtering effects due to partial and absolute bandgaps even in the presence of quite high structural damping.

The mitigation of noise pollution is a major societal challenge for which extensive research has been conducted[1] and NVH (Noise, Vibration, and Harshness) departments have been widely integrated notably in the transportation industry. Structure-borne sound results from bending vibrations and their couplings with other types of waves, due to the complex geometries classically encountered in industrial systems.[2] An effective reduction in the radiated sound levels then requires us to mitigate all types of waves. In this context, the approach presented here concerns the design of "total filters" that can be inserted into engine components acting as structural waveguides that transmit vibrations to other components able to radiate sound. To reach such total filter features, the design strategy is based on the concept of absolute bandgap.

The control of elastic waves by periodic structures has been dramatically developed during the last few decades by using Phononic Crystals (PCs)[3,4] as analogously done for light waves by Photonic crystals.[5] These systems, made of either periodic distributions of scatterers embedded in a physically dissimilar host material or simply periodic geometries, are driven by a particular dispersion relation showing bandgaps,[6,7] ranges of frequencies produced by the Bragg interference in which the propagation of waves is forbidden.[8] Significant progress has been made on the control of flexural or longitudinal waves by PCs showing different applications including filtering,[9,10] wave trapping,[11,12] wave-guiding,[13] focusing by refracting[14,15] or scattering[16] waves, and self-collimation,[17,18] among others.[4] One of the main challenges of PCs has been the design of absolute bandgaps over which the propagation of all elastic waves is forbidden, whatever their polarization and wave vector.

PCs with a fluid-type host medium, known as sonic crystals,[9] have theoretically and experimentally reported absolute bandgaps in broad ranges of frequencies.[10,19,20] These systems represent the most simple PC as only longitudinal waves are propagating in the medium. Perhaps the most known application of sonic crystals is the design of tunable sound screens.[21–23] However, once the host medium is a solid, the problem becomes more complex as different polarisation can be excited in the system. In this case, theoretical evidence of absolute bandgaps is also widely reported in the literature. 1D PCs exhibiting absolute bandgaps have been analyzed by the transfer matrix method,[24] and recently, 1D PCs with alternating materials in the radial and axial directions have been used to show absolute bandgaps.[25] Two-dimensional (2D) PC slabs consisting of either solid[26] or piezoelectric[27] inclusions placed periodically in an isotropic host material have been theoretically analyzed, showing absolute bandgaps with a variable bandwidth for elastic waves of any polarization and incidence. Bulk 2D PCs have also been proposed for bulk wave attenuation with solid[28] or magnetostrictive[29] inclusions. Using specialized genetic algorithms, 2D PCs formed from silicon and solid voids have been optimized to obtain unit cell designs exhibiting absolute bandgaps for both in- and out-of-plane motions.[30]

From the experimental point of view, absolute bandgaps have also been reported in the literature. 2D binary solid/solid composite media with cylindrical inclusions embedded in an epoxy resin matrix showed dips of transmission, evidencing the presence of absolute bandgaps.[31] More recently, the presence of absolute bandgaps in pillared PC slabs has been shown by double-vibrator three-components[32] and temperature-driven adaptive systems.[33] 3D PCs made of face-centered cubic unit cells composed of a single material have been used to experimentally show ultra-wide absolute bandgaps.[34,35] Recently, 3D load-bearing architected lattices, composed of a single material, have been designed for presenting broadband frequency bandgaps for all directions and polarizations for airborne sound and elastic vibrations simultaneously.[36] However, although 2D and 3D PCs have been widely validated experimentally, less attention has been paid to the experimental analysis of 1D cases acting simultaneously on longitudinal, flexural, and torsional waves. The control of vibrations in such 1D PC systems can impact the design of piping systems, which can be exploited in areas such as the automotive industry, heat exchanger tubes in chemical plants, oil pipelines, marine risers, and pump discharge lines, among others.[37]

In this work, we apply the concept of absolute bandgap in order to design and experimentally validate 1D PC pipes able to mitigate longitudinal, flexural, and torsional waves in the same target band. A 1D PC pipe made of a unit cell consisting of two different hollow cylinders made of aluminum and nylon (see Fig. 1) is optimized. Considering lossy constitutive materials, the eigenvalue problems of the three types of waves are analytically solved by imposing continuity conditions between the different parts of the unit cell and Floquet–Bloch periodic conditions at its extremities. The three problems are combined via a minimizing algorithm in order to reach the geometry of the 1D PC pipe that exhibits an absolute bandgap of target central frequency and bandwidth. Full 3D finite element simulations and experimental characterization of a demonstrator of finite size are in good agreement and show dips in the transfer functions associated with the predicted absolute bandgap.

Figures 1(a)–1(d) show the images of the 1D bi-material PC pipe used in the experiments. A detailed scheme with the geometrical parameters of the system is shown in Figs. 1(e) and 1(f). Each segment of the unit cell is assumed to be a thin-walled pipe of annular cross section. We define $\gamma = l_2/l_{tot}$ as the length ratio and $\beta = R_2/R_1$ as the outer radius ratio. The inner radius R_{int} is constant for the two segments of the unit cell. These two geometrical parameters will be used to describe the geometry in the optimization procedure. The 1D PC pipe is made of aluminum and nylon, considered as linear and isotropic elastic materials. Nylon is characterized by its Young modulus $E_N = 2.3$ GPa, its density $\rho_N = 1240$ kg/m^3, and its Poisson ratio $\nu_N = 0.3$. The aluminum characteristics are $E_A = 71$ GPa, $\rho_A = 2170$ kg/m^3, and $\nu_A = 0.3$.

Here, we consider harmonic wave motion with the time convention $e^{\imath\omega t}$. In what follows, the subindex $i = N, A$ and the superindex $w = l, t$ will represent each segment of the unit cell and the wave type (longitudinal, l, or torsional, t), respectively. On the one hand, the propagation of longitudinal and torsional waves in the i-th part of the unit cell is modeled by a 1D Helmholtz equation,[38]

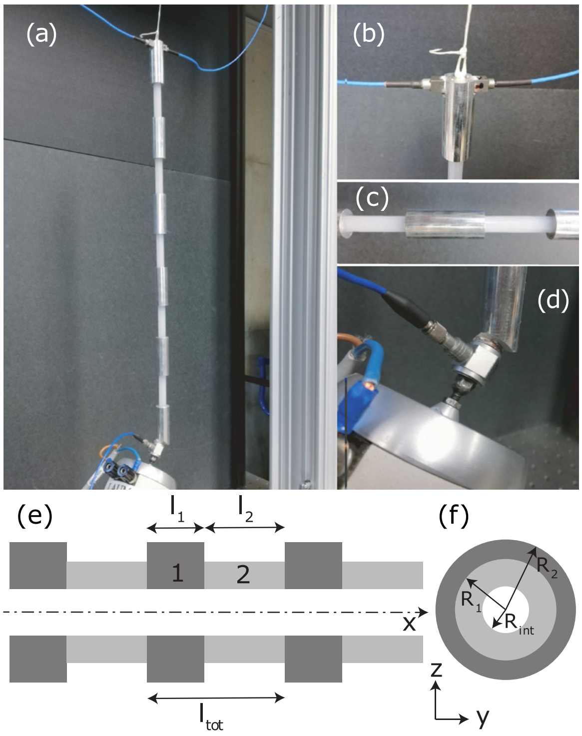

FIG. 1. Scheme and images of the manufactured PC pipe. Nylon and aluminum sections are nested by force fitting, which holds the assembly together without the use of glue and, therefore, minimizes unwanted losses. (a) Experimental setup; (b) details of the 2 face-to-face three-axis accelerometers; (c) view of the 2 aluminum/nylon unit cells of the demonstrator; (d) view of the shaker excitation implemented at the oblique position such that all wave types are excited. (e) and (f) show lateral and cross-sectional schematic representation of the modeled PC pipe, respectively.

$$\frac{\partial^2 u_i^w}{\partial x^2} + (k_i^w)^2 u_i^w = 0, \tag{1}$$

where u_i^w is the displacement of wave w of the i-th segment of the unit cell. $k_i^w = \frac{\omega}{c_i^w}$ is the wave number, with $c_i^w = \sqrt{E_i^w/\rho_i}$ being the speed of the wave; $E_i^l = E_i$ is the Young modulus, and $E_i^t \equiv G_i = E_i/2(1+\nu_i)$ is the shear modulus.

On the other hand, flexural waves are described using Timoshenko's beam theory[39,40] that takes into account shear deformation and rotational inertia effects. Even this framework is based on low frequency assumptions; this makes it possible to analyze the propagation at higher frequencies or for thicker beams than with Euler–Bernoulli's theory. Following Timoshenko assumption, the flexural displacement v_i satisfies the motion equation,

$$\frac{E_i}{\rho_i}\frac{\partial^4 v_i}{\partial x^4} + \omega^2\left(1 + \frac{E_i}{\kappa_i G_i}\right)\frac{\partial^2 v_i}{\partial x^2} + \left(\frac{S_i\omega^2}{I_i} - \frac{\rho_i I_i \omega^4}{\kappa_i G_i}\right)v_i = 0, \tag{2}$$

where κ_i, S_i, and I_i are the shear coefficient, the cross-sectional area, and quadratic moment, respectively. In order to obtain the eigenvalue problem whose solutions give the complex dispersion relation, $k_b = k(\omega)l_{tot}/\pi$, we apply the continuity boundary conditions at the interfaces between each segment of the unit cell as well as the

Floquet–Bloch periodic conditions at its extremities (see the supplementary material for more details). The resulting set of equations leads to a linear system $M(\omega, k_b).\mathbf{B} = \mathbf{0}$, where for each given ω of a frequency range of interest, the values of k_b satisfying $\det(\mathrm{M}) = 0$ are found numerically to provide the dispersion relation. By solving each 1D model in this way, we obtain the dispersion relations for all types of waves in the PC pipe. Solutions obtained by the previous semi-analytical methodology are compared with reference solutions provided by 3D elasticity finite element simulations (solid mechanics COMSOL package).

Figure 2(a) shows the real part of the dispersion relation for a PC pipe with the following geometry: $l_{tot} = 0.1$ m, $\gamma = 0.2$, $R_1 = 8$ mm, and $\beta = 0.5$. Colored dots (each color a wave type) represent the results obtained from the semi-analytical model, while gray circles represent the FEM reference solutions. The results are in very good agreement, and so the semi-analytical modeling is well validated. However, some disagreements appear for flexural waves at high frequencies (dispersion branch just under 20 kHz) due to the expected limitations of Timoshenko's beam model. Anyway, the dispersion relation obtained for this geometrical layout exhibits a wide absolute bandgap in the range of [3–10] kHz.

Figure 2(b) shows the evolution of the bandgaps as β changes. Each colored patch in the plot encloses the frequencies between the lower and the upper edge of the bandgap. The results indicate that β essentially controls the bandgap bandwidth and has a relatively weak effect on their central frequencies. Such tendency has already been observed in the case of monolithic corrugated beams.[41]

Analogously, Fig. 2(b) shows the evolution of the bandgaps as γ changes. Both the central frequency and the width display nonmonotonous variations of the same range. In particular, some optimal band widths appear around $\gamma = 0.2$. Finally, γ has a more complex effect on the bandgap features that do not follow any clearly identifiable law. Anyway, there are some configurations for which all bandgaps overlap, creating an absolute bandgap. This feature is obtained in the range of $[4 - 10]$ kHz for $\gamma = 0.2$, for example. In this case, the second flexural bandgap and the first longitudinal and torsional bandgaps are involved. However, Figs. 2(b) and 2(c) show that it is difficult to tune by hand the absolute bandgap to a target band. In order to achieve this goal, a numerical optimization procedure is proposed below.

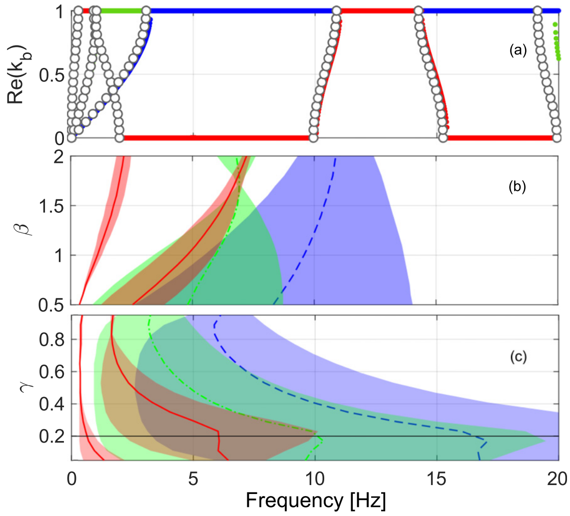

FIG. 2. Analysis of the dispersion relation of a bi-material PC pipe with $l_{tot} = 0.1$ m; (a) Real part of the dispersion relation with $\gamma = 0.2$, $R_1 = 8$ mm, and $\beta = 0.5$ calculated by both the semi-analytical model (colored dots, (blue) longitudinal, (red) flexural, and (green) torsional) and 3D full FEM simulation (open circles °); (b) and (c) evolution of the bandgap widths (colored patches) and mid frequencies (lines) for the three wave types [the same color legend as in (a)] as a function of (b) β with $\gamma = 0.5$ and (c) γ with $\beta = 0.5$. $l_{tot} = 0.1$ m. The horizontal black line denotes the configuration leading to the dispersion graph in (a).

A Nelder–Mead local minimisation algorithm[42] is used in this work to provide the geometrical parameters of a PC pipe with an absolute bandgap defined from both a target central frequency f_0 and a target bandwidth Δf_0. The set of parameters subject to the optimization is defined as $X = [l_{tot}, \gamma, R_1, \beta]$. It is worth noting here that the first unit cell segment will be made of aluminum and the second one of nylon. The cost function $\mathscr{F}$ is defined as a weighted sum of two convergence indicators and reads

$$\mathscr{F} = \alpha_{f_c} I_{fc} + \alpha_{\Delta f} I_{\Delta f}. \tag{3}$$

The weighting coefficients α_{f_c} and $\alpha_{\Delta f}$ are adjustable such that $\alpha_{f_c} + \alpha_{\Delta f} = 1$, and the convergence indicators are defined by

$$I_{\Delta f} = \left| 1 - \frac{\Delta f - \Delta f_0}{\Delta f + \Delta f_0} \right|, \tag{4}$$

$$I_{fc} = \left| 1 - \frac{f_c - f_0}{f_c + f_0} \right|, \tag{5}$$

with $\Delta f = \min\,(f^{(i)}_{max}) - \max\,(f^{(i)}_{min})$ being the absolute bandwidth and $f_c = \frac{1}{2}[\max(f^{(i)}_{min}) + \min(f^{(i)}_{max})]$ the central frequency. $f^{(i)}_{max,min}$ represents the upper (index *max*) and lower (index *min*) edges of the bandgap for the i-th wave, where the subindex i represents each type of wave type $i = F, L, T$ for flexural, longitudinal, and torsional waves, respectively. I_{f_c} and $I_{\Delta f}$ evaluate the deviation between the bandgap features f_c and Δf and the target features f_0 and Δf_0, respectively. These definitions are chosen so that the cost function is unitary $(0 < \mathscr{F} < 1)$.

This optimization procedure is applied to the solution of the semi-analytical eigenvalue problems described above with a target absolute bandgap of [3–6] kHz, which is a typical range of interest for injection applications in the context of automotive industry.[43] A detailed study of the optimization is given in the supplementary material and concludes that to ensure both accuracy and fast convergence, the best choice for the weighting coefficient of the cost function is $[\alpha_{f_c}, \alpha_{\Delta f}] = [5/6, 1/6]$. The optimal geometry of the 1D PC pipe obtained under these conditions and without considering material losses is $X = [87\,\mathrm{mm}, 0.44, 7.5\,\mathrm{mm}, 0.5]$. From the optimized geometry in the conservative case, the final complex dispersion relation of the PC pipe shown in Fig. 3(a) is calculated considering the viscoelastic losses for both aluminum and nylon via the complex Young modulus $E_i^c = E_i(1 + \imath\eta_i)$, with $\eta_A = 1 \times 10^{-4}$ and $\eta_N = 4 \times 10^{-2}$. Each wave type displays bandgaps where the real part of the wavenumber is low, while imaginary part is high [see the colored patches in Fig. 3(b)]. In the target range of frequencies, bandgaps are well overlapping, and the obtained absolute bandgap is [3.2–5.7] kHz [gray patch in Fig. 3(a)], which is slightly narrower than the target, due to the losses.

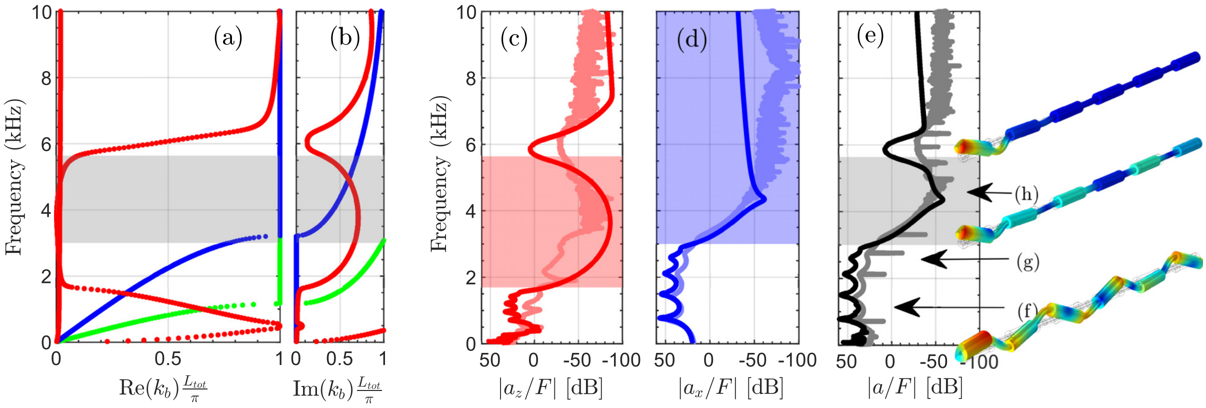

FIG. 3. Numerical analysis and experimental characterisation of the optimal PC pipe: (a) real part and (b) imaginary part of the optimized complex dispersion relation obtained by the Floquet–Bloch method and considering the viscoelastic losses (see the main text). (blue) Longitudinal, (red) flexural, and (green) torsional; measured (light line) and simulated (dark line) acceleration transfer functions in the (c) flexural, (d) longitudinal, and (e) full loading cases; 3D views of the simulated total displacement in the full loading case at (f) 900 Hz where all wave types propagate, (g) 2500 Hz where only the flexural bandgap is opened, and (h) 4500 Hz within the absolute bandgap.

In order to experimentally evaluate the vibration mitigation performances due to the absolute bandgap of the infinite PC pipe, a finite pipe demonstrator with 6 unit cells is manufactured [Fig. 1(a)]. In the experimental setup, the demonstrator is suspended vertically from rigid gallows mounted on an optical breadboard. A shaker (LDS V201) excites the demonstrator at its bottom end with a harmonic point force $\boldsymbol{F} = F_x.\boldsymbol{x} + F_y.\boldsymbol{y} + F_z.\boldsymbol{z}$ [see the axis definition in Figs. 1(e) and 1(f)] with a step-by-step sine in the range of [0–10] kHz with a frequency step of 5 Hz. 3 cases are considered: “flexural loading” such as $F_z \neq 0$ and $F_x = F_y = 0$ (when the shaker is perpendicular to the pipe x-axis, only flexural waves are excited), “longitudinal loading” such as $F_x \neq 0$ and $F_y = F_z = 0$ (when the shaker is aligned with the pipe x-axis, only longitudinal waves are excited), and “full loading” such as $F_{x,y,z} \neq 0$ as shown in Fig. 1(d) where the force of the shaker is applied obliquely on a cut plane and off-centre with respect to the pipe x-axis so that all wave types are generated. The acceleration response $\boldsymbol{a} = a_x.\boldsymbol{x} + a_y.\boldsymbol{y} + a_z.\boldsymbol{z}$ is measured at the upper end using 2 three-axial accelerometers (PCB 356A01) that face each other [Fig. 1(b)]. This experimental situation is also numerically simulated from a full wave 3D FEM model in order to compare transfer functions.

Figure 3(c) represents both numerical and experimental transfer functions $|a_z/F|$ in the flexural loading case. The transfer functions show an attenuation of about 70 dB in the frequency range corresponding to the predicted flexural bandgap. The same trend is exhibited in Fig. 3(d) that plots the transfer functions $|a_x/F|$ in the longitudinal loading case. Finally, the full loading case is shown in Fig. 3(e), evidencing a strong attenuation in the transfer function $|a/F|$ in the range corresponding to the predicted absolute bandgap. It is also worth noting that finite size effects can be seen at low frequencies with peaks of the transfer function corresponding to the Fabry–Pérot resonances of the system.

To complete the analysis, 3D views of the simulated total displacement field in the full loading case are shown in Figs. 3(f)–3(h). At 900 Hz where all wave types propagate [Fig. 3(f)], the superposition of all motions results in a complex total displacement field. At 2.5 kHz [Fig. 3(g)], the field mainly exhibits the longitudinal component, with the flexural component being strongly attenuated due to the bandgap effect. At 4.5 kHz [Fig. 3(h)], the total field vanishes close to the excitation due to the total filtering effect associated with the absolute bandgap.

To summarize, we apply the concept of absolute bandgap to a bi-material PC pipe. Three 1D analytical Floquet–Bloch models giving the dispersion of longitudinal, flexural, and torsional waves considering losses are combined in an optimization procedure to reach a unit cell design that exhibit absolute bandgaps with target features. The hand ability and reliability of such design methodology are shown through a set of cases detailed in the supplementary material, which brings a first main insight. On the top of that, the study of a 6-cell demonstrator shows both numerically and experimentally dips of the transfer functions corresponding to the absolute bandgap analytically predicted, bringing a second main insight. These results illustrate how absolute bandgaps in the high frequency domain can be applied to mitigate vibrations that may result in structure-borne sound in some industrial systems. In further works, the design and optimization of such PC pipes would be extended considering an enclosed pressurized liquid, hence considering couplings between acoustic and elastic waves.

See the supplementary material for both the analytical wave dispersion models and the numerical optimization procedure and its application to a set of optimization cases.

The authors thank the Vitesco Technologies company and ANRT French agency who funded this research, Julien Nicolas and Stanislas Renard who manufactured the demonstrator, and Félix Foucard for his fruitful contribution in the experiments.

DATA AVAILABILITY

The data that support the findings of this study are available from the corresponding author upon reasonable request.

REFERENCES

[1] M. Crocker, *Handbook of Noise and Vibration Control*, 3rd ed. (John Wiley & Sons, New Jersey, 2007).

[2] L. Cremer, M. Heckl, and B. A. T. Petersson, *Structure-Borne Sound: Structural Vibrations and Sound Radiation at Audio Frequencies*, 3rd ed. (Springer, Berlin; New York, 2005).
[3] *Acoustic Metamaterials and Phononic Crystals*, edited by P. Deymier (Springer, 2013).
[4] *Fundamentals and Applications of Acoustic Metamaterials: From Seismic to Radio Frequency*, edited by V. Romero-García and A.-C. Hladky-Hennion (Wiley-ISTE, 2019).
[5] J. D. Joannopoulus, S. G. Johnson, J. N. Winn, and R. D. Meade, *Photonic Crystals. Molding the Flow of Light* (Princeton University Press, 2008).
[6] E. Economou and M. Sigalas, "Classical wave propagation in periodic structures: Cermet versus network topology," Phys. Rev. B **48**(18), 13434 (1993).
[7] M. Kushwaha, P. Halevi, L. Dobrzynski, and B. Djafari-Rouhani, "Acoustic band structure of periodic elastic composites," Phys. Rev. Lett. **71**, 2022–2025 (1993).
[8] L. Brillouin and M. Parodi, *Propagation Des Ondes Dans Les Milieux Périodiques* (Masson et Cie, 1956).
[9] R. Martínez-Sala, J. Sancho, J. V. Sánchez, V. Gómez, J. Llinares, and F. Meseguer, "Sound attenuation by sculpture," Nature **378**, 241 (1995).
[10] J. V. Sánchez-Pérez, D. Caballero, R. Martínez-Sala, C. Rubio, J. Sánchez-Dehesa, F. Meseguer, J. Llinares, and F. Gálvez, "Sound attenuation by a two-dimensional array of rigid cylinders," Phys. Rev. Lett. **80**, 5325–5328 (1998).
[11] M. Sigalas and E. Economou, "Elastic and acoustic wave band structure," J. Sound Vib. **158**, 377 (1992).
[12] A. Khelif, A. Choujaa, B. Djafari-Rouhani, M. Wilm, S. Ballandras, and V. Laude, "Trapping and guiding of acoustic waves by defect modes in a full-band-gap ultrasonic crystal," Phys. Rev. B **68**, 214301 (2003).
[13] A. Khelif, M. Wilm, V. Laude, S. Ballandras, and B. Djafari-Rouhani, "Guided elastic waves along a rod defect of a two-dimensional phononic crystal," Phys. Rev. E **69**, 067601 (2004).
[14] F. Cervera, L. Sanchis, J. V. Sánchez-Pérez, R. Martínez-Sala, C. Rubio, and F. Meseguer, "Refractive acoustic devices for airborne sound," Phys. Rev Lett. **88**, 023902–023904 (2002).
[15] S.-C. Lin, T. Huang, J.-H. Sun, and T.-T. Wu, "Gradient-index phononic crystals," Phys. Rev. B **79**, 094302 (2009).
[16] L. Feng, X. Liu, Y. Chen, Z. Huang, Y. Mao, Y. Chen, J. Zi, and Y. Zhu, "Negative refraction of acoustic waves in two-dimensional sonic crystals," Phys. Rev. B **72**, 033108 (2005).
[17] I. Pérez-Arjona, V. J. Sánchez-Morcillo, J. Redondo, V. Espinosa, and K. Staliunas, "Theoretical prediction of the nondiffractive propagation of sonic waves through periodic acoustic media," Phys. Rev. B **75**, 014304 (2007).
[18] A. Cebrecos, V. Romero-García, R. Picó, I. Pérez-Arjona, V. Espinosa, V. J. Sánchez-Morcillo, and K. Staliunas, "Formation of collimated sound beams by three-dimensional sonic crystals," J. Appl. Phys. **111**, 104910 (2012).
[19] V. Romero-García, J. Sánchez-Pérez, S. C. neira Ibáñez, and L. Garcia-Raffi, "Evidences of evanescent bloch waves in phononic crystals," Appl. Phys. Lett. **96**, 124102 (2010).
[20] A. Cebrecos, V. Romero-García, and J. P. Groby, "Complex dispersion relation recovery from 2D periodic resonant systems of finite size," Appl. Sci. **9**, 478 (2019).
[21] J. Sánchez-Pérez, C. Rubio, R. Martínez-Sala, R. Sánchez-Grandia, and V. Gómez, "Acoustic barriers based on periodic arrays of scatterers," Appl. Phys. Lett. **81**, 5240 (2002).
[22] V. Romero-García, J. V. Sánchez-Pérez, and L. M. Garcia-Raffi, "Tunable wideband bandstop acoustic filter based on two-dimensional multiphysical phenomena periodic systems," J. Appl. Phys. **110**, 14904 (2011).
[23] T. Cavalieri, A. Cebrecos, J.-P. Groby, C. Chaufour, and V. Romero-García, "Three-dimensional multiresonant lossy sonic crystal for broadband acoustic attenuation: Application to train noise reduction," Appl. Acoust. **146**, 1–8 (2019).
[24] H. Shen, J. Wen, D. Yu, and X. Wen, "The vibrational properties of a periodic composite pipe in 3d space," J. Sound Vib. **328**, 57–70 (2009).
[25] Y. Zhang, D. Yu, and J. Wen, "Study on the band gaps of phononic crystal pipes with alternating materials in the radial and axial directions," Extreme Mech. Lett. **12**, 2–6 (2017).
[26] J. O. Vasseur, P. A. Deymier, B. Djafari-Rouhani, Y. Pennec, and A.-C. Hladky-Hennion, "Absolute forbidden bands and waveguiding in two-dimensional phononic crystal plates," Phys. Rev.B **77**, 085415 (2008).
[27] A. Khelif, B. Aoubiza, S. Mohammadi, A. Adibi, and V. Laude, "Complete band gaps in two-dimensional phononic crystal slabs," Phys. Rev. E **74**, 046610 (2006).
[28] M. S. Kushwaha, P. Halevi, G. Martínez, L. Dobrzynski, and B. Djafari-Rouhani, "Theory of acoustic band structure of periodic elastic composites," Phys. Rev. B **49**(4), 2313–2322 (1994).
[29] J.-F. Robillard, O. B. Matar, J. O. Vasseur, P. A. Deymier, M. Stippinger, A.-C. Hladky-Hennion, Y. Pennec, and B. Djafari-Rouhani, "Tunable magnetoelastic phononic crystals," Appl. Phys. Lett. **95**, 124104 (2009).
[30] O. R. Bilal and M. I. Hussein, "Ultrawide phononic band gap for combined in-plane and out-of-plane waves," Phys. Rev. E **84**, 065701 (2011).
[31] J. O. Vasseur, P. A. Deymier, G. Frantziskonis, G. Hong, B. Djafari-Rouhani, and L. Dobrzynski, "Experimental evidence for the existence of absolute acoustic band gaps in two-dimensional periodic composite media," J. Phys.: Condens. Matter **10**, 6051–6064 (1998).
[32] H.-J. Zhao, H.-W. Guo, M.-X. Gao, R.-Q. Liu, and Z.-Q. Deng, "Vibration band gaps in double-vibrator pillared phononic crystal plate," J. Appl. Phys. **119**, 014903 (2016).
[33] K. Billon, M. Ouisse, E. Sadoulet-Reboul, M. Collet, P. Butaud, G. Chevallier, and A. Khelif, "Design and experimental validation of a temperature-driven adaptive phononic crystal slab," Smart Mater. Struct. **28**, 035007 (2019).
[34] T. Delpero, S. Schoenwald, A. Zemp, and A. Bergamini, "Structural engineering of three-dimensional phononic crystals," J. Sound Vib. **363**, 156–165 (2016).
[35] L. D'Alessandro, E. Belloni, R. Ardito, A. Corigliano, and F. Braghin, "Modeling and experimental verification of an ultra-wide bandgap in 3D phononic crystal," Appl. Phys. Lett. **109**, 221907 (2016).
[36] O. R. Bilal, D. Ballagi, and C. Daraio, "Architected lattices for simultaneous broadband attenuation of airborne sound and mechanical vibrations in all directions," Phys. Rev. Appl. **10**, 054060 (2018).
[37] G. Koo and Y. Park, "Vibration analysis of a 3-dimensional piping system conveying fluid by wave approach," Int. J. Pressure Vessels Piping **67**, 249–256 (1996).
[38] K. F. Graff, *Wave Motion in Elastic Solids* (Dover Publications, 1975).
[39] L. Liu and M. I. Hussein, "Wave motion in periodic flexural beams and characterization of the transition between Bragg scattering and local resonance," J. Appl. Mech. **79**, 011003 (2012).
[40] A. Hvatov and S. Sorokin, "Free vibrations of finite periodic structures in pass- and stop-bands of the counterpart infinite waveguides," J. Sound Vib. **347**, 200–217 (2015).
[41] A. Pelat, T. Gallot, and F. Gautier, "On the control of the first bragg band gap in periodic continuously corrugated beam for flexural vibration," J. Sound Vib. **446**, 249–262 (2019).
[42] J. C. Lagarias, J. A. Reeds, M. H. Wright, and P. E. Wright, "Convergence properties of the Nelder–Mead simplex method in low dimensions," SIAM J. Optim. **9**, 112–147 (1998).
[43] T. Bourdon, R. Weber, and J. Massinger, "Virtual nvh prototyping of fuel components design—Focus on high pressure pumps and SCR injectors," in *SAE Technical Paper* (SAE International, 2017).

Chap. B

1D Model of periodic waveguide with locally resonant structures

B.1 Floquet Bloch model for longitudinal and torsional waves dispersion

The model shown in Chap. 2 is valid for a cell composed of two segments. In order to be able to add resonators on a periodic cell it is necessary to slightly modify the model so that it can express the presence of a spring mass. As shown in Fig.3.1, the resonant system is placed at the intersection of two segments. Although theoretically these two segments may have their own characteristics, for practical reasons it is preferable that the segments surrounding a resonator are identical.

The addition of a resonator impacts the continuity and equilibrium equations between two segment of the unit cell,Eq. 2.5, taking into account the force $F_x u(x_n)$ is the force applied by the mouvement $X(x_n)$ of the resonator on the waveguide in the longitudinal direction, see Fig. 3.1(b.2). It can be expressed as follows

$$\begin{array}{rcccl}
u^w_{n-1}(x_n) & = & u^w_n(x_n), & & \\
\dfrac{\partial u^w_{n-1}(x_n)}{\partial x} - k_l(X(x_n) - u(x_n)), & = & \Delta E \Delta S \dfrac{\partial u^w_n(x_n)}{\partial x}, & & \\
-k_l(X(x_n) - u(x_n)) & = & M\frac{\partial^2 X(x_n)}{\partial x^2} & = & -F_x u(x_n), \\
X(x_n) & = & \left(\frac{k_l}{k_l - M\omega^2}\right), & & \\
F_x & = & k_l(1 - \frac{k_l}{k_l - \omega^2 M}), & & \\
\dfrac{\partial u^w_{n-1}(x_n)}{\partial x} - F_x^{\theta_x} u^w_{n-1}(x_n) & = & \Delta E \Delta S \dfrac{\partial u^w_n(x_n)}{\partial x}, & &
\end{array} \tag{B.1}$$

with $\Delta E = \frac{E_n}{E_{n-1}}$ the ratio between the Young's moduli of the segments $n-1$and n, $\Delta S = \frac{S_n}{S_{n-1}}$ the ratio of segment areas $n-1$, n. For the torsional eigenfrequency the force $F_{\theta_x} = k_t(1 - \frac{k_t}{k_t - \omega^2 J_t})$ applied by the resonator on the waveguide, $J_t = \frac{M(r_m^2 + r_k^2)}{2}$ see Fig. 3.1(b.4) is express similarly.

$$\begin{array}{rcl}
u^w_{n-1}(x_n) & = & u^w_n(x_n), \\
\dfrac{\partial u^w_{n-1}(x_n)}{\partial x} - F_{\theta_x} u^w_{n-1}(x_n) & = & \Delta E \Delta S \dfrac{\partial u^w_n(x_n)}{\partial x},
\end{array} \tag{B.2}$$

The addition of resonators has also led to the periodic cell being considered as being composed of n segments, so that several resonators can be added to a periodic cell. The changes applied to the calculation of dispersion diagrams for longitudinal and torisonal waves also apply to flexural waves.

B.2 Floquet Bloch model for flexural wave dispersion

Each resonator impacts the beam segment on which it is placed with a force of $F_y v(x_n)$ for the flexural mode, $Y(x_n)$ displacement of the mass M, see Fig. 3.1(b.1), and an force of F_{θ_z} for the oscillatory mode, $\theta_z(x_n)$ displacement of the mass M, see Fig. 3.1(b.3).

The condition set then applies up to the n section,

$$\begin{aligned} v_{n-1}(x_n) &= v_n(x_n) \\ \Psi_{n-1}(x_n) &= \Psi_n(x_n) \\ M_{n-1}(x_n) - k_o(\theta_z(x_n) - \frac{\partial v(x_n)}{\partial x}) &= M_n(x_n) \\ Q_{n-1}(x_n) - k_f(Y(x_n) - v(x_n)) &= Q_n(x_n), \end{aligned} \tag{B.3}$$

Which can be simplified with

$$\begin{aligned} -k_f(Y(x_n) - v(x_n)) &= M\frac{\partial^2 Y(x_n)}{\partial x^2} &= -F_y v(x_n), \\ Y(x_n) &= \left(\frac{k_f}{k_f - M\omega^2}\right) \\ F_y &= k_f(1 - \frac{k_f}{k_f - \omega^2 M}) \end{aligned} \tag{B.4}$$

and

$$\begin{aligned} -k_o(\frac{\partial v(x_n)}{\partial x} - v(x_n)) &= J_o\frac{\partial^2 \theta_z(x_n)}{\partial x^2} &= -F_o\frac{\partial v(x_n)}{\partial x}, \\ (-J_o\omega^2 + k_o)\theta_z(x_n) &= k_o\frac{\partial v(x_n)}{\partial x}, \\ \theta_z(x_n) &= \left(\frac{k_o}{k_o - J_o\omega^2}\right) \\ F_o &= k_o(1 - \frac{k_o}{k_o - \omega^2 M}) \end{aligned} \tag{B.5}$$

with $J_o = \frac{M(r_m^2 + r_k^2)}{4} + \frac{Ml^2}{12}$

This allows us to rewrite Eq. B.3 :

$$\begin{aligned} v_{n-1}(x_n) &= v_n(x_n) \\ \Psi_{n-1}(x_n) &= \Psi_n(x_n) \\ M_{n-1}(x_n) - F_o\frac{\partial v(x_n)}{\partial x} &= M_n(x_n) \\ Q_{n-1}(x_n) - F_y v(x_n) &= Q_n(x_n), \end{aligned} \tag{B.6}$$

The interface and periodicity conditions between cells, Eq. 2.9, in the case of a periodic structure with n segment can be written as follows :

the linking conditions between the last section of the cell, section n and the first section of the next cell, section $n+1$ become :

$$\begin{aligned} v_n(x_n) &= v_{n+1}(x_n) \\ \Psi_n(x_n) &= \Psi_{n+1}(x_n) \\ M_n(x_n) &= M_{n+1}(x_n) \\ Q_n(x_n) &= Q_{n+1}(x_n). \end{aligned} \tag{B.7}$$

The periodicity of the system is translated by the Floquet conditions which are written at the junction between the last and the first section of the next cell,

$$\begin{gathered} v_1(0) = e^{ik_b} v_n(x_n) \\ \Psi_1(0) = e^{ik_b} \Psi_n(x_n) \\ M_1(0) = e^{ik_b} M_n(x_n) \\ Q_1(0) = e^{ik_b} Q_n(x_n) \end{gathered} \tag{B.8}$$

Eq. B.7 and Eq. B.8 are relevant for the flexural equations but similar reasoning can be applied for longitudinal and torsional waves.

This calculation method is relevant in the case of a waveguide consisting of a set of periodic cells. In the further part of the chapter, the effect of a single resonator, or a set of different resonators, on the waveguide is determined. In order to identify this influence, the reflection and transmission coefficients are calculated.

B.3 Reflection and transmission coefficients of locally resonant structures

Longitudinal and torsional wave propagation

For longitudinal and torsional waves the resonator can be represented using transfer matrix method [38], to analyze the wave propagation in the waveguide modeled by a 1D Helmholtz equation.

$$\frac{\partial^2 u_i^w}{\partial x^2} + (k_i^w)^2 u_i^w = 0, \tag{B.9}$$

where u_i^w is the displacement of the wave. $k = \frac{\omega}{c_l}$ is the wave number with $c_l = \sqrt{E/\rho_i}$ the speed of the wave.

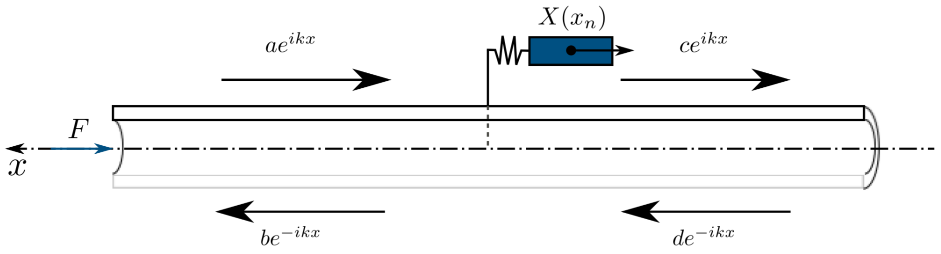

Figure B.1 – Locally resonant mass spring with longitudinal excitation

Consider the locally resonant structure as shown in Fig. B.1, the force incident wave ae^{ikx} are partly reflected and partly transmitted. The ratios of the reflected and transmitted waves amplitudes to those of the incident waves depend on the characteristics of the resonator. Suppressing the $e^{i\omega t}$ time dependance for clarity, the beam displacement is given by:

$$\begin{aligned} u(x) &= ae^{ikx} + be^{-ikx}, \quad upstream. \\ u(x) &= ce^{ikx} + de^{-ikx}, \quad downstream. \end{aligned} \tag{B.10}$$

The reflected and transmitted waves are expressed as:

$$\begin{aligned} ce^{ikx} &= Tae^{ikx}. \\ be^{-ikx} &= Rae^{ikx}. \end{aligned} \tag{B.11}$$

The scattering matrix S express the effect of the resonator on the support structure,

$$\begin{pmatrix} c \\ d \end{pmatrix} = S \begin{pmatrix} a \\ b \end{pmatrix},. \tag{B.12}$$

The resonator, placed "in parallel" to the longitudinal and torsional wave propagation, produce a discontinuity of velocity:

$$S = \begin{pmatrix} 1 & 0 \\ D_a & 1 \end{pmatrix} = \begin{pmatrix} T_{M_{11}} & T_{M_{12}} \\ T_{M_{21}} & T_{M_{22}} \end{pmatrix}. \tag{B.13}$$

with $D_a = \frac{(M.k_{l,t}.\omega^2)}{(k_{l,t} - M.\omega^2)}$.

From Eq. B.13, the reflection and transmission coefficients can be written as:

$$\begin{aligned} R &= \frac{T_{M_{11}} + \frac{T_{M_{12}}}{(iEkS)^{-1}} - \frac{T_{M_{21}}}{iEkS} - T_{M_{22}}}{T_{M_{11}} + \frac{T_{M_{12}}}{(iEkS)^{-1}} + \frac{T_{M_{21}}}{iEkS} + T_{M_{22}}}, \\ T &= \frac{2e^{ikx_{x=0}}}{T_{M_{11}} + \frac{T_{M_{12}}}{(iEkS)^{-1}} + \frac{T_{M_{21}}}{iEkS} + T_{M_{22}}}, \end{aligned} \tag{B.14}$$

Therefore,

$$\begin{aligned} R &= -\frac{\frac{D_a}{i.E.k.S}}{2 + \frac{D_a}{i.E.k.S}}, \\ T &= \frac{2}{2 + \frac{D_a}{i.E.k.S}}, \end{aligned} \tag{B.15}$$

with D_a describes the resonant character of the system by taking into account its resonant frequency, and can be expressed as $D_a = \frac{M\omega^2}{1 - \left(\frac{\omega}{\omega_a}\right)^2}$ with $\omega_a = \sqrt{\frac{k_{l,t}}{M}}$ the resonant frequency of the system.

We note that when the frequency of the incident wave ω tends towards ω_a we have $\lim_{\omega \to \omega_a} D_a(\omega) = +\infty$ which implies $\lim_{\omega \to \omega_a} R(\omega) = 1$ and $\lim_{\omega \to \omega_a} T(\omega) = 0$ which means that the incident wave will be totally reflected and not transmitted.

These reflection and transmission coefficients depend on the characteristics of the materials used for the waveguide and the resonators, in particular the complex Young modulus of the rubber. When losses are introduced with a complex Young's modulus, $E' = E(1 + \eta i)$, the incident wave will no longer be totally reflected and not transmitted. The absorption coefficient $\alpha = 1 - |R|^2 - |T|^2$ quantifies the portion of the wave that will be absorbed by the losses induced by the complex Young's modulus of the resonator. In the case of a configuration with a single resonator the absorption is maximal at $\lim_{\omega \to \omega_a} \alpha(\omega) = 1 - |R|^2 - |T|^2 = 0.5$ when $|R| = 1 - |T| = 0.5$ [54].

Flexural wave propagation

For flexural waves, the calculation of the transmission and reflection coefficients, is based on El-Khatib works [50]. In the present case, we evaluate the vibrations in the far field, i.e. that the incident wave is induced by the application of a force sufficiently distant from the resonator and that the measuring point are also far from both source and resonator. This assumption allows evanescent waves to be excluded from the calculation. Consider the locally resonant structure as shown in Fig. B.2, the incident wave $v_{incident}$ are partly reflected and partly transmitted. The ratios of the reflected and transmitted wave amplitudes to those of the incident waves depend on the characteristics of the resonator and of the waveguide. Assuming Euler-Bernouilli conditions, the flexural wave propagation is modeled with:

$$\frac{\partial^4 v(x)}{\partial x^4} - k^4 v(x) = 0, \tag{B.16}$$

where $k^4 = \frac{\rho S \omega^2}{EI}$ is the flexural wavenumber, S the cross section, I the quadratic moment.

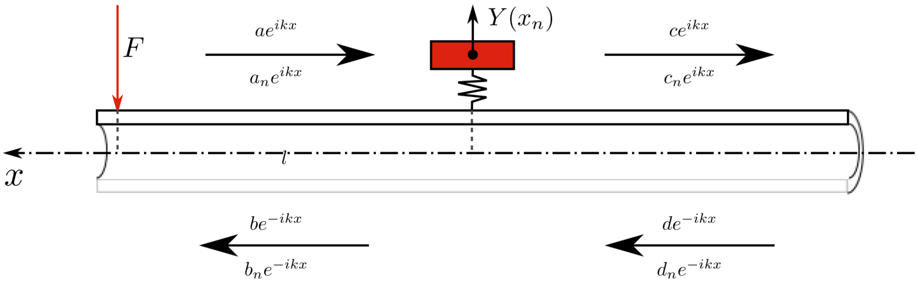

Figure B.2 – Locally resonant mass spring with flexural excitation

Consider the locally resonant structure as shown in Fig. B.2, the incident wave $v_{incident}$ is partly reflected, partly transmitted and partly absorbed if losses are considered. The ratios of the reflected and transmitted wave amplitudes to those of the incident waves depend on the characteristics of the resonator and on the waveguide. The absorption of the resonator is defined as $\alpha = 1 - |T|^2 - |R|^2$ where T and R are the transmission and reflection coefficients. Suppressing the $e^{i\omega t}$ time dependence for clarity, the beam displacement is given by:

$$v_i(x) = ae^{ikx} + a_N e^{-kx} + be^{-ikx} + b_N e^{kx}, \tag{B.17}$$

The complex amplitudes of the incident, $v^{incident}$, reflected, $v_{reflected}$ and transmitted, $v_{transmitted}$, waves are composed by propagative and evanescent waves:

$$v_{incident} = \begin{pmatrix} a \\ a_N \end{pmatrix}, \quad v_{reflected} = \begin{pmatrix} b \\ b_N \end{pmatrix}, \quad v_{transmitted} = \begin{pmatrix} c \\ c_N \end{pmatrix} \tag{B.18}$$

The transmitted and reflected waves can be expressed as [50]:

$$\begin{pmatrix} c \\ c_N \end{pmatrix} = t \begin{pmatrix} a \\ a_N \end{pmatrix}, \quad \begin{pmatrix} b \\ b_N \end{pmatrix} = r \begin{pmatrix} a \\ a_N \end{pmatrix}. \tag{B.19}$$

The reflection and transmission matrice can be expressed considering the continuity and equilibrium condition,

$$\begin{array}{ccccc} v_{incident}(x_n) & + & v_{reflected}(x_n) & = & v_{transmitted}(x_n) \\ \Psi_{incident}(x_n) & + & \Psi_{reflected}(x_n) & = & \Psi_{transmitted}(x_n) \\ M_{incident}(x_n) & + & M_{reflected}(x_n) & = & M_{transmitted}(x_n) \\ Q_{incident}(x_n) & + & Q_{reflected}(x_n) - F_y v(x_n) & = & Q_{transmitted}(x_n), \end{array} \tag{B.20}$$

with

$$F_y = k_f\left(1 - \frac{k_f}{k_f - \omega^2 M}\right). \tag{B.21}$$

Assuming that we are in far field condition, the reflection and transmission coefficients can be expressed by $R = |c/a|$ and $T = |b/a|$ which gives according to El-Khatib [50]:

$$\begin{aligned} T &= \frac{\Omega^2-(1+\gamma\sqrt{\Omega})}{(\Omega^2-(1+\gamma.\sqrt{\Omega}.(1+1i)))}, \\ R &= 1-\left|1+ie^{-2ikx_n}\left(\frac{\gamma\sqrt{\Omega}}{\Omega^2(1+\gamma\sqrt{\Omega}(1+1i))}\right)\right|, \end{aligned} \tag{B.22}$$

With $\gamma = \frac{\pi M}{2\rho S\lambda_a}$, $\lambda_a = \frac{2\pi}{\left(\frac{\rho S}{EI}\omega_a^2\right)^4}$, $\Omega = \frac{\omega}{\omega_a}$, $\omega_a = \sqrt{\frac{k_f}{M}}$.

The analytical reflection and transmission coefficients obtained are compared in Fig. B.3 with results obtained numerically for a structure composed of a steel ring on a rubber ring forming a local resonator positioned on a support beam as defined in Fig. 3.1(a).

Figure B.3, shows the analytical results by the solid line. We do not consider structural damping in the materials, $E'_{rubber} = E_{rubber}(1+\eta i)$ with $\eta = 0$, wich lead to the absence of the absorption $\alpha = 1-|R|^2-|T|^2 = 0$. It can be seen that for a resonator we obtain at the corresponding resonance frequency a peak of total reflection $|R| = 1$ and zero transmission $|T| = 0$ for the flexural mode, in red. The torsional mode, in green, and the longitudinal mode, in blue, have also a peak in reflection and transmission but less pronounced with a smaller frequency range, the frequency position of these peaks corresponds to the frequencies of the longitudinal and torsional modes.

In this section the transmission and reflection coefficients of a resonator, obtained analytically and numerically, are compared. Figure B.3, the analytical results, straight line, are obtained analytically from Eqs. B.15 and B.22. The numerical results, dot line, are obtained from a numerical model described in Chap. 3.

We observe a slight shift in frequency between the results obtained by the numerical and analytical methods, this is probably due to the mass of the support which is not taken into account in the same way between analytical and numerical methods. The visible differences between the two models are due to the inclusion in the numerical calculation of the coupling between the host structure and the resonator, Chap. 3. The model considers the resonator and its influence on the waveguide but also the influence of the waveguide on the resonator, which leads to a modification of the resonance frequency. The assumption of a local resonator adopted for the analytical calculation shows here its limits.

Another important difference is the influence of the flexural resonator, which is underestimated by the analytical model. The transmission value is relatively well correlated, but this is not the case for the reflection value, the numerical values illustrate a reflection coefficient that has much more impact than that predicted by the analytical method. Also around 500 Hz there is an impact on the numerical reflection coefficient, the red dotted curve. This corresponds to the oscillating resonance mode illustrated in Fig. 3.1(b.3), a mode whose influence is not predicted by the analytical model used, only the flexural motion Fig. 3.1(b.1) is calculated.

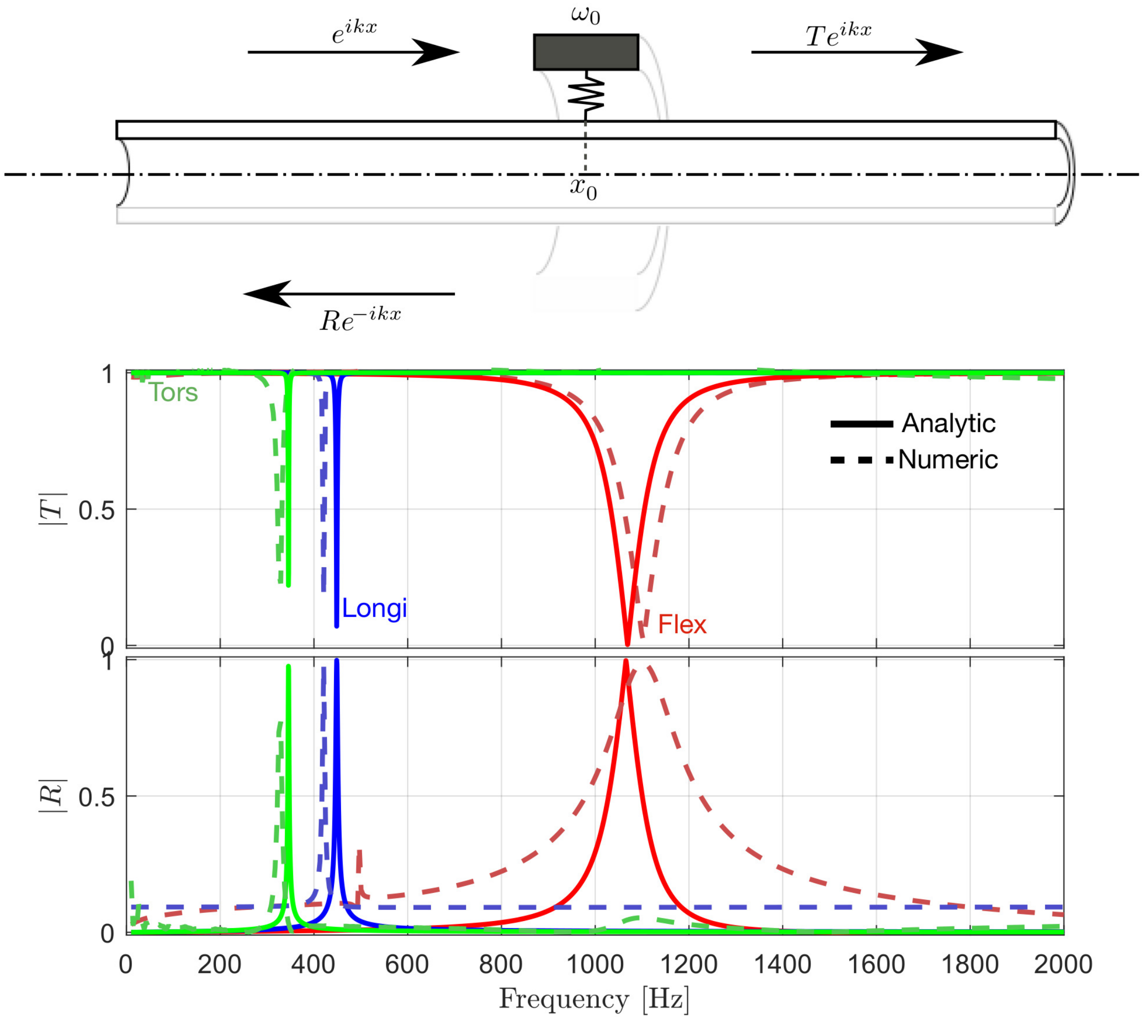

Figure B.3 – Comparison between the numerical, dotted line, and analytical, solid line values of a local resonator. The reflection $|R|$ and transmission $|T|$ values are plotted for each type of movement through the waveguide. Longitudinal waves in blue (●), torsional in green (●), flexural in red (●).

Despite a close estimate of the transmission coefficients for the three calculated wave types, the analytical method described here, does not give a sufficiently close estimate of the finite element reflection coefficients. However, for simpler resonator geometries it is possible that the analytical method could become competitive with the numerical method.

DOCTORAT
BRETAGNE SCIENCES
LOIRE POUR L'INGENIEUR

Le Mans
Université

Titre : Conduits périodiques et localement résonants pour le contrôle des ondes vibratoires en contexte industriel

Mot clés : Guide d'ondes à cristal phononique, Filtre anti-vibration, Absorbeur de vibrations, Structure à résonance locale, Contrôle des vibrations multi-ondes.

Résumé : La maîtrise des vibrations structurelles est un sujet récurrent dans l'industrie. Le contexte de l'industrie automobile ne fait pas exception, car les vibrations et le confort acoustique ne sont pas seulement un argument de vente mais aussi une contrainte législative. Une automobile, qu'elle soit à propulsion thermique ou électrique, doit faire face à d'importants problèmes de vibrations.

Le système peut être représenté par trois éléments : une source de vibrations (par exemple, un moteur ou une pompe), un guide d'ondes (une conduite de carburant, un câble d'alimentation) et un élément rayonnant (une cloison pare-feu, une rail d'injection). Dans ce travail, l'accent est mis sur le guide d'ondes et sur la manière de le transformer pour qu'il empêche les vibrations de la source d'atteindre l'élément rayonnant. Ce travail explore les effets de l'atténuation et de l'absorption des vibrations permises par la conception d'un filtre de vibrations multi-ondes basé sur un cristal phononique et la conception de filtres et d'absorbeurs de vibrations multi-ondes 1D basés sur des résonateurs locaux. Les cristaux phononiques permettent d'obtenir des effets de filtrage avec l'obtention de la bande interdite. Les résonateurs locaux sont utilisés pour obtenir des effets d'atténuation ou d'absorption vibratoire.

Le potentiel applicatif de ce type de système dans le contexte automobile est ensuite discuté autour des effets liés à la courbure d'un guide d'ondes, à son couplage avec une plaque rayonnante et enfin à l'influence d'un fluide lourd dans un guide d'ondes périodique. A travers cette thèse, des modèles analytiques, des simulations numériques et des expériences sont utilisés pour valider le comportement physique des systèmes présentés. Ceci permet de proposer des conceptions pour contrôler la propagation vibratoire dans un guide d'ondes.

Title: Periodic and locally resonant waveguides for vibration control in an industrial context

Keywords: Phononic crystal waveguide, Vibration filter, Vibration absorber, Locally resonant structure, Multi-wave vibration control

Abstract: The control of structural vibrations is a recurrent topic in industry. The automotive industry is no exception, as vibration and acoustic comfort are not only a selling point but also a legislative constraint. An automobile, whether thermally or electrically driven, has to deal with significant vibration problems.

The system can be represented by three elements: a vibration source (e.g., engine or pump), a waveguide (e.g., fuel line, power cable), and a radiating element (e.g., firewall or fuel rail). In this work, the focus is on the waveguide and how to transform it so that it prevents source vibrations from reaching the radiating element. This work explores the effects of vibration attenuation and absorption enabled by the design of a phononic crystal based multi-wave vibration filter and the design of local resonator based 1D multi-wave vibration filters and absorbers. Phononic crystals are used to achieve filtering effects with band gap achievement. Local resonators are used to obtain attenuation or vibration absorption effects.

The applicative potential of this type of system in the automotive context is then discussed around the effects related to the curvature of a waveguide, its coupling with a radiating plate and finally the influence of a heavy fluid in a periodic waveguide. Through this thesis, analytical models, numerical simulations and experiments are used to validate the physical behavior of the presented systems. This allows to propose designs to control the vibratory propagation in a waveguide.